Politecnico di Milano
Dept. of Aerospace Science and Technology
Doctoral Programme in Aerospace Engineering

EFFICIENT INDIRECT OPTIMIZATION OF LOW-THRUST TRAJECTORIES WITH INTERIOR-POINT CONSTRAINTS

Doctoral Dissertation of:
Yang Wang

Supervisor:
Prof. Francesco Topputo

Tutor:
Prof. Camilla Colombo

Coordinator:
Prof. Pierangelo Masarati

Academic year 2021/22 – Cycle XXXIII

Dedicated to my family

ABSTRACT

THIS dissertation addresses the challenging low-thrust trajectory optimization problems. The goal is to improve the efficiency and effectiveness of the indirect method to advance and mature the mission design methods.

First, analytic gradients are achieved and leveraged to improve both computational efficiency and convergence robustness of the indirect method for low-thrust optimization with interior-point constraints. Particular attention is placed on the analysis of discontinuities produced by interior-point constraints and bang-bang control. The presented methods are able to offer desired discontinuous bang-bang solutions and their accurate gradients. A variety of problems have been solved, including interplanetary transfers with a variable specific impulse and power-limited engine, Earth-orbit transfers with eclipses, and interplanetary transfers with multiple flyby, rendezvous and gravity-assist events. Also, preliminary asteroid screening of the M-ARGO (Miniaturised Asteroid Remote Geophysical Observer) mission has been carried out by using the developed method.

Second, tailored homotopy continuation methods are designed to effectively solve fuel-optimal many-revolution Earth-orbit transfers with eclipses, thrust continuation of time-optimal many-revolution orbital transfers, and asteroid porkchops in the M-ARGO mission. A generic homotopy method based on Theory of Functional Connections (TFC) is also developed. The TFC-based homotopy method implicitly defines infinite homotopy paths, allowing for the selection and switching of homotopy paths to remedy the failure of the continuation process.

SOMMARIO

Questa tesi affronta i difficili problemi di ottimizzazione delle traiettorie spaziali a bassa spinta. Il suo obiettivo è migliorare l'efficienza e l'efficacia dei metodi indiretti per far avanzare e maturare i metodi di progettazione della missione.

Innanzitutto, i gradienti analitici vengono ottenuti e sfruttati per migliorare sia l'efficienza computazionale sia la robustezza dei metodi indiretti per traiettorie a bassa spinta con interior-point constraints. Particolare attenzione è posta all'analisi delle discontinuità prodotte dagli interior-point constraints e dal controllo bang-bang. I metodi presentati sono in grado di offrire le soluzioni bang-bang discontinue desiderate e i loro gradienti in maniera accurata. È stata risolta una serie di problemi, inclusi i trasferimenti interplanetari con un impulso specifico variabile e un motore a potenza limitata, i trasferimenti in orbita terrestre con eclissi e i trasferimenti interplanetari con flyby multipli, rendez-vous e gravity-assist. Inoltre, utilizzando il metodo sviluppato, è stato effettuato lo screening preliminare degli asteroidi della missione M-ARGO (Miniaturised Asteroid Remote Geophysical Observer).

In secondo luogo, vengono presentati schemi di continuazione specificamente progettati per risolvere trasferimenti orbitali a molte rivoluzioni con eclissi che minimizzino il consumo di combustibile, e per risolvere trasferimenti orbitali a molte rivoluzioni al fine di minimizzare il tempo di volo; inoltre, questi schemi di continuazione vengono utilizzati per definire i cosiddetti porkchop plots relativi alla missione M-ARGO. Viene infine sviluppato un metodo basato sulla teoria chiamata Theory of Functional Connections (TFC). Il metodo dell'omotopia basato su TFC definisce implicitamente percorsi di omotopia infiniti, consentendo la selezione dei percorsi e la commutazione tra gli stessi per rimediare all'eventuale fallimento del processo di continuazione.

ACKNOWLEDGEMENTS

The 4-year doctoral journey at Politecnico di Milano is the most treasured experience in my life. I would like to thank sincerely to my supervisor and friend, Prof. Francesco Topputo. Thank you not only for offering me with a fantastic research opportunity to pursue the doctorate at 2017, but also for your time and patience to instruct me step by step. Without your fruitful suggestions and constant encouragement, there would not have this thesis work.

I would like to acknowledge Prof. Roberto Furfaro and Prof. Daniele Mortari for introducing the cutting-edge work on machine learning and Theory of Functional Connections to us. Thanks to Prof. Franco Bernelli-Zazzera for your kindness and warmhearted assistance.

It is my honor to be a member of Deep-Space Astrodynamics Research & Technology (DART) group which is composed of many nice people. Thanks to Diogene Alessandro Dei Tos for your boundless enthusiasm and energy that help me assimilate into the new environment at the 1st year. Thanks to Karthik Mani for introducing your amazing friends to me. The Negroni time is doubtlessly one of my favorite memories. Thanks to Christian Hofmann, the lunch partner and academic collaborator. The rich discussions with you sparked my research. Thanks to Andrea Carlo Morelli for helping me check Italian abstract. Thanks to Vittorio Franzese and Carmine Giordano. I learned a lot from you in the M-ARGO project.

I am also deeply indebted to my Chinese friends. Thanks to Simeng Huang for supporting me in my PhD application and helping me overcome many difficulties subsequently. Thanks to my flatmates: Lang Xu, Bin Fu, Jinbin Fu, and Zhandong Yuan, for making my life at Italy easier. Thanks to Zhenkai Zhang, Haiyang Li, Zhemin Chi, Meiliwen Wu, Yahui Li, Bo Zheng, Yingying Zhang, Shanshan Pan, etc. I cherish friendships and pleasure time with you. Thanks to Zhen Wang, Dongrun Liu, Jiurui Liu and Ling Qin for accompanying me through the difficult COVID period.

I would like to express my gratitude to my thesis reviewers: Prof. Fanghua Jiang and Prof. Lorenzo Casalino. Thank you for taking precious time to read my thesis. I greatly appreciate your valuable comments for improving this thesis.

Thanks to staff and colleagues in Dept. of Aerospace Science and Technology for providing comfortable research environment.

Thanks to China Scholarship Council for the financial support to me to study at Italy (No. 201706290024). Also, part of this work has been funded by European Space Agency through contract No. 4000127373/19/NL/AF.

Last but not the least, words cannot describe how grateful I am for my family. Your unconditional love and support are the powerful impetus for me to strive for my life goals.

TABLE OF CONTENTS

LIST OF FIGURES

LIST OF TABLES

LIST OF ACRONYMS

A

ACT Adjoint Control Transformation

C

CP Chemical Propulsion

CPO close-proximity operations

D

DART Deep-Space Astrodynamics Research & Technology

DCM Discrete Continuation Method

E

ECI Earth-centered inertial

EIGSO Elliptic Inclined Geosynchronous Orbits

EP Electric Propulsion

ESA European Space Agency

G

GEO Geostationary Orbit

GTO Geostationary Transfer Orbit

H

HTS hyperbolic tangent smoothing

L

LCDB Asteroid Lightcurve Database

LEO Low Earth Orbit

LT2.0 Low-Thrust Trajectory Optimizer

M

M-ARGO Miniaturised Asteroid Remote Geophysical Observer

MEE modified equinoctial elements

MPBVP multiple point boundary value problem

MPC Minor Planet Center

N

NEA Near Earth Asteroid

NEO near-Earth object

NLP nonlinear programming problem

NOCP nonlinear optimal control problem

P

PAM Pseudo-arclength Method

PhD Philosophiae Doctor

PMP Pontryagin minimum principle

S

SEP Solar electric propulsion

SPICE Spacecraft Planet Instrument Camera-matrix Events

STM state transition matrix

T

TFC Theory of Functional Connections

TOC Theory of Connections

TOF time of flight

TPBVP two-point boundary value problem

CHAPTER 1

INTRODUCTION

Exploration and exploitation of the uncharted universe is an essential direction to push the scientific frontier, boom technological innovations and thrive the society. Ambitious space missions are envisioned to be implemented in the foreseeable future, involving expeditions to outer Solar System, human station construction on the Moon and Mars, asteroid mining, etc. Space activities are further flourishing with the emerging and thriving of CubeSat missions. The growing complexities of space missions, meanwhile the eternal pursuing of low-cost, high-risk and high-gain goals, pose a high requirement on the mission analysis and design. This thesis aims to advance and mature low-thrust trajectory design methods to benefit newer mission scenarios.

1.1 Spacecraft Propulsion System

A propulsion subsystem is indispensable for effective orbital manoeuvring. From momentum conservation principle, the thrust to accelerate the spacecraft is acquired by ejecting propellants at high kinetic energy [1]. There are mainly two types of propulsion systems for in-space missions [2], i.e., Chemical Propulsion (CP) and Electric Propulsion (EP). CP produces the thrust by converting the chemical energy of the propellant combustion into spacecraft kinetic energy, achieved by accelerating the exhaust gas through an expansion procedure [2–4]. Meanwhile, EP accelerates the spacecraft by making use of electrical power to ionize and eject the propellant at high exhaust speed [2–4].

The Tsiolkovsky rocket equation [1]

$$\Delta v = c \ln \left(1 + \frac{m_p}{m_f} \right)$$

relates the velocity increment Δv to the propellant exhaust velocity c, propellant mass m_p and final mass m_f. To achieve the desired Δv, the thruster with high exhaust velocity is preferable since it allows delivering more payload, which further increases scientific return. In this aspect, the exhaust velocity of CP is limited by the energy stored in the propellant [3]. EP solves this problem since the electric energy is delivered from external energy source, and a high exhaust velocity is consequently achieved [3]. The efficiency of the thruster in terms of fuel consumption is indicated by the specific impulse I_{sp}, defined as the thrust $T = \dot{m}_p c$ per sea-level weight of propellant consumption. Also, it is the impulse delivered per unit of propellant consumption. That is

$$I_{\mathrm{sp}} = \frac{T}{\dot{m}_p \, g_0} = \frac{c}{g_0} = \frac{I}{g_0 \, m_p}$$

where I is the total impulse, defined as the integral of the thrust over time duration. To reach a desired total impulse, the higher I_{sp} implies a lower fuel consumption. The high exhaust velocity of EP offers a higher I_{sp}, thus lower fuel consumption than CP.

However, the thrust level of EP is low, around two orders of magnitude lower than that of CP, since the mass rate $\dot{m}_p$ is very small, limited by the onboard power level [4]. To achieve the desired final velocity and total impulse, EP is usually required to work for a long period of time [3]. Distinct characteristics of CP and EP culminate in their different application scenarios of orbital manoeuvring. The high-thrust feature of CP allows effective orbital changes of the spacecraft in a short amount of time, and the spacecraft flies ballistically during the majority of the mission time. On the other hand, EP burns a long duration to steer the spacecraft to the desired orbit and the spacecraft follows a non-Keplian orbit.

Trajectory design is critical for the feasibility and cost of the mission, since the selected trajectory implies the propellant consumption, time of flight and the corresponding steering law [5]. For the spacecraft equipped with CP, the orbital manoeuvring is always approximated as instantaneous increment of the velocity. For the spacecraft equipped with EP, the control is considered to be continuously varied. This work focuses on the trajectory design for the spacecraft equipped with EP, mainly because EP allows to deliver more payload to boost scientific return and it also allows missions with high Δv that are prohibitive with CP [3]. The success of a number of missions in recent decades, e.g., Deep Space 1 [6], Hayabusa [7], SMART-1 [8], and Dawn mission [9], has validated the reliability of EP. It is noticed that EP is the collection of high specific impulse engines, e.g., Solar electric propulsion (SEP), nuclear propulsion, solar sails and tether techniques. SEP-based trajectory design is considered in this work.

The low-thrust trajectory design is always formulated and solved as a nonlinear optimal control problem (NOCP). The NOCP seeks to determine the control profile that optimize the prescribed objective function while taking into account a set of dynamic constraints, boundary constraints and path constraints. Two types of objectives are commonly minimized: one is related to the quantity of control efforts, also the fuel consumption, the other is the transfer time, or the combination of these two [10]. However, the low-thrust trajectory optimization is difficult to solve due to the following reasons: 1) The thrust allows for two modes of operation, i.e., thrusting and coasting modes. The thrust structure is always not known a priori, thus the solver should determine the sequences of mode switching; 2) Discontinuities in the state and costate variables may be present in the optimal trajectory. For example, the costate is discontinuous when the SEP-based spacecraft enters and exists the shadow region of the Earth, see Chapter 4; 3) Time-dependent forces and constraints may exist; 4) The long-duration time of flight may result in multi-revolution planetocentric transfers, which increases the convergence difficulty.

1.2 Numerical Methods for Trajectory Optimization

Analytical solutions are challenging to obtain in space applications due to the high nonlinear dynamics. Instead, numerical methods are always sought. Numerical methods dedicated to solving NOCPs are mainly categorized as direct methods, indirect methods, dynamical programming and evolutionary algorithms, based on their solving philosophies. In literature, there are already extensive survey papers regarding the available numerical optimal control methods and their advantages and disadvantages for trajectory optimization [5, 10–15]. For the sake of brevity, these methods are briefly reported.

Direct methods Direct methods discretize an infinite dimensional NOCP into a finite dimensional nonlinear programming problem (NLP), then optimize the NLP by searching for the discretized state and control solution, such that the Karush-Kuhn-Tucker conditions are fulfilled [16]. Methods for solving the differential equations and quadrature of functions are the foundation, mainly classified as time-marching and collocation methods [11]. The former implements integration methods, such as Euler and Runge-Kutta methods, to obtain the trajectory at each time step sequentially. The later approximates the trajectory by piecewise polynomials. Dynamical constraints are transformed to nonlinear constraints that are required to satisfy at each collocation points.

Based on the way to transcribe differential equations, direct methods are mainly categorized as three types, i.e., direct single shooting, direct multiple shooting and direct collocation. In direct single shooting, only the control is discretized and time-marching method is executed in the whole duration. In direct multiple shooting, the time domain is partitioned by multiple segments and direct single shooting is executed over each segment. Defect constraints to continuously connect each segment are imposed. In direct collocation methods, both state and control are discretized, and collocation methods are employed to transform differential equations to nonlinear constraints. Many types of collocation methods characterized by quadrature rules have been developed in literature [10]. Nowadays, some commercial-off-the-shelf softwares such as General Purpose OPtimal Control Software (GPOPS) [17] and PseudoSpectral OPTimization (PSOPT) [18] for general NOCPs have been developed that are able to automatically transform the NOCP to the NLP, and solve the NLP with state-of-the-art optimization methods [11]. Also, some softwares tailored to trajectory optimization have been developed to solve complex problems [19–21].

The main benefits of using direct methods are the easy handling of complicated path and boundary constraints, and the broad convergence domain, making it easy for the user to provide the initial guess solution. Additionally, there is no need for the user to derive analytical differentiations [10]. However, the obtained solution offers few information for the possible improvement [10]. Besides, direct methods usually require much computational efforts, especially for many-revolution trajectories [14]. A large number of parameters and high-order integrator are usually required to obtain an accurate solution [22]

Indirect methods Based on calculus of variations, indirect methods formulate the Euler-Lagrange equations, i.e., first-order necessary conditions for local optimality, that the state and costate should satisfy [10]. From Pontryagin's Minimum Principle, the optimal control, which is always the function of state and costate, is derived such that the Hamiltonian is minimized at any time on the optimal trajectory [10]. Indirect methods then transforms the NOCP to a two-point boundary value problem (TPBVP) or a multiple point boundary value problem (MPBVP) if interior-point constraints are involved [23]. The transformed problem is mainly comprised of Euler-Lagrange equations, boundary conditions, transversality conditions and complementary conditions [10]. The NOCP is further solved as a zero-finding problem [24].

Similar to direct methods, three indirect methods are commonly used to solve the NOCP, i.e., indirect single shooting, indirect multiple shooting and indirect collocation [5]. In indirect single shooting, differential equations of state and costate are integrated using time-marching methods to the terminal time. The decision variables are guessed first, and iteratively updated to match conditions in TPBVP/MPBVP using techniques such as the shooting method [24]. Indirect single shooting is straightforward, but it suffers from the numerical difficulty caused by the high sensitivity to the initial guess such that small changes in the initial costate can lead to abrupt change of the trajectory at the terminal time [12]. The indirect multiple shooting is one of techniques to circumvent the sensitivity problem by dividing the time interval into multiple subintervals. The sensitivity is reduced with the sacrifice of markedly increased number of unknowns and constraints [12]. The other commonly used method to mitigate the sensitivity is combining the shooting method with continuation methods, which gradually approach the solution by solving a series of auxiliary problems, starting from the solution of an easier problem [12]. The continuation process enables to effectively expand the convergence domain, but with the cost of higher computational burden. The indirect collocation method employs piecewise polynomial to represent the solution and a set of nonlinear constraints are imposed to ensure that dynamical constraints are satisfied. The difference with respect to direct collocation is that the state and costate dynamical equations are required in indirect collocation [12].

The main benefits of indirect methods are that the solution produced is highly accurate and guaranteed to be at least extremal [5, 11]. Also, it provides more theoretical insight about the optimal solution [5]. The main drawback is the small convergence domain of a zero-finding method. The guess of costate values becomes more difficult due to the possibility of non-physical interpretation of the costate [12].

Dynamic programming In dynamic programming approaches, Bellman's Principle of Optimality is fundamental, stated as: "An optimal policy has the property that whatever the initial state and initial decision are, the remaining decisions must constitute an optimal policy with regard to the state resulting from the first decision" [25]. Based on Bellman's Principle of Optimality, dynamic programming handles the NOCP by searching the cost-to-go function which satisfies a first-order nonlinear partial differential equations known as the Hamilton–Jacobi–Bellman equation (HJB) [26]. The solution of HJB equation over domain of interest provides optimal feedback control law, instead of the open-loop solution. However, the solution is difficult to determine due to the curse of dimensionality, i.e., the memory and computational time grow rapidly with dimensionality, which limits its applications to complicated NOCPs [5].

A variety of dynamic programming methods have been developed to alleviate the curse of dimensionality [27]. One category gradually approaches the solution by solving a sequence of approximate problems, such as series solution method [28], differential dynamic programming (DDP) [29] and generating function method [30], etc. The other category is to solve the cost-to-go function directly, such as finite difference method [31] and neural network method [32], etc. Among them, DDP has been applied to various studies on trajectory optimization [29, 33, 34]. The idea of DDP is to approach the optimal solution through a succession of quadratic subproblems around a reference trajectory [5]. The curse of dimensionality is eased with the cost by achieving a local optimal solution, instead of a global optimal solution [5].

Evolutionary methods Evolutionary methods are global techniques that mimic the process of natural evolution [15]. Various methods have been developed in literature, e.g., genetic algorithm [35], differential evolution [36] and particle swarm algorithms [37], etc. To implement evolutionary algorithms, the unknowns should be represented by a relatively smaller number of discrete parameters [10]. Some features of evolutionary methods are distinct from other methods [10]. Firstly, evolutionary methods do not require the initial guess solution, since they search from a population of solutions; Secondly, the optimization process uses the information of objective function but does not require gradient information. Thirdly, evolutionary methods employ stochastic ways, instead of deterministic ways, to iteratively search the solution. Even though they are more likely to converge to a global solution, it is not guaranteed and more than one optimizer is suggested to verify the solution [10]. Evolutionary methods have proven to be effective for various trajectory optimisation problems [38–40].

1.3 The Research Questions

In preliminary space mission phase, mission designers are interested in exploring and assessing as many trajectory options as possible, in a short duration and with limited resources [5]. However, mission tasks related to low-thrust trajectory optimization are challenging that often require high computational load. For example, in asteroid missions, the trajectory designer has the task of filtering appropriate targets from thousands of asteroids, which involves assessment of tremendously high number of trajectories. However, numerical optimization methods are usually time consuming and their convergence is questionable. Thus, the efforts to enhance the rapid trajectory search capability with broader domains of convergence of the mission design tool are desirable. This thesis aims to improve the efficiency, robustness and reliability of the indirect method to favor the mission analysis and design.

In literature, the methods to improve the performance of indirect methods for low-thrust trajectory optimization have been extensively studied from various aspects, including effective continuation methods [41–43], initialization of non-intuitive costates [44–46], analytic gradients [45, 47], switch detection [48], etc. These techniques have been proposed to effectively expand the convergence domain and determine the sequence of bang-bang control in the fuel-optimal problem. However, most works did not consider some realistic constraints which are critical for the mission analysis, thus the corresponding techniques may fail in more complex environments. For instance, in Earth-orbit transfers considering shadow eclipses, the costate is discontinuous when the spacecraft enters or exits the shadow region [49–51]. This extra discontinuity causes the failure of techniques such as analytic gradients derived in [47].

Constraints for NOCPs can be roughly categorized as interior-point constraints and path constraints. This thesis mainly considers low-thrust trajectory optimization with interior-point constraints, corresponding to a variety of low-thrust transfer problems, such as Earth-orbit transfers with eclipses, interplanetary transfers with multiple flyby, rendezvous and gravity-assist events, etc. The NOCP with interior-point constraints is actually a MPBVP [23]. Also, these problems can be categorized as hybrid optimal control problems, which are NOCPs involving discontinuous state, costate, dynamics and decision-making where the discontinuity is produced by discrete events [5]. The aim of this thesis is to enhance the efficiency and effectiveness of the indirect method for these problems. The improvement in aspect of computational efficiency and robust convergence is achieved by developing analytic gradients and homotopy continuation methods.

Analytic gradients In trajectory optimization, the gradients of problem functions with respect to problem decision variables are at the heart of most methods [52]. Finite difference methods are classical gradient estimation methods which approximate the gradients by truncating Taylor series of a function at a given point [53]. Although these methods are straightforward and easy to implement, the computational load is usually high, and the accuracy inherently relies on the selected perturbation size, which is difficult to tune [54]. For example, the forward difference first-order formula is

$$f'(x) = \frac{f(x+h) - f(x)}{h} + \mathcal{O}(h)$$

where h is the perturbation step-size and $\mathcal{O}(h)$ is the truncation error. When this formula is employed to estimate the gradients, h has to be a small value to reduce truncation errors. However, h cannot be too small, in order to avoid subtractive cancellation errors. This step-size dilemma makes it difficult to select h that ensures accurate gradients.

Advanced techniques such as automatic differentiation (AD) [55], complex step differentiation (CSD) [53] and the variational method [47] improve the numerical accuracy using different philosophies. AD exploits the facts the complicated function can be expressed by the combination of elementary arithmetic operators and functions, and evaluated by repeatedly applying the chain rule [56]. CSD estimates gradients by making use of complex variables [57]. The higher gradient accuracy is achieved since it elegantly eliminates the subtractive cancellation error [57, 58]. However, both AD and CSD require extensive implementation and the execution time could be high [54]. The variational method is a promising method that offers accurate gradients with generally short computational time [52]. In the variational method, gradients are computed through the state transition matrix (STM) and the chain rule, where the STM provides sensitivities between states and costates at different time instants along a given trajectory [45]. Unlike finite-difference methods, the STM offers accurate gradients without tuning the perturbation step-size for each independent variable [59]. The drawback is that symbolic manipulations are generally required, and the integration becomes more complicated when discontinuities are involved.

Finite difference methods are sufficiently accurate in most cases. However, for trajectory optimization with interior-point constraints, the gradient accuracy of finite difference methods is problematic due to the discontinuity produced by interior-point constraints and bang-bang control, see Section 4.3. It is worth to exploit analytic gradients due to their high benefits on computational efficiency and gradient accuracy. Impulsive transfer problems are typical NOCPs with interior-point constraints [60], and a number of works have been devoted to exploiting the analytic gradients [54, 61–64]. However, for low-thrust optimization problems, analytic gradients are only available for cases without interior-point constraints [45, 47]. To the best of the author's knowledge, analytic gradients for low-thrust optimization problems that involve interior-point constraints are still vacant for indirect methods. Thus, the first research question is:

> For low-thrust trajectory optimization problems with interior-point constraints, how to derive, calculate and assess analytic gradients in the indirect method ?

Homotopy continuation methods Since the smoothing technique was introduced in [41], the homotopy continuation methods have been extensively developed in low-thrust trajectory design as an effective way to determine the solution with broader convergence domain [43, 44, 65]. The homotopy method solves the objective problem by tracking the homotopy path, which is comprised of solutions of a series of auxiliary problems [66]. The design of homotopy continuation process for complicated low-thrust transfer problems is the concern of this thesis.

Moreover, it is observed that the continuation process has the potential to fail to proceed when the homotopy path encounters unfavorable conditions, such as limit points (where the Jacobian matrix is ill-conditioned) or the path goes off to infinity [65]. In this aspect, pseudo-arclength method is a general method to effectively pass limit points by reversing the homotopy path direction and augmenting the Jacobian matrix [66]. Additionally, in [67, 68], the continuation parameter was extended to the complex domain to avoid singular points. However, these methods may still fail, e.g., when the homotopy path grows indefinitely [69, 70]. This in turn calls for enhancements to improve the algorithmic robustness in homotopy methods. These raise the second research question:

> How to design homotopy continuation methods to widen the convergence domain, reduce computational load and recover failures in low-thrust trajectory optimization ?

1.4 Overview and Contributions

The structure of this thesis is illustrated in Fig. 1.1, including research pillars, research problems, space applications and corresponding chapters. The work is based on three pillars, M-ARGO CubeSat mission, indirect optimization and Theory of Functional Connections (TFC). M-ARGO is the first European Space Agency (ESA) stand-alone CubeSat mission to independently rendezvous with and characterise a NEA [71]. Whereas, TFC is a mathematical framework to perform linear functional interpolation. It has the property that no matter what the auxiliary function is, the constrained function always satisfies a prescribed set of constraints [72].

Research problems are abstracted from space applications and the corresponding algorithms in turn are dedicated to enhancing the low-thrust trajectory optimization. Mainly two types of research problems are studied: low-thrust optimization with interior-point constraints and continuation methods in optimization. Research problems about low-thrust optimization with scalar and multi-dimensional interior-point constraints are studied separately since the former allows analytical expressions of scalar Lagrange multipliers corresponding to interior-point constraints. In this work, this fact is explored to enable the indirect method to solve a MPBVP as a TPBVP. Yet, scalar multipliers can also be treated as unknowns like the multi-dimensional case, but the user has to provide good initial guesses and their number.

The contributions from a broader point of view:

1. Analytic gradients are achieved and leveraged to improve both computational efficiency and convergence robustness of the indirect method for low-thrust optimization with interior-point constraints.
2. Tailored homotopy continuation methods are designed to effectively solve a variety of low-thrust optimization problems. A TFC-based homotopy method for general problems is developed that enables to remedy the failure of the continuation process by selecting and switching homotopy paths.

In the following, the introduction and contributions of each chapter are depicted:

1. Chapter 2 studies power-limited asteroid rendezvous trajectory optimization by a SEP-based spacecraft, motivated by M-ARGO and dedicated to the task of asteroid screening (Chapter 3). The engine characterised with variable specific impulsive and limited power input is taken into consideration. Particular attention is paid to analyzing the impact of power constraints on the indirect optimization and the optimal solution. Methods and contributions:
   - The low-thrust optimization with scalar interior-point constraints is formulated. Analytical multipliers related to interior-point constraints are obtained. This result is leveraged to transform this MPBVP as a TPBVP.
   - The STM across costate and dynamics discontinuities produced by power constraints and bang-bang control is derived.
   - In order to ease the costate initialization, two continuation methods are used to approach a discontinuous control by a consecutive sequence of continuous controls: 1) energy-optimal to fuel-optimal continuation, to mitigate the convergence difficulty associated to bang-bang control in the fuel-optimal problem, and 2) Hyperbolic Tangent Smoothing (HTS), to handle engine switch on/off related to power bounds. The advancement to the HTS in [42] consists of the capability to achieve the desired discontinuous solution.
   - The flowchart in [47] is augmented by involving power-related branches. The computational framework is established by combining analytic derivatives, switching detection and continuation into the augmented flowchart. The core capability is the accurate computation for both time-optimal and fuel-optimal trajectories and their gradients.
2. Chapter 3 reports the preliminary asteroid screening in the M-ARGO mission. The paramount task is to search reachable NEA targets with mission constraints. Methods and contributions:
   - The original and systematic multi-step selection process to extract the reachable near-Earth asteroids and subsequently down-select asteroids is developed.
   - Thousands of both time-optimal and fuel-optimal low-thrust trajectory optimisation problems have been solved, using the indirect method and the thruster model featuring variable input power, thrust, and specific impulse presented in Chapter 2. The down-selection of asteroids are further executed by analyzing and filtering porkchops, and fulfilling scientific requirements.
   - Initial results indicate mission feasibility for M-ARGO, which has the potential to enable a completely new class of low-cost deep-space exploration missions.
3. Chapter 4 concerns fuel-optimal Earth-orbit transfers with eclipses. This problem inherently belongs to the same problem category as Chapter 2. Here, many-revolution solutions are sought. Methods and contributions:
   - The events of shadow entrance and exit are modelled as scalar interior-point constraints. The analytical expression of the scalar multiplier is derived.
   - The STM across costate and dynamics discontinuities produced by shadow constraints and bang-bang control is derived. It is found that the ill-conditioned STM

may occur when the spacecraft flies over the edge of the shadow on the optimal trajectory. The energy-optimal to fuel-optimal continuation may fail in many-revolution transfers due to the ill-conditioned STM.

- To effectively find fuel-optimal many-revolution solutions, a continuation scheme is proposed. It consists of determining the fuel-optimal solution without shadow constraints starting from the energy-optimal solution without shadow constraints first, then determining the fuel-optimal solution with shadow constraints by gradually increasing the number of eclipse arcs.
- The integration flowchart in [47] is augmented to involve event branches of shadow entrance and exit. Fuel-optimal bang-bang solutions and their accurate gradients for many-revolution transfers are achieved by using the indirect method for the first time.

4. Chapter 5 studies fuel-optimal deep-space transfers with multi-dimensional interior-point constraints. Interplanetary transfers with intermediate flyby, rendezvous and gravity-assist events belong to this category. The corresponding NOCP is challenging since the state and costate are instantaneously varied due to discrete events, and interior-point constraints are time-dependent. Moreover, the multipliers have to be sought along with other decision variables. Methods and contributions:
   - The time domain is partitioned into multiple segments with interior-point time, initial and terminal time as boundaries. The derivatives of state, costate and each constraint are carried out in each segment first, then extend to the whole domain using the chain rule.
   - The recursive formulae of derivatives of each constraint with respect to unknowns at previous interior-point time instants are established in the chain rule.
   - Analytic gradients of indirect optimization for deep-space transfers are achieved. Compared to the finite difference method, the proposed method enables to improve the performance of the shooting method effectively.
5. Chapter 6 investigates the thrust continuation for many-revolution time-optimal Earth-orbit transfers, where the terminal orbit is specified by a subset of orbital elements. Starting from the time-optimal solution with large thrust level and few revolutions, the thrust continuation is implemented to approach the time-optimal solution with small thrust level. However, it is observed that the thrust continuation fails at certain thrust level due to the failure to determine the solution to the lower thrust, in the vicinity of current solution. Methods and contributions:
   - Based on the observation that many local solutions exist for the considered orbital transfer problem, an enhanced thrust continuation scheme is presented that embeds the method to connect local solutions with different revolutions. The thrust continuation allows to proceed by starting from another local solution with more revolutions.
   - The solution connection is achieved by augmenting the dynamics and solving a series of auxiliary problems. This method can effectively search local solutions with different revolutions for a specific thrust level.
   - Numerical evident indicates the near constancy of $t_f \times T_{\max}$ exists for more general orbital transfers.

6. Chapter 7 develops the TFC-based homotopy continuation algorithm to solve zero-finding problems. Current homotopy algorithms' success highly relies on empirical knowledge, due to manually, inherently selected homotopy paths. This calls for enhancements to improve the algorithmic robustness in homotopy methods. Methods and contributions:

    - The TFC-based homotopy function is defined. Different from existing homotopy functions, the TFC-based homotopy function implicitly defines infinite homotopy paths, from which the most promising ones are selected.

    - A two-layer continuation algorithm is devised, where the first layer tracks the homotopy path by monotonously varying the continuation parameter, while the second layer recovers possible failures resorting to a TFC representation of the homotopy function.

    - Compared to the pseudo-arclength method, the proposed TFC-based method retains the simplicity of direct continuation while allowing a flexible path switching. Thus, TFC-based method represents another general strategy to remedy the failure of the homotopy path.

The core output of this work is the enhanced version of Low-Thrust Trajectory Optimizer (LT2.0), which is the software toolkit initially developed by DART group. The development of this thesis enhances and extends LT2.0 for more complex space applications.

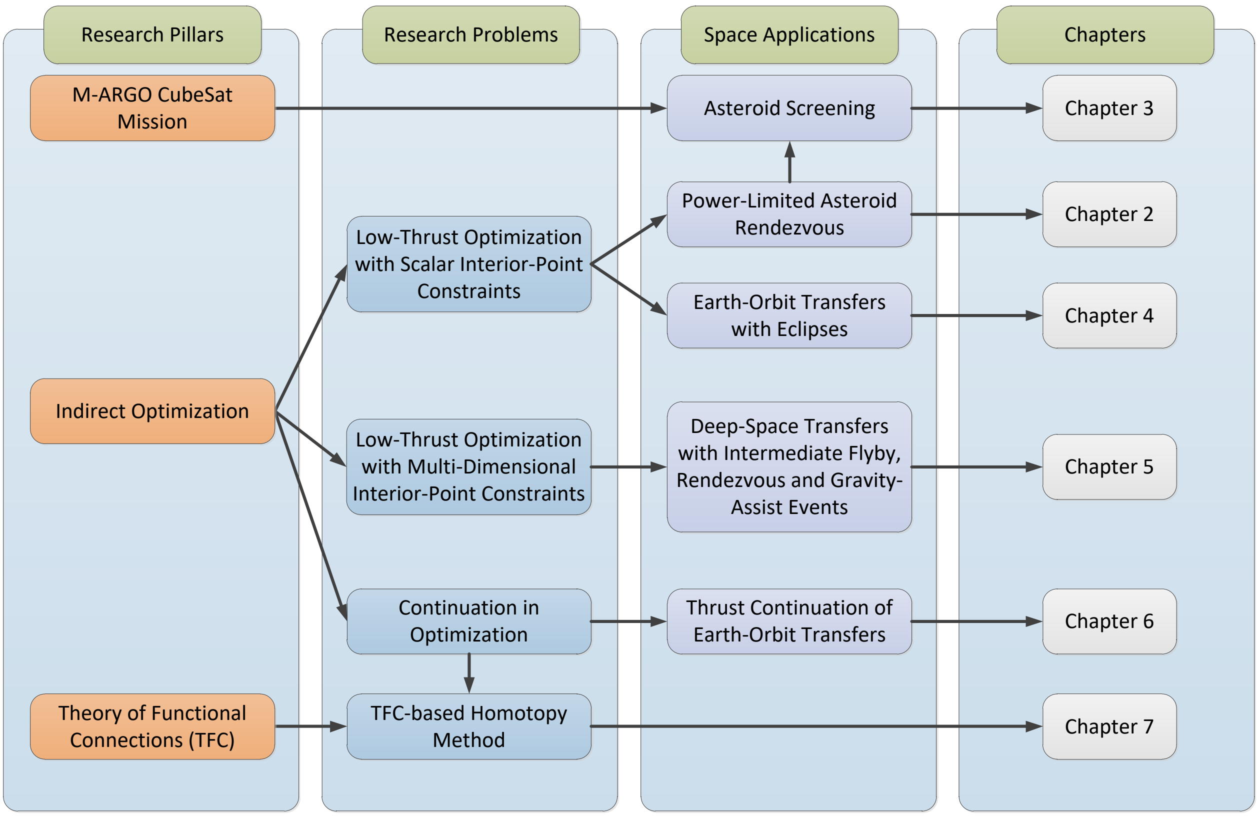

Figure 1.1: *Thesis structure.*

1.5 Publications

Some conference papers and journal papers based on this Philosophiae Doctor (PhD) thesis have been published. The paper about the contents of Chapter 4 is currently under review. The published papers include:

1. Y. Wang, F. Topputo, Indirect Optimization of Power-Limited Asteroid Rendezvous Trajectories. Journal of Guidance, Control and Dynamics.
   Accepted. See Chapter 2
2. Y. Wang, F. Topputo, A TFC-based Homotopy Continuation Algorithm with Application to Dynamics and Control Problems. Journal of Computational and Applied Mathematics, 2022, 401: 113777.
   doi: 10.1016/j.cam.2021.113777. See Chapter 7
3. F. Topputo, Y. Wang, C. Giordano, et al, Envelop of Reachable Asteroids by M-ARGO CubeSat. Advances in Space Research, 2021, 67(12): 4193–4221.
   doi: 10.1016/j.asr.2021.02.031. See Chapter 3
4. Y. Wang, F. Topputo, Indirect Optimization for Low-Thrust Transfers with Earth-Shadow Eclipses. 31st AAS/AIAA Space Flight Mechanics Meeting, virtual, 2021: 1-17.
   AAS 21–368. See Chapter 4

The following papers are based techniques used in this thesis, but not included in this thesis.

1. Y. Wang, F. Topputo, Robust Bang-Off-Bang Low-Thrust Guidance Using Model Predictive Static Programming. Acta Astronautica, 2020, 176: 357-370.
   doi: 10.1016/j.actaastro.2020.06.037.
2. Y. Wang, F. Topputo, Model Predictive Static Programming for Bang-off-Bang Low-Thrust Neighboring Control Law Design. 70th International Astronautical Congress, 2019. Washington D.C., IAC-19,C1,9,3,x49975.

CHAPTER 2

POWER-LIMITED ASTEROID RENDEZVOUS TRAJECTORY OPTIMIZATION

Energized by the electric power from solar panels, SEP is a paramount option to enable cost-effective space access. The electrical power to accelerate the propellant used by most SEP thrusters varies with heliocentric distance [73]. In turn, the thrust, propellant mass flow rate, and specific impulse vary as a function of the input power [73–75]. Incorporating an accurate SEP engine model into indirect optimization improves mass budget estimation. Due to technological constraints, the input power to the engine is limited, and the related bounded values are key thruster parameters [73–75]. The spacecraft flies ballistically if insufficient power is provided [76], while the input power is capped when excess power is available [77]. Therefore, the convergence difficulty is exacerbated by dynamics discontinuities produced by power constraints [78]. Smoothing techniques have been employed in [78–80]. Power operation detection was developed in [81] to improve solution accuracy. In indirect optimization, the gradients of nonlinear boundary constraints with respect to problem decision variables are critical for most zero-finding methods [52]. However, the effects of power constraints on the gradients and the optimal solution are still unexplored. This chapter analyzes this issue and further presents an efficient indirect method featuring analytic gradients for SEP-based trajectory optimization. The method is tailored for target screening of M-ARGO mission in Chapter 3.

2.1 Problem Statement

2.1.1 Mathematical Model

The heliocentric phase of an interplanetary orbit transfer problem is considered. The equations of motion are

$$\dot{\boldsymbol{x}} = \boldsymbol{f}(\boldsymbol{x}, u, \boldsymbol{\alpha}) \Rightarrow \begin{cases} \dot{\boldsymbol{r}} = \boldsymbol{v} \\ \dot{\boldsymbol{v}} = -\dfrac{\mu}{r^3}\boldsymbol{r} + u\dfrac{T_{\max}}{m}\boldsymbol{\alpha} \\ \dot{m} = -u\dfrac{T_{\max}}{I_{\text{sp}}\, g_0} \end{cases} \tag{2.1}$$

where $\boldsymbol{r}$, $\boldsymbol{v}$, and m are the spacecraft position vector, velocity vector, and mass, respectively; $\boldsymbol{x} := [\boldsymbol{r}^\top, \boldsymbol{v}^\top, m]^\top$ is the state vector, $u \in [0, 1]$ is the thrust throttle factor and $\boldsymbol{\alpha}$ is the thrust direction unit vector; g_0 is the gravitational acceleration at sea level. Both the maximum thrust $T_{\max}$ and the specific impulse I_{sp} are assumed to vary with the engine input power P_{in}, i.e. , $T_{\max} = T_{\max}(P_{\text{in}})$ and $I_{\text{sp}} = I_{\text{sp}}(P_{\text{in}})$. It is assumed that $P_{\text{in}} = P_{\text{in}}(r)$ is a function of the spacecraft-Sun distance.

We define $S_p = S_p(r)$ as the power switching function used to detect the thruster operation logic (see Fig. 2.1):

$$\text{if } S_p(r) \geqslant P_{\max} \quad \text{then} \quad P_{\text{in}} = P_{\max},\ u \in [0, 1] \tag{2.2}$$

$$\text{if } S_p(r) \in [P_{\min}, P_{\max}) \quad \text{then} \quad P_{\text{in}} = S_p(r),\ u \in [0, 1] \tag{2.3}$$

$$\text{if } S_p(r) < P_{\min} \quad \text{then} \quad P_{\text{in}} = S_p(r),\ u = 0 \tag{2.4}$$

where $P_{\max}$ and $P_{\min}$ are upper and lower bounds of power input to the engine, respectively.

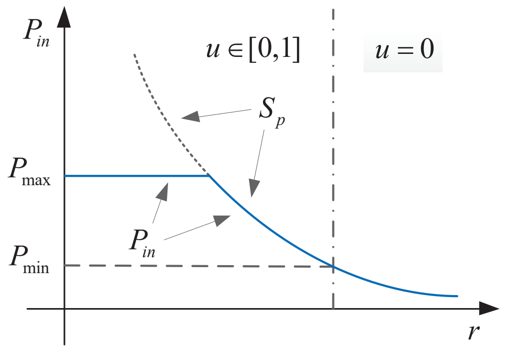

Figure 2.1: *Geometric relationship between P_{in} and S_p.*

It is convenient to define the following gradients

$$\boldsymbol{t}_r := \left(\frac{\partial T_{\max}}{\partial \boldsymbol{r}}\right)^\top = \begin{cases} \dfrac{\partial T_{\max}}{\partial P_{\text{in}}} \dfrac{\partial P_{\text{in}}}{\partial r} \left(\dfrac{\partial r}{\partial \boldsymbol{r}}\right)^\top & \text{if } S_p < P_{\max} \\ \boldsymbol{0}_{3\times 1} & \text{otherwise} \end{cases} \tag{2.5}$$

$$\boldsymbol{i}_r := \left(\frac{\partial I_{\text{sp}}}{\partial \boldsymbol{r}}\right)^\top = \begin{cases} \dfrac{\partial I_{\text{sp}}}{\partial P_{\text{in}}} \dfrac{\partial P_{\text{in}}}{\partial r} \left(\dfrac{\partial r}{\partial \boldsymbol{r}}\right)^\top & \text{if } S_p < P_{\max} \\ \boldsymbol{0}_{3\times 1} & \text{otherwise} \end{cases} \tag{2.6}$$

and $(\partial r/\partial \boldsymbol{r})^\top = \boldsymbol{r}/r$.

Remark 2.1. *In actual flight, the engine switches off when $S_p < P_{\min}$, so implying $P_{\text{in}} = 0$. However, to mimic a ballistic flight, we set $P_{\text{in}} = S_p$ and $u = 0$ for trajectory optimization purposes. Setting P_{in} to 0 creates discontinuity that artificially increases the complexity of the problem.*

2.1.2 Fuel-Optimal Problem

With t_i and t_f given, the fuel-optimal problem is to minimize

$$J_f = \int_{t_i}^{t_f} u \frac{T_{\max}}{I_{\text{sp}}\, g_0} \, \mathrm{d}t \tag{2.7}$$

under the following boundary conditions

$$\boldsymbol{r}(t_i) - \boldsymbol{r}_i = 0, \quad \boldsymbol{v}(t_i) - \boldsymbol{v}_i = 0, \quad m(t_i) - m_i = 0 \tag{2.8}$$

$$\boldsymbol{r}(t_f) - \boldsymbol{r}_T(t_f) = 0, \quad \boldsymbol{v}(t_f) - \boldsymbol{v}_T(t_f) = 0 \tag{2.9}$$

where $\boldsymbol{r}_T(t)$ are $\boldsymbol{v}_T(t)$ are the known time-dependent position and velocity vectors of the moving target body, respectively.

The Hamiltonian function reads

$$H = \boldsymbol{\lambda}_r \cdot \boldsymbol{v} + \boldsymbol{\lambda}_v \cdot \left(-\frac{\mu}{r^3}\boldsymbol{r} + u\frac{T_{\max}}{m}\boldsymbol{\alpha} \right) + \lambda_m \left(-u\frac{T_{\max}}{I_{\text{sp}}\, g_0} \right) + u\frac{T_{\max}}{I_{\text{sp}}\, g_0} \tag{2.10}$$

where $\boldsymbol{\lambda} := [\boldsymbol{\lambda}_r^\top, \boldsymbol{\lambda}_v^\top, \lambda_m]^\top$ is the vector of Lagrange multipliers (costates) associated to $\boldsymbol{x}$.

The optimal thrust direction is such that H is minimized at any time by virtue of the Pontryagin minimum principle (PMP) [26], i.e.,

$$\boldsymbol{\alpha}^* = -\frac{\boldsymbol{\lambda}_v}{\lambda_v} \tag{2.11}$$

where $\lambda_v = \|\boldsymbol{\lambda}_v\|_2$ is the Euclidean norm of $\boldsymbol{\lambda}_v$. The optimal throttle factor u^* is determined by the PMP and the power availability, as

$$u^* = \begin{cases} 0 & S_f > 0 \quad \text{or} \quad S_p < P_{\min} \\ 1 & S_f < 0 \quad \text{and} \quad S_p \geqslant P_{\min} \\ \in [0, 1] & S_f = 0 \quad \text{and} \quad S_p \geqslant P_{\min} \end{cases} \tag{2.12}$$

where the fuel-optimal throttle switching function S_f is

$$S_f = 1 - \lambda_m - \frac{I_{\text{sp}}\, g_0}{m}\lambda_v \tag{2.13}$$

Remark 2.2. *An interior-point constraint should be addressed to ensure that Eq.* (2.12) *satisfies necessary conditions of optimality; see Section 2.1.4.*

It is clear from Eq. (2.12) that u^* exhibits a bang-bang profile. In order to alleviate the numerical difficulty, a smoothing technique is implemented to gradually enforce this discontinuity. The following objective function [41]

$$J_\varepsilon = \int_{t_i}^{t_f} \frac{T_{\max}}{I_{\text{sp}}\, g_0} \left[u - \varepsilon u(1-u) \right] \mathrm{d}t \tag{2.14}$$

yields an energy-optimal problem for $\varepsilon = 1$ and a fuel-optimal problem for $\varepsilon = 0$. The idea is to solve an energy-optimal problem (with t_i, t_f given and the boundary conditions in Eqs. (2.8)-(2.9)) and to continue the solution manifold while gradually reducing ε, until the fuel-optimal problem is solved [47].

The Hamiltonian of the auxiliary problem is

$$H_\varepsilon = \boldsymbol{\lambda}_r \cdot \boldsymbol{v} + \boldsymbol{\lambda}_v \cdot \left(-\frac{\mu}{r^3}\boldsymbol{r} + u\frac{T_{\max}}{m}\boldsymbol{\alpha}\right) + \lambda_m \left(-u\frac{T_{\max}}{I_{\mathrm{sp}}\, g_0}\right) + \frac{T_{\max}}{I_{\mathrm{sp}}\, g_0}\left[u - \varepsilon u(1-u)\right] \tag{2.15}$$

The optimal thrusting direction $\boldsymbol{\alpha}^*$ is the same as in Eq. (2.11). Substituting Eq. (2.11) into Eq. (2.15) yields

$$H_\varepsilon = \boldsymbol{\lambda}_r \cdot \boldsymbol{v} - \frac{\mu}{r^3}\boldsymbol{r} \cdot \boldsymbol{\lambda}_v + \frac{T_{\max}}{I_{\mathrm{sp}}\, g_0}\, u\left(S_\varepsilon - \varepsilon + \varepsilon u\right) \tag{2.16}$$

where the throttle switching function S_ε is

$$S_\varepsilon = 1 - \lambda_m - \frac{I_{\mathrm{sp}}\, g_0}{m}\lambda_v \tag{2.17}$$

The optimal throttle factor u^* is determined by the PMP and the power availability, as

$$u^* = \begin{cases} 0 & S_\varepsilon > \varepsilon \quad \text{or} \quad S_p < P_{\min} \\ 1 & S_\varepsilon < -\varepsilon \quad \text{and} \quad S_p \geqslant P_{\min} \\ \dfrac{\varepsilon - S_\varepsilon}{2\varepsilon} & |S_\varepsilon| \leqslant \varepsilon \quad \text{and} \quad S_p \geqslant P_{\min} \end{cases} \tag{2.18}$$

The motion of the spacecraft can be determined by integrating the following state-costate dynamics

$$\dot{\boldsymbol{y}} = \boldsymbol{F}_\varepsilon(\boldsymbol{y}) \Rightarrow \begin{pmatrix} \dot{\boldsymbol{r}} \\ \dot{\boldsymbol{v}} \\ \dot{m} \\ \dot{\boldsymbol{\lambda}}_r \\ \dot{\boldsymbol{\lambda}}_v \\ \dot{\lambda}_m \end{pmatrix} = \begin{pmatrix} \boldsymbol{v} \\ -\dfrac{\mu}{r^3}\boldsymbol{r} - u\dfrac{T_{\max}}{m}\dfrac{\boldsymbol{\lambda}_v}{\lambda_v} \\ -u\dfrac{T_{\max}}{I_{\mathrm{sp}}\, g_0} \\ -\dfrac{3\mu}{r^5}\left(\boldsymbol{r}\cdot\boldsymbol{\lambda}_v\right)\boldsymbol{r} + \dfrac{\mu}{r^3}\boldsymbol{\lambda}_v + \dfrac{u\lambda_v}{m}\boldsymbol{t}_r + \dfrac{(\lambda_m - 1 + \varepsilon)u - \varepsilon u^2}{I_{\mathrm{sp}}\, g_0}\left(\boldsymbol{t}_r - \dfrac{T_{\max}}{I_{\mathrm{sp}}}\boldsymbol{i}_r\right) \\ -\boldsymbol{\lambda}_r \\ -\dfrac{u\,\lambda_v\, T_{\max}}{m^2} \end{pmatrix} \tag{2.19}$$

where $\boldsymbol{y} := [\boldsymbol{x}^\top, \boldsymbol{\lambda}^\top]^\top$. Note that $\boldsymbol{\alpha}^*$ in Eq. (2.11) is already embedded into Eq. (2.19).

Since the terminal mass is free and the augmented terminal cost does not explicitly depend on the mass, there exists

$$\lambda_m(t_f) = 0 \tag{2.20}$$

From Eq. (2.19), $\dot{\lambda}_m$ is always non-positive, thus $\lambda_m(t) \geqslant 0$ due to $\lambda_m(t_f) = 0$, for $t \in [t_i, t_f]$.

2.1.3 Time-Optimal Problem

In a time-optimal problem, the spacecraft has to rendezvous with a moving target. The terminal conditions are the same as in Eq. (2.9), but in this case t_f is free. The objective function is

$$J_t = \int_{t_i}^{t_f} 1 \, \mathrm{d}t \tag{2.21}$$

thus the Hamiltonian reads

$$H_t = \boldsymbol{\lambda}_r \cdot \boldsymbol{v} + \boldsymbol{\lambda}_v \cdot \left(-\frac{\mu}{r^3}\boldsymbol{r} + u\frac{T_{\max}}{m}\boldsymbol{\alpha} \right) - \lambda_m u \frac{T_{\max}}{I_{\mathrm{sp}}\, g_0} + 1 \tag{2.22}$$

The optimal thrust direction $\boldsymbol{\alpha}^*$ is again given by Eq. (2.11), whereas the optimal throttle factor u^* is

$$u^* = \begin{cases} 0 & S_t > 0 \quad \text{or} \quad S_p < P_{\min} \\ 1 & S_t < 0 \quad \text{and} \quad S_p \geqslant P_{\min} \\ \in [0,1] & S_t = 0 \quad \text{and} \quad S_p \geqslant P_{\min} \end{cases} \tag{2.23}$$

where the time-optimal throttle switching function is

$$S_t = -\lambda_v \frac{I_{\mathrm{sp}}\, g_0}{m} - \lambda_m \tag{2.24}$$

The transversality condition at terminal time t_f is [81]

$$H_t(t_f) - \boldsymbol{\lambda}_r(t_f) \cdot \boldsymbol{v}_T(t_f) - \boldsymbol{\lambda}_v(t_f) \cdot \boldsymbol{a}_T(t_f) = 0 \tag{2.25}$$

where $\boldsymbol{a}_T$ is the acceleration of the target body.

The motion of the spacecraft can be determined by integrating the following state-costate dynamics

$$\dot{\boldsymbol{y}} = \boldsymbol{F}_t(\boldsymbol{y}) \Rightarrow \begin{pmatrix} \dot{\boldsymbol{r}} \\ \dot{\boldsymbol{v}} \\ \dot{m} \\ \dot{\boldsymbol{\lambda}}_r \\ \dot{\boldsymbol{\lambda}}_v \\ \dot{\lambda}_m \end{pmatrix} = \begin{pmatrix} \boldsymbol{v} \\ -\frac{\mu}{r^3}\boldsymbol{r} - u\frac{T_{\max}}{m}\frac{\boldsymbol{\lambda}_v}{\lambda_v} \\ -u\frac{T_{\max}}{I_{\mathrm{sp}}\, g_0} \\ -\frac{3\mu}{r^5}\left(\boldsymbol{r} \cdot \boldsymbol{\lambda}_v\right)\boldsymbol{r} + \frac{\mu}{r^3}\boldsymbol{\lambda}_v + \frac{u\lambda_v}{m}\boldsymbol{t}_r + \frac{u\lambda_m}{I_{\mathrm{sp}} g_0}\left(\boldsymbol{t}_r - \frac{T_{\max}}{I_{\mathrm{sp}}}\boldsymbol{i}_r\right) \\ -\boldsymbol{\lambda}_r \\ -\frac{u\,\lambda_v\, T_{\max}}{m^2} \end{pmatrix} \tag{2.26}$$

2.1.4 Interior-Point Constraint

When $S_p < P_{\min}$ in Eq. (2.4), insufficient power is generated, and the engine switches off ($u = 0$). However, according to the PMP, this action may not be optimal since it is not related to the minimization of the Hamiltonian (Eqs. (2.16) and (2.22)). In order to satisfy the necessary conditions of optimality, this event should be treated as an interior-point constraint [26]. Suppose that S_p crosses $P_{\min}$ at t_s, the following conditions have to be satisfied [26]

$$H(t_s^-) = H(t_s^+) - \pi\frac{\partial S_p}{\partial t} \tag{2.27}$$

$$\boldsymbol{\lambda}_r^\top(t_s^-) = \boldsymbol{\lambda}_r^\top(t_s^+) + \pi\frac{\partial S_p}{\partial \boldsymbol{r}} \tag{2.28}$$

where t_s^- and t_s^+ are time instants before and after t_s, and π is a scalar Lagrange multiplier, and $\partial S_p/\partial t = 0$. In Eq. (2.28), only the component $\boldsymbol{\lambda}_r$ of the costate is discontinuous since $\partial S_p/\partial \boldsymbol{r} \neq \mathbf{0}^\top$. Let π_t and π_ε be the scalar multipliers for the time- and energy-to-fuel-optimal problems, respectively. The following can be said:

Energy-to-fuel-optimal problem The Hamiltonian function at t_s^- and t_s^+ is

$$H_\varepsilon(t_s^-) = \boldsymbol{\lambda}_r(t_s^-) \cdot \boldsymbol{v} - \frac{\mu}{r^3}\boldsymbol{\lambda}_v \cdot \boldsymbol{r} + u(t_s^-)\frac{T_{\max}}{I_{\text{sp}}\, g_0}(S_\varepsilon - \varepsilon + \varepsilon u(t_s^-)) \tag{2.29}$$

$$H_\varepsilon(t_s^+) = \boldsymbol{\lambda}_r(t_s^+) \cdot \boldsymbol{v} - \frac{\mu}{r^3}\boldsymbol{\lambda}_v \cdot \boldsymbol{r} + u(t_s^+)\frac{T_{\max}}{I_{\text{sp}}\, g_0}(S_\varepsilon - \varepsilon + \varepsilon u(t_s^+)) \tag{2.30}$$

Combining Eq. (2.27), (2.29), and (2.30) yields

$$\pi_\varepsilon = \Delta u \frac{T_{\max}}{I_{\text{sp}}\, g_0} \frac{S_\varepsilon - \varepsilon + (u(t_s^+) + u(t_s^-))\varepsilon}{\dot{S}_p} \tag{2.31}$$

where $\Delta u = u(t_s^+) - u(t_s^-)$ and $\dot{S}_p = (\partial S_p/\partial \boldsymbol{r})\dot{\boldsymbol{r}}$.

Remark 2.3. *Let $\boldsymbol{y}(t) = \boldsymbol{\varphi}_\varepsilon(\boldsymbol{y}_i, t_i, t)$ be the solution flow for a specific ε value of Eq.* (2.19) *integrated from the initial time t_i to a generic time t, using $\boldsymbol{x}_i$, $\boldsymbol{\lambda}_i$ at t_i, $\boldsymbol{\alpha}^*$ in Eq.* (2.11) *and u^* in Eq.* (2.18)*. $\boldsymbol{\lambda}_r(t_s^+)$ is computed through Eq.* (2.28) *if S_p crosses $P_{\min}$ at t_s. The energy-to-fuel optimal problem is to find $\boldsymbol{\lambda}_i^*$ such that $\boldsymbol{y}(t_f) = \boldsymbol{\varphi}_\varepsilon([\boldsymbol{x}_i, \boldsymbol{\lambda}_i^*], t_i, t_f)$ satisfies*

$$\begin{pmatrix} \boldsymbol{r}(t_f) - \boldsymbol{r}_T(t_f) \\ \boldsymbol{v}(t_f) - \boldsymbol{v}_T(t_f) \\ \lambda_m(t_f) \end{pmatrix} = \mathbf{0} \tag{2.32}$$

Time-optimal problem The Hamiltonian function at t_s^- and t_s^+ is

$$H_t(t_s^-) = \boldsymbol{\lambda}_r(t_s^-) \cdot \boldsymbol{v} - \frac{\mu}{r^3}\boldsymbol{\lambda}_v \cdot \boldsymbol{r} + u(t_s^-)\frac{T_{\max}}{I_{\text{sp}}\, g_0} S_t + 1 \tag{2.33}$$

$$H_t(t_s^+) = \boldsymbol{\lambda}_r(t_s^+) \cdot \boldsymbol{v} - \frac{\mu}{r^3}\boldsymbol{\lambda}_v \cdot \boldsymbol{r} + u(t_s^+)\frac{T_{\max}}{I_{\text{sp}}\, g_0} S_t + 1 \tag{2.34}$$

Combining Eqs. (2.27), (2.33), and (2.34) yields

$$\pi_t = \Delta u \frac{T_{\max}}{I_{\text{sp}}\, g_0} \frac{S_t}{\dot{S}_p} \tag{2.35}$$

Remark 2.4. *Let $\boldsymbol{y}(t) = \boldsymbol{\varphi}_t(\boldsymbol{y}_i, t_i, t)$ be the solution flow of Eq.* (2.26) *integrated from initial time t_i to a generic time t, using $\boldsymbol{x}_i$, $\boldsymbol{\lambda}_i$ at t_i, $\boldsymbol{\alpha}^*$ in Eq.* (2.11) *and u^* in Eq.* (2.23)*. $\boldsymbol{\lambda}_r(t_s^+)$ is computed through Eq.* (2.28) *if S_p crosses $P_{\min}$ at t_s. The time-optimal problem is to find $\boldsymbol{\lambda}_i^*$ and t_f^* such that $\boldsymbol{y}(t_f) = \boldsymbol{\varphi}_t([\boldsymbol{x}_i, \boldsymbol{\lambda}_i^*], t_i, t_f^*)$ satisfies*

$$\begin{pmatrix} \boldsymbol{r}(t_f) - \boldsymbol{r}_T(t_f) \\ \boldsymbol{v}(t_f) - \boldsymbol{v}_T(t_f) \\ \lambda_m(t_f) \\ H_t(t_f) - \boldsymbol{\lambda}_r(t_f) \cdot \boldsymbol{v}_T(t_f) - \boldsymbol{\lambda}_v(t_f) \cdot \boldsymbol{a}_T(t_f) \end{pmatrix} = \mathbf{0} \tag{2.36}$$

Remark 2.5. *It is assumed that singular arcs where $S_t = 0$ in the time-optimal problem and $S_\varepsilon = 0$ in the fuel-optimal problem are absent over finite time intervals. Also, it is assumed that S_p crosses $P_{\min}$ isolated with $\dot{S}_p \neq 0$.*

Remark 2.6. *A NOCP with interior-point constraints is inherently a MPBVP [23]. By leveraging the analytical expressions of π_ε in Eq. (2.31) and π_t in Eq. (2.35), this MPBVP is transformed into a TPBVP as stated in Remarks 2.3 and 2.4.*

2.2 Solution Method

2.2.1 Initialization of Guess Solution

The Adjoint Control Transformation (ACT) [45] is used to guess the initial costate. The idea is to map the estimation of physical control variables and their derivatives to initial costates at t_i, i.e., $\mathcal{M} : (\alpha_i, \dot{\alpha}_i, \beta_i, \dot{\beta}_i, S_i, \dot{S}_i) \to (\boldsymbol{\lambda}_{ri}, \boldsymbol{\lambda}_{vi})$, where α_i and β_i are the in-plane and out-of-plane thrust angles in a spacecraft-centered frame [45], S_i and $\dot{S}_i$ are initial values of the switching function and its derivative. However, as shown in Eqs. (2.18) and (2.23), power constraints may cause discontinuities in u for time- and energy-optimal problems, which deteriorates the performance of ACT. In these cases, the Hyperbolic Tangent Smoothing (HTS) method in [42] is used. The idea is to replace $T_{\max}$ in the above equations with $\tilde{T}_{\max}$ defined as

$$\tilde{T}_{\max} := \begin{cases} T_{\max} \times \hbar(\rho, \boldsymbol{r}) = T_{\max} \times \dfrac{1}{2}\left[\tanh\left(\dfrac{P_{\text{in}} - P_{\min}}{\rho/\text{PU}}\right) + 1\right] & \rho > 0 \\ T_{\max} & \rho = 0 \end{cases} \tag{2.37}$$

where ρ is a smoothing factor, PU is the power unit, P_{in} and $P_{\min}$ are normalized values by PU. Since the power unit PU used in the simulations (see Table 2.1 in Section 2.3) is large, normalized P_{in} and $P_{\min}$ in Eq. (2.37) are very small. PU is inserted in Eq. (2.37) to ease the selection of ρ_0. The variations of $\tilde{T}_{\max}$ w.r.t. input power for various ρ are shown in Fig. 2.2.

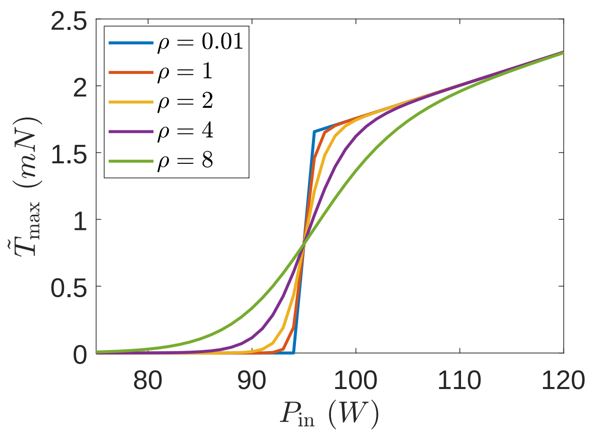

Figure 2.2: *Variations of $\tilde{T}_{\max}$ w.r.t. input power, with $P_{\min} = 95$ W, and P_{in} determined by Eq. (2.59).*

Then the derivative of $\tilde{T}_{\max}$ w.r.t. $\boldsymbol{r}$ for $\rho > 0$ becomes

$$\tilde{\boldsymbol{t}}_r := \left(\frac{\partial \tilde{T}_{\max}}{\partial \boldsymbol{r}}\right)^\top = \begin{cases} \hbar(\rho, \boldsymbol{r})\boldsymbol{t}_r + T_{\max}\left(\dfrac{\partial \hbar}{\partial \boldsymbol{r}}\right)^\top & \text{if } S_p < P_{\max} \\ \boldsymbol{0}_{3\times 1} & \text{otherwise} \end{cases} \tag{2.38}$$

where

$$\left(\frac{\partial \hbar}{\partial \boldsymbol{r}}\right)^{\top} = 2(\hbar - \hbar^2)\frac{\mathrm{PU}}{\rho}\left(\frac{\partial S_p}{\partial \boldsymbol{r}}\right)^{\top} \tag{2.39}$$

Starting from $\rho = \rho_0 > 0$ (a manually selected value that enables the algorithm to find the solution with ρ_0 after several attempts of ACT), $\tilde{T}_{\max}$ approaches $T_{\max}$ while gradually reducing $\rho \to 0$. Here, ACT is used to guess the initial costate to the problem with ρ_0. The improvement to the HTS method in [42] is that the proposed method enables to reach $\rho = 0$, which corresponds to the desired discontinuous solution. This feature is desirable to better assess the HTS method and better understand the optimal solution.

The approximate Hamiltonian functions when using Eq. (2.37) are given by replacing $T_{\max}$ in Eqs. (2.15) and (2.22) with $\tilde{T}_{\max}$. The switching functions (Eqs. (2.17) and (2.24)) and the optimal control policies (Eqs. (2.18) and (2.23)) remain unaltered because they are independent on $T_{\max}$. Since discontinuous control is approximated by continuous control, the interior-point constraints are not triggered. Thus, the HTS approaches the solution to the MPBVP by solving a consecutive sequence of TPBVPs. The dynamics for the approximate energy-to-fuel-optimal and time-optimal problems are simply given by replacing $T_{\max}$ and $\boldsymbol{t}_r$ in Eqs. (2.19) and (2.26) with $\tilde{T}_{\max}$ and $\tilde{\boldsymbol{t}}_r$. Let the right-hand side in Eqs. (2.19) and (2.26) be $\boldsymbol{F}_\varepsilon(\boldsymbol{y}, T_{\max})$ and $\boldsymbol{F}_t(\boldsymbol{y}, T_{\max})$, respectively, then, the approximate dynamics for $\rho > 0$ are $\dot{\boldsymbol{y}} = \boldsymbol{F}_\varepsilon(\boldsymbol{y}, \tilde{T}_{\max})$ and $\dot{\boldsymbol{y}} = \boldsymbol{F}_t(\boldsymbol{y}, \tilde{T}_{\max})$.

2.2.2 Analytic Derivatives

The variational method exploits the STM and the chain rule to compute the gradients [45]. The STM maps small variations in the initial conditions $\delta \boldsymbol{y}_i$ over $t_i \to t$, i.e., $\delta \boldsymbol{y}(t) = \Phi(t, t_i)\delta \boldsymbol{y}(t_i)$. The STM is subject to the variational equation

$$\dot{\Phi}(t, t_i) = D_y \boldsymbol{F}\ \Phi(t, t_i), \quad \Phi(t_i, t_i) = \boldsymbol{I}_{14\times 14} \tag{2.40}$$

where $D_{\boldsymbol{y}}\boldsymbol{F}$, the Jacobian matrix of $\boldsymbol{F}(\boldsymbol{y})$, has two different expressions based on whether u^* is constant ($\boldsymbol{F}(\boldsymbol{y}) := \boldsymbol{F}_t(\boldsymbol{y})$ for the time-optimal problem and $\boldsymbol{F}(\boldsymbol{y}) := \boldsymbol{F}_\varepsilon(\boldsymbol{y})$ for the energy-to-fuel-optimal problem). Let $\boldsymbol{z} := [\boldsymbol{y}^\top, \mathrm{vec}(\Phi)^\top]^\top$ be a 210-dimensional vector containing $\boldsymbol{y}$ and the columns of Φ, where 'vec' is the operator that converts a matrix into a column vector. There exists

$$\dot{\boldsymbol{z}} = \boldsymbol{G}(\boldsymbol{z}) \Rightarrow \begin{pmatrix} \dot{\boldsymbol{y}} \\ \mathrm{vec}(\dot{\Phi}) \end{pmatrix} = \begin{pmatrix} \boldsymbol{F}(\boldsymbol{y}) \\ \mathrm{vec}(D_{\boldsymbol{y}}\boldsymbol{F}\ \Phi) \end{pmatrix} \tag{2.41}$$

Note that Φ maps states and costates along a continuous orbit. When a discontinuity is encountered at the switching time t_s, the STM compensation $\Psi(t_s)$ across the discontinuity should be determined [45]. Suppose there are N discontinuities at $t_1,\ t_2, \cdots, t_N$, the STM is calculated using the chain rule as

$$\Phi(t_f, t_i) = \Phi(t_f, t_N^+)\Psi(t_N)\Phi(t_N^-, t_{N-1}^+)\Psi(t_{N-1})\cdots\Phi(t_2^-, t_1^+)\Psi(t_1)\Phi(t_1^-, t_i) \tag{2.42}$$

Suppose that the discontinuity detected at t_s is indicated by a switching function S crossing a threshold η, then there are three possible cases:

- Case 1: $S = S_\varepsilon$, $\varepsilon = 0$, $\eta = 0$; u jumps between 0 and 1 at t_s.
- Case 2: $S = S_p$, $u \neq 0$, $\eta = P_{\min}$; u jumps between a non-zero value and 0 at t_s.

- Case 3: $S = S_p$, $\eta = P_{\max}$; u remains the same, but the costate dynamics are discontinuous at t_s.

Cases 1 and 3 belong to the first category, where $\boldsymbol{y}$ is continuous but $\dot{\boldsymbol{y}}$ is discontinuous. Case 2 belongs to the second category, where both $\boldsymbol{y}$ and $\dot{\boldsymbol{y}}$ are discontinuous. For both categories, the switching function S at $t_s^- + \delta t_s$ of the neighboring extremal trajectory must satisfy

$$S(\boldsymbol{y}(t_s^- + \delta t_s)) = 0 \tag{2.43}$$

Expanding S at t_s^- yields

$$\mathrm{d}S = \frac{\partial S}{\partial \boldsymbol{y}} \mathrm{d}\boldsymbol{y}(t_s^-) = \frac{\partial S}{\partial \boldsymbol{y}} \delta \boldsymbol{y}(t_s^-) + \frac{\partial S}{\partial \boldsymbol{y}} \dot{\boldsymbol{y}}(t_s^-) \delta t_s = 0 \tag{2.44}$$

thus there exists

$$\delta t_s = -\frac{1}{\dot{S}} \frac{\partial S}{\partial \boldsymbol{y}} \delta \boldsymbol{y}(t_s^-) \tag{2.45}$$

First category Since $\boldsymbol{y}$ is continuous across t_s, then

$$\boldsymbol{y}(t_s^+) = \boldsymbol{y}(t_s^-) \tag{2.46}$$

Taking full differentials on both sides of Eq. (2.46) yields

$$\delta \boldsymbol{y}(t_s^+) = \delta \boldsymbol{y}(t_s^-) + (\dot{\boldsymbol{y}}(t_s^-) - \dot{\boldsymbol{y}}(t_s^+)) \delta t_s \tag{2.47}$$

Substituting Eq. (2.45) into Eq. (2.47) yields $\Psi(t_s)$ as

$$\Psi(t_s) = \frac{\partial \boldsymbol{y}(t_s^+)}{\partial \boldsymbol{y}(t_s^-)} = I_{14\times 14} + \left(\dot{\boldsymbol{y}}(t_s^+) - \dot{\boldsymbol{y}}(t_s^-)\right) \frac{1}{\dot{S}} \frac{\partial S}{\partial \boldsymbol{y}} \tag{2.48}$$

The expressions of $\partial S / \partial \boldsymbol{y}$ and $\dot{S}$ are based on S:

- For $S = S_\varepsilon$, there exists

$$\frac{\partial S_\varepsilon}{\partial \boldsymbol{y}} = \left[-\boldsymbol{i}_r^\top \frac{g_0}{m} \lambda_v, \boldsymbol{0}_{1\times 3}, \frac{I_{\mathrm{sp}}\, g_0}{m^2} \lambda_v, \boldsymbol{0}_{1\times 3}, -\frac{I_{\mathrm{sp}}\, g_0}{m} \frac{\boldsymbol{\lambda}_v^\top}{\lambda_v}, -1\right], \quad \dot{S}_\varepsilon = \frac{I_{\mathrm{sp}}\, g_0}{m \lambda_v} \boldsymbol{\lambda}_r \cdot \boldsymbol{\lambda}_v - \frac{g_0 \lambda_v}{m} \boldsymbol{i}_r \cdot \boldsymbol{v} \tag{2.49}$$

- For $S = S_p$, there exists

$$\frac{\partial S_p}{\partial \boldsymbol{y}} = \left[\frac{\partial S_p}{\partial \boldsymbol{r}}, \boldsymbol{0}_{1\times 11}\right], \quad \dot{S}_p = \frac{\partial S_p}{\partial \boldsymbol{r}} \boldsymbol{v} \tag{2.50}$$

The geometric relationship between $\delta \boldsymbol{y}(t_s^-)$ and $\delta \boldsymbol{y}(t_s^+)$ is shown in Fig. 2.3, where $\delta \boldsymbol{y}(t_s^+)$ is

$$\begin{aligned}
\delta \boldsymbol{y}(t_s^+) &= \delta \boldsymbol{y}(t_s^-) + \Delta \\
&= \delta \boldsymbol{y}(t_s^-) + \left(\dot{\boldsymbol{y}}(t_s^-) - \dot{\boldsymbol{y}}(t_s^+)\right) \delta t_s \\
&= \left[\boldsymbol{I}_{14\times 14} + \left(\dot{\boldsymbol{y}}(t_s^+) - \dot{\boldsymbol{y}}(t_s^-)\right) \frac{1}{\dot{S}} \frac{\partial S}{\partial \boldsymbol{y}}\right] \delta \boldsymbol{y}(t_s^-) \\
&= \Psi(t_s) \delta \boldsymbol{y}(t_s^-)
\end{aligned} \tag{2.51}$$

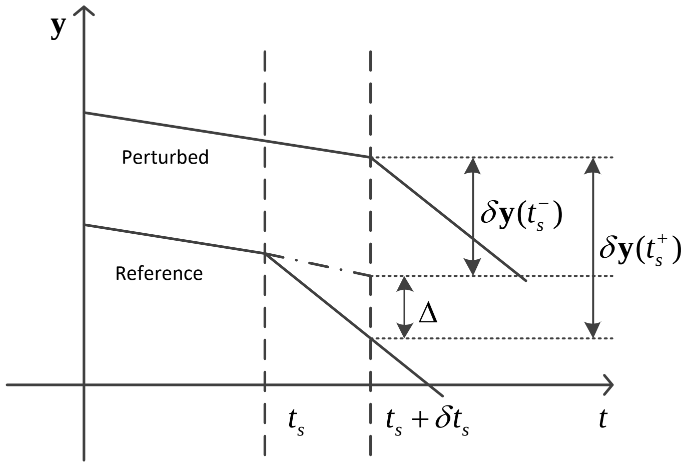

Figure 2.3: *The geometric relationship between $\delta\boldsymbol{y}(t_s^-)$ and $\delta\boldsymbol{y}(t_s^+)$ for the first category.*

Second category This category corresponds to the case when S_p crosses $P_{\min}$. Let us denote the increment of $\boldsymbol{y}$ as $\Delta\boldsymbol{y}(t,\boldsymbol{y}) = [\mathbf{0}_{7\times1},\ \Delta\boldsymbol{\lambda}_r,\ \mathbf{0}_{4\times1}]$ where $\Delta\boldsymbol{\lambda}_r = -\pi(\partial S_p/\partial\boldsymbol{r})^\top$, $\boldsymbol{y}(t_s^+)$ is computed as

$$\boldsymbol{y}(t_s^+) = \boldsymbol{y}(t_s^-) + \Delta\boldsymbol{y} \tag{2.52}$$

Taking full differential on both sides of Eq. (2.52) yields

$$\delta\boldsymbol{y}(t_s^+) = \delta\boldsymbol{y}(t_s^-) + \frac{\partial\Delta\boldsymbol{y}}{\partial\boldsymbol{y}}\delta\boldsymbol{y}(t_s^-) + (\dot{\boldsymbol{y}}(t_s^-) - \dot{\boldsymbol{y}}(t_s^+) + \Delta\dot{\boldsymbol{y}})\delta t_s \tag{2.53}$$

where

$$\Delta\dot{\boldsymbol{y}} = \frac{\partial\Delta\boldsymbol{y}}{\partial\boldsymbol{y}}\dot{\boldsymbol{y}}(t_s^-) \tag{2.54}$$

Substituting Eq. (2.45) into Eq. (2.53) yields $\Psi(t_s)$ as

$$\Psi(t_s) = \frac{\partial\boldsymbol{y}(t_s^+)}{\partial\boldsymbol{y}(t_s^-)} = I_{14\times14} + \frac{\partial\Delta\boldsymbol{y}}{\partial\boldsymbol{y}} + \left(\dot{\boldsymbol{y}}(t_s^+) - \dot{\boldsymbol{y}}(t_s^-) - \Delta\dot{\boldsymbol{y}}\right)\frac{1}{\dot{S}_p}\frac{\partial S_p}{\partial\boldsymbol{y}} \tag{2.55}$$

The geometric relationship between $\delta\boldsymbol{y}(t_s^-)$ and $\delta\boldsymbol{y}(t_s^+)$ is shown in Fig. 2.4. Let us denote the increment of $\boldsymbol{y}$ as $\Delta\boldsymbol{y}(\boldsymbol{y})$, then $\delta\boldsymbol{y}(t_s^+)$ satisfies

$$\begin{aligned}
\delta\boldsymbol{y}(t_s^+) &= \delta\boldsymbol{y}(t_s^-) + [\Delta\boldsymbol{y}(\boldsymbol{y}(t_s+\delta t_s)) - \Delta\boldsymbol{y}(\boldsymbol{y}(t_s))] + \Delta \\
&= \delta\boldsymbol{y}(t_s^-) + \left(\frac{\partial\Delta\boldsymbol{y}}{\partial\boldsymbol{y}}\delta\boldsymbol{y}(t_s^-) + \Delta\dot{\boldsymbol{y}}\delta t_s\right) + (\dot{\boldsymbol{y}}(t_s^-) - \dot{\boldsymbol{y}}(t_s^+))\delta t_s \\
&= \delta\boldsymbol{y}(t_s^-) + \frac{\partial\Delta\boldsymbol{y}}{\partial\boldsymbol{y}}\delta\boldsymbol{y}(t_s^-) + \left(\dot{\boldsymbol{y}}(t_s^-) - \dot{\boldsymbol{y}}(t_s^+) + \Delta\dot{\boldsymbol{y}}\right)\delta t_s \\
&= \left[I_{14\times14} + \frac{\partial\Delta\boldsymbol{y}}{\partial\boldsymbol{y}} + \left(\dot{\boldsymbol{y}}(t_s^+) - \dot{\boldsymbol{y}}(t_s^-) - \Delta\dot{\boldsymbol{y}}\right)\frac{1}{\dot{S}_p}\frac{\partial S_p}{\partial\boldsymbol{y}}\right]\delta\boldsymbol{y}(t_s^-) \\
&= \Psi(t_s)\delta\boldsymbol{y}(t_s^-)
\end{aligned} \tag{2.56}$$

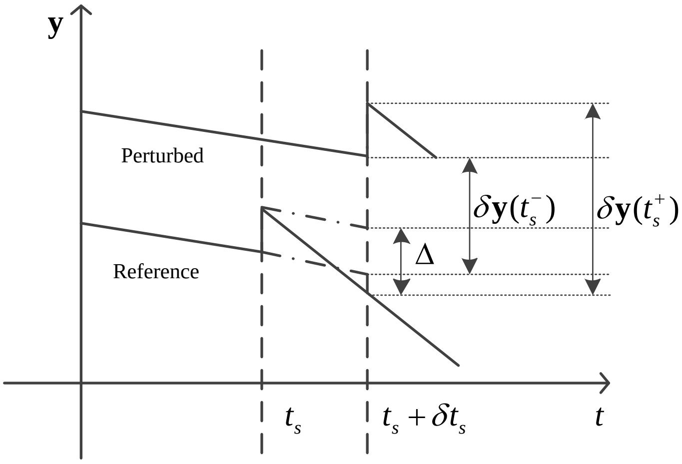

Figure 2.4: *The geometric relationship between $\delta\boldsymbol{y}(t_s^-)$ and $\delta\boldsymbol{y}(t_s^+)$ for the second category.*

2.2.3 Switching Detection Technique

The detection of the switching time t_s is essential because of two facts. Firstly, computing $\Psi(t_s)$ at t_s is necessary for the STM accuracy. Secondly, the integration error accumulates when crossing the discontinuity if the switching time is not explicitly detected. Let us consider a switching function S and the constant threshold η, the task is to find t_s such that $S(\boldsymbol{y}(t_s)) = \eta$. Suppose that at consecutive times t_k and t_{k+1}, there exists $(S(\boldsymbol{y}_k)-\eta)\times(S(\boldsymbol{y}_{k+1})-\eta) < 0$, where $\boldsymbol{y}_k := \boldsymbol{y}(t_k)$ and $\boldsymbol{y}_{k+1} := \boldsymbol{y}(t_{k+1})$. Then the switching time determination algorithm depicted in [47] is used to search $t_s \in [t_k, t_{k+1}]$, with 10^{-12} tolerance.

2.2.4 Augmented Integration Flowchart

To ease the discussion, let p_{type} and u_{type} be the status of the available power input and the thrust throttle, respectively. When $\rho = 0$, the logic is

$$p_{\text{type}} = \begin{cases} \text{On}, & \text{if} \quad S_p \geqslant P_{\max} \\ \text{Medium}, & \text{if} \quad S_p \in [P_{\min}, P_{\max}) \\ \text{Off}, & \text{if} \quad S_p < P_{\min} \end{cases}, \quad u_{\text{type}} = \begin{cases} \text{On}, & \text{if} \quad u = 1 \\ \text{Medium}, & \text{if} \quad u \in (0,1) \\ \text{Off}, & \text{if} \quad u = 0 \end{cases} \tag{2.57}$$

When $\rho \neq 0$, u_{type} is the same as in Eq. (2.57), but p_{type} becomes

$$p_{\text{type}} = \begin{cases} \text{On}, & \text{if} \quad S_p \geqslant P_{\max} \\ \text{Medium}, & \text{if} \quad S_p < P_{\max} \end{cases} \tag{2.58}$$

thus $p_{\text{type}} = \text{Off}$ is not used for $\rho \neq 0$.

The presented integration flowchart in Fig. 2.5 augments the flowchart in [47] (shown with dashed blocks) in order to effectively tackle power constraints. The inputs required to execute an integration step are 1) t_k, the k–th integration time; 2) h_p, the step size predicted by previous integration step; 3) $\boldsymbol{z}_k$, the 210-dimensional state at t_k; 4) u_{type}, the logical type of the thrust throttle; 5) p_{type}, the logical type of the power input; 6) ρ, the smoothing factor.

Three branches emanate according to u_{type}, and for each integration block, a prediction on $\boldsymbol{z}_{k+1}$, e.g., $\boldsymbol{z}_{k+1} = \boldsymbol{\psi}_{\text{RK}}(\boldsymbol{z}_k, t_k, t_k + h_p, u_{\text{type}}, p_{\text{type}}, \rho)$, is executed, using a variable-step seventh/eighth Runge–Kutta integration scheme. Note that $\boldsymbol{z}_{k+1}$ is the state corresponding to $t_{k+1} = t_k + h_f$, where h_f is the corrected time step during Runge–Kutta integration [47]. For the time-optimal problem, $\varepsilon = 0$ in Fig. 2.5.

For $u_{\rm type}$ being On or Medium and $\rho = 0$, the execution blocks are similar. The branch $u_{\rm type}$ = On is analyzed below without losing generality. Since the engine is enforced to switch off in case of insufficient power $P_{\rm in}$, the fist task after one-step integration prediction is to check the power status $p_{{\rm type},k+1}$ corresponding to $\boldsymbol{z}_{k+1}$. If $p_{{\rm type},k+1}$ = Off, indicating that S_p crosses $P_{\min}$, it is then required to execute Block 2 where the power switching time t_s is detected. Let $\boldsymbol{z}_s$ be the 210-dimensional vector, and S_c be the value of S_ε (energy-to-fuel-optimal problem) or S_t (time-optimal problem) at t_s. If $S_c < -\varepsilon$, the STM is computed using Eq. (2.55) which is then stored in $\boldsymbol{z}_s$. $\boldsymbol{z}_{k+1}$ and t_{k+1} used for the next integration step are saved as $\boldsymbol{z}_{k+1} = \boldsymbol{z}_s$ and $t_{k+1} = t_s$. $u_{\rm type}$ is updated to Off and $p_{\rm type}$ is updated to $p_{{\rm type},k+1}$. Otherwise if $S_c > -\varepsilon$, indicating that the throttle switching arises within $[t_k, t_{k+1}]$, thus h_p is reduced.

If $p_{{\rm type},k+1} \neq$ Off, the comparison of $p_{\rm type}$ and $p_{{\rm type},k+1}$ is made. If $p_{\rm type} \neq p_{{\rm type},k+1}$, indicating that S_p crosses $P_{\max}$, then Block 2 is executed. If $S_c < -\varepsilon$ is further satisfied, the STM is computed using Eq. (2.48). $\boldsymbol{z}_{k+1}$ and t_{k+1} are saved as $\boldsymbol{z}_{k+1} = \boldsymbol{z}_s$ and $t_{k+1} = t_s$. $p_{\rm type}$ is updated to $p_{{\rm type},k+1}$. Otherwise, if $p_{\rm type} = p_{{\rm type},k+1}$, the thrust throttle is determined by throttle switching function S_{k+1} that is the value of S_ε (energy-to-fuel-optimal problem) or S_t (time-optimal problem) at t_{k+1}, and the branch $u_{\rm type}$ = On of the flowchart in [47] is executed. For the case $\rho \neq 0$, the implementation is the same except that the branch $p_{{\rm type},k+1}$ = Off is not executed.

For $u_{\rm type}$ being Off, the first task after the one-step integration prediction is to verify the reason that causes the engine to switch off. If $p_{\rm type}$ = Off, then $u = 0$ is caused by insufficient input power. In this case, if $p_{{\rm type},k+1}$ = Off, the solution is saved. Otherwise if $p_{{\rm type},k+1} \neq$ Off, indicating that sufficient power is available for the next step, then Block 2 is executed. The $u(t_s^+)$ after t_s is determined by S_c. For example, if $S_c < -\varepsilon$, then the STM is calculated using Eq. (2.55). $\boldsymbol{z}_{k+1}$ and t_{k+1} are saved as $\boldsymbol{z}_{k+1} = \boldsymbol{z}_s$ and $t_{k+1} = t_s$. $u_{\rm type}$ is updated to On. $p_{\rm type}$ is updated to $p_{{\rm type},k+1}$.

If $p_{\rm type} \neq$ Off, meaning that the engine switches off due to $S_k > \varepsilon$. If $p_{{\rm type},k+1}$ = Off, Block 2 is executed. Since no discontinuity exists, it is not necessary to update the STM, but the power status is updated if $S_c > \varepsilon$. Otherwise if $p_{{\rm type},k+1} \neq$ Off, the check whether $p_{{\rm type},k}$ equals to $p_{{\rm type},k+1}$ is executed. If $p_{\rm type} \neq p_{{\rm type},k+1}$, implying that S_p crosses $P_{\max}$, Block 2 is executed. The power status is updated if $S_c > \varepsilon$. If $p_{\rm type} = p_{{\rm type},k+1}$, the branch $u_{\rm type}$ = Off of the flowchart in [47] is executed.

2.3 Numerical Simulations

The M-ARGO Cubesat mission to the near-Earth asteroid 2000 SG344 is simulated [82]. The physical constants are listed in Table 2.1. The thruster model is handled using fourth-order polynomials as in [82]

$$T_{\max}(P_{\rm in}) = a_0 + a_1 P_{\rm in} + a_2 P_{\rm in}^2 + a_3 P_{\rm in}^3 + a_4 P_{\rm in}^4 \tag{2.59}$$

$$I_{\rm sp}(P_{\rm in}) = b_0 + b_1 P_{\rm in} + b_2 P_{\rm in}^2 + b_3 P_{\rm in}^3 + b_4 P_{\rm in}^4 \tag{2.60}$$

$$S_p(r) = c_0 + c_1 r + c_2 r^2 + c_3 r^3 + c_4 r^4 \tag{2.61}$$

where the coefficients are listed in Table 2.2. All coefficients are normalized before conducting simulations. Figure 2.6 illustrates the variations of $P_{\rm in}$, $T_{\max}$ and $I_{\rm sp}$ w.r.t. the scaled Sun-spacecraft distance r, with $P_{\max}$ = 120 W. It can be seen that at 1 AU we have $P_{\rm in}$ = 105.4 W,

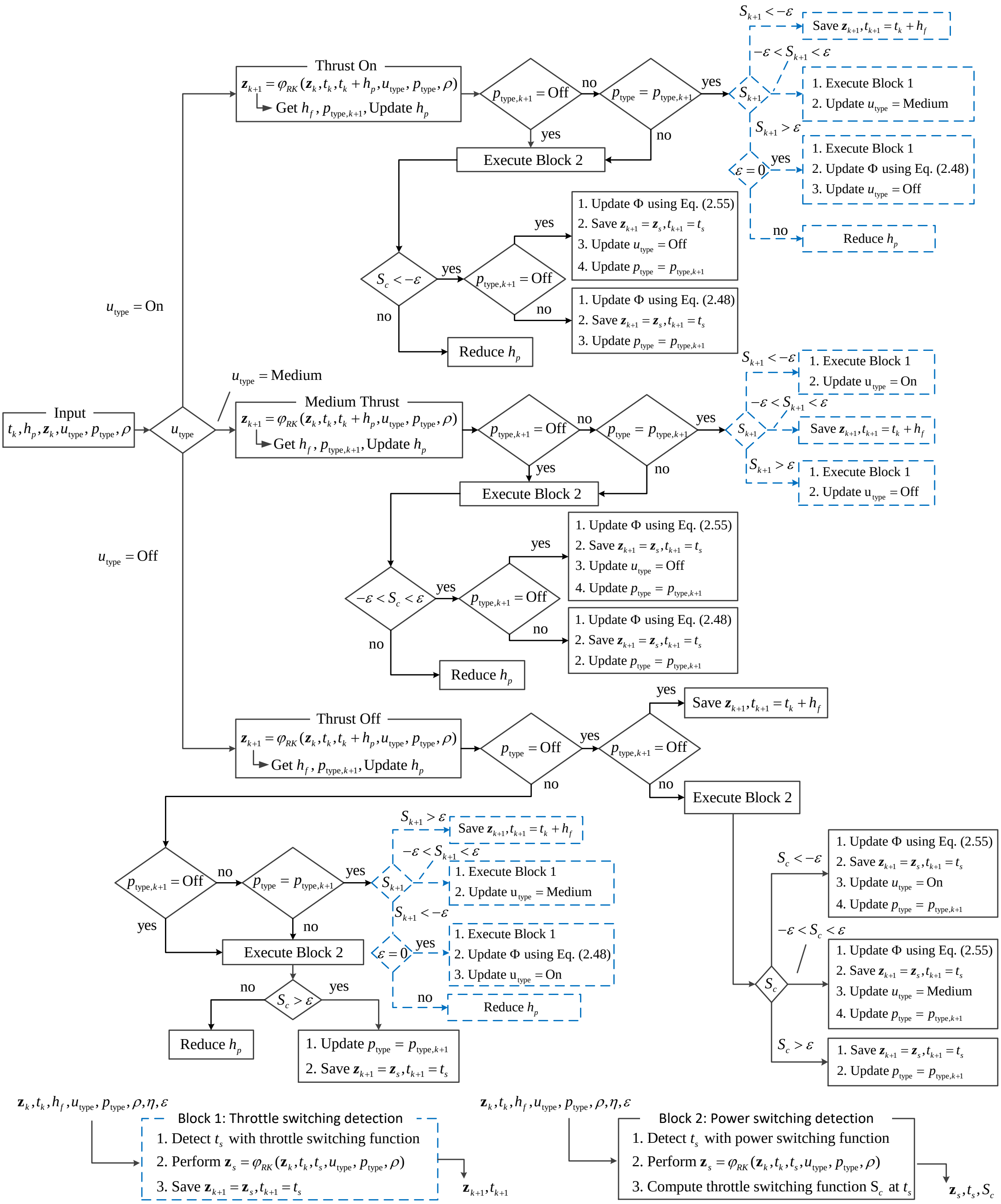

Figure 2.5: *Flowchart for the implementation of a generic integration step. Dashed blocks are from [47].*

$T_{\max} = 1.89$ mN and $I_{\rm sp} = 3022.59$ s. The comparison between the $1/r^2$ law, S_p and $P_{\rm in}$ is also shown in Fig. 2.6a, where $P_{\rm in}$ reaches $P_{\max}$ when $r \leqslant 0.928$ AU.

Table 2.1: *Physical constants.*

Physical constant	Value
Mass parameter, μ	1.327124×10^{11} km^3/s^2
Gravitational field, g_0	9.80665 m/s^2
Astronomical unit, AU	1.495979×10^8 km
Time unit, TU	5.022643×10^6 s
Velocity unit, VU	29.784692 km/s
Mass unit, MU	22.6 kg
Power unit, PU	3991.74 W

Table 2.2: *Thruster coefficients.*

$T_{\max}$	Value	Unit	$I_{\rm sp}$	Value	Unit	S_p	Value	Unit
a_0	-0.7253	mN	b_0	2652	s	c_0	840.11	W
a_1	0.02481	mN/W	b_1	-18.123	s/W	c_1	-1754.3	W/AU
a_2	0		b_2	0.3887	s/W^2	c_2	1625.01	W/AU^2
a_3	0		b_3	-0.00174	s/W^3	c_3	-739.87	W/AU^3
a_4	0		b_4	0		c_4	134.45	W/AU^4

The asteroid ephemerides are given by Spacecraft Planet Instrument Camera-matrix Events (SPICE) kernel from HORIZONS system [83] [1]. As a study case, the launch time is set to 1st Jan 2022, whereas the arrival date is set to 1st Jun 2024 for the energy-optimal and fuel-optimal problems. The spacecraft is supposed to depart from Sun–Earth L_2 Lagrange point, and corresponding boundary conditions provided by HORIZON system are shown in Table 2.3, where terminal position and velocity conditions are used for the energy- and fuel-optimal problems in Sec. 2.3.2. Terminal position and velocity conditions for the time-optimal problem in Sec. 2.3.1 depend on guessed transfer time and are varied during the optimization. The initial mass is set to 22.6 kg, the same as MU in Table 2.1. All simulations are conducted under an Intel Core i7–9750H, CPU@2.6GHz, Windows 10 system with MATLAB R2019a. The integration code is converted to MEX file to speed up simulations.

Table 2.3: *Boundary conditions.*

Boundary Condition	Value
Initial position vector, AU	$[-0.1764352209, 0.9774432047, -4.6698040914 \times 10^{-5}]^\top$
Initial velocity vector, VU	$[-1.0105715460, -0.1832792298, 1.2539059040 \times 10^{-5}]^\top$
Terminal position vector, AU	$[-0.6547598563, 0.6446483464, -1.5061497361 \times 10^{-3}]^\top$
Terminal velocity vector, VU	$[-0.7759381160, -0.7425308483, 1.1204008105 \times 10^{-3}]^\top$

A total of 6 cases in Table 2.4 are simulated. The inputs $(\alpha_i, \dot{\alpha}_i, \beta_i, \dot{\beta}_i, S_i, \dot{S}_i)$ of ACT are randomly generated at the initial time within given bounds. The shape-based method in [84] has been employed for case 5 to provide an intuition of initial thrust angles, using $T_{\max}$ value at 1 AU. It shows that the thrust direction at the initial time is close to the velocity. Thus the bounds are set up as follows: $\alpha_i \in [-10, 10]$ deg, $\dot{\alpha}_i \in [-5, 5]$ deg/TU, $\beta_i \in [-1, 1]$ deg and

[1] See https://ssd.jpl.nasa.gov/?horizons

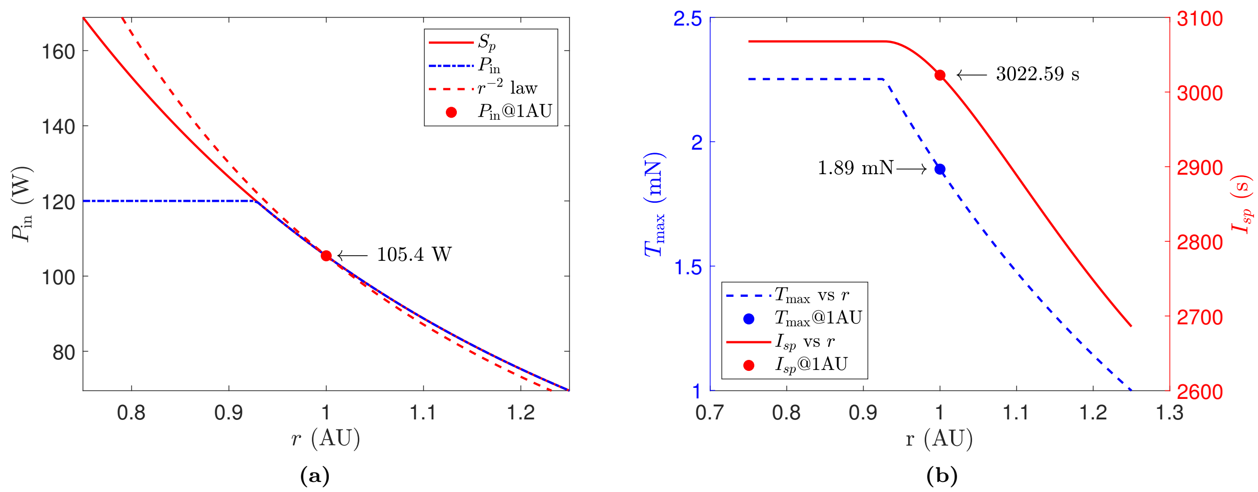

Figure 2.6: *Variations of P_{in}, $T_{\max}$ and I_{sp} w.r.t. r with $P_{\max} = 120$ W [82].*

$\dot{\beta}_i \in [-0.1, 0.1]$ deg/TU. The initial mass costate is set to 1. From Eq. (2.17) and (2.24), S_i has to be negative. The bounds of S_i and $\dot{S}_i$ are: $S_i \in [-1.5, -0.001]$ and $\dot{S}_i \in [-0.01, 0.01]$. The parameter bounds are applied to all simulation examples.

Table 2.4: *Simulation results.*

Case	Type	$P_{\min}$, W	Optimal costate vector $\boldsymbol{\lambda}_0^*$	t_f, days	m_f, kg
1	TO[a]	0	$[15.42735, -61.81391, 0.18480, 74.40205, 4.50555, 0.04902, 4.38101]^\top$	593.2311	19.7994
2	TO	95	$[-11.00728, -175.41465, 1.40145, 155.51247, 57.39753, 0.24116, 7.10106]^\top$	699.0125	20.6825
3	EO[b]	0	$[0.32576, -0.97280, 0.03702, 1.20654, 0.00762, 0.00254, 0.05948]^\top$	821	21.1738
4	EO	95	$[0.31165, -2.07603, 0.06691, 2.45955, 0.32964, 0.00996, 0.14322]^\top$	821	20.8288
5	FO[c]	0	$[0.31717, -0.97395, 0.22169, 1.19851, 0.01910, 0.01280, 0.05682]^\top$	821	21.4370
6	FO	95	$[0.23645, -1.28756, 0.08292, 1.61084, 0.17194, 0.04682, 0.11054]^\top$	821	20.9239

[a] time-optimal solution; [b] energy-optimal solution; [c] fuel-optimal solution;

2.3.1 Time-Optimal Transfers

Two time-optimal problems for $P_{\min} = 0\ W$ and $P_{\min} = 95\ W$ are solved for comparison. The transfer time is monotonically increased (starting from 1 year) until one solution is found. For each assumed t_f, the optimization runs at most 5 times with different initial guesses generated randomly using parameter bounds of ACT mentioned above. The corresponding solutions are summarized as cases 1–2 in Table 2.4. For case 1, since $S_p < P_{\min}$ is not triggered, the hyperbolic tangent smoothing (HTS) is not used. The time-optimal trajectory is shown in Fig. 2.7a. The variations of u, S_t, m, P_{in}, I_{sp} and $T_{\max}$ are shown in Fig. 2.7b, where the engine is always 'on'. The minimum transfer time is 593.2311 days and the final mass of the spacecraft is 19.7994 kg.

For case 2, the HTS is used first to find the approximate solution corresponding to $\rho_0 = 4$, then ρ is gradually reduced to approach the optimal solution ($\rho = 0$) with the step $\Delta\rho = 0.5$ (8 iterations are needed). The corresponding time-optimal trajectory is shown in Fig. 2.8a, and the variations of u, S_t, m, P_{in}, I_{sp} and $T_{\max}$ are shown in Fig. 2.8b. The minimum transfer time 699.0125 days, and the final mass of the spacecraft is 20.6825 kg. Compared to case 1, the engine switches off twice due to insufficient input power, after 95.57 and 552.54

days of flight. The engine-off lasts for 273.02 and 58.69 days, respectively. The transfer time is 105.78 days longer than that of case 1, whereas 0.8831 kg of fuel is saved. Figure 2.9 shows the variations of $\boldsymbol{\lambda}_r$, where $\boldsymbol{\lambda}_r$ is discontinuous when P_{in} crosses $P_{\min}$ and $\Delta u \neq 0$. The values of π_t when P_{in} crosses $P_{\min}$ are -943.3126, -149.9713, -308.6871 and -659.5547.

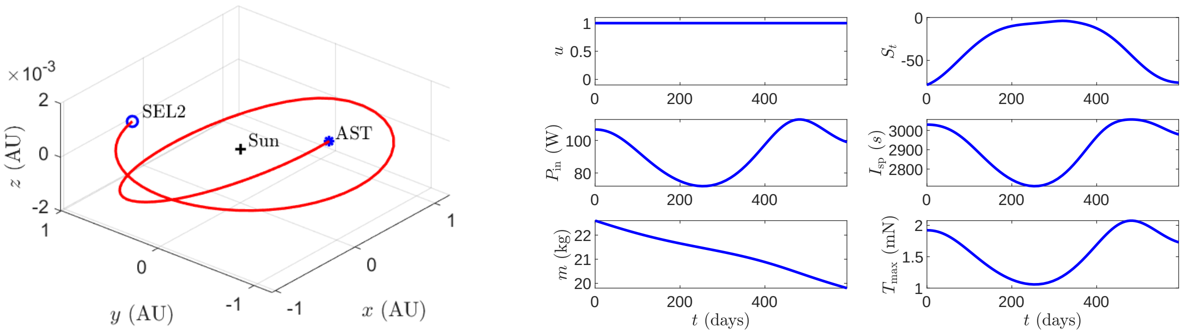

(a) *Time-optimal trajectory.* **(b)** *Variations of u, P_{in}, m, S_t, I_{sp} and $T_{\max}$.*

Figure 2.7: *Time-optimal solution (case 1). SEL2: Sun–Earth* L_2 *Lagrange point; AST: asteroid position at arrival.*

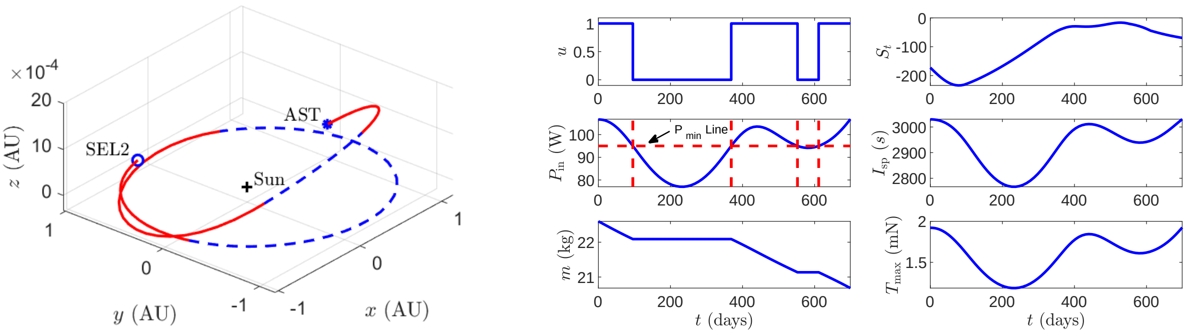

(a) *Time-optimal trajectory.* **(b)** *Variations of u, P_{in}, m, S_t, I_{sp} and u $T_{\max}$.*

Figure 2.8: *Time-optimal solution (case 2). SEL2: Sun–Earth* L_2 *Lagrange point; AST: asteroid position at arrival.*

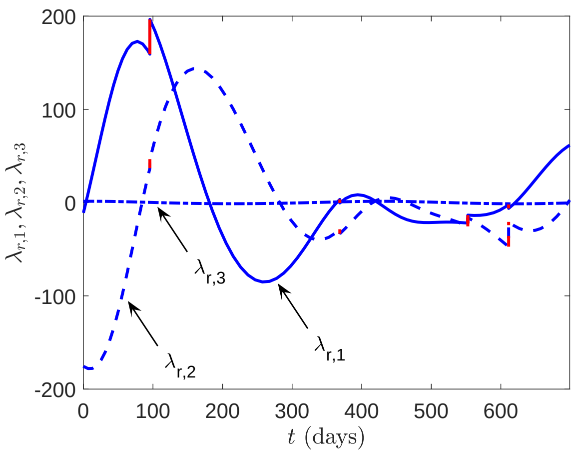

Figure 2.9: *Variations of optimal $\boldsymbol{\lambda}_r$ w.r.t. time for case 2. The discontinuities of $\boldsymbol{\lambda}_r$ are labeled red.*

2.3.2 Fuel-Optimal Transfers

Fuel-optimal transfers for $P_{\min} = 0\ W$ and $P_{\min} = 95\ W$ are solved. The algorithm is able to find the solution after several attempts of ACT. The energy-optimal (cases 3 and 4) and fuel-optimal (cases 5 and 6) solutions are shown in Table 2.4, respectively. For cases 3-4, the HTS is not used. The corresponding fuel-optimal trajectory is shown in Fig. 2.10a. The variations of u, S_f, m, P_{in}, I_{sp} and $T_{\max}$ are shown in Fig. 2.10b, where $P_{\max}$ is reached after around 767.60 days of flight. The final mass of the spacecraft is 21.4370 kg.

For cases 5-6, the HTS is used to solve the approximate energy-optimal problem first, with $\rho_0 = 4$. The energy-optimal solution is found by gradually reducing ρ to 0 with the step $\Delta\rho = 0.5$ (8 iterations are needed). Then, the fuel-optimal solution is gradually approached by reducing ε to 0, with $\Delta\varepsilon = 0.05$ step. The step is halved if the continuation fails. The corresponding fuel-optimal trajectory is shown in Fig. 2.11a. The variations of u, S_f and m, P_{in}, I_{sp} and $T_{\max}$ are shown in Fig. 2.11b. The variations of $\boldsymbol{\lambda}_r$ is shown in Fig. 2.12. The final mass of the spacecraft is 20.9239 kg. The insufficient input power is encountered twice, after 92.16 and 532.08 days of flight, and the engine-off lasts for 262.26 and 107.69 days, respectively. The maximum input power is encountered after 764.47 days of flight until to the end. Compared to the fuel-optimal solution of case 5, case 6 requires 0.5131 kg more fuel. The values of π_ε when P_{in} crosses $P_{\min}$ are 0, 0, -8.6735 and -9.0279. In terms of computational time, the HTS and energy- to fuel-optimal continuation (not involving ACT) in case 6 takes around 4 s, while it takes around 27 s if the gradients are computed by finite differences. The benefits of the variational method become tremendous in terms of computational time especially when a multitude of trajectories are required [82].

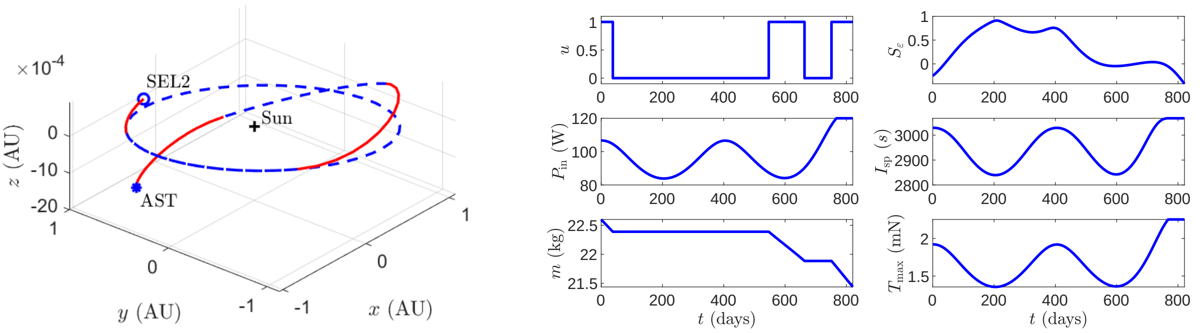

(a) *Fuel-optimal trajectory.* **(b)** *Variations of u, P_{in}, m, S_f, u $T_{\max}$ and I_{sp}.*

Figure 2.10: *Fuel-optimal solution (case 5). SEL2: Sun–Earth* L_2 *Lagrange point; AST: asteroid position at arrival.*

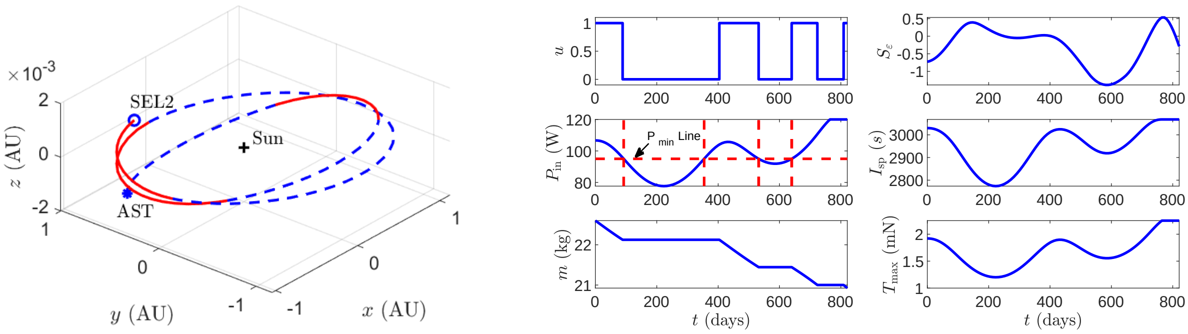

(a) *Fuel-optimal trajectory.* (b) *Variations of u, P_{in}, m, S_f, $T_{\max}$ and I_{sp}.*

Figure 2.11: *Fuel-optimal solution (case 6). SEL2: Sun–Earth* L_2 *Lagrange point; AST: asteroid position at arrival.*

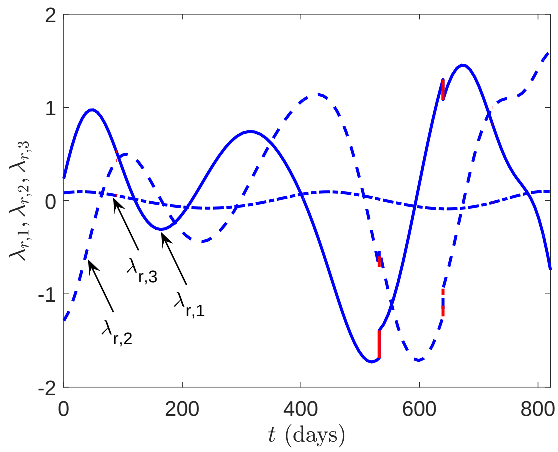

Figure 2.12: *Variations of optimal $\boldsymbol{\lambda}_r$ w.r.t. time for case 6. The discontinuities of $\boldsymbol{\lambda}_r$ labeled red.*

2.3.3 Discussion

A comparison of thrust level ($u \times T_{\max}$) profiles for both time-optimal and fuel-optimal problems using GPOPS [17] is performed (Fig. 2.13). It is clear that GPOPS solutions coincide with solutions obtained by using the proposed method. Note that GPOPS handles cases 1 and 5 as single phase problems, while it solves cases 2 and 6 as multi-phase problems, since these are inherently MPBVPs. When the desired discontinuous solution is required, the presented method has the advantage of solving the MPBVP as a TPBVP. Thus HTS can be embedded into the computational framework. Also, there is no need to 1) guess the values and number of multipliers related to interior-point constraints; 2) specify the solution structure a priori. On the other hand, GPOPS has to solve the MPBVP separately with HTS, and the solution structure must be guessed beforehand.

Additionally, it can been seen that the values of π_t and π_ε obtained in simulations have different order of magnitude w.r.t. the optimal costates. When the MPBVP is solved by the indirect method without transforming it to a TPBVP, it is difficult to provide good initial guesses to the multiplier. In [85], it is concluded that eliminating multipliers benefits to improve the convergence robustness of the indirect method.

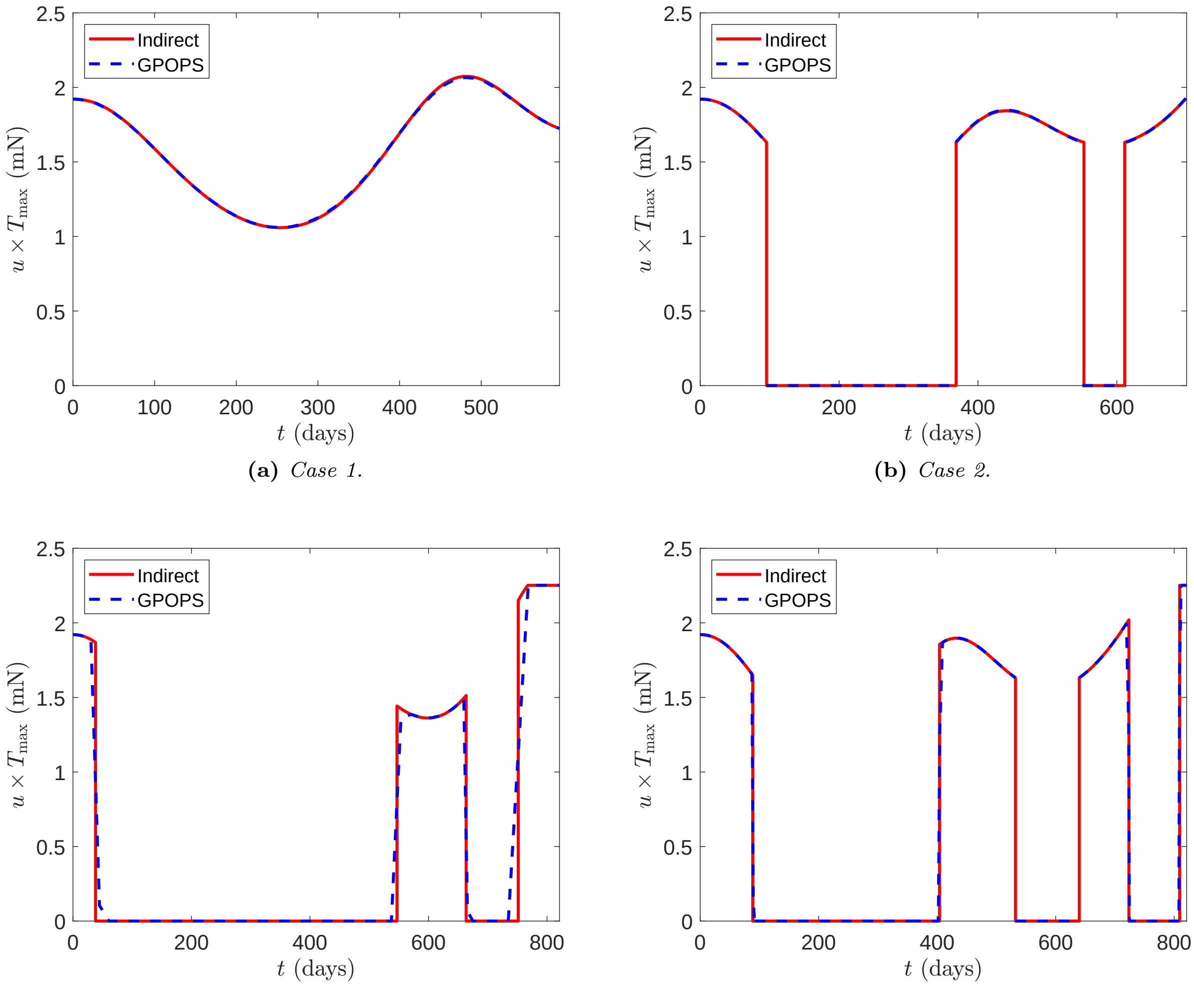

(a) *Case 1.* **(b)** *Case 2.* **(c)** *Case 5.* **(d)** *Case 6.*

Figure 2.13: *Comparisons of time-optimal and fuel-optimal thrust level ($u \times T_{\max}$) profiles to GPOPS solutions.*

2.4 Summary

The effects of thruster power constraints on indirect optimization are studied. The problem becomes complicated when the input power reaches its lower bound, and costates become discontinous. The gradients at discrete, discontinuous points produced by power constraints are investigated by analyzing the behavior of the state transition matrix. By leveraging the analytical multipliers related to the scalar interior-point constraints, an efficient indirect method has been developed, which allows for solving a MPBVP as a TPBVP. The computational framework for solving both time- and fuel-optimal problems is established by combining analytic derivatives, continuation, and switching detection into an augmented flowchart. The outcome is an algorithm that features accurate bang-bang solutions and gradients with broader convergence domain and high computational efficiency. Thus, the presented method is useful when solving a multitude of problems in the context of asteroid target screening in Chapter 3. Moreover, the proposed computational framework is general for solving bang-bang control problems with scalar interior point constraints, such as the Earth-orbit low-thrust transfer problem with shadow constraints in Chapter 4.

CHAPTER 3

TARGET SCREENING OF M-ARGO MISSION

Target selection is essential in preliminary design of many asteroid missions. This process should take into account of specific mission requirements and objectives, and as such, it differs from one mission to another. In this context, this chapter aims to find the reachable NEA targets considering the requirements and constraints of the M-ARGO mission, using the method developed in Chapter 2. A preliminary work along these lines was executed by ESA's Concurrent Design Facility. The present work is an enhancement with a more comprehensive and sophisticated target asteroid search, cooperated with F. Topputo, C. Giordano, and V. Franzese, etc. My responsibility is the computation of time-optimal and fuel-optimal trajectories for the filtering purpose. For the completeness, the whole target selection process is reported in this chapter.

3.1 M-ARGO Mission Outline

The success of CubeSats spurred increasing interests towards nano-satellite missions [86]. The low-cost nature of CubeSats allows small companies and universities to take part in space missions, expanding the access to space to a wider community. Nowadays, CubeSats have reduced the entry-level cost for space missions in Low Earth Orbit (LEO) by more than one order of magnitude [87]. This is owing to the advances in miniaturized commercial-off-the-shelf components and to the short design-to-launch time. CubeSats as M-ARGO, have the potential to reduce the entry-level cost of interplanetary missions as well. Moreover, deep-space CubeSats offer the possibility of augmenting and diversifying the Solar System exploration at a lower cost compared to traditional missions, thus providing high science-to-investment ratios. For instance, deep-space CubeSats would allow the characterization of several asteroids in the Solar System, so contributing tremendously to the understanding of its evolution.

M-ARGO is a 12U CubeSat that is planned to piggyback on the launch of another large spacecraft going towards the Sun–Earth Lagrange point L_2. The first ESA mission to independently explore asteroids. After insertion into a parking orbit at L_2, M-ARGO will depart from there performing a deep-space cruise towards a NEA target using low-thrust electric propulsion. M-ARGO will perform an in-orbit demonstration of key technologies such as [87] i) a miniaturized X-band transponder and reflectarray high gain antenna for communication with Earth at distances of up to 1.5 AU; ii) a miniaturized solar drive array mechanism for maximising solar power generation from two deployable steerable wings; iii) miniaturized electric propulsion for orbital manoeuvres.

The M-ARGO mission objectives are reported in Table 3.1. These are to: (1) demonstrate the capability of CubeSat nano-spacecraft systems to independently explore deep space for the first time; (2) rendezvous with a near-Earth asteroid and characterize its physical properties for the presence of in-situ resources; (3) advance miniaturized technologies currently under development in Europe; (4) test autonomous guidance, navigation, and control techniques and components performance during transfer to target object.

Table 3.1: *M-ARGO mission objectives.*

ID	Title	Statement
1	CubeSat Demonstration	Demonstrate the capability of CubeSat nano-spacecraft systems to independently explore deep space for the first time.
2	Scientific Investigation	Rendezvous with a near-Earth asteroid and characterize its physical properties for the presence of in-situ resources.
3	Technology Advancement	Advance miniaturized technologies currently under development in Europe.
4	Autonomy Experimentation	Test autonomous guidance, navigation, and control techniques and components performance during transfer to target object.

M-ARGO is planned to depart from the Sun–Earth L_2 point within 1 Jan 2023 and 31 Dec 2024. The maximum transfer time to the asteroid is set to up to 3 years, and the close-proximity operations (CPO) are planned to last up to 6 months. The preliminary spacecraft mass amounts to m_0 = 22.6 kg, where $m_{p,\max}$ = 2.8 kg is the maximum available propellant. The Sun-projected area for the computation of the solar radiation pressure is A = 0.30 m^2 with a reflectivity coefficient of (C_r = 1.3). These values are given in Table 3.2.

Table 3.2: *Mission time frame and spacecraft data assumptions.*

S–E L_2 Departure	Transfer	CPO	m_0	$m_{p,\max}$	A	C_r
2023 – 2024	$\leqslant$ 3 years	$\leqslant$ 6 months	22.6 kg	2.8 kg	0.30 m^2	1.3

3.2 Approach to Target Selection

This section shows the approach undertaken to down-select the NEA targets for M-ARGO. To this aim, it is required to identify the subset of asteroids that are reachable considering the constraints of a 12U deep-space CubeSat. Figure 3.1 shows the procedure developed to filter the database of known asteroids.

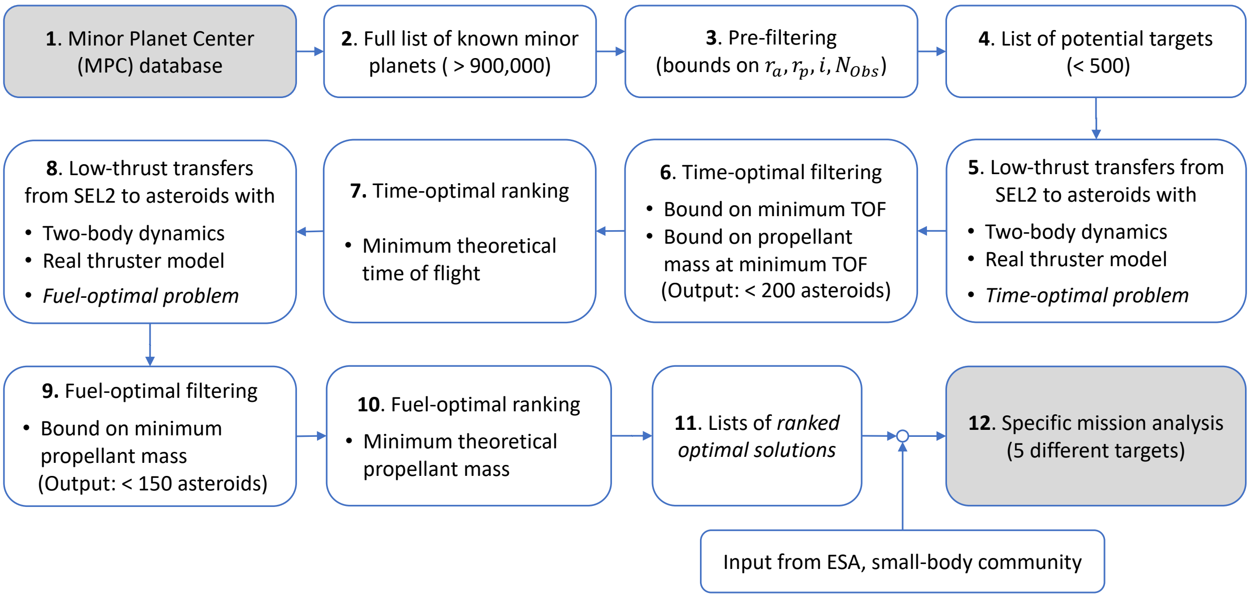

Figure 3.1: *Methodology of the NEA target screening.*

The procedure is as follows:

1-2 **Database retrieval.** The Minor Planet Center (MPC) Database[1] is considered as the source of information for the minor planets in the Solar System. It comprehends the designation and the orbit computation of all the discovered minor planets and it is updated daily. More than $900,000$ objects are accounted for as of October 2020.

3-4 **Pre-Filtering.** The full list of asteroids is pre-filtered using ranges of orbital parameters. Educated guesses on these parameters have been inferred from [88]. These involve capping the aphelion, bottoming the perihelion, and bounding the inclination as well as the number of observations. This filtering reduces the full list of asteroids to a preliminary list of approximately 500 potential targets; see Section 3.3.

5-6 **Time-optimal transfers.** A massive search is conducted to compute time-optimal transfers to each of the asteroids in the preliminary list. The optimisation considers the two-body problem with the realistic thruster model in Section 2.3, departure from Sun–Earth L_2, and departure window as specified in Section 3.1. The aim of this step is to determine the *minimum theoretical transfer time* to each asteroid for each departure epoch. The targets whose minimum transfer time is greater than 900 days are filtered-out.

7 **Time-optimal ranking.** The filtered time-optimal solutions are ordered to produce a time-optimal ranking. The number of targets is then reduced to ~ 170 objects; see Section 3.4.

8-9 **Fuel-optimal transfers.** The objects resulting feasible after the time-optimal analysis are processed under the perspective of a fuel-optimal optimisation, using the same model and boundary conditions as in the time-optimal optimisation. This analysis finds the minimum propellant mass for each combination of departure epoch and transfer time.

[1]See `https://minorplanetcenter.net/`; last accessed on October 2020.

Table 3.3: *Asteroids data sources.*

Source	Acronym	Type	Data
Minor Planet Center[2]	MPC	Database	Asteroids Orbital Parameters
Asteroid Lightcurve[3]	Asteroid Lightcurve Database (LCDB)	Database	Asteroids Physical Data
HORIZONS[4]	HORIZONS	SPICE Kernels	Asteroids Ephemerides

The targets whose minimum required propellant mass is greater than 2.8 kg are excluded from the list.

10 **Fuel-optimal ranking.** The fuel-optimal solutions as output of step 9 are ordered to produce a fuel-optimal ranking made of approximately 150 reachable objects; see Section 3.5.

11 **Lists of ranked optimal solutions.** The ranked lists of time-optimal and fuel-optimal solutions produced as output of the filtering chain has been examined in view of operational and scientific criteria; see Section 3.6. The 5 shortlisted targets have been then selected; see Section 3.6.

3.3 Database Filtering

The MPC (Table 3.3) accounts for more than 900,000 objects in the Solar System. Figure 3.2a shows the semi-major axis (a) versus the eccentricity (e) for all the near-Earth asteroids as a scatter plot, while Figure 3.2b displays the semi-major axis (a) versus the inclination (i) for the same bodies.

Consistently with the preliminary work in [88], the subset of potential targets has been defined by restricting the aphelion (r_a) upper bound (UB) to 1.25 AU and the perihelion (r_p) lower bound (LB) to 0.75 AU. Moreover, in order to comply with realistic CubeSat propulsive capabilities, an upper bound on the inclination equal to 10 degrees has been set. Higher inclinations are unlikely to be reached due to the limited amount of propellant available. This is confirmed by the outcome of the analysis (see Section 3.5). Eventually, a lower bound of 10 observations (N_{obs}) is enforced to assure accuracy in the orbital elements of the asteroids. Table 3.4 summarises the filtering parameters used. It is worth highlighting that the intervals considered in this study are larger than those in [88]: this choice is to perform a more comprehensive search not influenced by existing results. As a result, 456 objects satisfy the bounds in Table 3.4. These have been represented as black dots in Figure 3.2.

Table 3.4: *NEA database filtering parameters.*

Parameter	Lower Bound	Upper Bound
r_a	–	1.25 AU
r_p	0.75 AU	–
i	0 deg	10 deg
N_{obs}	10	–

[2] See `https://minorplanetcenter.net/`
[3] See `http://www.minorplanet.info/lightcurvedatabase.html`
[4] See `https://ssd.jpl.nasa.gov/?horizons`

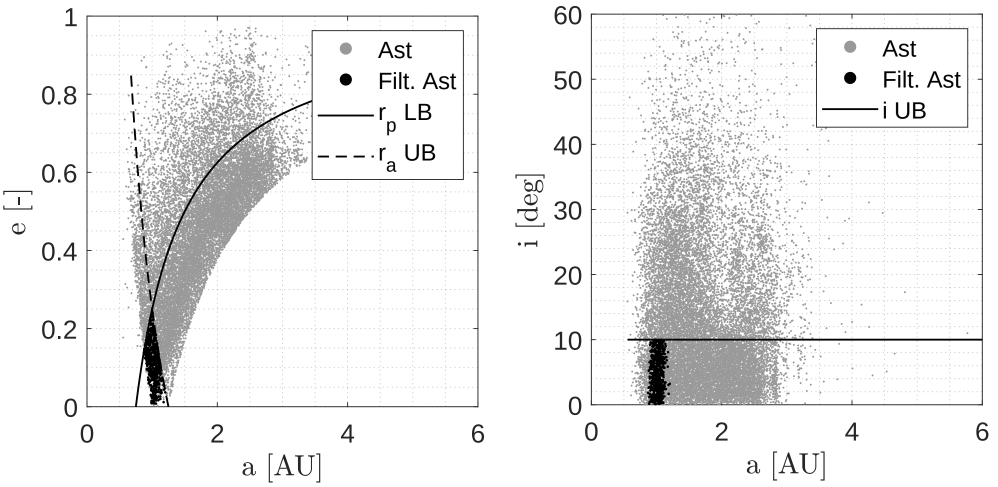

(a) *a vs e* **(b)** *a vs i*

Figure 3.2: *Minor planets semi-major axis (a), eccentricity (e), and inclination (i). The filtering bounds are the solid and dashed lines, while the filtered asteroids are highlighted in black.*

Figure 3.3 shows the estimated diameter (D) of the minor planets with respect to their semimajor axis (a), eccentricity (e), and inclination (i). In Fig. 3.3, the diameter D is estimated as[5] [89, 90]

$$D = 10^{3.1236 - 0.5 \log_{10}(a_L) - 0.2H} \tag{3.1}$$

where H is absolute magnitude and a_L is albedo, whose values are retrieved from the databases in Table 3.3. The filtered asteroids are highlighted as black dots. The diameter of the filtered asteroids ranges between 10^{-3} and 10^{-1} km.

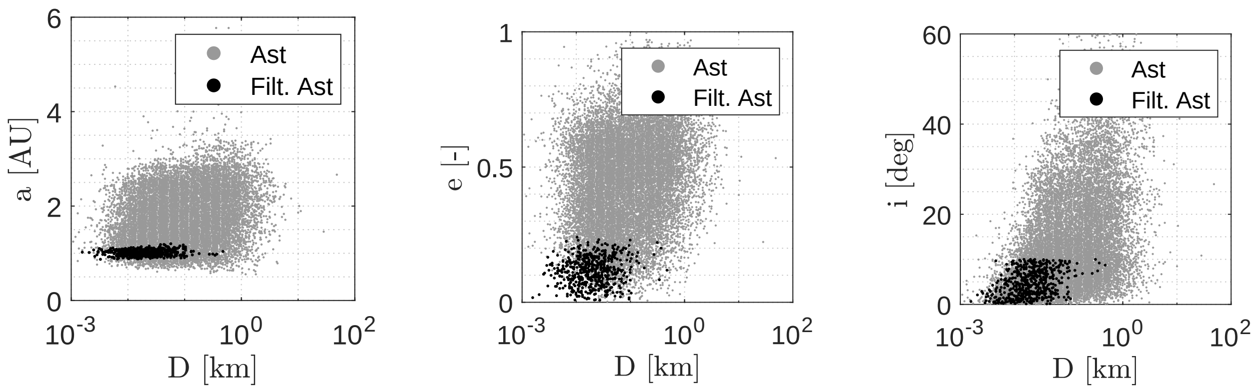

(a) *D vs a* **(b)** *D vs e* **(c)** *D vs i*

Figure 3.3: *Minor planets diameter (D) versus semi-major axis (a), eccentricity (e), and inclination (i). Filtered asteroids are the black dots.*

Figure 3.4 shows the estimated size versus the rotational period of the asteroids catalogued in the LCDB [91]; see Table 3.3. The plot highlights the so called spin barrier (horizontal dashed line). Most of the big asteroids (with a diameter larger than 1 km) lie below the spin barrier, meaning that they have a rotational period higher than 2 hours, while for small asteroids the rotational period can be small, in the order of 1 hour or less. The filtered asteroids for which light curves are known are also highlighted in black in Fig. 3.4.

[5] See `https://cneos.jpl.nasa.gov/tools/ast_size_est.html`

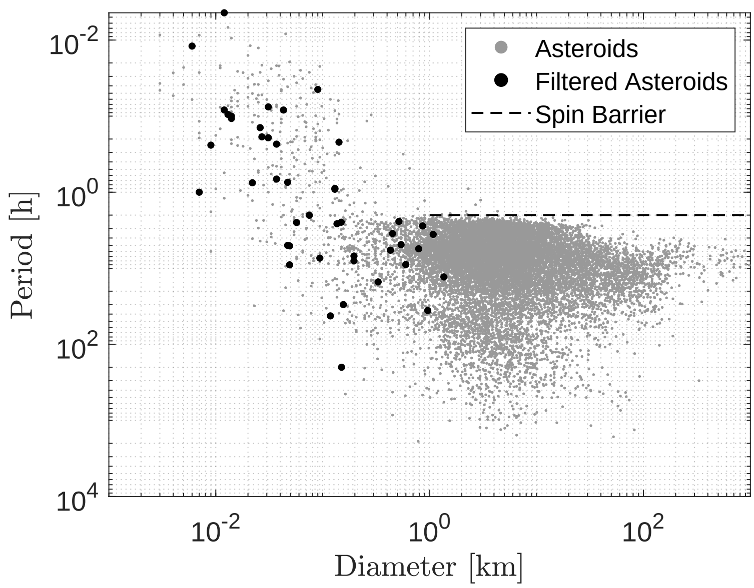

Figure 3.4: *Rotational period against diameter for minor planets. Filtered asteroids in black. Data retrieved from the MPC and the LCDB; see Table 3.3. The U code defined in the LCDB database provides a measure of the quality of the period solution. Only asteroids with $U \geqslant 2$ are illustrated.*

3.4 Time-Optimal Transfers

Performing a time-optimal search in a two-year departure window for different objects requires solving approximately 3.3×10^5 optimisation problems with a one-day time discretisation. The indirect solver developed in Chapter 2 has been adapted for this purpose. The dynamic model used is a standard two-body problem implementing the realistic thruster model depicted in Section 2.3. Second-order effects such as third-body perturbation and solar radiation pressure have been implemented in following phases of the mission analysis.

3.4.1 Methodology for Time-Optimal Solutions

Reconstructing the time-optimal transfers for 456 objects over a two-year departure window requires solving approximately 3.3×10^5 time-optimal problems. Thus, an agile strategy has been developed to scan the solution space.

The continuation strategy illustrated in Fig. 3.5 to scan the two-year window is employed to reduce computational load. Specifically, the time-optimal solution for a given t_0 is found first. Then, the solution for $t_0 + \Delta t$ is sought, using the optimal solution of the former step (t_0) as initial guess, with $\Delta t = 1$ day. If a new solution is found, the continuation proceeds. Otherwise, the time step Δt is halved. This process is repeated until the final departure date is reached. Consequently, the two-year window is processed with a nonuniform discretisation. The initial guess solution to the first problem is generated using ACT [45], along with a monotonically increasing transfer duration guess.

While these solutions are not feasible in practical applications, because they involve thrust on for all times, they yield the minimum theoretical transfer time

$$\tau_{\min} = \min_{t_0 \in [\underline{t}_0, \bar{t}_0]} \tau(t_0) \tag{3.2}$$

where $\tau(t_0) := t_f(t_0) - t_0$, and $[\underline{t}_0, \bar{t}_0]$ is the two-year departure window. $\tau_{\min}$ is used to prune out those solutions not complying with the requirement in Table 3.2.

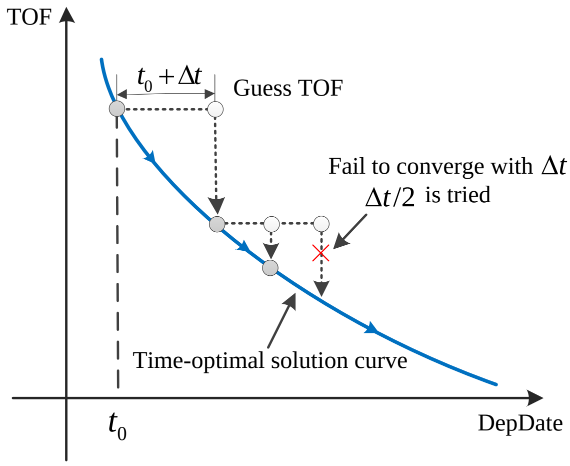

Figure 3.5: *Continuation strategy to solve time-optimal transfers within the two-year departure window.*

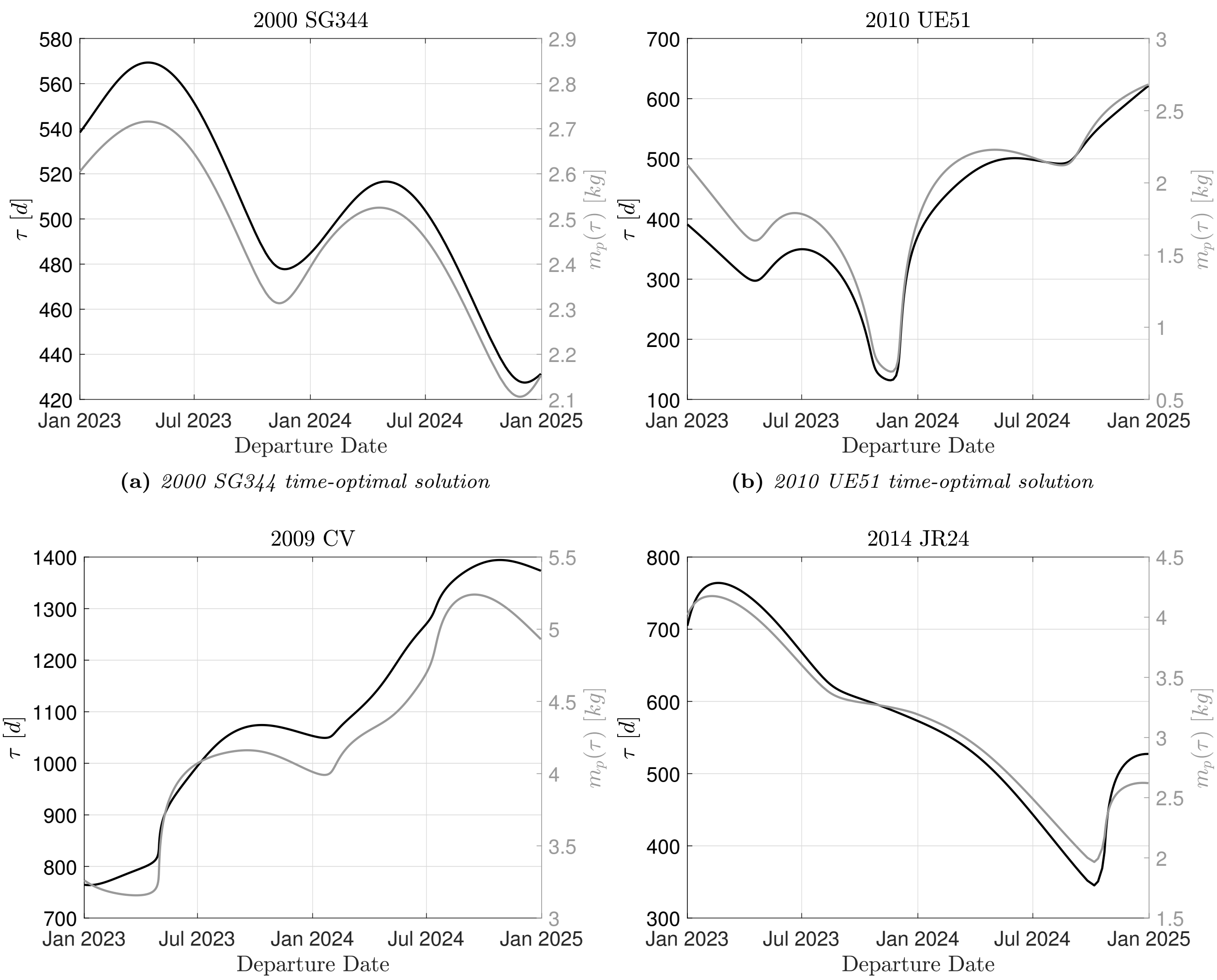

(a) *2000 SG344 time-optimal solution*

(b) *2010 UE51 time-optimal solution*

(c) *2009 CV time-optimal solution*

(d) *2014 JR24 time-optimal solution*

Figure 3.6: *Minimum transfer time τ and associated propellant mass $m_p(\tau)$ profiles as function of the departure day for four sample asteroids.*

The results of the time-optimal search for four sample asteroids are shown in Fig. 3.6, where the minimum transfer duration $\tau = t_f - t_0$ (left y-axis) and its associated propellant mass $m_p(\tau)$ (right y-axis) profiles are shown as function of the departure day t_0 (in MJD2000[6]). It can be seen that there are considerable variations of the transfer time in the two-year window. The minima of the transfer time corresponds to minima of the propellant mass because the thrust is always on.

3.4.2 Search Space Pruning

For each of the asteroids processed, $\tau_{\min}$ is retrieved, as well as its corresponding propellant mass $m_p(\tau_{\min})$. The two quantities are reported in Fig. 3.7 in the form of cumulative distribution functions. This information has been used to further narrow the set of asteroids that can be reached by M-ARGO. Indeed, using the requirements in Table 3.2, and considering that the *real* transfer time is longer than the one resulting from time-optimal computations, the following criteria have been used.

1) Minimum theoretical transfer time lower than 900 days: $\tau_{\min} \leqslant 900$ days. There are 299 asteroids out of the ones processed satisfying this condition; see Fig. 3.7a.
2) Minimum propellant mass lower than 4 kg: $m_p(\tau_{\min}) \leqslant 4$ kg. There are 181 asteroids out of the one processed whose minimum propellant mass is below this threshold; see Fig. 3.7b.

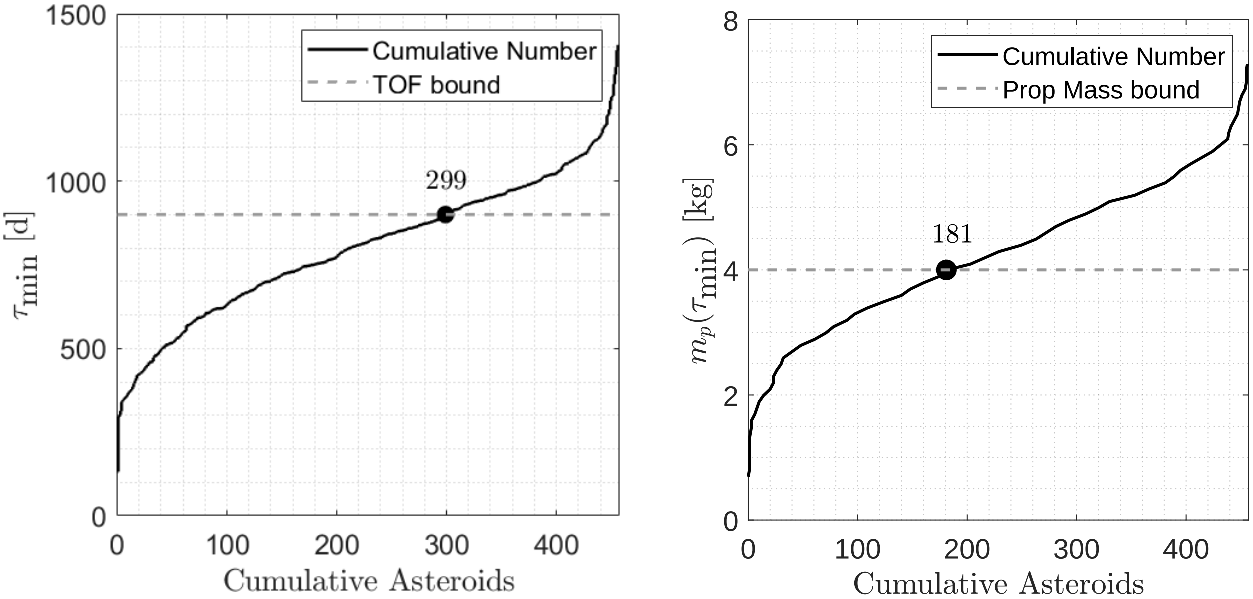

(a) *Cumulative number of asteroids vs* $\tau_{\min}$

(b) *Cumulative number of asteroids vs* $m_p(\tau_{\min})$

Figure 3.7: *Cumulative number of asteroids for increasing* $\tau_{\min}$ *and associated* $m_p(\tau_{\min})$*. The filtering bounds are the dashed lines, while the number indicates the asteroids below the threshold.*

We further impose that these two conditions have to be verified simultaneously. The graphical representation in Fig. 3.8 shows that the propellant mass condition is the more stringent one. As a result of this pruning process, we have 172 asteroids ranked after the time-optimal screening. The ranking is reported in Appendix A.1, and it is the input of the fuel-optimal step as per the approach in Fig. 3.1.

[6]Julian Date is the interval of time measured in days from the epoch Jan 1, 4713 B.C., 12:00. Modified Julian Date (MJD2000) is the adjustment of Julian Date from Jan 1, 2000, 12:00 [92].

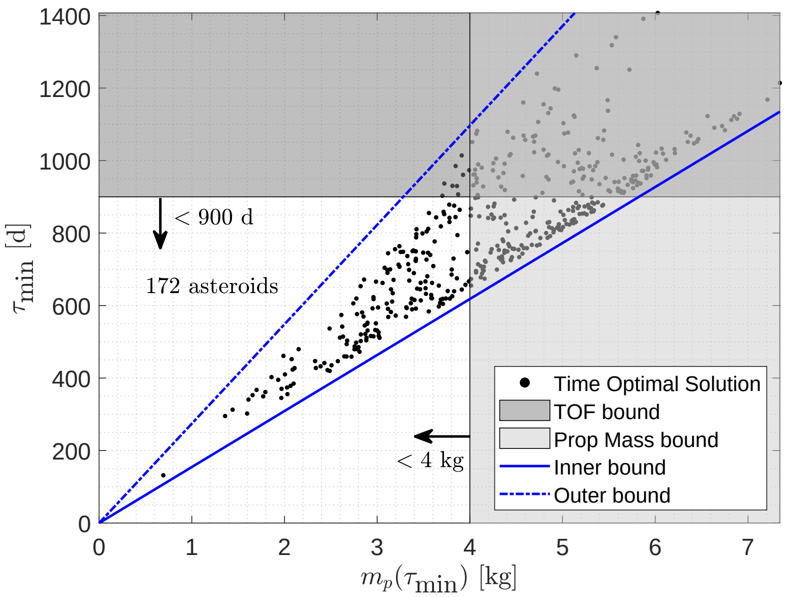

Figure 3.8: *Time of flight for the time-optimal solutions against the associated propellant mass. The filtering bounds are the black solid lines, while the number indicates the asteroids below both thresholds. All time-optimal solutions lie within the inner and outer lines.*

Inspection of Fig. 3.8 reveals that the points therein are the solution of the following differential equation

$$\dot{m} = -\frac{T_{\max}(P_{in}(t))}{g_0\, I_{sp}(P_{in}(t))} \tag{3.3}$$

because $u(t) = 1\ \forall t \in [t_0, t_f]$. Differently from the standard cases in which $T_{\max}$ and I_{sp} are both constant, Eq. (3.3) cannot be solved in closed form because $P_{in} = P_{in}(r(t))$. However, it is easy to verify that $T_{\max}(P_{in}(t))/I_{sp}(P_{in}(t))$ is monotonously increasing w.r.t. P_{in}. Thus, transfers to inner and outer targets (where inner and outer is referred to the Earth orbit) are bounded by $P_{in}(t) = P_{\max}$ and $P_{in}(t) = P_{\min}$, respectively. These conditions define the limiting minimum time to reach inner and outer targets, i.e.,

$$\tau_{\text{min,in}} = \frac{g_0\, I_{sp}(P_{\max})}{T_{\max}(P_{\max})} m_p \tag{3.4}$$

$$\tau_{\text{min,out}} = \frac{g_0\, I_{sp}(P_{\min})}{T_{\max}(P_{\min})} m_p \tag{3.5}$$

which correspond to the two blue lines in Fig. 3.8. Note that $P_{\min} = 75$ W is considered in the outer line in Fig. 3.8, since this is approximately the minimum power found in the time-optimal screening. We can infer the following:

- For a given propellant mass, inner targets need shorter times than outer ones;
- For a given transfer time, outer targets need less propellant than inner ones.

3.5 Fuel-Optimal Transfers

The 172 potential targets that passed the time-optimal pruning are then processed under the perspective of a fuel-optimal step. It is worth highlighting that the fuel-optimal process widens the variable space as both the departure epoch t_0 and the time of flight (TOF) are let to vary. That is, while time-optimal problems have a one-dimensional search space (t_0), the fuel-optimal problems have a two-dimensional search space: [t_0, TOF]. A two-dimensional grid is therefore used to construct pork chop plots[7].

3.5.1 Methodology for Fuel-Optimal Solutions

Figure 3.9 shows the continuation strategy used for the fuel-optimal transfers. For each departure day t_0, the time of flight TOF is bottomed by the corresponding minimum transfer time $\tau(t_0)$ (blue lines in Fig. 3.9) and capped by $\overline{\tau}$, the 3-year condition in Table 3.2. This variable range has been discretised using a nonuniform grid, to ease efficiency. Specifically, the time-optimal solution is retrieved for each departure date t_0. From this point, the search continues along vertical lines (see Fig. 3.9). Suppose that the solution for a given pair $\{t_0, \mathrm{TOF}\}$ is found; then, the fuel-optimal solution for $\{t_0, \mathrm{TOF} + \Delta\tau\}$ is sought using the previous solution as initial guess, with $\Delta\tau = 15$ days. If a new solution is found, the scanning proceeds. Otherwise, the time step $\Delta\tau$ is halved. This process is repeated until the maximum TOF is reached.

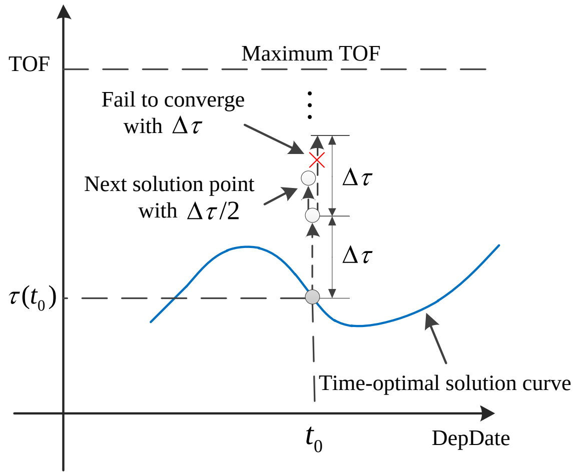

Figure 3.9: *Continuation strategy to solve fuel-optimal transfers for the two-year departure window.*

The outcome porkchop plots are shown for four sample targets in Fig. 3.10, where the same asteroids as in Fig. 3.6 have been used for consistency. The departure day (t_0) is on the x-axis, whereas the TOF is on the y-axis; the color code indicates the propellant mass m_p for each combination of (t_0, TOF). The red thick lines are the minimum-time profiles, and correspond to the dark lines in Fig. 3.6. The dashed region below the red line is therefore unfeasible: for a given departure date, M-ARGO can not take shorter than the corresponding point on the red line.

A number of optimal solutions are sampled arbitrarily from the plot of asteroid 2000 SG344 in Fig. 3.11. The points are labelled A–I, and the corresponding coordinates are given in Table 3.5. This exercise is performed to reveal the structure of the solutions inherent in the porkchop plots. Note that the samples are evenly spaced in terms of departure epoch and transfer time, except for A, D, and G that correspond to time-optimal solutions. The solutions that correspond to each of the nine points are reported in Figs. 3.12–3.14. In these figures, the following subfigures are given: Left: transfer trajectory in heliocentric frame (red:

[7] In practice, the search space of fuel-optimal transfers is three-dimensional because there is an homotopy parameter that is used to map energy-optimal problems into fuel-optimal problems [47].

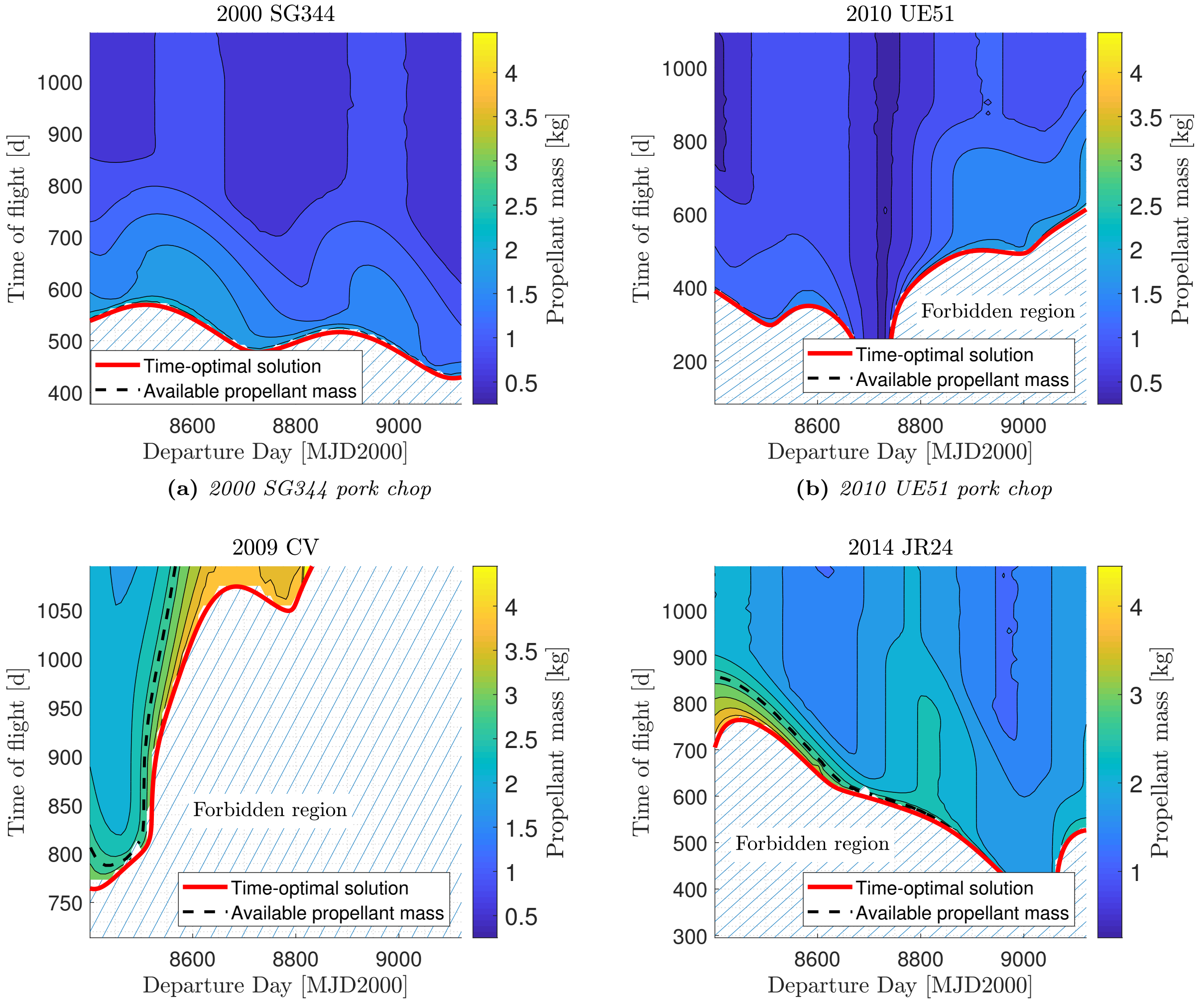

(a) *2000 SG344 pork chop*

(b) *2010 UE51 pork chop*

(c) *2009 CV pork chop*

(d) *2014 JR24 pork chop*

Figure 3.10: *Pork chop plots for some sample asteroids. The available propellant mass ($m_{p,\max} = 2.8$ kg) is indicated with a black dashed line, while the red thick line shows the time-optimal solution. The color code is the propellant mass used, see the bars on the right.*

thrust arc, blue: coast arc); Center: throttle factor $u(t)$, switching function $S(t)$ ($S(t) = S_t(t)$ for time-optimal problems and $S(t) = S_f(t)$ for fuel-optimal problems), and spacecraft mass $m(t)$ profiles; Right: thruster input power $P_{in}(t)$, specific impulse $I_{sp}(t)$, and maximum thrust $T_{\max}(t)$ profiles.

Table 3.5: *Coordinates of the samples in Fig. 3.11. The values of t_0 are in MJD2000.*

Point	t_0	TOF [d]	Point	t_0	TOF [d]	Point	t_0	TOF [d]
A	8600	$\tau(t_0)$	D	8800	$\tau(t_0)$	G	9000	$\tau(t_0)$
B	8600	700	E	8800	700	H	9000	700
C	8600	900	F	8800	900	I	9000	900

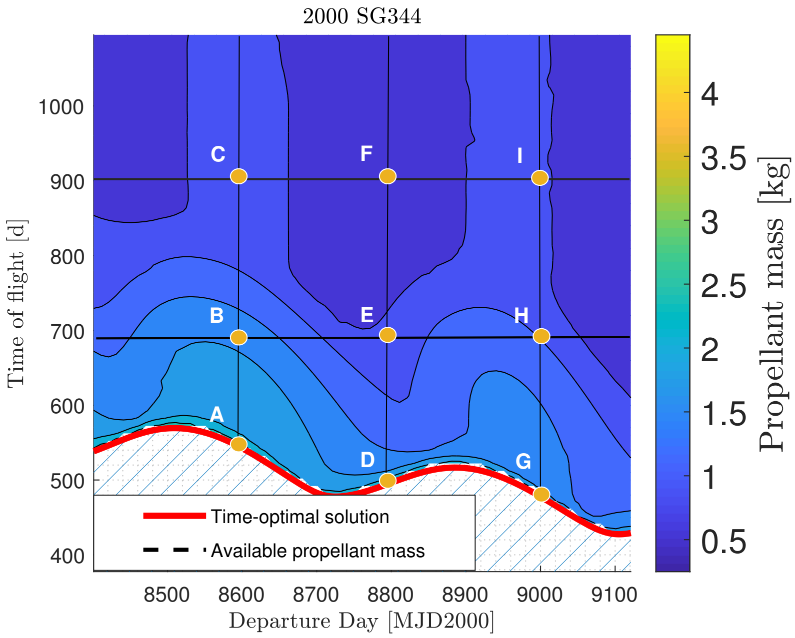

Figure 3.11: *Pork chop plot for 2000 SG344 with sample points.*

From Figs. 3.12–3.14 we can infer that: (1) the time-optimal solutions (A, D, G) have always thrust on ($u = 1$) as predicted by the theory; (2) the longer the transfer time, the higher the final mass, and therefore the lower the propellant used (this trend is reflected in different shades of blue in Fig. 3.11, though it is not always valid); (3) there is a 10–15% variability of I_{sp} and 40–80% variability of $T_{\max}$ during the transfer, due to the variable P_{in}.

3.5.2 Search Space Pruning

For each target, worth to extract is the global minimum of the propellant mass, that is

$$m_{p,\min} = \min_{\substack{t_0 \in [\underline{t}_0, \bar{t}_0] \\ \text{TOF} \in [\tau(t_0), \bar{\tau}]}} m_p(t_0, \text{TOF}) \tag{3.6}$$

Graphically, $m_{p,\min}$ is the blue-most point in the pork chop plots. For the 172 asteroid processed, $m_{p,\min}$ is retrieved, as well as the corresponding value of t_0 and TOF. The global minimum propellant mass $m_{p,\min}$ is shown in the form of a cumulative distribution function in Fig. 3.15. This information has been used to further reduce the search space by enforcing

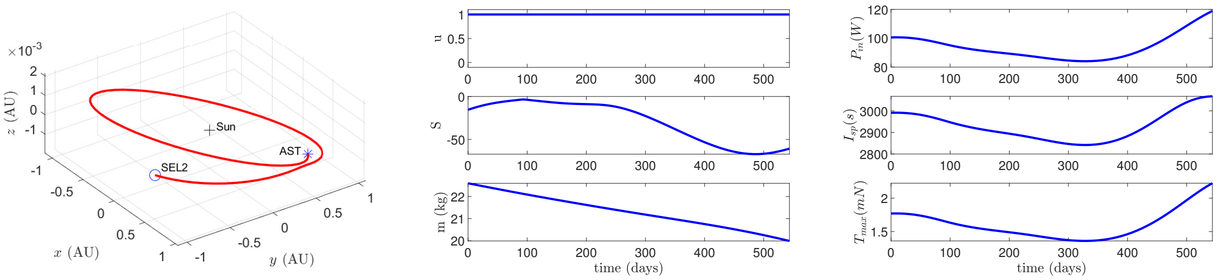

(a) *Solution corresponding to point A in Fig. 3.11 (left: transfer trajectory; center: u, S, m; right: P_{in}, I_{sp}, $T_{\max}$).*

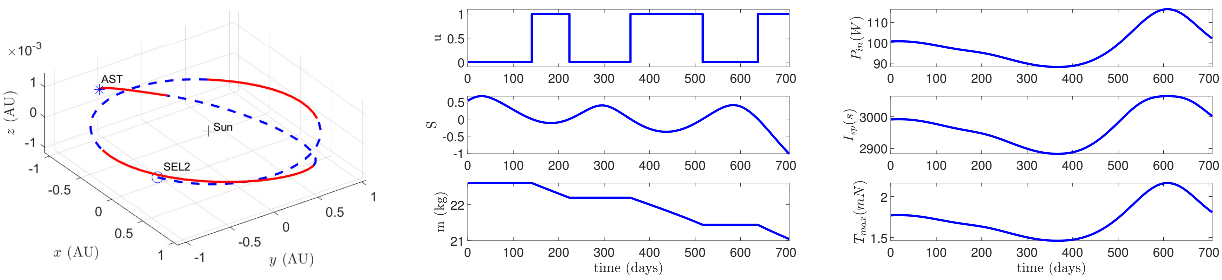

(b) *Solution corresponding to point B in Fig. 3.11 (left: transfer trajectory; center: u, S, m; right: P_{in}, I_{sp}, $T_{\max}$).*

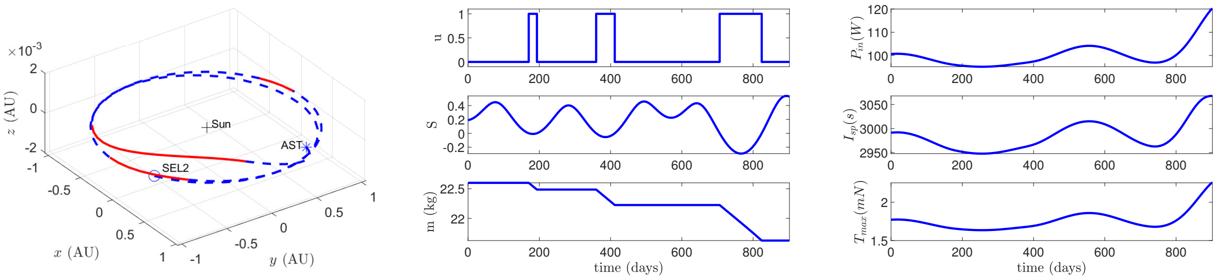

(c) *Solution corresponding to point C in Fig. 3.11 (left: transfer trajectory; center: u, S, m; right: P_{in}, I_{sp}, $T_{\max}$).*

Figure 3.12: *Solutions corresponding to points A, B, C in Fig. 3.11 (departure epoch: 8600 MJD 2000). In trajectory plots, AST: asteroid location upon arrival; SEL2: Sun-Earth Lagrange L_2; red solid line: thrust segment; blue dashed line: coast segment.*

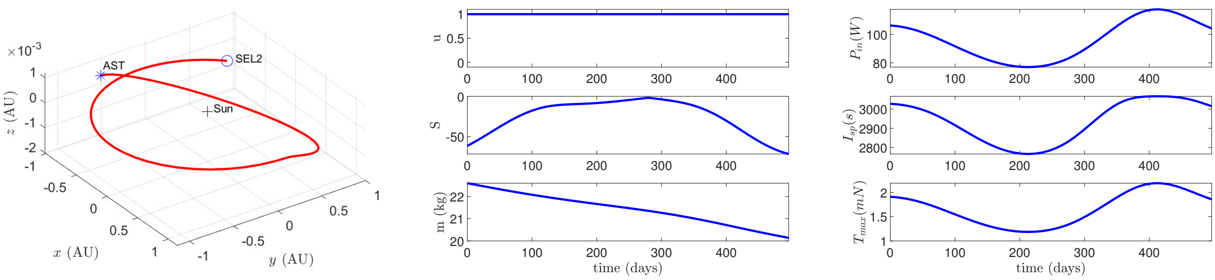

(a) *Solution corresponding to point D in Fig. 3.11 (left: transfer trajectory; center: u, S, m; right: P_{in}, I_{sp}, $T_{\max}$).*

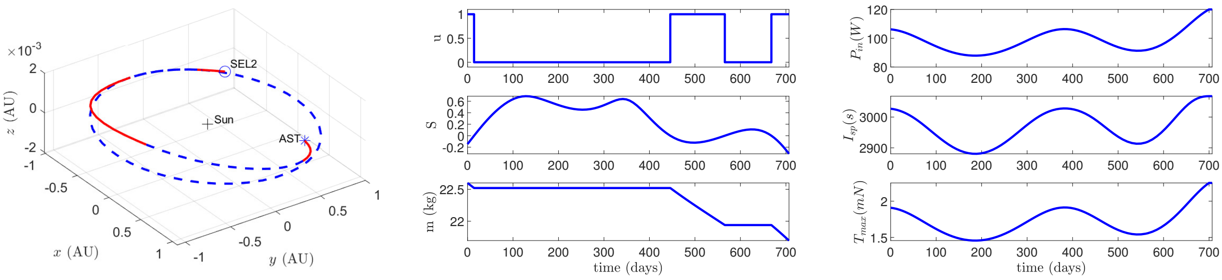

(b) *Solution corresponding to point E in Fig. 3.11 (left: transfer trajectory; center: u, S, m; right: P_{in}, I_{sp}, $T_{\max}$).*

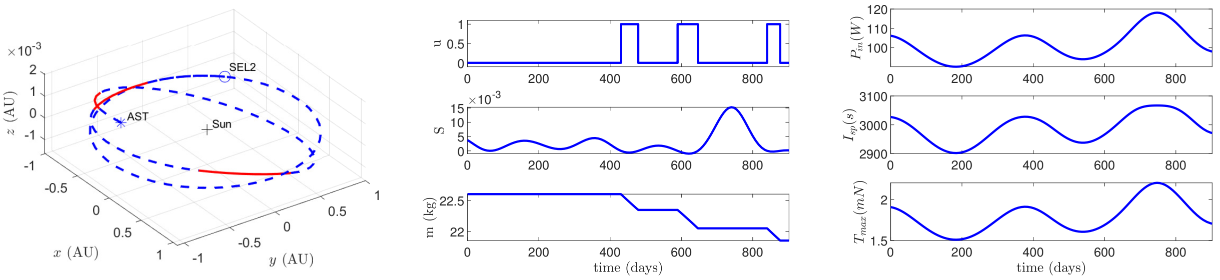

(c) *Solution corresponding to point F in Fig. 3.11 (left: transfer trajectory; center: u, S, m; right: P_{in}, I_{sp}, $T_{\max}$).*

Figure 3.13: *Solutions corresponding to points D, E, F in Fig. 3.11 (departure epoch: 8800 MJD 2000). In trajectory plots, AST: asteroid location upon arrival; SEL2: Sun-Earth Lagrange L_2; red solid line: thrust segment; blue dashed line: coast segment.*

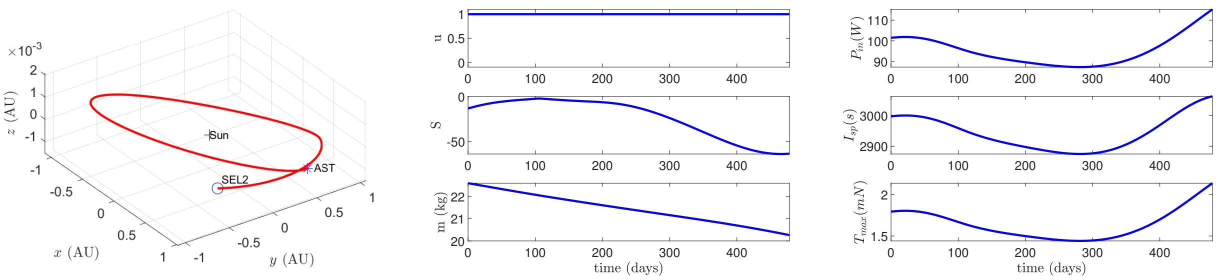

(a) *Solution corresponding to point G in Fig. 3.11 (left: transfer trajectory; center: u, S, m; right:* P_{in}*,* I_{sp}*,* $T_{\max}$*).*

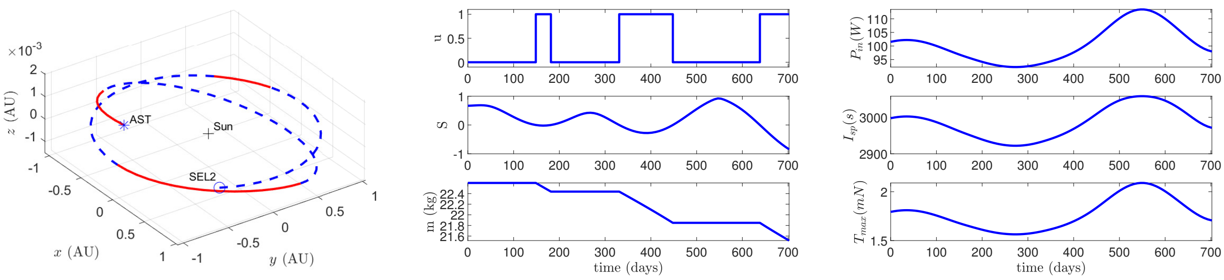

(b) *Solution corresponding to point H in Fig. 3.11 (left: transfer trajectory; center: u, S, m; right:* P_{in}*,* I_{sp}*,* $T_{\max}$*).*

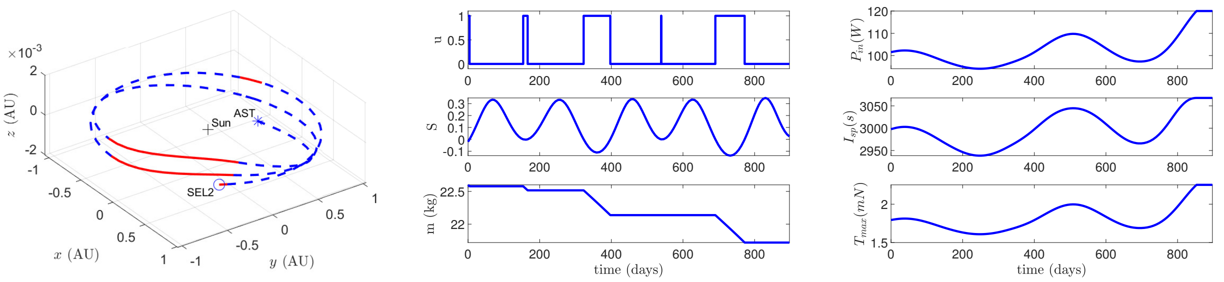

(c) *Solution corresponding to point I in Fig. 3.11 (left: transfer trajectory; center: u, S, m; right:* P_{in}*,* I_{sp}*,* $T_{\max}$*).*

Figure 3.14: *Solutions corresponding to points G, H, I in Fig. 3.11 (departure epoch: 9000 MJD 2000). In trajectory plots, AST: asteroid location upon arrival; SEL2: Sun-Earth Lagrange* L_2*; red solid line: thrust segment; blue dashed line: coast segment.*

the maximum propellant mass requirement in Table 3.2. It can be seen that 148 asteroids result feasible when enforcing this requirement. The list of these 148 asteroids is reported in Appendix A.2 where they are ranked in terms of the global minimum propellant mass.

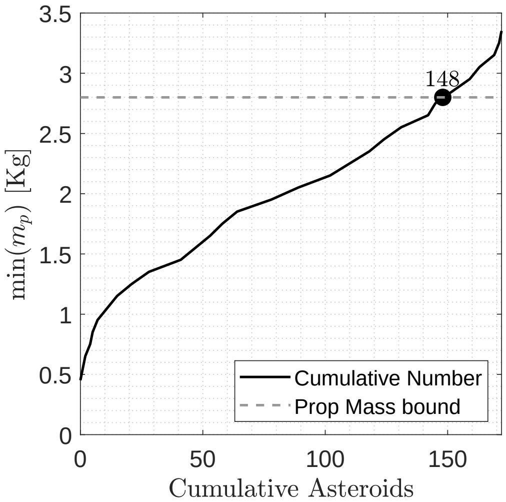

Figure 3.15: *Cumulative number of asteroids for increasing global minimum propellant mass. The available propellant mass ($m_{p,\max} = 2.8$ kg) is indicated by the dashed line, while the number shows the number of asteroids below the threshold.*

Remark 3.1. *The computational time for solving all time-optimal and fuel-optimal problems above takes around 2 months, using parallel computation with* 60 *cores. As shown in Section 2.3.2 of Chapter 2, the computational time by using analytic gradients is about 6 times faster than the finite difference method. Thus, much longer time is needed if the finite-difference method is used. The average number of solution points for one asteroid over 2-year window is: 1) around 818 solutions for the time-optimal curve; 2) around 2171 solutions for the fuel-optimal pock chop.*

3.6 Target Down-Selection

With reference to the procedure developed for the near-Earth object (NEO) target screening, out of more than 900,000 minor bodies in the MPC database, 456 objects passed the pre-filtering, which was based on simple geometrical criteria. For these 456 objects, a minimum-time optimization was carried out, and a subset made of 172 targets passed the pruning process when enforcing both a transfer time and a propellant mass thresholds (Section 3.4). These asteroids were then processed under the perspective of a minimum-fuel optimisation, and a subset of them made of 148 reachable targets was found (Section 3.5).

The whole process undertaken as well as the intermediate results are summarised in Table 3.6 (steps #1–#4). The focus is now on reducing further the set of reachable targets by pruning out those ones associated to transfers that are not desirable from the mission design point of view. This has been done through a one-by-one inspection of the porkchop plots, and yields a subset of downselected asteroids (step #5 in Table 3.6).

The pork chop plots related to the 148 reachable targets are reported in Appendix A.3. These figures embed relevant information, and their close-up analysis suggests that some targets might be more desirable than others in the time frame under consideration. Indeed, the following *qualitative* filtering criteria have been used:

Table 3.6: *NEO target screening process and results.*

Step	Target screening step	No. of objects
#1	Asteroids in the Minor Planet Center database	900,000+
#2	Potential targets after orbital parameters pre-filtering	456
#3	Possible targets after minimum-time optimisation and pruning	172
#4	Reachable targets after minimum-fuel optimisation and pruning	148
#5	Downselected targets after statistical, pork chop analysis	41

A. Although the transfer time of the reachable targets is below the 3-year threshold, short-lasting solutions are preferred over relatively longer ones (this involves, e.g., less mission operation costs, less spacecraft cumulated radiation, etc.);

B. Although the propellant mass of the reachable targets is below the 2.8-kg threshold, low-propellant solutions are preferred over those requiring relatively higher values (this involves, e.g., having more room for avionics, launching a lighter CubeSat, etc.);

C. Although the reachable targets have at least one feasible solution within the 2-year departure window, those spanning the entire window are preferred over those that partially cover it, the departure epoch not being fixed (this assures mission robustness against uncertainties in the departure time).

By enforcing criteria A, B, and C above, a high number of targets can be excluded from the subsequent analysis. In particular, with reference to Appendix A.3: 40 asteroids have a relatively long transfer time (condition A, see Table 3.7); 31 asteroids have a relatively high propellant mass (condition B, see Table 3.8); 36 asteroids do not span the full departure window (condition C, see Table 3.9). Thus, a total number of 107 asteroids is excluded from the solution space. It is worth mentioning that sometimes two or even three of the conditions above apply simultaneously.

Table 3.7: *List of targets requiring long transfer time (40).*

2007 WU3	2008 GM2	2011 MQ3	2012 WH	2016 FZ13	2016 RN20
2016 YR	2017 BZ6	2017 HK1	2017 JB2	2017 KJ32	2017 QB35
2017 RL16	2018 FM2	2018 LE1	2018 LQ2	2018 NX	2019 AU
2019 AC3	2019 DH1	2019 KM2	2019 LB1	2009 CV	YORP
2004 QA22	2007 VU6	2010 FY9	2011 OJ45	2013 VM13	2014 HN2
2014 MZ17	2014 UN114	2014 WU200	2015 JD3	2015 TC25	2016 TY55
2017 QW1	2018 FH1	2018 PR7	2018 WV1		

Table 3.8: *List of targets requiring high propellant mass (31).*

2014 EK24	1999 CG9	2005 QP11	2007 BB	2007 RO17	2010 WU8
2011 AA37	2012 AQ	2012 HK31	2012 PB20	2012 SX49	2012 VC26
2013 TG6	2014 FW32	2014 HW	2015 XD169	2015 XC352	2015 YK
2016 CH30	2016 EU84	2016 HF19	2018 FM3	2018 PN22	2018 SD2
2018 UE1	2019 GE1	2016 SX1	2017 UQ6	2017 YD1	2017 YS1
2017 VT7					

Table 3.9: *List of targets not spanning the full departure window (36).*

1991 VG	1999 AO10	2000 SZ162	2001 GP2	2004 VJ1	2006 JY26
2006 RH120	2007 UN12	2008 EA9	2008 KT	2009 HC	2010 HA
2011 CE22	2011 CL50	2011 ED12	2012 FM35	2013 GH66	2013 RZ53
2014 BA3	2015 DU	2017 TP4	2018 GR4	2018 KP1	2018 PK21
2018 PM28	2018 TS4	2018 VN5	2019 ED	2019 GV5	2008 UA202
2010 TE55	2013 BS45	2014 QN266	2014 YP44	2015 PS228	2016 GK135

Table 3.10: *List of downselected targets (41).*

2012 UV136	2000 SG344	2001 QJ142	2008 CM74	2008 DL4	2008 HU4
2008 JL24	2008 ST	2009 BD	2010 JR34	2010 UE51	2011 BQ50
2011 MD	2011 WU2	2012 BB14	2012 EP10	2012 TF79	2014 JR24
2014 LJ	2014 YD	2014 YN	2015 BM510	2015 KK57	2015 VU64
2015 VO142	2015 XZ378	2016 BQ	2016 CF137	2016 DF	2016 FU12
2016 TB18	2016 TB57	2016 WQ3	2017 DV35	2017 RL2	2017 YW3
2018 DC4	2018 GE	2019 AP8	2019 DJ1	2019 GF1	

After filtering the list of reachable asteroids by virtue of criteria A, B, and C, the 41 targets listed in Table 3.10 are found. Since the mission and spacecraft design had to be tailored over five reference cases, (as per the statement of work), a choice has been made considering the following properties:

- Information in LCDB: this is a desirable information to have as it is associated to more knowledge of the target;
- Information known on spin-rate: like the light curve, this is desirable to have;
- Observability in future: the possibility to observe the target in the future allows refining the orbital uncertainty, so increasing the chances of in-orbit detection;
- Promising targets: the targets being less sensitive to the departure epoch and transfer time have been favoured over others.

Table 3.11: *Orbital elements for the selected 5 asteroids (ecliptic J2000).*

Name	a [AU]	e [-]	i [deg]	ω [deg]	Ω [deg]
2000 SG344	0.9775	0.0669	0.1121	275.3026	191.9599
2010 UE51	1.0552	0.0597	0.6239	47.2479	32.2993
2011 MD	1.0562	0.0371	2.4455	5.9818	271.5986
2012 UV136	1.0073	0.1392	2.2134	288.6071	209.9001
2014 YD	1.0721	0.0866	1.7357	34.1161	117.6401

The five temporary targets suggested for the mission and spacecraft design are:

1. **2014 YD**: Known high spin rate close to barrier and favourable mission opportunity;
2. **2010 UE51**: #1 on time-optimal and fuel-optimal solution list;
3. **2011 MD**: Present in light curve database and favourable mission opportunity.

4. **2000 SG344**: Chance for observation, higher inclination, good OCC [8];
5. **2012 UV136**: Known spin rate, largest target size/brightest.

The orbital parameters of these five sample targets are reported in Table 3.11.

3.7 Summary

This chapter elaborates on the NEA targets screening for the M-ARGO mission. A multi-step filtering activity has been performed to identify a subset of asteroids reachable by the M-ARGO CubeSat. Bounds on orbital elements have reduced the Minor Planet Center database list of asteroids to 456 objects. Out of these, 172 objects require less than 900 days and 4 kg for the time-optimal solution. Then, 148 asteroids require less than 2.8 kg for the fuel-optimal solution. The list of 148 shapes the envelop of reachable targets by the M-ARGO CubeSat. Considering desirable mission parameters, the list is further reduced to 41 downselected objects, out of which 5 samples are extracted.

[8] OCC is the Orbit Condition Code, where 0 implies a well-determined orbit and 9 implies a poorly determined orbit [93].

CHAPTER 4

FUEL-OPTIMAL MANY-REVOLUTION EARTH-ORBIT TRANSFERS WITH ECLIPSES

THIS chapter studies the SEP-based Earth-orbit low-thrust optimization with eclipses. This task is challenging because the low thrust-to-mass radio usually requires long flight times and thus large number of revolutions to steer the spacecraft to the desired orbit. Additionally, the lack of power from solar panels when flying inside Earth-shadow eclipses prevents using the engine, which makes this NOCP even more difficult to solve. In literature, thrust discontinuity was avoided in [94, 95] by smoothing the thrust modulus during shadow entrance and exit. Earth-shadow constraints were modelled as interior-point constraints in [50, 51] to solve time-optimal transfers. Averaging technique was integrated into indirect optimization in [96] to rapidly search nearly time-optimal solutions. However, many-revolution fuel-optimal transfers with accurate bang-bang control have not been achieved yet by indirect methods. Based on the method presented in Chapter 2, this chapter tackles this issue by developing an efficient and robust indirect method.

4.1 Problem Statement

4.1.1 Dynamical Equations

The modified equinoctial elements (MEE) are used to describe the orbital dynamics of the SEP-based spacecraft since they are non-singular orbital elements and are well behaved in low-thrust optimization [97]. The relationship between MEE and classical orbital elements is

$$\begin{aligned} p &= a(1-e^2) \\ e_x &= e\cos(\omega+\Omega) \\ e_y &= e\sin(\omega+\Omega) \\ h_x &= \tan(i/2)\cos\Omega \\ h_y &= \tan(i/2)\sin\Omega \\ L &= \omega+\Omega+\theta \end{aligned} \tag{4.1}$$

where a is the semi-major axis, e is the eccentricity, i is the orbital inclination, Ω is the right ascension of the ascending node, ω is the argument of perigee, θ is the true anomaly, p is the semilatus rectum and L is the true longitude. Equations of motion of the spacecraft under equatorial Earth-centered inertial (ECI) coordinate are

$$\dot{\boldsymbol{x}} = \boldsymbol{f}(\boldsymbol{x},\boldsymbol{\alpha},u) \Rightarrow \begin{pmatrix} \dot{\boldsymbol{x}}_{\text{mee}} \\ \dot{m} \end{pmatrix} = \begin{pmatrix} u\dfrac{T_{\max}}{m}\boldsymbol{B}\,\boldsymbol{\alpha}+\boldsymbol{A} \\ -\dfrac{T_{\max}}{c}u \end{pmatrix} \tag{4.2}$$

where $\boldsymbol{x}_{\text{mee}} = [p, e_x, e_y, h_x, h_y, L]^\top$ is the MEE vector, $\boldsymbol{x} = [\boldsymbol{x}_{\text{mee}}^\top, m]^\top$ is the state vector, m is the spacecraft mass; $u \in [u_{\min}, 1]$ is the thrust throttle factor. $u_{\min} = 0$ when the SEP engine is off. $0 \leqslant u_{\min} \leqslant 1$ is used in the continuation scheme, see Section 4.2.3; $\boldsymbol{\alpha}$ is the thrust direction unit vector, $T_{\max}$ is the maximum thrust magnitude, $c = I_{\text{sp}}g_0$ is the exhaust velocity where I_{sp} is the specific impulse and g_0 is the gravity acceleration at sea level. Both I_{sp} and $T_{\max}$ are assumed constant. In Eq. (4.2),

$$\boldsymbol{A} = [0,0,0,0,0,\kappa]^\top \tag{4.3}$$

$$\boldsymbol{B} = \begin{bmatrix} 0 & \dfrac{2p}{\nu}\sqrt{\dfrac{p}{\mu}} & 0 \\ \sqrt{\dfrac{p}{\mu}}\sin L & \sqrt{\dfrac{p}{\mu}}[(\nu+1)\cos L + e_x]\dfrac{1}{\nu} & -\sqrt{\dfrac{p}{\mu}}[h_x\sin L - h_y\cos L]\dfrac{e_y}{\nu} \\ -\sqrt{\dfrac{p}{\mu}}\cos L & \sqrt{\dfrac{p}{\mu}}[(\nu+1)\sin L + e_y]\dfrac{1}{\nu} & \sqrt{\dfrac{p}{\mu}}[h_x\sin L - h_y\cos L]\dfrac{e_x}{\nu} \\ 0 & 0 & \sqrt{\dfrac{p}{\mu}}\dfrac{s^2}{2\nu}\cos L \\ 0 & 0 & \sqrt{\dfrac{p}{\mu}}\dfrac{s^2}{2\nu}\sin L \\ 0 & 0 & \dfrac{1}{\nu}\sqrt{\dfrac{p}{\mu}}(h_x\sin L - h_y\cos L) \end{bmatrix} \tag{4.4}$$

where μ is the gravitational parameter and

$$\nu = 1 + e_x\cos L + e_y\sin L, \quad s^2 = 1 + h_x^2 + h_y^2, \quad \kappa = \sqrt{\mu p}\left(\frac{\nu}{p}\right)^2 \tag{4.5}$$

The boundary conditions are

$$\begin{gathered} p(t_i) = p_i, \quad e_x(t_i) = e_{xi}, \quad e_y(t_i) = e_{yi}, \\ h_x(t_i) = h_{xi}, \quad h_y(t_i) = h_{yi}, \quad L(t_i) = L_i, \quad m(t_i) = m_i \\ p(t_f) = p_f, \quad e_x(t_f) = e_{xf}, \quad e_y(t_f) = e_{yf}, \\ h_x(t_f) = h_{xf}, \quad h_y(t_f) = h_{yf}, \quad L(t_f) = \text{free}, \quad m(t_f) = \text{free} \end{gathered} \tag{4.6}$$

where t_i and t_f are fixed initial and terminal time instants.

The MEE are related to the Cartisian coordinate $(\boldsymbol{r}, \boldsymbol{v})$ through [98]

$$\boldsymbol{r} = \begin{bmatrix} \frac{p}{s^2\nu}\left(\cos L + \alpha^2 \cos L + 2h_x h_y \sin L\right) \\ \frac{p}{s^2\nu}\left(\sin L - \alpha^2 \sin L + 2h_x h_y \cos L\right) \\ \frac{2p}{s^2\nu}\left(h_x \sin L - h_y \cos L\right) \end{bmatrix} \tag{4.7}$$

$$\boldsymbol{v} = \begin{bmatrix} -\frac{1}{s^2}\sqrt{\frac{\mu}{p}}\left(\sin L + \alpha^2 \sin L - 2h_x h_y \cos L + e_y - 2e_x h_x h_y + \alpha^2 e_y\right) \\ -\frac{1}{s^2}\sqrt{\frac{\mu}{p}}\left(-\cos L + \alpha^2 \cos L + 2h_x h_y \sin L - e_x + 2e_y h_x h_y + \alpha^2 e_x\right) \\ \frac{2}{s^2}\sqrt{\frac{\mu}{p}}\left(h_x \cos L + h_y \sin L + e_x h_x + e_y h_y\right) \end{bmatrix} \tag{4.8}$$

where

$$\alpha^2 = h_x^2 - h_y^2 \tag{4.9}$$

4.1.2 Earth-Shadow Eclipses

A shadow switching function to discriminate between eclipsed and illuminated arcs is essential. It is now derived from the shadow model. In literature, mainly two shadow models, i.e., cylindrical model [50, 94, 95] and cone model [98, 99], are widely used. In the following, the cone model in [99] is employed here since it is more accurate. When the spacecraft passes through the umbra shadow, the solar energy is completely lost, while limited solar energy is received in the penumbra shadow. To be on the safe side, we assume that the engine switches off when the spacecraft passes through either umbra or penumbra. Since umbra shadow is a portion of the penumbra shadow [98], only penumbra geometry in Fig. 4.1 is discussed.

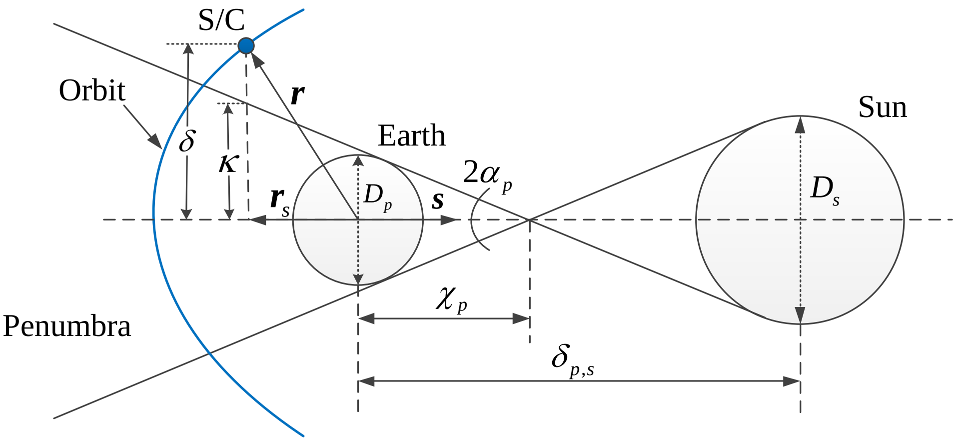

Figure 4.1: *Geometry of penumbra shadow. S/C: the spacecraft position.*

Several assumptions are made to simplify the penumbra shadow model. Firstly, both the Sun and the Earth are assumed spherical bodies, thus the penumbra shadow is conical. Secondly, the Earth orbit is assumed planar and circular with respect to the Sun. In the ecliptic ECI, the Sun–Earth angle is $\theta_s = \theta_{s,i} + n(t - t_i)$, where $\theta_{s,i}$ is the Sun–Earth angle at t_i and $n = 360/365.25636306$ deg/day, and the solar unit vector is $\boldsymbol{s}_{\text{ec}} = [\cos\theta_s, \sin\theta_s, 0]^\top$. Transforming $\boldsymbol{s}_{\text{ec}}$ to $\boldsymbol{s}$ in equatorial ECI yields $\boldsymbol{s} = [\cos(\theta_s), \cos(i_e)\sin(\theta_s), \sin(i_e)\sin(\theta_s)]$, where $i_e = 23°26'21.448''$ is the ecliptic obliquity, i.e., the angle between the equatorial plane and the ecliptic plane.

In Fig. 4.1, D_p and D_s are diameters of the Earth and the Sun, $\delta_{p,s}$ is the distance between them, and χ_p satisfies

$$\chi_p = \frac{D_p\,\delta_{p,s}}{D_s + D_p} \tag{4.10}$$

The angle α_p is

$$\alpha_p = \sin^{-1}\frac{D_p}{2\chi_p} \tag{4.11}$$

The projection of the spacecraft position vector on the solar unit vector $\boldsymbol{s}$ is

$$\boldsymbol{r}_s = (\boldsymbol{r}\cdot\boldsymbol{s})\boldsymbol{s} \tag{4.12}$$

The vertical vector between the center of the penumbra cone and the spacecraft is

$$\boldsymbol{\delta} = \boldsymbol{r} - \boldsymbol{r}_s \tag{4.13}$$

The distance between the penumbra terminator point and the center of the penumbra cone at the projection point is

$$\kappa = (\chi_p + \|\boldsymbol{r}_s\|)\tan\alpha_p \tag{4.14}$$

The difference of the magnitude of $\boldsymbol{\delta}$ to the distance κ is

$$S_d(t,\boldsymbol{r}) = \|\boldsymbol{\delta}\| - \kappa \tag{4.15}$$

along with its partial derivatives as

$$\frac{\partial S_d}{\partial \boldsymbol{r}} = \frac{\boldsymbol{\delta}^\top}{\|\boldsymbol{\delta}\|}\left(\boldsymbol{I}_{3\times3} - \boldsymbol{s}\boldsymbol{s}^\top\right) - \frac{\tan\alpha_p}{\|\boldsymbol{r}_s\|}\boldsymbol{r}_s^\top\boldsymbol{s}\boldsymbol{s}^\top \tag{4.16}$$

$$\frac{\partial S_d}{\partial t} = -\left(\frac{\boldsymbol{\delta}^\top}{\|\boldsymbol{\delta}\|} + \frac{\boldsymbol{r}_s^\top}{\|\boldsymbol{r}_s\|}\tan\alpha_p\right)\left(\boldsymbol{r}^\top\boldsymbol{s}\boldsymbol{I}_{3\times3} + \boldsymbol{s}\boldsymbol{r}^\top\right)\frac{\partial \boldsymbol{s}}{\partial\theta_s}n \tag{4.17}$$

where $\partial\boldsymbol{s}/\partial\theta_s = [-\sin(\theta_s), \cos(i_e)\cos(\theta_s), \sin(i_e)\cos(\theta_s)]^\top$. The spacecraft is inside the penumbra cone if $\boldsymbol{r}\cdot\boldsymbol{s} < 0$ and $S_d < 0$. The shadow entrance and exit occur when $S_d = 0$ and $\boldsymbol{r}\cdot\boldsymbol{s} < 0$. Thus, S_d is defined as the shadow switching function, under the condition $\boldsymbol{r}\cdot\boldsymbol{s} < 0$.

To ease the discussion, a signal variable p_{type} is defined to label the position of the spacecraft with respect to the shadow

$$p_{\text{type}} = \begin{cases} \text{In}, & \text{if} \quad S_d < 0 \quad \text{and} \quad \boldsymbol{r}\cdot\boldsymbol{s} < 0 \\ \text{Out}, & \text{if} \quad \text{otherwise} \end{cases} \tag{4.18}$$

To favor the explanation of the continuation scheme in Section 4.2.3, the following definitions are given. Let $N_s(t)$ be the number of accumulated eclipses at a time t, and let $N_{\max}$ be the user-defined maximum number of eclipses. The shadow is deemed active when $N_s \leqslant N_{\max}$. Inactive shadows contribute to N_s, yet they do not affect the engine status. Let $\tilde{p}_{\text{type}}$ denote the spacecraft position with respect to the active shadow. Then

$$\tilde{p}_{\text{type}} = \begin{cases} \text{In}, & \text{if} \quad S_d < 0 \quad \text{and} \quad \boldsymbol{r}\cdot\boldsymbol{s} < 0 \quad \text{and} \quad N_s \leqslant N_{\max} \\ \text{Out}, & \text{if} \quad \text{otherwise} \end{cases} \tag{4.19}$$

Thus $\tilde{p}_{\text{type}} = p_{\text{type}}$ if sufficiently large $N_{\max}$ is adopted. If the initial point is located outside the active shadow, $N_s(t_i) = 0$, otherwise, $N_s(t_i) = 0.5$. The rule $N_s \leftarrow N_s + 0.5$ is executed every time p_{type} switches its value. The updated N_s is then used to evaluate $\tilde{p}_{\text{type}}$. Thus, $N_{\max} = 0$ indicates that the shadow constraints are inactive.

4.1.3 Fuel-Optimal Problem

The fuel-optimal performance index is

$$J_f = \frac{T_{\max}}{c} \int_{t_i}^{t_f} u \, \mathrm{d}t \tag{4.20}$$

Since the optimal thrust throttle profile u^* is bang-bang [95], a continuation parameter ε is employed [47]. The performance index becomes

$$J_\varepsilon = \frac{T_{\max}}{c} \int_{t_i}^{t_f} [u - \varepsilon u(1-u)] \, \mathrm{d}t \tag{4.21}$$

The energy-optimal problem ($\varepsilon = 1$) is solved first, then the solution manifold is traced by gradually reducing ε, until the fuel-optimal problem ($\varepsilon = 0$) is obtained.

The Hamiltonian function reads

$$H_\varepsilon = \frac{T_{\max}}{c} [u - \varepsilon u(1-u)] + \lambda_L \kappa + u \, \frac{T_{\max}}{m} \boldsymbol{\lambda}_{\text{mee}}^\top \boldsymbol{B} \, \boldsymbol{\alpha} - \lambda_m \, u \, \frac{T_{\max}}{c} \tag{4.22}$$

where $\boldsymbol{\lambda} = [\boldsymbol{\lambda}_{\text{mee}}^\top, \lambda_m]^\top$ is the costate vector associated to $\boldsymbol{x}$. By virtue of the PMP, the optimal thrust direction $\boldsymbol{\alpha}^*$ satisfies [95]

$$\boldsymbol{\alpha}^* = -\frac{\boldsymbol{B}^\top \boldsymbol{\lambda}_{\text{mee}}}{\|\boldsymbol{B}^\top \boldsymbol{\lambda}_{\text{mee}}\|} \tag{4.23}$$

Substituting $\boldsymbol{\alpha}^*$ into Eq. (4.22) yields

$$H_\varepsilon = \lambda_L \kappa + u \frac{T_{\max}}{c} [S_\varepsilon - \varepsilon(1-u)] \tag{4.24}$$

where the throttle switching function S_ε is

$$S_\varepsilon = -\frac{c}{m} \|\boldsymbol{B}^\top \boldsymbol{\lambda}_{\text{mee}}\| - \lambda_m + 1 \tag{4.25}$$

u^* is determined by PMP and the Earth-shadow constraint (4.19) as

$$u^* = \begin{cases} u_{\min}, & \text{if} \quad S_\varepsilon > (1-2u_{\min})\varepsilon \quad \text{or} \quad \tilde{p}_{\text{type}} = \text{In} \\ (\varepsilon - S_\varepsilon)/2\varepsilon & \text{if} \quad -\varepsilon < S_\varepsilon < (1-2u_{\min})\varepsilon \quad \text{and} \quad \tilde{p}_{\text{type}} = \text{Out} \\ 1, & \text{if} \quad S_\varepsilon < -\varepsilon \quad \text{and} \quad \tilde{p}_{\text{type}} = \text{Out} \end{cases} \tag{4.26}$$

Remark 4.1. *An interior-point constraint should be addressed to ensure that Eq.* (4.26) *satisfies necessary conditions of optimality, see Section 4.1.4.*

Let $\boldsymbol{y} := [\boldsymbol{x}^\top, \boldsymbol{\lambda}^\top]^\top$ be the combined state and costate vector, the motion of the spacecraft is determined by integrating the following state-costate dynamics

$$\dot{\boldsymbol{y}} = \boldsymbol{F}(t, \boldsymbol{y}) \Rightarrow \begin{cases} \dot{\boldsymbol{x}}_{\text{mee}} & = u\,\dfrac{T_{\max}}{m}\,\boldsymbol{B}\,\boldsymbol{\alpha} + \boldsymbol{A} \\ \dot{m} & = -\dfrac{T_{\max}}{c}\,u \\ \dot{\boldsymbol{\lambda}}_{\text{mee}} & = -\lambda_L \left[\dfrac{\partial \kappa}{\partial \boldsymbol{x}_{\text{mee}}}\right]^\top - u\dfrac{T_{\max}}{m}\left[\dfrac{\partial \boldsymbol{B}^\top \boldsymbol{\lambda}_{\text{mee}}}{\partial \boldsymbol{x}_{\text{mee}}}\right]^\top \boldsymbol{\alpha} \\ \dot{\lambda}_m & = u\,\dfrac{T_{\max}}{m^2}\boldsymbol{\lambda}_{\text{mee}}^\top \boldsymbol{B}\boldsymbol{\alpha} \end{cases} \tag{4.27}$$

with $\boldsymbol{\alpha}$ and u as in Eqs. (4.23) and (4.26), respectively.

Since the terminal true longitude and mass are free, and the augmented terminal cost does not explicitly depend on the true longitude and the mass, there exists

$$\lambda_L(t_f) = 0, \quad \lambda_m(t_f) = 0 \tag{4.28}$$

4.1.4 Interior-Point Constraint

The SEP engine switches on/off when the spacecraft exits/enters Earth-shadow eclipses. However, this operation maybe not optimal since it is not related to the minimization of H_ε. In order to satisfy necessary conditions of optimality, the events of shadow entrance and exit should be treated as interior-point constraints [50]. Suppose that $S_d(t_s) = 0$, and $\tilde{p}_{\text{type}}$ switches between In and Out at t_s, the following conditions should be satisfied [26]

$$H_\varepsilon(t_s^-) = H_\varepsilon(t_s^+) - \pi_\varepsilon \frac{\partial S_d}{\partial t}(t_s) \tag{4.29}$$

$$\boldsymbol{\lambda}_{\text{mee}}^\top(t_s^-) = \boldsymbol{\lambda}_{\text{mee}}^\top(t_s^+) + \pi_\varepsilon \frac{\partial S_d}{\partial \boldsymbol{x}_{\text{mee}}}(t_s) \tag{4.30}$$

where t_s^- and t_s^+ are time instants instantaneously before and after t_s, and π_ε is a scalar Lagrange multiplier. In Eq. (4.30), costate $\boldsymbol{\lambda}_{\text{mee}}$ is discontinuous since $\partial S_d/\partial \boldsymbol{x}_{\text{mee}}(t_s) \neq \boldsymbol{0}^\top$. It can be verified that

$$\frac{\partial \boldsymbol{r}}{\partial \boldsymbol{x}_{\text{mee}}}\boldsymbol{B} = \boldsymbol{0}_{3\times 3} \tag{4.31}$$

Then we have

$$\boldsymbol{B}^\top \boldsymbol{\lambda}_{\text{mee}}(t_s^+) = \boldsymbol{B}^\top \left[\boldsymbol{\lambda}_{\text{mee}}(t_s^-) - \pi_\varepsilon \left(\frac{\partial S_d}{\partial \boldsymbol{x}_{\text{mee}}}\right)^\top\right] = \boldsymbol{B}^\top \boldsymbol{\lambda}_{\text{mee}}(t_s^-) \tag{4.32}$$

Thus $\boldsymbol{\alpha}^*$ in Eq. (4.23) and S_ε in Eq. (4.25) are continuous across t_s. The time derivative of S_d is simplified as

$$\dot{S}_d = \frac{\partial S_d}{\partial \boldsymbol{x}_{\text{mee}}}\left(\boldsymbol{A} + u\frac{T_{\max}}{m}\boldsymbol{B}\boldsymbol{\alpha}\right) + \frac{\partial S_d}{\partial t} = \frac{\partial S_d}{\partial L}\kappa + \frac{\partial S_d}{\partial t} \tag{4.33}$$

The Hamiltonian function at t_s^- and t_s^+ is

$$H_\varepsilon(t_s^-) = \lambda_L(t_s^-)\kappa + u(t_s^-)\frac{T_{\max}}{c}\left(S_\varepsilon - \varepsilon + \varepsilon u(t_s^-)\right) \tag{4.34}$$

$$H_\varepsilon(t_s^+) = \lambda_L(t_s^+)\kappa + u(t_s^+)\frac{T_{\max}}{c}\left(S_\varepsilon - \varepsilon + \varepsilon u(t_s^+)\right) \tag{4.35}$$

Combining Eq. (4.29), (4.30), (4.33), (4.34) and (4.35) yields the analytical expression of π_ε as

$$\pi_\varepsilon = \Delta u \frac{T_{\max}}{c}\frac{S_\varepsilon - \varepsilon + (u(t_s^+) + u(t_s^-))\varepsilon}{\dot{S}_d} \tag{4.36}$$

where $\Delta u = u(t_s^+) - u(t_s^-)$.

Remark 4.2. *Let $\boldsymbol{y}(t) = \boldsymbol{\varphi}_\varepsilon([\boldsymbol{x}_i, \boldsymbol{\lambda}_i], t_i, t)$ be the solution flow of Eq. (4.27) integrated from the initial time t_i to a generic time t, using $\boldsymbol{x}_i$, $\boldsymbol{\lambda}_i$ at t_i, u^* in Eq. (4.26), $\boldsymbol{\alpha}^*$ in Eq. (4.23) and $\boldsymbol{\lambda}_{\text{mee}}(t_s^+)$ in Eq. (4.30). The energy-to-fuel-optimal problem is to find $\boldsymbol{\lambda}_i^*$ such that $\boldsymbol{y}(t_f) = \boldsymbol{\varphi}_\varepsilon([\boldsymbol{x}_i, \boldsymbol{\lambda}_i^*], t_i, t_f)$ satisfies Eqs. (4.6) and (4.28).*

4.2 Solution Method

4.2.1 Analytic Derivatives

The variational method evaluates the gradients through tht STM and the chain rule. The STM maps small variations in the initial conditions $\delta\boldsymbol{y}_i$ over $t_i \to t$, i.e., $\delta\boldsymbol{y} = \Phi(t_i, t)\delta\boldsymbol{y}_i$. STM is subject to

$$\dot{\Phi}(t, t_i) = D_y\boldsymbol{F}\,\Phi(t, t_i) \tag{4.37}$$

where $D_y\boldsymbol{F}$, the Jacobian matrix of dynamical equations Eq. (4.27), has two different expressions based on whether u is constant or not. $\Phi(t_i, t_i) = I_{14\times 14}$. Let $\boldsymbol{z} := [\boldsymbol{y}, \text{vec}(\Phi)]$ be the 210-dimensional vector consisting of $\boldsymbol{y}$ and the columns of Φ, where the operator 'vec' converts the matrix into a column vector. There exists

$$\dot{\boldsymbol{z}} = \boldsymbol{G}(\boldsymbol{z}) \Rightarrow \begin{cases} \dot{\boldsymbol{y}} & = \boldsymbol{F}(\boldsymbol{y}) \\ \text{vec}(\dot{\Phi}) & = \text{vec}(D_y\boldsymbol{F}\,\Phi) \end{cases} \tag{4.38}$$

Note that the integration of Φ matrix maps states and costates along a continuous trajectory. When the discontinuity is encountered at the switching time t_s, the STM compensation matrix, $\Psi(t_s)$, across the discontinuity should be determined [45]. Suppose that there are N discontinuities at $t_1,\ t_2, \cdots, t_N$, $\Phi(t_f, t_i)$ is calculated through the chain rule as

$$\Phi(t_f, t_i) = \Phi(t_f, t_N^+)\Psi(t_N)\Phi(t_N^-, t_{N-1}^+)\Psi(t_{N-1})\ldots\Phi(t_2^-, t_1^+)\Psi(t_1)\Phi(t_1^-, t_i) \tag{4.39}$$

Suppose the discontinuity detected at t_s is indicated by a switching function S crossing a constant threshold η, there are two possible cases:

- Case 1: $S = S_\varepsilon$, $\varepsilon = 0$, $\eta = 0$ in the fuel-optimal problem. In this case, $\boldsymbol{y}$ is continuous but $\dot{\boldsymbol{y}}$ is discontinuous. The thrust throttle u jumps between 0 and 1 at t_s.
- Case 2: $S = S_d$, $u \neq 0$, $\eta = 0$ for energy-to-fuel-optimal problems. In this case, both $\boldsymbol{y}$ and $\dot{\boldsymbol{y}}$ are discontinuous. The thrust throttle u jumps between $u(t_s^\pm)$ and $u_{\min}$ at t_s, if $u(t_s^\pm) \neq u_{\min}$.

For both cases, the switching function S at $t_s^- + \mathrm{d}t_s$ on the neighboring extremal trajectory must satisfy

$$S(\boldsymbol{y}(t_s^- + \mathrm{d}t_s), t_s^- + \mathrm{d}t_s) = \eta \tag{4.40}$$

Expanding S at t_s^- yields

$$\mathrm{d}S = \frac{\partial S}{\partial \boldsymbol{y}}\mathrm{d}\boldsymbol{y}(t_s^-) + \frac{\partial S}{\partial t}\mathrm{d}t_s = \left(\frac{\partial S}{\partial \boldsymbol{y}}\delta\boldsymbol{y}(t_s^-) + \frac{\partial S}{\partial \boldsymbol{y}}\dot{\boldsymbol{y}}(t_s^-)\delta t_s\right) + \frac{\partial S}{\partial t}\delta t_s = 0 \tag{4.41}$$

thus there exists

$$\delta t_s = -\frac{1}{\dot{S}}\frac{\partial S}{\partial \boldsymbol{y}}\delta \boldsymbol{y}(t_s^-) \tag{4.42}$$

In Case 1, since $\boldsymbol{y}$ is continuous across t_s, there satisfies

$$\boldsymbol{y}(t_s^+) = \boldsymbol{y}(t_s^-) \tag{4.43}$$

and $\Psi(t_s)$ satisfies

$$\Psi(t_s) = \frac{\partial \boldsymbol{y}(t_s^+)}{\partial \boldsymbol{y}(t_s^-)} = I_{14\times 14} + \left(\dot{\boldsymbol{y}}(t_s^+) - \dot{\boldsymbol{y}}(t_s^-)\right)\frac{1}{\dot{S}_\varepsilon}\frac{\partial S_\varepsilon}{\partial \boldsymbol{y}} \tag{4.44}$$

In Case 2, $\boldsymbol{y}(t_s^+)$ is computed as

$$\boldsymbol{y}(t_s^+) = \boldsymbol{y}(t_s^-) + \Delta \boldsymbol{y} \tag{4.45}$$

where $\Delta \boldsymbol{y} = [\boldsymbol{0}_{7\times 1},\ \Delta \boldsymbol{\lambda}_{\text{mee}},\ 0]$. $\Psi(t_s)$ satisfies

$$\Psi(t_s) = \frac{\partial \boldsymbol{y}(t_s^+)}{\partial \boldsymbol{y}(t_s^-)} = I_{14\times 14} + \frac{\partial \Delta \boldsymbol{y}}{\partial \boldsymbol{y}} + \left(\dot{\boldsymbol{y}}(t_s^+) - \dot{\boldsymbol{y}}(t_s^-) - \Delta\dot{\boldsymbol{y}}\right)\frac{1}{\dot{S}_d}\frac{\partial S_d}{\partial \boldsymbol{y}} \tag{4.46}$$

where

$$\Delta\dot{\boldsymbol{y}} = \frac{\partial \Delta \boldsymbol{y}}{\partial \boldsymbol{y}}\dot{\boldsymbol{y}}(t_s^-) + \frac{\partial \Delta \boldsymbol{y}}{\partial t} \tag{4.47}$$

Remark 4.3. *From Eqs.* (4.44) *and* (4.46)*, it is clear that the STM becomes ill-conditioned on singular arcs indicated by either* $\dot{S}_\varepsilon(t_s) = 0$ *or* $\dot{S}_d(t_s) = 0$*. The case* $\dot{S}_\varepsilon(t_s) = 0$ *is not considered in this work. The case* $\dot{S}_d(t_s) = 0$*, implying that the spacecraft flies over the edge of the shadow at* t_s*, may occur for optimal trajectories with many revolutions. The ill-conditioned STM deteriorates the performance of the shooting method.*

4.2.2 Switching Detection Technique

A switching time detection is twofold. Firstly, knowing $\Psi(t_s)$ at the switching time t_s is indispensable for the accuracy of gradients. Secondly, the integration error accumulates across the discontinuity if the switching time is not explicitly detected. Suppose that at consecutive time instants t_k and t_{k+1}, a switching function S and the constant threshold η satisfy $(S_k - \eta) \times (S_{k+1} - \eta) < 0$, where $S_k := S(t_k, \boldsymbol{y}(t_k))$ and $S_{k+1} := S(t_{k+1}, \boldsymbol{y}(t_{k+1}))$, the switching detection in [47] is then implemented to find t_s such that $S(t_s) = \eta$. The switching detection is embedded into the integration process, with the accuracy set as 10^{-12}.

However, the assumption $(S_k - \eta) \times (S_{k+1} - \eta) < 0$ may not hold. For example, suppose the shadow entrance is detected at t_k, but the spacecraft flies out of the shadow at t_{k+1}, the time detection of the shadow exit fails since $S(t_k) = 0$. In this case, the time instant $\tilde{t}_k \in (t_k, t_{k+1})$ that satisfies $(S(\tilde{t}_k, \boldsymbol{y}(\tilde{t}_k)) - \eta) \times (S_{k+1} - \eta) < 0$ and $|S(\tilde{t}_k, \boldsymbol{y}(\tilde{t}_k))| > 10^{-12}$ is searched first using the bisection method. Then the switching time $t_s \in (\tilde{t}_k, t_{k+1})$ is detected using the method in [47].

Remark 4.4. *It is assumed that the throttle switching time and shadow switching time do not coincide.*

4.2.3 Continuation Scheme

Since the discontinuity produced by shadow constraints narrows the convergence domain, the $N_{\max}$ continuation is proposed to approach the solution by gradually turning inactive shadows into active shadows, achieved by increasing $N_{\max}$. The combination of ε continuation and $N_{\max}$ continuation is employed.

There are mainly two possible schemes. The starter of both schemes is the solution to the energy-optimal problem without shadow constraints. The first strategy consists of determining the energy-optimal solution with shadow constraints by using $N_{\max}$ continuation, and then determining the fuel-optimal solution with shadow constraints by using ε continuation. However, this strategy maybe not effective for many-revolution transfers, since the ill-conditioned STM maybe occur during ε continuation process. The second strategy consists of determining the fuel-optimal solution without shadow constraints by using ε continuation, and then determining the fuel-optimal solution with shadow constraints by using $N_{\max}$ continuation. This scheme is preferred since the ill-conditioned STM will not be encountered unless at final few steps.

Figure 4.2 shows five possible cases related to the position of the inactive shadow with respect to the bang-bang u profile. When the inactive shadow is switched to the active shadow, the u profile of case (e) is unchanged, while a new u profile has to be sought for cases (a)-(d). The continuation process is shown in Fig. 4.3, where the case (a) is employed without loss of generality. In Fig. 4.3, let u_ζ be the thrust throttle for $N_{\max}$–th time passage of the shadow, the fuel-optimal solution without shadow constraints ($N_{\max} = 0$ and $u_\zeta = 0$) is obtained first through ε continuation. This solution is used as the initial guess to search the fuel-optimal solution with $N_{\max} = 1$ and $u_\zeta = 0$ using the single shooting method. The algorithm may fail due to the narrow convergence domain produced by the control and costate discontinuity. Suppose that the fuel-optimal solution with $N_{\max} = 1$ and $u_\zeta = 0$ is obtained, but fails for $N_{\max} = 2$ and $u_\zeta = 0$, then the fuel-optimal problem with $N_{\max} = 2$ and $u_\zeta = 1$ is solved first. The u_ζ continuation proceeds by gradually reducing u_ζ from $u_\zeta = 1$ to $u_\zeta = 0$. Once the solution is obtained, the fuel-optimal solution with $N_{\max} = 3$ and $u_\zeta = 0$ is sought. This process continues until $N_s \leqslant N_{\max}$ is true, or fails due to the ill-conditioned STM.

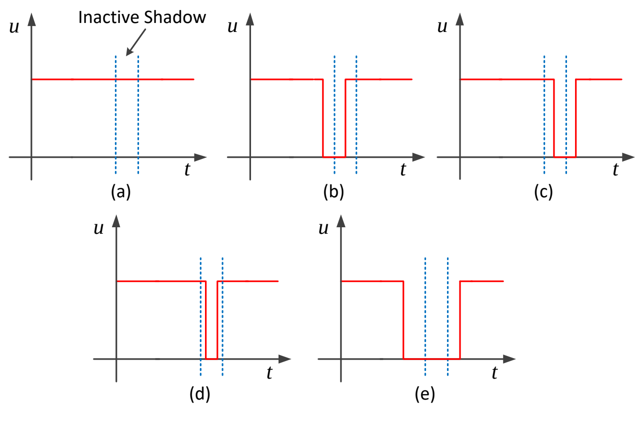

Figure 4.2: *Position of the inactive shadow with respect to the bang-bang thrust throttle profile.*

Since u is set to $u_{\min}$ in Eq. (4.26) when the spacecraft is located inside the active shadow,

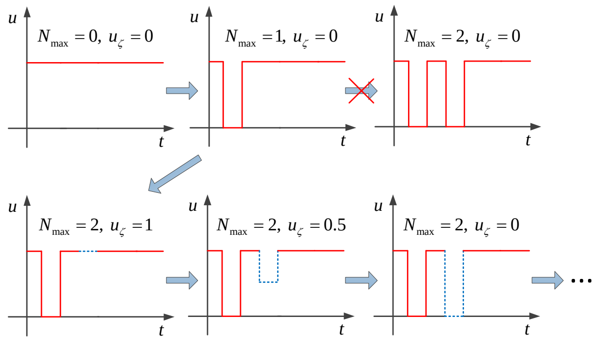

Figure 4.3: $N_{\max}$ *Continuation scheme from the fuel-optimal solution without shadow constraint* ($N_{\max}=0$ *and* $u_\varsigma=0$) *to the fuel-optimal solution with* $N_{\max}=2$ *and* $u_\varsigma=0$.

incorporating $N_{\max}$ continuation leads to the setting of $u_{\min}$ as

$$u_{\min} = \begin{cases} u_\varsigma, & \text{if} \quad N_s > N_{\max}-1 \quad \text{and} \quad N_s < N_{\max} \\ 0 & \text{Otherwise} \end{cases} \tag{4.48}$$

4.2.4 Augmented Integration Flowchart

The integration flowchart presented in [47] is insufficient to solve low-thrust transfers involving Earth-shadow eclipses. In this section, the flowchart is augmented to involve shadow related branches.

For simplicity of discussion, let u_{type} be the engine status, the logic of which is

$$u_{\text{type}} = \begin{cases} \text{On}, & \text{if} \quad u = 1 \\ \text{Medium}, & \text{if} \quad u \in (u_{\min}, 1) \\ \text{Off}, & \text{if} \quad u = u_{\min} \end{cases} \tag{4.49}$$

The augmented flowchart is presented in Fig. 2.5. The inputs required to execute one-step integration are 1) t_k, the k–th time step; 2) h_p, the size of time step predicted by previous step of integration; 3) $\boldsymbol{z}_k$, the full 210-dimensional state; 4) u_{type}, the engine status; 5) $N_s(t)$, number of accumulated eclipses; 6) p_{type}, the position of the spacecraft with respect to the shadow defined in Eq. (4.18); 7) $\tilde{p}_{\text{type}}$, the position of the spacecraft with respect to the active shadow defined in Eq. (4.19); 8) $u_{\min}$, the minimum level of thrust throttle; 9) u_ς, the thrust throttle of the $N_{\max}$–th time of the shadow crossing.

In Fig. 2.5, three branches separate at the beginning of integration according to u_{type}. For each integration block, a prediction on $\boldsymbol{z}_{k+1}$, i.e., $\boldsymbol{z}_{k+1} = \boldsymbol{\psi}_{\text{RK}}(\boldsymbol{z}_k, t_k, t_k + h_p)$, is executed, using variable-step seventh/eighth Runge–Kutta integration scheme. Note that $\boldsymbol{z}_{k+1}$ is the state corresponding to $t_{k+1} = t_k + h_f$, where h_f is the corrected time step according to the integration accuracy set as 1×10^{-14}. The value of $p_{\text{type},k+1}$ corresponding to $\boldsymbol{z}_{k+1}$ is computed using Eq. (4.18). N_s is updated as $N_s \leftarrow N_s + 0.5$ if $p_{\text{type}} \neq p_{\text{type},k+1}$, which is then used to compute $\tilde{p}_{\text{type},k+1}$ in Eq. (4.19).

For u_{type} being On or Medium, execution blocks are similar. The branch of u_{type} = On is depicted in the following. u_{type} = On implies that $\tilde{p}_{\text{type}}$ = Out and $u_{\min} = 0$. Since the engine switches off when the active shadow is entered into, the first task after the one-step integration prediction is to check $\tilde{p}_{\text{type},k+1}$ at t_{k+1}. If $\tilde{p}_{\text{type},k+1}$ = Out, the next step is to check whether p_{type} equals to $p_{\text{type},k+1}$. Even though p_{type} does not affect the status of the engine, the detection of p_{type} switching offers more information of the trajectory. If $p_{\text{type}} \neq p_{\text{type},k+1}$, Block 2 is executed to detect the shadow switching time. Let S_c be the value of S_ε at the swithing time t_s. If $S_c < -\varepsilon$ is satisfied, the solution is saved and p_{type} is updated to $p_{\text{type},k+1}$. Otherwise, if $S_c \geqslant -\varepsilon$, it indicates that the throttle switching exists between $[t_k, t_{k+1}]$, the step h_p is reduced and N_s is rollback as $N_s \leftarrow N_s - 0.5$. When $\tilde{p}_{\text{type},k+1}$ = Out and $p_{\text{type}} = p_{\text{type},k+1}$, the same execution block on the branch u_{type} = On of the flowchart in [47] is implemented. Otherwise, if $\tilde{p}_{\text{type},k+1}$ = In, Block 2 is required to execute to determine the shadow switching time t_s. If $S_c < -\varepsilon$ is satisfied, $u_{\min}$ is set by Eq. (4.48). Block 3 is executed, and u_{type} is set to Off.

The most complex branch is the case when $u_{\text{type},k}$ = Off. The first task after one-step prediction is to check $\tilde{p}_{\text{type}}$ to verify the reason that the engine switches off. If $\tilde{p}_{\text{type}}$ = In, implying that the spacecraft is located inside the active shadow at k–th step, the next task is to check whether the spacecraft is still inside the active shadow at t_{k+1}. If $\tilde{p}_{\text{type},k+1}$ = In, the solution is saved. Otherwise, if $\tilde{p}_{\text{type},k+1}$ = Out, the spacecraft flies out of the active shadow at t_{k+1}. Block 2 is executed to determine the shadow switching time t_s. The $u(t_s^+)$ instantaneous after t_s is determined by the value of S_c with $u_{\min} = 0$. For example, if $S_c < -\varepsilon$, u_{type} is updated to On and Block 3 is executed.

If $\tilde{p}_{\text{type}}$ = Out, the spacecraft is located outside the active shadow and the engine switches off due to $S_\varepsilon > \varepsilon$. If $\tilde{p}_{\text{type},k+1}$ = In, the spacecraft flies inside the shadow at t_{k+1}. Then the shadow switching time is detected. Since $\Delta u = 0$, there is no need to update STM, but the shadow status is updated if $S_c > \varepsilon$. Otherwise, if $\tilde{p}_{\text{type},k+1}$ = Out and $p_{\text{type}} = p_{\text{type},k+1}$, it indicates that the Earth's shadow is not encountered at t_{k+1}, the same execution block on the branch u_{type} = Off of the flowchart in [47] is implemented.

4.3 Numerical Simulations

The physical constants used are listed in Table 4.1, where LU is the Earth radius, VU = $\sqrt{\mu/\text{LU}}$ and TU = LU/VU. The Geostationary Transfer Orbit (GTO) to Geostationary Orbit (GEO) transfer example from [95] is simulated, and the corresponding initial and terminal orbital elements are listed in Table 4.2. Since the terminal inclination and eccentricity are both set to null, the definitions of Ω and w are invalid, thus they are set as free variables. Then the terminal conditions Eq. (4.6) are determined by Eq. (4.1). Moreover, $m_0 = 100\,\text{kg}$, $I_{\text{sp}} = 3100\,\text{s}$. All simulations are conducted under an Intel Core i7–9750H, CPU@2.6 GHz, Windows 10 system with MATLAB R2019a. The steps in ε continuation and u_ζ continuation are $\Delta\varepsilon = 0.025$ and $\Delta u_\zeta = 0.1$, respectively. Slightly larger steps $\Delta\varepsilon \leftarrow 1.01 \times \Delta\varepsilon$ and $\Delta u_\zeta \leftarrow 1.01 \times \Delta u_\zeta$ are used for the next step if the current step succeeds, otherwise, half of the step is used. u_ζ continuation fails if $\Delta u_\zeta < 0.005$. The maximum iteration for solving the NOCP is set as 150.

Numerical simulations for various thrust level $T_{\max} = [2, 0.5, 0.1, 0.035]$ N are executed. The corresponding energy-optimal and fuel-optimal solutions, as well as the transfer time t_f, final mass m_f, $N_{\max}$, N_s and computational time (CT) are reported in Table 4.3. The energy-optimal solutions without shadow constraints (cases 1, 4, 7 and 10) are solved first, which is used as the starter to find fuel-optimal solutions without shadow constraints (cases 2, 5, 8 and 11) using ε continuation. Fuel-optimal solutions with shadow constraints for various $T_{\max}$ and $\theta_{s,i}$ (case 3, 6, 9, 12-15) are further found through the second continuation

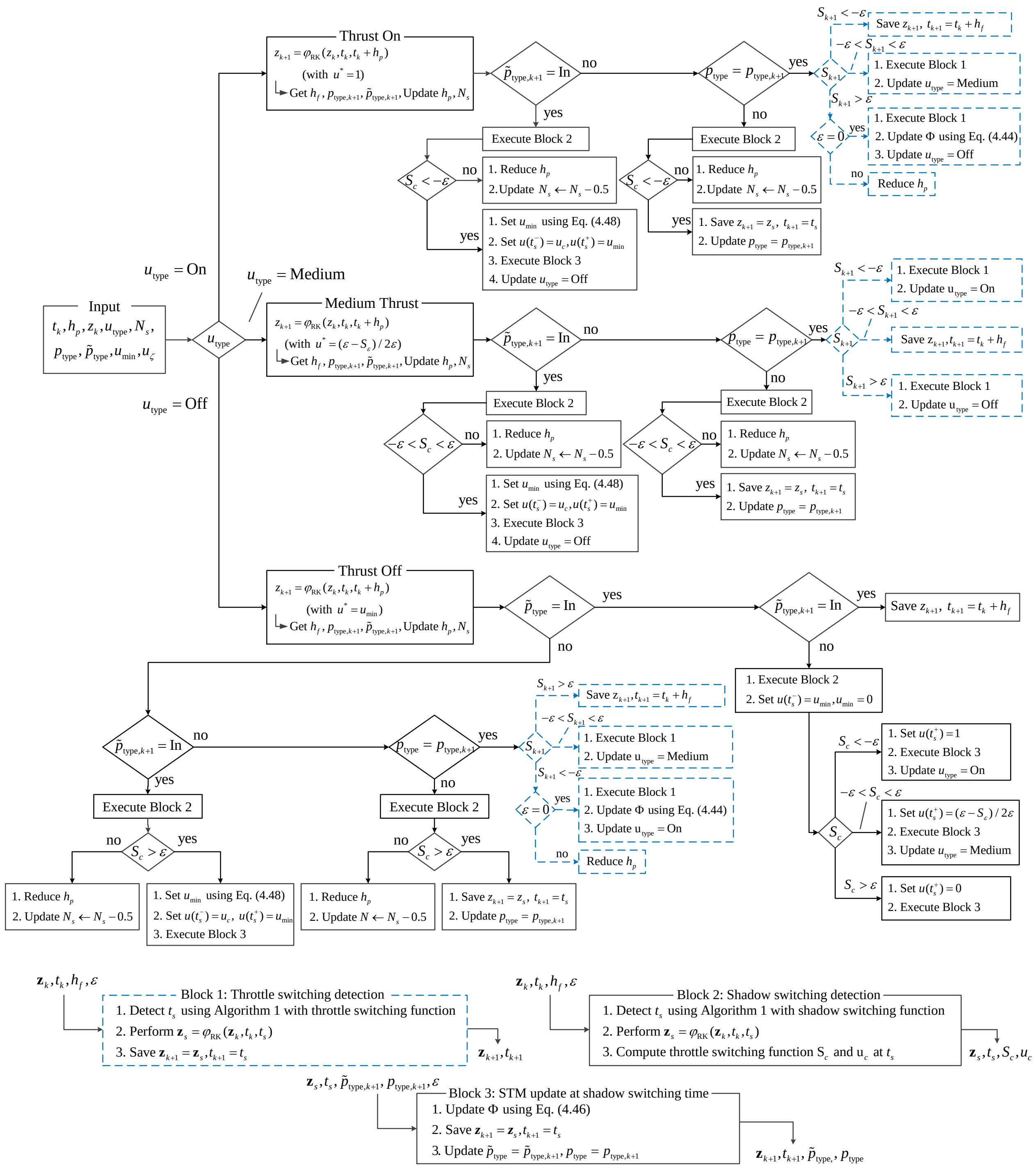

Figure 4.4: *Flowchart for the implementation of a generic integration step. Dashed blocks are from [47].*

scheme. For cases with $\theta_{s,i} = 0^\circ$ (vernal equinox departure), accurate fuel-optimal solutions are returned without encountering ill-conditioned STM for $T_{\max} = 2$ N (case 3), 0.5 N (case 6) and 0.1 N (case 9). On the other hand, an approximate fuel-optimal solution is obtained for $T_{\max} = 0.035$ N (case 12). More computational time is required when the thrust level is reduced and when ill-conditioned STM occurs. Fuel-optimal solutions for different thrust levels (cases 3, 6, 9, 12) are shown in Figs. 4.5. It can be seen that the shadow of fuel-optimal trajectories exists near apogee and thrust-off segments indicated by S_ε appear around perigee. From variations of u, S_ε and S_d, we can see that the bang-bang switching becomes more frequent as $T_{\max}$ is reduced. Variations of a, e and i imply that the fuel-optimal trajectories successfully reach the terminal conditions. The corresponding fuel-optimal costate variations are shown in Fig. 4.6, where costate discontinuities produced by shadow constraints are clearly demonstrated.

Table 4.1: *Physical constants.*

Physical constant	Value
Earth gravitational constant, μ	398600.4418 km^3/s^2
Gravitational field, g_0	9.80665 m/s^2
Length unit, LU	6378.1371 km
Time unit, TU	806.8111 s
Velocity unit, VU	7.9054 km/s
Mass unit, MU	100 kg
Earth diameter, D_p	2 LU
Sun diameter, D_s	1391020 km
Earth-Sun distance, $\delta_{p,s}$	1.4959787069×10^8 km

Table 4.2: *Initial and terminal classical orbital elements.*

Type	a (km)	e	i (deg)	Ω (deg)	w (deg)	θ (deg)
GTO	24505	0.725	7	0	0	0
GEO	42165	0	0	free	free	free

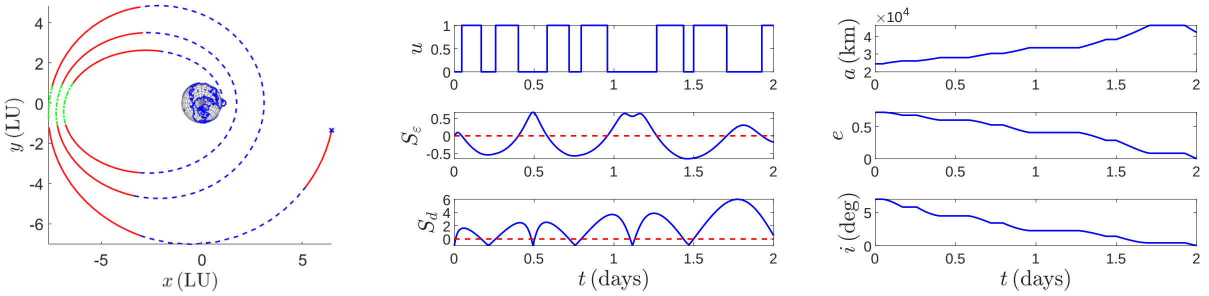

(a) *Solution with* $T_{\max} = 2$ *N (case 3).*

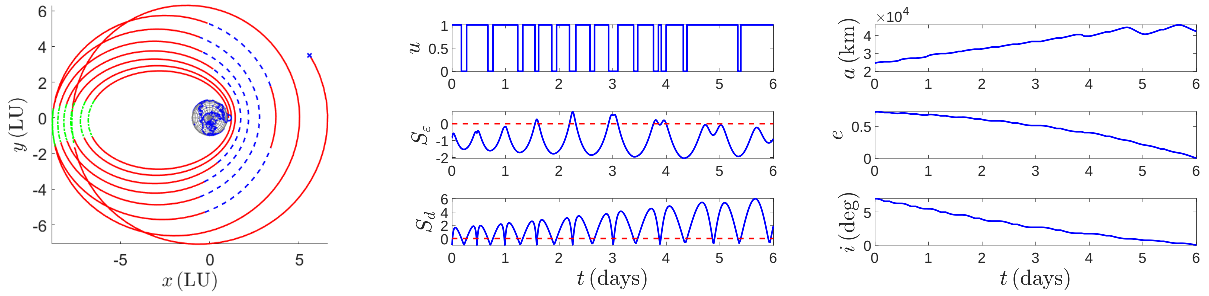

(b) *Solution with* $T_{\max} = 0.5$ *N (case 6).*

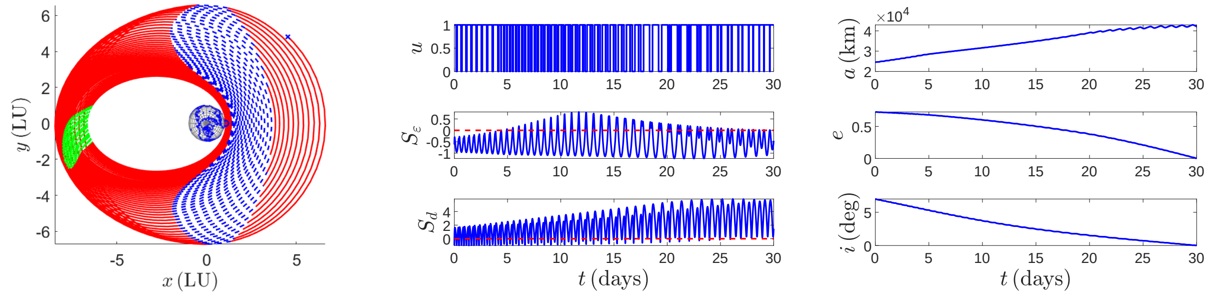

(c) *Approximate solution with* $T_{\max} = 0.1$ *N (case 9).*

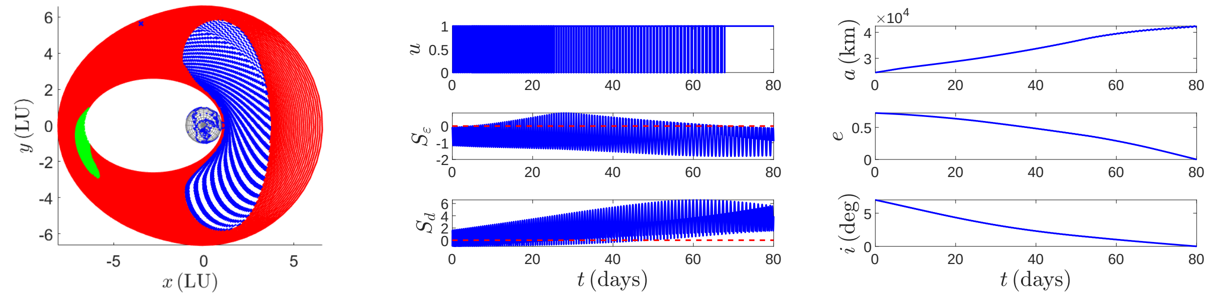

(d) *Approximate solution with* $T_{\max} = 0.035$ *N (case 12).*

Figure 4.5: *Fuel-optimal solutions with different thrust levels and* $\theta_{s,i} = 0^\circ$ *of cases 3, 6, 9, 12 in Table 4.3. Left: fuel-optimal trajectories. Blue dashed line: thrust-off segments outside shadow; red line: thrust-on segments; green dashed dot line: thrust-off segments inside shadow 'o': initial point; 'x': terminal point. Middle: variations of* u, S_ε *and* S_d *w.r.t. time. Red dash line: threshold of* S_d. *Right: variations of* a, e *and* i *w.r.t. time. Line types are the same for Figs. 4.8 and 4.9.*

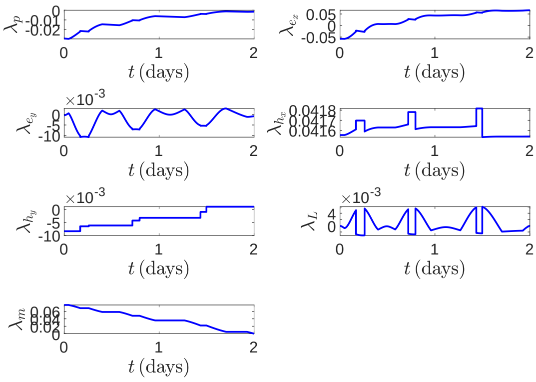

(a) *Costate variations for $T_{\max} = 2$ N (case 3).*

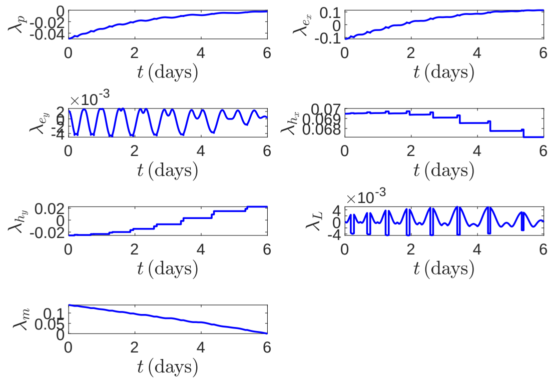

(b) *Costate variations for $T_{\max} = 0.5$ N (case 6).*

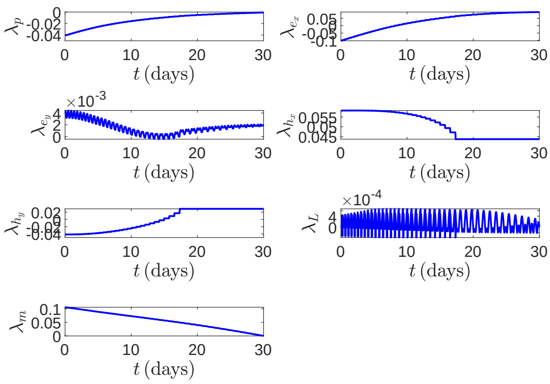

(c) *Costate variations for $T_{\max} = 0.1$ N (case 9).*

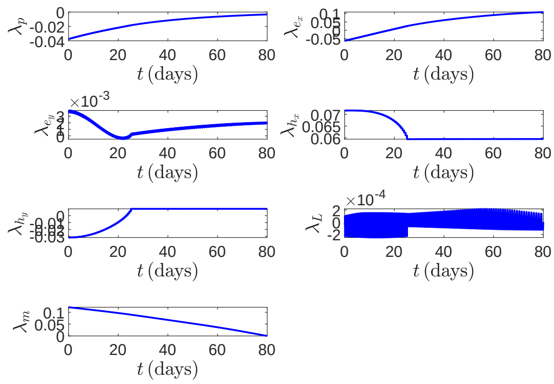

(d) *Costate variations for $T_{\max} = 0.035$ N (case 12).*

Figure 4.6: *Fuel-optimal costate variations with different $T_{\max}$ levels and $\theta_{s,i} = 0^\circ$ (cases 3, 6, 9, 12 in Table 4.3).*

More solution information of case 6 is provided. The computational time for this case is $\simeq 7$ mins, while the continuation fails when the finite difference method inherently embedded in MATLAB is used. The failure is caused by the inaccuracy of the finite difference method analyzed in the following. Differently from the energy-optimal to fuel-optimal continuation, the control of auxiliary solutions in the second continuation scheme is discontinuous. Based on the optimal trajectory in Fig. 4.5b, the gradient accuracy of the finite difference method is assessed. The Jacobian matrix obtained by analytic gradients is used as the reference value, denoted as $J_{\mathrm{AG}}(t)$. The formula of the central finite difference method is used, as [100]

$$f'(x) = \frac{-f(x+2\eta) + 8f(x+\eta) - 8f(x-\eta) + f(x-2\eta)}{12\eta}$$

where $\eta = 1 \times 10^{-6}$ is a small perturbation step. The obtained Jacobian matrix is denoted as $J_{\mathrm{FD}}(t)$. The gradient accuracy of the finite difference method at a given time t is calculated as the maximum value in the element of the matrix $|J_{\mathrm{FD}}(t) - J_{\mathrm{AG}}(t)|$.

Figure 4.7 shows the variation of the gradient accuracy using the finite difference method. It can be clearly seen that the accuracy deteriorates rapidly around the time of the discontinuous control and the error is accumulated as time increases. Thus, when the terminal state of an

Table 4.3: *Simulation results.*

Case	Type	$\theta_{s,i}$	$T_{\max}$ (N)	$(\boldsymbol{\lambda}_i^*)^\top$	t_f (days)	m_f (kg)	$N_{\max}$	N_s	CT (mins)[d]
1	EO w/o[a]	/	2	$[-0.024240, -0.042279, 0.000130, 0.039448, -0.000181, -0.000083, 0.075124]$	2	93.84	/	/	/
2	FO w/o[b]	/	2	$[-0.026538, -0.062339, 0.000234, 0.033722, -0.002614, -0.000009, 0.062911]$	2	94.74	/	/	0.62
3	FO[c]	0°	2	$[-0.029159, -0.057720, -0.000427, 0.041554, -0.008385, -0.000079, 0.077206]$	2	94.22	3	3	1.54
4	EO w/o	/	0.5	$[-0.043971, -0.122824, 0.000083, 0.052453, -0.001645, 0.000040, 0.106335]$	6	93.66	/	/	/
5	FO w/o	/	0.5	$[-0.041008, -0.132771, 0.000090, 0.040169, -0.002677, 0.000098, 0.083086]$	6	94.12	/	/	1.7
6	FO	0°	0.5	$[-0.049630, -0.111368, 0.002182, 0.069476, -0.025579, -0.000004, 0.138935]$	6	93.18	8	8	7.0
7	EO w/o	/	0.1	$[-0.042528, -0.114285, 0.000011, 0.052643, -0.000245, 0.000007, 0.103373]$	30	93.73	/	/	/
8	FO w/o	/	0.1	$[-0.036987, -0.104961, 0.000024, 0.042263, -0.000462, 0.000011, 0.083938]$	30	94.15	/	/	6.0
9	FO	0°	0.1	$[-0.040920, -0.102379, 0.004436, 0.058269, -0.041627, 0.000006, 0.105747]$	30	93.63	29	29	43
10	EO w/o	/	0.035	$[-0.036844, -0.054583, 0.000016, 0.065573, -0.000096, -0.000006, 0.124880]$	80	93.67	/	/	/
11	FO w/o	/	0.035	$[-0.033988, -0.063944, 0.000014, 0.054932, -0.000116, -0.000003, 0.102696]$	80	93.96	/	/	10
12	FO	0°	0.035	$[-0.037486, -0.062639, 0.003888, 0.071624, -0.031690, -0.000004, 0.121337]$	80	93.61	49	50	95
13	FO	90°	0.035	$[-0.034889, -0.067054, -0.000268, 0.056064, -0.000141, -0.000003, 0.103954]$	80	93.94	118	118	28
14	FO	180°	0.035	$[-0.028093, -0.021725, 0.000015, 0.059236, -0.000069, -0.000007, 0.109418]$	80	93.93	87	87	26
15	FO	270°	0.035	$[-0.034330, -0.063464, -0.000270, 0.056766, 0.002185, -0.000004, 0.105290]$	80	93.92	45	45	73

[a] energy-optimal solution without shadow constraints; [b] fuel-optimal solution without shadow constraints; [c] fuel-optimal solution with shadow constraints; [d] approximate computational time starting from EO w/o.

auxiliary trajectory is close to the shadow region, the gradient accuracy obtained by the finite difference method is low, which deteriorates the performance of the zero-finding method.

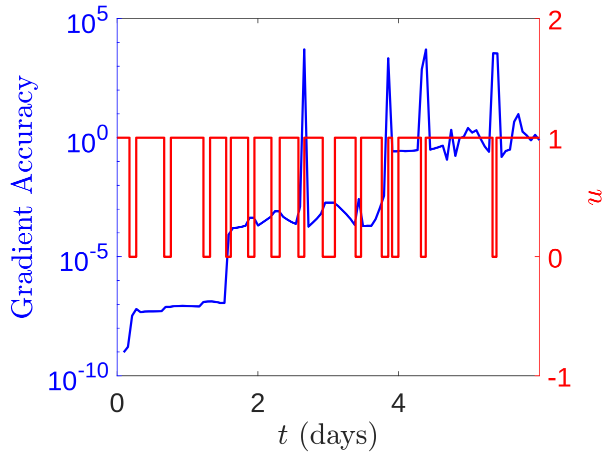

Figure 4.7: *Variation of the gradient accuracy w.r.t. the time using the finite difference method.*

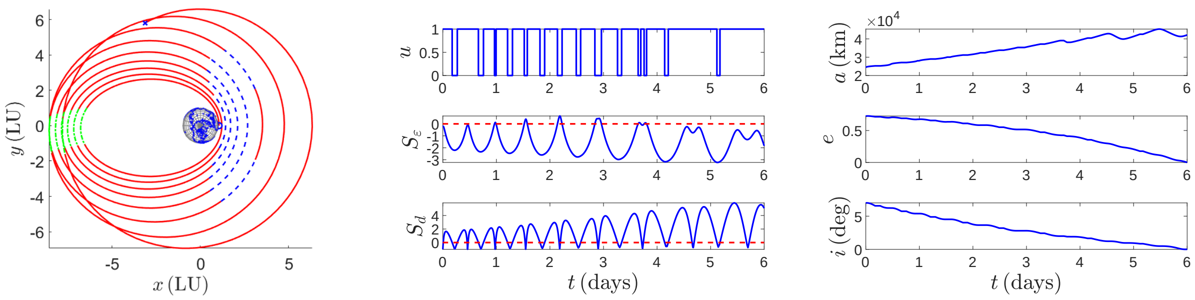

Figure 4.8: *Second fuel-optimal solution for $T_{\max} = 0.5$ N and $\theta_{s,i} = 0^\circ$.*

Additionally, the second fuel-optimal solution for this case is obtained by using the first continuation scheme, as

$$\boldsymbol{\lambda}_i^* = [-0.048686, -0.049344, 0.003478, 0.093319, -0.042607, -0.000173, 0.180324]^\top$$

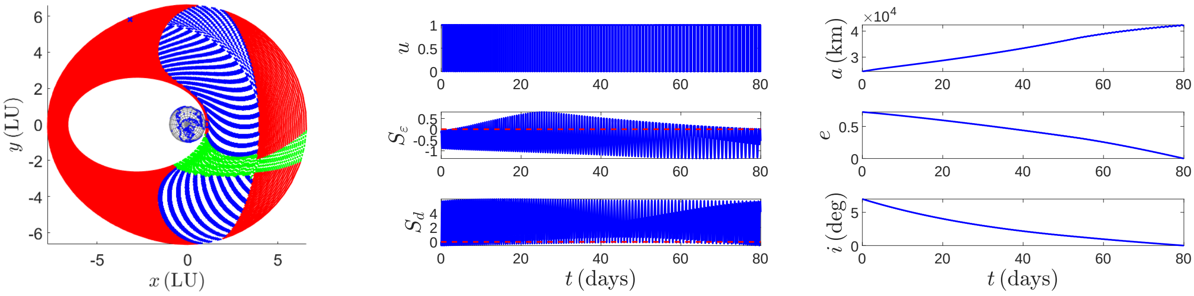

(a) *Solution with $\theta_{s,i} = 90°$ (case 13).*

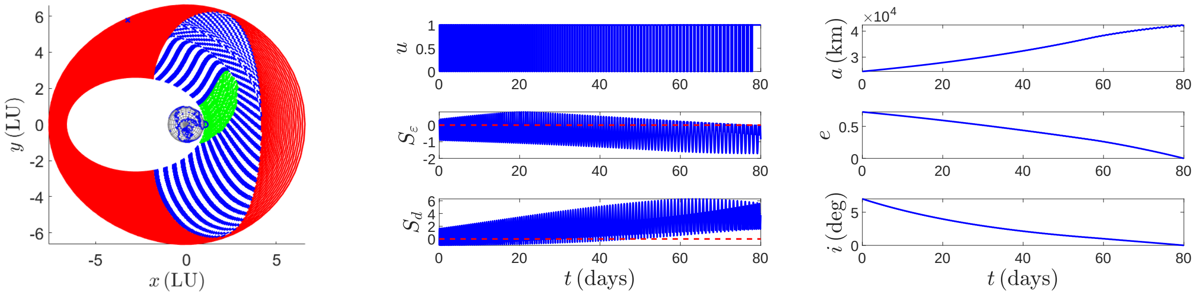

(b) *Solution with $\theta_{s,i} = 180°$ (case 14).*

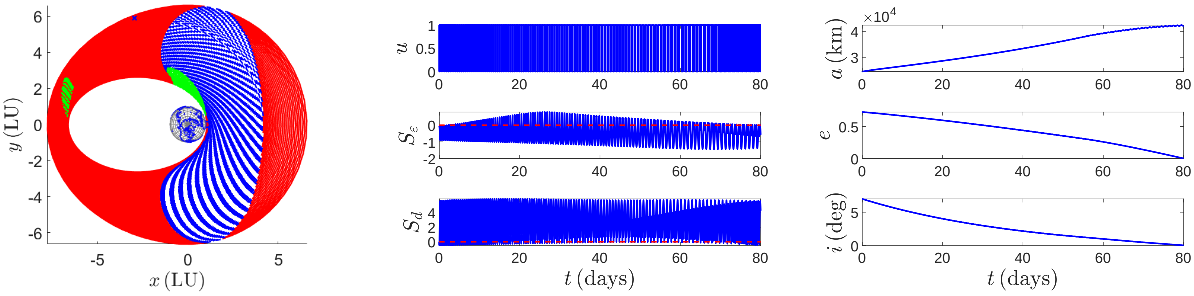

(c) *Solution with $\theta_{s,i} = 270°$ (case 15).*

Figure 4.9: *Fuel-optimal solutions for $T_{\max} = 0.035$ N and different $\theta_{s,i}$ (cases 13, 14, and 15 in Table 4.3).*

The corresponding fuel-optimal trajectory, variations of u, S_ε and S_d, and variations of a, e and i are shown in Fig. 4.8. The accurate bang-bang solution is returned with $N_{\max} = 8$ and $N_s = 8$. Compared to the solution in [95], both fuel-optimal trajectories pass through 8 times the shadow, and the variations of u almost coincide with each other. The final mass of fuel-optimal solution in [95] is 93.085 kg, while our solution results in 92.955 kg. The slight difference exists since the explicit time dependence of the shadow model is considered here. Compared to the hyperbolic tangent smoothing method in [95], the desired accurate bang-bang solution is obtained by our method. The first scheme requires only $\simeq 1.1$ mins to obtain the solution, faster than the second scheme, and $\simeq 20$ mins is required when the finite-difference method is used. However, for $T_{\max} = 0.1$ N (case 9), an accurate energy-optimal solution with shadow constraints is obtained but ε continuation fails. For $T_{\max} = 0.035$ N (case 12), an approximate energy-optimal solution with shadow constraints is obtained by using the first continuation scheme, which fails to proceed ε continuation.

In order to further verify the effectiveness of the developed method (second continuation scheme), fuel-optimal solutions for $T_{\max} = 0.035$ with summer solstice ($\theta_0 = 90°$), autumnal equinox ($\theta_0 = 180°$) and winter solstice ($\theta_0 = 270°$) departures are summarized as cases 13–15 in Table 4.3. The corresponding fuel-optimal trajectories, variations of u, S_ε and S_d, and variations of a, e and i are shown in Figs. 4.9. For all three cases, accurate solutions are obtained without encountering singularity, and final mass of these three cases are close to each other. For the summer solstice transfer, the spacecraft travels through the shadow region at each revolution. For autumnal equinox transfer, the initial point locates inside the shadow, and the shadow region appear in the beginning of the transfer. On the other hand, additional shadow region appears in the last few revolutions in the winter solstice transfer. Simulation tests reveal that the first scheme solves cases 13 and 14 taking $\simeq$ 45 mins and $\simeq$ 70 mins, respectively, slower than the second scheme, and it fails to converge for case 15.

4.4 Summary

This work considers the low-thrust optimization in presence of Earth-shadow eclipses. The developed method incorporates analytic derivatives, switching detection, and continuation with an augmented integration flowchart. The advantages of the proposed indirect method include that: 1) there is no need to prescribe the thrust structure a priori; 2) it enables to find fuel-optimal many-revolution bang-bang solutions; 3) it provides accurate gradients for robust convergence. GTO to GEO transfer simulations are conducted to test the algorithm performance.

CHAPTER 5

FUEL-OPTIMAL DEEP-SPACE TRANSFERS WITH MULTI-DIMENSIONAL INTERIOR-POINT CONSTRAINTS

SPACE applications considered in Chapters 2-4 require to tackle NOCPs with scalar interior-point constraints. This chapter aims to address NOCPs with multi-dimensional interior-point constraints. Here, the multipliers corresponding to the interior-point constraints cannot be solved in closed form, thus they have to be solved along with other unknowns. The benefits of the variational method are more distinct, because the computational burden of finite-difference methods grows rapidly when more unknowns, and thus more derivatives, have to be computed. Deep-space transfers involving intermediate flyby, rendezvous and gravity-assist events belong to this category. The combination of low-thrust propulsion with gravity-assist maneuvers allows new type of trajectories that shorten mission duration and reduce fuel consumption [101]. This chapter depicts the detailed procedure to calculate the gradients in deep-space transfers using the variational method.

5.1 Problem Statement

5.1.1 Fuel-Optimal Problem

The heliocentric phase of an interplanetary transfer is studied. Equation (2.1) is employed to model the motion of the spacecraft in the heliocentric inertial frame, rewritten here as

$$\dot{\boldsymbol{x}} = \boldsymbol{f}(\boldsymbol{x}, u, \boldsymbol{\alpha}) \Rightarrow \begin{cases} \dot{\boldsymbol{r}} = \boldsymbol{v} \\ \dot{\boldsymbol{v}} = -\dfrac{\mu}{r^3}\boldsymbol{r} + u\dfrac{T_{\max}}{m}\boldsymbol{\alpha} \\ \dot{m} = -u\dfrac{T_{\max}}{I_{\text{sp}}\, g_0} \end{cases} \tag{5.1}$$

where $T_{\max}$ and I_{sp} are assumed constant. With the initial time t_i and the terminal time t_f given, the fuel-optimal problem is to minimize

$$J_f = \lambda_0 \frac{T_{\max}}{c} \int_{t_i}^{t_f} u \, \mathrm{d}t \tag{5.2}$$

with boundary conditions

$$\boldsymbol{r}(t_i) - \boldsymbol{r}_i = 0, \quad \boldsymbol{v}(t_i) - \boldsymbol{v}_i = 0, \quad m(t_i) - m_i = 0 \tag{5.3}$$

$$\boldsymbol{r}(t_f) - \boldsymbol{r}_T(t_f) = 0, \quad \boldsymbol{v}(t_f) - \boldsymbol{v}_T(t_f) = 0 \tag{5.4}$$

where $\boldsymbol{r}_T(t_f)$ and $\boldsymbol{v}_T(t_f)$ are the position and velocity vectors of the final target body at t_f, respectively.

The positive factor λ_0 does not inherently change the NOCP. On the other hand, it restricts the initial costates on a unit hypersphere [44]. In order to gradually approach bang-bang discontinuity, ε continuation is used with the performance index as [41]

$$J_\varepsilon = \lambda_0 \frac{T_{\max}}{c} \int_{t_i}^{t_f} [u - \varepsilon u(1-u)] \, \mathrm{d}t \tag{5.5}$$

The Hamiltonian function is

$$H_\varepsilon = \boldsymbol{\lambda}_r \cdot \boldsymbol{v} + \boldsymbol{\lambda}_v \cdot \left(-\frac{\mu}{r^3}\boldsymbol{r} + u\frac{T_{\max}}{m}\boldsymbol{\alpha} \right) + \lambda_m \left(-u\frac{T_{\max}}{c} \right) + \lambda_0 \frac{T_{\max}}{c} [u - \varepsilon u(1-u)] \tag{5.6}$$

where $\boldsymbol{\lambda} = [\boldsymbol{\lambda}_r^\top, \boldsymbol{\lambda}_v^\top, \lambda_m]^\top$ is the costate vector associate to $\boldsymbol{x}$. According to PMP [26], the optimal thrusting direction unit vector $\boldsymbol{\alpha}^*$ satisfies

$$\boldsymbol{\alpha}^* = -\frac{\boldsymbol{\lambda}_v}{\lambda_v} \tag{5.7}$$

Substituting Eq. (5.7) into Eq. (5.6) yields

$$H_\varepsilon = \boldsymbol{\lambda}_r \cdot \boldsymbol{v} - \frac{\mu}{r^3}\boldsymbol{r} \cdot \boldsymbol{\lambda}_v + \lambda_0 \frac{T_{\max}}{c} u \left(S - \varepsilon + \varepsilon u \right) \tag{5.8}$$

where the throttle switching function S is

$$S = 1 - \frac{\lambda_m}{\lambda_0} - \frac{c}{m\,\lambda_0}\lambda_v \tag{5.9}$$

along with its derivatives as

$$\frac{\partial S}{\partial \boldsymbol{y}} = \left[\mathbf{0}_{1\times 6},\ \frac{c\,\lambda_v}{m^2\,\lambda_0},\ \mathbf{0}_{1\times 3},\ -\frac{c\,\boldsymbol{\lambda}_v^\top}{m\,\lambda_0\,\lambda_v}\right], \quad \dot{S} = \frac{c}{m\lambda_0}\frac{\boldsymbol{\lambda}_r\cdot\boldsymbol{\lambda}_v}{\lambda_v}, \quad \frac{\partial S}{\partial \lambda_0} = \frac{\lambda_m}{\lambda_0^2} + \frac{c\,\lambda_v}{m\,\lambda_0^2} \tag{5.10}$$

where $\boldsymbol{y} = [\boldsymbol{x}^\top, \boldsymbol{\lambda}^\top]^\top \in \mathbb{R}^{14}$ is the canonical vector. The optimal thrust throttle u^* is stated in terms of S and ε as

$$u^* = \begin{cases} 0 & S > \varepsilon \\ 1 & S < -\varepsilon \\ \dfrac{\varepsilon - S}{2\varepsilon} & |S| \leqslant \varepsilon \end{cases} \tag{5.11}$$

The corresponding equations of costate dynamics are

$$\begin{cases} \dot{\boldsymbol{\lambda}}_r = -\dfrac{3\mu}{r^5}\left(\boldsymbol{r}\cdot\boldsymbol{\lambda}_v\right)\boldsymbol{r} + \dfrac{\mu}{r^3}\boldsymbol{\lambda}_v \\ \dot{\boldsymbol{\lambda}}_v = -\boldsymbol{\lambda}_r \\ \dot{\lambda}_m = -\dfrac{u\,\lambda_v\,T_{\max}}{m^2} \end{cases} \tag{5.12}$$

where $\boldsymbol{\alpha}^*$ in Eq. (5.7) is already embedded into Eq. (5.12).

Since the terminal mass is free and the augmented terminal cost does not explicitly depend on the mass, there exists

$$\lambda_m(t_f) = 0 \tag{5.13}$$

The motion of the spacecraft is determined by integrating the following state-costate dynamics

$$\dot{\boldsymbol{y}} = \boldsymbol{F}(\boldsymbol{y}) \Rightarrow \begin{pmatrix} \dot{\boldsymbol{r}} \\ \dot{\boldsymbol{v}} \\ \dot{m} \\ \dot{\boldsymbol{\lambda}}_r \\ \dot{\boldsymbol{\lambda}}_v \\ \dot{\lambda}_m \end{pmatrix} = \begin{pmatrix} \boldsymbol{v} \\ -\dfrac{\mu}{r^3}\boldsymbol{r} - u\dfrac{T_{\max}}{m}\dfrac{\boldsymbol{\lambda}_v}{\lambda_v} \\ -u\dfrac{T_{\max}}{c} \\ -\dfrac{3\mu}{r^5}\left(\boldsymbol{r}\cdot\boldsymbol{\lambda}_v\right)\boldsymbol{r} + \dfrac{\mu}{r^3}\boldsymbol{\lambda}_v \\ -\boldsymbol{\lambda}_r \\ -\dfrac{u\,\lambda_v\,T_{\max}}{m^2} \end{pmatrix} \tag{5.14}$$

5.1.2 Interior-Point Constraint

Let $\boldsymbol{h}_j(t_j, \boldsymbol{x}_c(t_j)) = \mathbf{0}$ and $\phi_j(t_j, \boldsymbol{x}_d(t_j^-), \boldsymbol{x}_d(t_j^+)) = 0$ be the interior-point constraints determined by the continuous state $\boldsymbol{x}_c$ and discontinuous state $\boldsymbol{x}_d$ at t_j respectively, where the subscript j denotes the interior-point constraints at t_j, $j = 1, 2, \cdots, w$. That is

$$\boldsymbol{h}_j(t_j, \boldsymbol{x}_c(t_j)) = \mathbf{0} \quad \boldsymbol{h}_j \in \mathbb{R}^{p_j} \tag{5.15}$$

$$\phi_j(t_j, \boldsymbol{x}_d(t_j^-), \boldsymbol{x}_d(t_j^+)) = 0 \tag{5.16}$$

where p_j is the dimension of the constraint $\boldsymbol{h}_j$. ϕ_j in Eq. (5.16) and σ_j in Eq. (5.17) are scalar constraints. The inequality constraint at t_j is

$$\sigma_j(t_j, \boldsymbol{x}_d(t_j^-), \boldsymbol{x}_d(t_j^+)) \leqslant 0 \tag{5.17}$$

Let $\boldsymbol{\lambda}_c$ and $\boldsymbol{\lambda}_d$ be the costate vectors corresponding to $\boldsymbol{x}_c$ and $\boldsymbol{x}_d$ respectively. The state and costate components that are not involved in $\boldsymbol{x}_c$, $\boldsymbol{x}_d$, $\boldsymbol{\lambda}_c$ and $\boldsymbol{\lambda}_d$ are denoted as $\tilde{\boldsymbol{x}}$ and $\tilde{\boldsymbol{\lambda}}$. The bold vectors $\tilde{\boldsymbol{x}}$ and $\tilde{\boldsymbol{\lambda}}$ are used in the following even though they may be scalar variables in specific applications. The discussions below clarify expressions of Eqs. (5.15)-(5.17) for two types of transfers: 1) deep-space transfers with intermediate flyby and rendezvous; 2) deep-space transfers with intermediate gravity-assist events.

Intermediate flyby and rendezvous transfer

1. Intermediate flyby. In this case, $\boldsymbol{x}_c = \boldsymbol{r}$, $\tilde{\boldsymbol{x}} = [\boldsymbol{v}, m]$, $\boldsymbol{\lambda}_c = \boldsymbol{\lambda}_r$, $\tilde{\boldsymbol{\lambda}} = [\boldsymbol{\lambda}_v, \lambda_m]$, then

$$\boldsymbol{h}_j(t_j, \boldsymbol{x}_c(t_j)) = \boldsymbol{r}(t_j) - \boldsymbol{r}_{T,j}(t_j), \quad p_j = 3 \tag{5.18}$$

   where $\boldsymbol{r}_{T,j}(t_j)$ is the position vector of jth target body at t_j.

2. Intermediate rendezvous. In this case, $\boldsymbol{x}_c = [\boldsymbol{r}, \boldsymbol{v}]$, $\tilde{\boldsymbol{x}} = m$, $\boldsymbol{\lambda}_c = [\boldsymbol{\lambda}_r, \boldsymbol{\lambda}_v]$, $\tilde{\boldsymbol{\lambda}} = \lambda_m$, then

$$\boldsymbol{h}_j(t_j, \boldsymbol{x}_c(t_j)) = [\boldsymbol{r}(t_j) - \boldsymbol{r}_{T,j}(t_j), \quad \boldsymbol{v}(t_j) - \boldsymbol{v}_{T,j}(t_j)] \quad p_j = 6 \tag{5.19}$$

   where $\boldsymbol{v}_{T,j}(t_j)$ is the velocity vector of jth target body at t_j.

In this category, there is no constraints expressed by ϕ_j and σ_j. According to the optimal control theory, the necessary conditions of optimality are [26]

$$\boldsymbol{\chi}_j^\top \frac{\partial \boldsymbol{h}_j}{\partial t_j} + H_\varepsilon(\boldsymbol{y}(t_j^-), \lambda_0) - H_\varepsilon(\boldsymbol{y}(t_j^+), \lambda_0) = 0 \tag{5.20}$$

$$\boldsymbol{\chi}_j^\top \frac{\partial \boldsymbol{h}_j}{\partial \boldsymbol{x}_c} - \boldsymbol{\lambda}_c^\top(t_j^-) + \boldsymbol{\lambda}_c^\top(t_j^+) = \boldsymbol{0}^\top \tag{5.21}$$

where $\boldsymbol{\chi}_j \in \mathbb{R}^{p_j}$ is jth multiplier vector corresponding to the constraint $\boldsymbol{h}_j$.

Remark 5.1. *Let $\boldsymbol{y}(t) = \boldsymbol{\varphi}_\varepsilon(\boldsymbol{y}_i, \lambda_0, t_i, t)$ be the solution flow integrating Eq. (5.14) from the initial time t_i to the generic time t, using $\boldsymbol{y}_i$ at t_i, λ_0, and $\boldsymbol{\lambda}_c(t_j^+)$ in Eq. (5.21). The energy-to-fuel-optimal problem is to find $[\lambda_0, \boldsymbol{\lambda}_i, \boldsymbol{\chi}_j, t_j] \in \mathbb{R}^{8+(p_j+1)w}$ such that $\boldsymbol{y}(t)$ satisfies*

$$\begin{pmatrix} \boldsymbol{r}(t_f) - \boldsymbol{r}_T(t_f) \\ \boldsymbol{v}(t_f) - \boldsymbol{v}_T(t_f) \\ \lambda_m(t_f) \\ \boldsymbol{h}_j(t_j, \boldsymbol{x}_c(t_j)) \\ \boldsymbol{\chi}_j^\top \dfrac{\partial \boldsymbol{h}_j}{\partial t_j} + H_\varepsilon(\boldsymbol{y}(t_j^-), \lambda_0) - H_\varepsilon(\boldsymbol{y}(t_j^+), \lambda_0) \\ \sqrt{\lambda_0^2 + \boldsymbol{\lambda}_i^\top \boldsymbol{\lambda}_i + \sum_{l=1}^{w} \boldsymbol{\chi}_l^\top \boldsymbol{\chi}_l} - 1 \end{pmatrix} = \boldsymbol{0}, \quad j = 1, \cdots, w \tag{5.22}$$

Intermediate gravity-assist transfer The unpowered gravity-assist transfer illustrated in Fig. 5.1 is considered. Let r_p be the radius of gravity-assist maneuver and $\boldsymbol{u} = \boldsymbol{v}_\infty^\pm / v_\infty^\pm$ where $v_\infty^\pm = \|\boldsymbol{v}_\infty^\pm\|$ and $\boldsymbol{v}_\infty^\pm = \boldsymbol{v}(t_j^\pm) - \boldsymbol{v}_{T,j}(t_j^\pm)$, then r_p is computed as [44]

$$\cos\theta = \boldsymbol{u}^- \cdot \boldsymbol{u}^+ \tag{5.23}$$

$$r_p = \frac{\mu_j}{v_\infty^- v_\infty^+} \left(\frac{1}{\sin(\theta/2) - 1} \right) \tag{5.24}$$

where θ is the deflection angle and μ_j is the gravity parameter of jth gravity-assist planet.

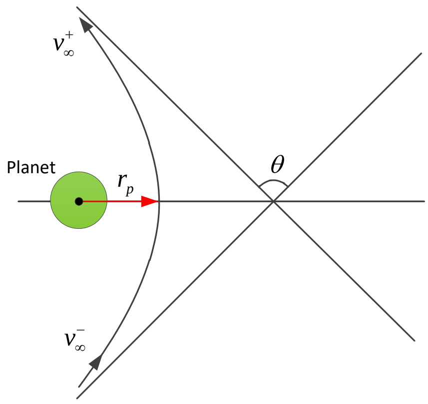

Figure 5.1: *Illustration of the unpowered gravity-assist transfer.*

In this case, $\boldsymbol{x}_c = \boldsymbol{r}$, $\boldsymbol{x}_d = \boldsymbol{v}$, $\tilde{\boldsymbol{x}} = m$, $\boldsymbol{\lambda}_c = \boldsymbol{\lambda}_r$, $\boldsymbol{\lambda}_d = \boldsymbol{\lambda}_v$, $\tilde{\boldsymbol{\lambda}} = \lambda_m$, and

$$\boldsymbol{h}_j(t_j, \boldsymbol{x}_c(t_j)) = \boldsymbol{r}(t_j) - \boldsymbol{r}_{T,j}(t_j) \quad p_j = 3 \tag{5.25}$$

$$\phi_j(t_j, \boldsymbol{x}_d(t_j^-), \boldsymbol{x}_d(t_j^+)) = v_\infty^- - v_\infty^+ \tag{5.26}$$

$$\sigma_j(t_j, \boldsymbol{x}_d(t_j^-), \boldsymbol{x}_d(t_j^+)) = 1 - r_p/r_{\min} \leqslant 0 \tag{5.27}$$

where $r_{\min}$ is the minimum radius required to perform the gravity-assist maneuver.

The slack variable α_j is introduced to transform the inequality constraint Eq. (5.27) to the equality constraint, as [102]

$$\sigma_j(t_j, \boldsymbol{x}_d(t_j^-), \boldsymbol{x}_d(t_j^+)) + \alpha_j^2 = 0 \tag{5.28}$$

Suppose the corresponding multiplier is κ_j, it must satisfy

$$\kappa_j \alpha_j = 0 \tag{5.29}$$

The necessary conditions of optimality for jth interior-point constraints are

$$\boldsymbol{\chi}_j^\top \left[\frac{\partial \boldsymbol{h}_j}{\partial t_j}, \frac{\partial \phi_j}{\partial t_j} \right] + \kappa_j \frac{\partial \sigma_j}{\partial t_j} + H_{\varepsilon,j}(\boldsymbol{y}(t_j^-), \lambda_0) - H_{\varepsilon,j}(\boldsymbol{y}(t_j^+), \lambda_0) = 0 \tag{5.30}$$

$$\boldsymbol{\chi}_{c,j}^\top \frac{\partial \boldsymbol{h}_j}{\partial \boldsymbol{x}_c} - \boldsymbol{\lambda}_c^\top(t_j^-) + \boldsymbol{\lambda}_c^\top(t_j^+) = \boldsymbol{0}^\top \tag{5.31}$$

$$\chi_{d,j} \frac{\partial \phi_j}{\partial \boldsymbol{x}_d(t_j^-)} - \boldsymbol{\lambda}_d^\top(t_j^-) + \kappa_j \frac{\partial \sigma_j}{\partial \boldsymbol{x}_d(t_j^-)} = \boldsymbol{0}^\top \tag{5.32}$$

$$\chi_{d,j} \frac{\partial \phi_j}{\partial \boldsymbol{x}_d(t_j^+)} + \boldsymbol{\lambda}_d^\top(t_j^+) + \kappa_j \frac{\partial \sigma_j}{\partial \boldsymbol{x}_d(t_j^+)} = \boldsymbol{0}^\top \tag{5.33}$$

where $\boldsymbol{\chi}_j = [\boldsymbol{\chi}_{c,j}^\top, \chi_{d,j}]^\top \in \mathbb{R}^{p_j+1}$ is the multiplier vector corresponding to the constraints Eqs. (5.25) and (5.26).

Remark 5.2. *Let $\boldsymbol{y}(t) = \boldsymbol{\varphi}_\varepsilon(\boldsymbol{y}_i, \lambda_0, t_i, t)$ be the solution flow integrating Eq. (5.14) from the initial time t_i to the generic time t, using $\boldsymbol{y}_i$ at t_i, λ_0, $\boldsymbol{\lambda}_c(t_j^+)$ and $\boldsymbol{\lambda}_d(t_j^+)$ in Eq. (5.31)* *and Eq. (5.33). The energy-to-fuel-optimal problem is to find* $[\lambda_0, \boldsymbol{\lambda}_i, \boldsymbol{\chi}_j, \boldsymbol{x}_d(t_j^+), \alpha_j, \kappa_j, t_j] \in \mathbb{R}^{8+10w}$ *such that* $\boldsymbol{y}(t)$ *satisfies*

$$\begin{pmatrix} \boldsymbol{r}(t_f) - \boldsymbol{r}_T(t_f) \\ \boldsymbol{v}(t_f) - \boldsymbol{v}_T(t_f) \\ \lambda_m(t_f) \\ \boldsymbol{h}_j(t_j, \boldsymbol{x}_c(t_j)) \\ \phi_j(t_j, \boldsymbol{x}_d(t_j^-), \boldsymbol{x}_d(t_j^+)) \\ \sigma_j(t_j, \boldsymbol{x}_d(t_j^-), \boldsymbol{x}_d(t_j^+)) + \alpha_j^2 \\ \kappa_j \alpha_j \\ \boldsymbol{\chi}_j^\top \left[\dfrac{\partial \boldsymbol{h}_j}{\partial t_j}, \dfrac{\partial \phi_j}{\partial t_j}\right] + \kappa_j \dfrac{\partial \sigma_j}{\partial t_j} + H_{\varepsilon,j}(\boldsymbol{y}(t_j^-), \lambda_0) - H_{\varepsilon,j}(\boldsymbol{y}(t_j^+), \lambda_0) \\ \chi_{d,j} \dfrac{\partial \phi_j}{\partial \boldsymbol{x}_d(t_j^-)} - \boldsymbol{\lambda}_d^\top(t_j^-) + \kappa_j \dfrac{\partial \sigma_j}{\partial \boldsymbol{x}_d(t_j^-)} \\ \sqrt{\lambda_0^2 + \boldsymbol{\lambda}_i^\top \boldsymbol{\lambda}_i + \sum_{l=1}^{w} (\boldsymbol{\chi}_l^\top \boldsymbol{\chi}_l + \kappa_l^2)} - 1 \end{pmatrix} = \mathbf{0}, \quad j = 1, \cdots, w \tag{5.34}$$

Remark 5.3. *For transfers involving both two types of events, let* $\boldsymbol{y}(t) = \boldsymbol{\varphi}_\varepsilon(\boldsymbol{y}_i, \lambda_0, t_i, t)$ *be the solution flow integrating Eq. (5.14) from the initial time* t_i *to the generic time* t*, using* $\boldsymbol{y}_i$ *at* t_i*,* λ_0*,* $\boldsymbol{\lambda}_c(t_{j1}^+)$ *and* $\boldsymbol{\lambda}_d(t_{j1}^+)$ *in Eq. (5.31) and Eq. (5.33) at gravity-assist time* t_{j1} *(*$j1 = 1, \cdots, \hat{w}$*),* $\boldsymbol{\lambda}_c(t_{j2}^+)$ *in Eq. (5.21) at flyby and rendezvous time* t_{j2} *(*$j2 = \hat{w}+1, \cdots, w$*), the energy-to-fuel-optimal problem is to find* $[\lambda_0, \boldsymbol{\lambda}_i, \boldsymbol{\chi}_{j1}, \boldsymbol{x}_d(t_{j1}^+), \alpha_{j1}, \kappa_{j1}, t_{j1}, \boldsymbol{\chi}_{j2}, t_{j2}]$ *such that* $\boldsymbol{y}(t)$ *satisfies*

$$\begin{pmatrix} \boldsymbol{r}(t_f) - \boldsymbol{r}_T(t_f) \\ \boldsymbol{v}(t_f) - \boldsymbol{v}_T(t_f) \\ \lambda_m(t_f) \\ \boldsymbol{h}_{j1}(t_{j1}, \boldsymbol{x}_c(t_{j1})) \\ \phi_{j1}(t_{j1}, \boldsymbol{x}_d(t_{j1}^-), \boldsymbol{x}_d(t_{j1}^+)) \\ \sigma_{j1}(t_{j1}, \boldsymbol{x}_d(t_{j1}^-), \boldsymbol{x}_d(t_{j1}^+)) + \alpha_{j1}^2 \\ \kappa_{j1} \alpha_{j1} \\ \boldsymbol{\chi}_{j1}^\top \left[\dfrac{\partial \boldsymbol{h}_{j1}}{\partial t_{j1}}, \dfrac{\partial \phi_{j1}}{\partial t_{j1}}\right] + \kappa_{j1} \dfrac{\partial \sigma_{j1}}{\partial t_{j1}} + H_{\varepsilon,j1}(\boldsymbol{y}(t_{j1}^-), \lambda_0) - H_{\varepsilon,j1}(\boldsymbol{y}(t_{j1}^+), \lambda_0) \\ \chi_{d,j1} \dfrac{\partial \phi_{j1}}{\partial \boldsymbol{x}_d(t_{j1}^-)} - \boldsymbol{\lambda}_d^\top(t_{j1}^-) + \kappa_{j1} \dfrac{\partial \sigma_{j1}}{\partial \boldsymbol{x}_d(t_{j1}^-)} \\ \boldsymbol{h}_{j2}(t_{j2}, \boldsymbol{x}_c(t_{j2})) \\ \boldsymbol{\chi}_{j2}^\top \dfrac{\partial \boldsymbol{h}_{j2}}{\partial t_{j2}} + H_\varepsilon(\boldsymbol{y}(t_{j2}^-), \lambda_0) - H_\varepsilon(\boldsymbol{y}(t_{j2}^+), \lambda_0) \\ \sqrt{\lambda_0^2 + \boldsymbol{\lambda}_i^\top \boldsymbol{\lambda}_i + \sum_{j1=1}^{\hat{w}} (\boldsymbol{\chi}_{j1}^\top \boldsymbol{\chi}_{j1} + \kappa_{j1}^2) + \sum_{j2=\hat{w}+1}^{w} \boldsymbol{\chi}_{j2}^\top \boldsymbol{\chi}_{j2}} - 1 \end{pmatrix} = \mathbf{0} \tag{5.35}$$

5.2 Solution Method

5.2.1 State Transition Matrix

As shown in Fig. 5.2, the state transition matrix is computed by sweeping each segment consecutively, with interior-point time t_j, initial time t_0 (equals to t_i) and terminal time t_f as the boundary. Within the segment $[t_k^+, t_{(k+1)}^-]$, the STM subjects to

$$\dot{\Phi}(t, t_k^+) = D_y \boldsymbol{F}\, \Phi(t, t_k^+), \quad k = 0, 1, \cdots, w \tag{5.36}$$

where $D_y \boldsymbol{F}$ is the derivative of dynamical equations Eq. (5.14) w.r.t. $\boldsymbol{y}$, $\Phi(t_k^+, t_k^+) = I_{2n\times 2n}$. In the following, $t_k = t_j$ if $k = 1, \cdots, w$, and $t_0^+ := t_i$, $t_{w+1}^- := t_f$. Note that $D_y \boldsymbol{F}$ has two different expressions based on whether u^* is constant.

The time derivative of $\boldsymbol{\zeta} = \mathrm{d}\boldsymbol{y}/\mathrm{d}\lambda_0$ is

$$\dot{\boldsymbol{\zeta}} = D_y \boldsymbol{F}\, \boldsymbol{\zeta} + \frac{\partial \boldsymbol{F}}{\partial \lambda_0} \tag{5.37}$$

where $\partial \boldsymbol{F}/\partial \lambda_0$ is non-zero if $u^* = (\varepsilon - S)/(2\varepsilon)$. The value of $\boldsymbol{\zeta}(t_i)$ at t_i is $\mathbf{0}_{14\times 1}$.

Let $\boldsymbol{z} = [\boldsymbol{y}, \mathrm{vec}(\Phi), \boldsymbol{\zeta}] \in \mathbb{R}^{224}$ be the vector consisting of $\boldsymbol{y}$, the columns of Φ converted by 'vec' operator, and $\boldsymbol{\zeta}$, there exists

$$\dot{\boldsymbol{z}} = \boldsymbol{G}(\boldsymbol{z}) \Rightarrow \begin{cases} \dot{\boldsymbol{y}} & = \boldsymbol{F}(\boldsymbol{y}) \\ \mathrm{vec}(\dot{\Phi}) & = \mathrm{vec}(D_y \boldsymbol{F}\, \Phi) \\ \dot{\boldsymbol{\zeta}} & = D_y \boldsymbol{F}\, \boldsymbol{\zeta} + \dfrac{\partial \boldsymbol{F}}{\partial \lambda_0} \end{cases} \tag{5.38}$$

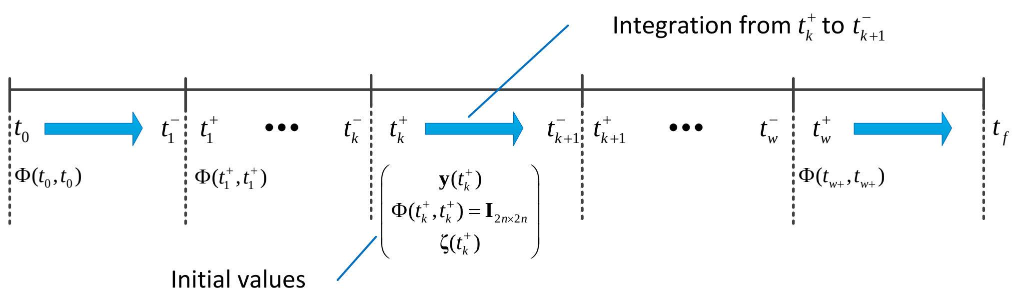

Figure 5.2: *Integration of STM by sweeping each segment consecutively.*

Note that the integration of Eq. (5.38) maps states and costates along a continuous trajectory. Since the fuel-optimal solution exhibits bang-bang control, the value of $\boldsymbol{z}(t_s^+)$ instantaneously after the throttle switching time $t_s \in (t_k^+, t_{k+1}^-)$ should be determined. The switching function S at $t_s^- + \delta t_s$ of the neighboring extremal trajectory must satisfy

$$S(t_s^- + \delta t_s, \boldsymbol{y}(t_s^- + \delta t_s), \lambda_0 + \mathrm{d}\lambda_0) = 0 \tag{5.39}$$

Expanding S at t_s^- yields

$$\mathrm{d}S = \frac{\partial S}{\partial \boldsymbol{y}} \delta \boldsymbol{y}(t_s^-) + \frac{\partial S}{\partial \lambda_0} \mathrm{d}\lambda_0 + \dot{S} \mathrm{d}t_s = 0 \tag{5.40}$$

thus

$$\mathrm{d}t_s = -\frac{1}{\dot{S}}\left(\frac{\partial S}{\partial \boldsymbol{y}}\delta\boldsymbol{y}(t_s^-) + \frac{\partial S}{\partial \lambda_0}\mathrm{d}\lambda_0\right) \tag{5.41}$$

Since $\boldsymbol{y}$ is continuous across t_s, there satisfies

$$\boldsymbol{y}(t_s^+) = \boldsymbol{y}(t_s^-) \tag{5.42}$$

Taking full differentials of both sides of Eq. (5.42) yields

$$\delta\boldsymbol{y}(t_s^+) = \delta\boldsymbol{y}(t_s^-) + \left(\dot{\boldsymbol{y}}(t_s^-) - \dot{\boldsymbol{y}}(t_s^+)\right)\mathrm{d}t_s \tag{5.43}$$

The derivatives of $\Psi(t_s)$ and $\partial\boldsymbol{y}(t_s^+)/\partial\lambda_0$ are only related to the derivatives of $\delta\boldsymbol{y}(t_s^\pm)$ w.r.t. $\boldsymbol{y}_i$ and λ_0. Thus, substituting

$$\delta\boldsymbol{y}(t_s^\pm) = \frac{\partial\boldsymbol{y}(t_s^\pm)}{\partial\boldsymbol{y}_i}\mathrm{d}\boldsymbol{y}_i + \frac{\mathrm{d}\boldsymbol{y}(t_s^\pm)}{\mathrm{d}\lambda_0}\mathrm{d}\lambda_0 \tag{5.44}$$

and Eq. (5.41) into Eq. (5.43) yields

$$\frac{\partial\boldsymbol{y}(t_s^+)}{\partial\boldsymbol{y}_i}\mathrm{d}\boldsymbol{y}_i+\frac{\mathrm{d}\boldsymbol{y}(t_s^+)}{\mathrm{d}\lambda_0}\mathrm{d}\lambda_0 = \frac{\partial\boldsymbol{y}(t_s^-)}{\partial\boldsymbol{y}_i}\mathrm{d}\boldsymbol{y}_i+\frac{\mathrm{d}\boldsymbol{y}(t_s^-)}{\mathrm{d}\lambda_0}\mathrm{d}\lambda_0+\left(\dot{\boldsymbol{y}}(t_s^+) - \dot{\boldsymbol{y}}(t_s^-)\right)\frac{1}{\dot{S}}\left(\frac{\partial S}{\partial\boldsymbol{y}}\frac{\partial\boldsymbol{y}(t_s^-)}{\partial\boldsymbol{y}_i}\mathrm{d}\boldsymbol{y}_i + \frac{\partial S}{\partial\boldsymbol{y}}\frac{\mathrm{d}\boldsymbol{y}(t_s^-)}{\mathrm{d}\lambda_0}\mathrm{d}\lambda_0 + \frac{\partial S}{\partial\lambda_0}\mathrm{d}\lambda_0\right) \tag{5.45}$$

Note that Eq. (5.44) is only used to derive $\Psi(t_s)$ and $\partial\boldsymbol{y}(t_s^+)/\partial\lambda_0$. The true expressions of $\delta\boldsymbol{y}(t_s^\pm)$ should involve derivatives w.r.t. other unknowns. Collecting factors of $\mathrm{d}\boldsymbol{y}_i$ and $\mathrm{d}\lambda_0$ in Eq. (5.45) yields

$$\Psi(t_s) = \frac{\partial\boldsymbol{y}(t_s^+)}{\partial\boldsymbol{y}(t_s^-)} = I_{14\times14} + \left(\dot{\boldsymbol{y}}(t_s^+) - \dot{\boldsymbol{y}}(t_s^-)\right)\frac{1}{\dot{S}}\frac{\partial S}{\partial\boldsymbol{y}} \tag{5.46}$$

and

$$\frac{\mathrm{d}\boldsymbol{y}(t_s^+)}{\mathrm{d}\lambda_0} = \frac{\mathrm{d}\boldsymbol{y}(t_s^-)}{\mathrm{d}\lambda_0} + \left(\dot{\boldsymbol{y}}(t_s^+) - \dot{\boldsymbol{y}}(t_s^-)\right)\frac{1}{\dot{S}}\left(\frac{\partial S}{\partial\boldsymbol{y}}\frac{\mathrm{d}\boldsymbol{y}(t_s^-)}{\mathrm{d}\lambda_0} + \frac{\partial S}{\partial\lambda_0}\right) \tag{5.47}$$

Suppose there are N discontinuities at $t_{s,1}, t_{s,2}, \cdots, t_{s,N} \in (t_k^+, t_{k+1}^-)$, $\Phi(t_{k+1}^-, t_k^+)$ is calculated following the chain rule as

$$\begin{aligned}\Phi(t_{k+1}^-, t_k^+) &= \Phi(t_{k+1}^-, t_{s,N}^+)\Psi(t_{s,N})\Phi(t_{s,N}^-, t_k^+)\\ &= \Phi(t_{k+1}^-, t_{s,N}^+)\Psi(t_{s,N})\Phi(t_{s,N}^-, t_{s,N-1}^+)\Psi(t_{s,N-1})\cdots\Phi(t_{s,2}^-, t_{s,1}^+)\Psi(t_{s,1})\Phi(t_{s,1}^-, t_k^+)\end{aligned} \tag{5.48}$$

At the same time, $\boldsymbol{\zeta}(t_{k+1}^-)$ is obtained by integrating Eq. (5.37) with $\boldsymbol{\zeta}(t_s^+)$ determined by Eq. (5.47).

The integration of Eq. (5.38) from t_i to t_f is achieved by integrating each segment consecutively. Then $\Phi(t_f, t_i)$ is computed as

$$\begin{aligned}\Phi(t_f, t_i) &= \Phi(t_f, t_w^+)\frac{\partial\boldsymbol{y}_w^+}{\partial\boldsymbol{y}_w^-}\Phi(t_w^-, t_{w-1}^+)\cdots\Phi(t_2^-, t_1^+)\frac{\partial\boldsymbol{y}_1^+}{\partial\boldsymbol{y}_1^-}\Phi(t_1^-, t_i)\\ &= \Phi(t_f, t_w^+)\Phi(t_w^+, t_{w-1}^+)\cdots\Phi(t_2^+, t_1^+)\Phi(t_1^+, t_i)\end{aligned} \tag{5.49}$$

where $\Phi(t_k^+, t_{k-1}^+) = \partial\boldsymbol{y}_k^+/\partial\boldsymbol{y}_{k-1}^+$. The value of $\boldsymbol{z}(t_k^+)$ used as the initial point for the integration of the segment $[t_k^+, t_{k+1}^-]$, as well as $\Phi(t_k^+, t_{k-1}^+)$, requires the gradient information of $\boldsymbol{y}(t_k^+)$ stated in Section 5.2.2.

5.2.2 Partial Derivatives of the Canonical Vector

In this section, the partial derivatives of $\boldsymbol{y}(t_j^+)$ at interior-point time t_j is derived. For simplicity of notations, the subscript j of a general variable $\boldsymbol{x}(t_j^{\pm})$ is simplified as $\boldsymbol{x}_j^{\pm}$, unless specific statements.

Intermediate flyby and rendezvous transfer The differential of $\boldsymbol{y}_j^-$ is

$$\mathrm{d}\boldsymbol{y}_j^- = \frac{\partial \boldsymbol{y}_j^-}{\partial \boldsymbol{y}_{j-1}^+}\mathrm{d}\boldsymbol{y}_{j-1}^+ + \frac{\partial \boldsymbol{y}_j^-}{\partial \lambda_0}\mathrm{d}\lambda_0 + \dot{\boldsymbol{y}}_j^-\mathrm{d}t_j + \sum_{q=1}^{j-1}\frac{\partial \boldsymbol{y}_j^-}{\partial t_q}\mathrm{d}t_q \tag{5.50}$$

There exists

$$\boldsymbol{\zeta}_j^- = \frac{\mathrm{d}\boldsymbol{y}_j^-}{\mathrm{d}\lambda_0} = \frac{\partial \boldsymbol{y}_j^-}{\partial \boldsymbol{y}_{j-1}^+}\frac{\partial \boldsymbol{y}_{j-1}^+}{\partial \lambda_0} + \frac{\partial \boldsymbol{y}_j^-}{\partial \lambda_0} \tag{5.51}$$

The term $\partial \boldsymbol{y}_j^-/\partial\lambda_0$ is non-zero since S is explicitly dependent on λ_0. Both $\partial \boldsymbol{y}_j^-/\partial \boldsymbol{y}_{j-1}^+$ and $\boldsymbol{\zeta}_j^-$ are obtained directly from the integration of Eq. (5.38). The last term in Eq. (5.50), and similar terms related to $\mathrm{d}t_q$ in the following, will be discussed in Section 5.2.4.

Since $\boldsymbol{x}$ is continuous across t_j, the differential of $\boldsymbol{x}_j^+$ is

$$\mathrm{d}\boldsymbol{x}_j^+ = \mathrm{d}\boldsymbol{x}_j^- = \frac{\partial \boldsymbol{x}_j^-}{\partial \boldsymbol{y}_{j-1}^+}\mathrm{d}\boldsymbol{y}_{j-1}^+ + \frac{\partial \boldsymbol{x}_j^-}{\partial \lambda_0}\mathrm{d}\lambda_0 + \dot{\boldsymbol{x}}_j^-\mathrm{d}t_j + \sum_{q=1}^{j-1}\frac{\partial \boldsymbol{x}_j^-}{\partial t_q}\mathrm{d}t_q \tag{5.52}$$

From Eq. (5.21), the differential of $\mathrm{d}\boldsymbol{\lambda}_{c,j}^+$ is

$$\begin{aligned}\mathrm{d}\boldsymbol{\lambda}_{c,j}^+ &= \mathrm{d}\boldsymbol{\lambda}_{c,j}^- - \mathrm{d}\left(\boldsymbol{h}_{c,j}^\top\boldsymbol{\chi}_j\right)\\ &= \frac{\partial \boldsymbol{\lambda}_{c,j}^-}{\partial \boldsymbol{y}_{j-1}^+}\mathrm{d}\boldsymbol{y}_{j-1}^+ - \boldsymbol{h}_{c,j}^\top\mathrm{d}\boldsymbol{\chi}_j + \frac{\partial \boldsymbol{\lambda}_{c,j}^-}{\partial \lambda_0}\mathrm{d}\lambda_0 + \dot{\boldsymbol{\lambda}}_{c,j}^-\mathrm{d}t_j + \sum_{q=1}^{j-1}\frac{\partial \boldsymbol{\lambda}_{c,j}^-}{\partial t_q}\mathrm{d}t_q\end{aligned} \tag{5.53}$$

where $\boldsymbol{h}_{c,j} = \partial \boldsymbol{h}_j/\partial \boldsymbol{x}_c$ is the constant matrix.

The differential of $\tilde{\boldsymbol{\lambda}}$ is

$$\mathrm{d}\tilde{\boldsymbol{\lambda}}_j^+ = \mathrm{d}\tilde{\boldsymbol{\lambda}}_j^- = \frac{\partial \tilde{\boldsymbol{\lambda}}_j^-}{\partial \boldsymbol{y}_{j-1}^+}\mathrm{d}\boldsymbol{y}_{j-1}^+ + \frac{\partial \tilde{\boldsymbol{\lambda}}_j^-}{\partial \lambda_0}\mathrm{d}\lambda_0 + \dot{\tilde{\boldsymbol{\lambda}}}_j^-\mathrm{d}t_j + \sum_{q=1}^{j-1}\frac{\partial \tilde{\boldsymbol{\lambda}}_j^-}{\partial t_q}\mathrm{d}t_q \tag{5.54}$$

Combining Eqs. (5.52), (5.53) and (5.54) yields

$$\mathrm{d}\boldsymbol{y}_j^+ = \frac{\partial \boldsymbol{y}_j^+}{\partial \boldsymbol{y}_{j-1}^+}\mathrm{d}\boldsymbol{y}_{j-1}^+ + \frac{\partial \boldsymbol{y}_j^+}{\partial \boldsymbol{\chi}_j}\mathrm{d}\boldsymbol{\chi}_j + \frac{\partial \boldsymbol{y}_j^+}{\partial \lambda_0}\mathrm{d}\lambda_0 + \frac{\mathrm{d}\boldsymbol{y}_j^+}{\mathrm{d}t_j}\mathrm{d}t_j + \sum_{q=1}^{j-1}\frac{\partial \boldsymbol{y}_j^+}{\partial t_q}\mathrm{d}t_q \tag{5.55}$$

where

$$\frac{\partial \boldsymbol{y}_j^+}{\partial \boldsymbol{y}_{j-1}^+} = \frac{\partial \boldsymbol{y}_j^-}{\partial \boldsymbol{y}_{j-1}^+},\quad \frac{\partial \boldsymbol{y}_j^+}{\partial \boldsymbol{\chi}_j} = \begin{bmatrix}\mathbf{0}\\ -\boldsymbol{h}_{c,j}^\top\\ \mathbf{0}\end{bmatrix},\quad \frac{\partial \boldsymbol{y}_j^+}{\partial \lambda_0} = \frac{\partial \boldsymbol{y}_j^-}{\partial \lambda_0},\quad \frac{\partial \boldsymbol{y}_j^+}{\partial t_q} = \frac{\partial \boldsymbol{y}_j^-}{\partial t_q} \tag{5.56}$$

and

$$\frac{\mathrm{d}\boldsymbol{y}_j^+}{\mathrm{d}t_j} = \hat{\boldsymbol{y}}_{t,j}^+ + \check{\boldsymbol{y}}_{t,j}^+ \tag{5.57}$$

with $\hat{\boldsymbol{y}}_{t,j}^{+} = \dot{\boldsymbol{y}}_j^{-}$ and $\check{\boldsymbol{y}}_{t,j}^{+} = \mathbf{0}$. The term $\mathrm{d}\boldsymbol{y}_j^{+}/\mathrm{d}t_j$ is splitted into two parts based on whether the time is explicitly dependent on.

The value of $\boldsymbol{\zeta}_j^{+}$ is

$$\boldsymbol{\zeta}_j^{+} = \frac{\partial \boldsymbol{y}_j^{+}}{\partial \boldsymbol{y}_{j-1}^{+}} \frac{\mathrm{d}\boldsymbol{y}_{j-1}^{+}}{\mathrm{d}\lambda_0} + \frac{\partial \boldsymbol{y}_j^{+}}{\partial \lambda_0} = \frac{\partial \boldsymbol{y}_j^{-}}{\partial \boldsymbol{y}_{j-1}^{+}} \frac{\mathrm{d}\boldsymbol{y}_{j-1}^{+}}{\mathrm{d}\lambda_0} + \frac{\partial \boldsymbol{y}_j^{-}}{\partial \lambda_0} = \boldsymbol{\zeta}_j^{-} \tag{5.58}$$

The vectors $\boldsymbol{y}_j^{+} = [\boldsymbol{x}_j^{-}, \boldsymbol{\lambda}_{c,j}^{-} - \boldsymbol{h}_{c,j}^{\top}\boldsymbol{\chi}_j, \tilde{\boldsymbol{\lambda}}_j^{-}]$, and $\boldsymbol{\zeta}_j^{+}$ in Eq. (5.58) are used to integrate Eq. (5.38) within $[t_j^{+}, t_{j+1}^{-}]$. The matrix $\Phi(t_j^{+}, t_{j-1}^{+})$ is computed using Eq. (5.55).

Intermediate gravity-assist transfer The differential of $\boldsymbol{y}_j^{-}$ at t_j is

$$\mathrm{d}\boldsymbol{y}_j^{-} = \frac{\partial \boldsymbol{y}_j^{-}}{\partial \boldsymbol{y}_{j-1}^{+}} \mathrm{d}\boldsymbol{y}_{j-1}^{+} + \frac{\partial \boldsymbol{y}_j^{-}}{\partial \lambda_0} \mathrm{d}\lambda_0 + \dot{\boldsymbol{y}}_j^{-} \mathrm{d}t_j + \sum_{q=1}^{j-1} \frac{\partial \boldsymbol{y}_j^{-}}{\partial t_q} \mathrm{d}t_q \tag{5.59}$$

The differential of $\boldsymbol{x}_{c,j}^{+}$ at t_j is,

$$\mathrm{d}\boldsymbol{x}_{c,j}^{+} = \mathrm{d}\boldsymbol{x}_{c,j}^{-} = \frac{\partial \boldsymbol{x}_{c,j}^{-}}{\partial \boldsymbol{y}_{j-1}^{+}} \mathrm{d}\boldsymbol{y}_{j-1}^{+} + \frac{\partial \boldsymbol{x}_{c,j}^{-}}{\partial \lambda_0} \mathrm{d}\lambda_0 + \dot{\boldsymbol{x}}_{c,j}^{-} \mathrm{d}t_j + \sum_{q=1}^{j-1} \frac{\partial \boldsymbol{x}_{c,j}^{-}}{\partial t_q} \mathrm{d}t_q \tag{5.60}$$

The differential of $\boldsymbol{x}_{d,j}^{+}$ is not required since $\boldsymbol{x}_{d,j}^{+}$ is the decision variable to solve. The differential of $\tilde{\boldsymbol{x}}_j^{+}$ is

$$\mathrm{d}\tilde{\boldsymbol{x}}_j^{+} = \mathrm{d}\tilde{\boldsymbol{x}}_j^{-} = \frac{\partial \tilde{\boldsymbol{x}}_j^{-}}{\partial \boldsymbol{y}_{j-1}^{+}} \mathrm{d}\boldsymbol{y}_{j-1}^{+} + \frac{\partial \tilde{\boldsymbol{x}}_j^{-}}{\partial \lambda_0} \mathrm{d}\lambda_0 + \dot{\tilde{\boldsymbol{x}}}_j^{-} \mathrm{d}t_j + \sum_{q=1}^{j-1} \frac{\partial \tilde{\boldsymbol{x}}_j^{-}}{\partial t_q} \mathrm{d}t_q \tag{5.61}$$

From Eq. (5.31), the differential of $\boldsymbol{\lambda}_{c,j}^{+}$ is

$$\begin{aligned} \mathrm{d}\boldsymbol{\lambda}_{c,j}^{+} &= \mathrm{d}\boldsymbol{\lambda}_{c,j}^{-} - \mathrm{d}\left(\boldsymbol{h}_{c,j}^{\top}\boldsymbol{\chi}_{c,j}\right) \\ &= \frac{\partial \boldsymbol{\lambda}_{c,j}^{+}}{\partial \boldsymbol{y}_{j-1}^{+}} \mathrm{d}\boldsymbol{y}_{j-1}^{+} + \frac{\partial \boldsymbol{\lambda}_{c,j}^{+}}{\partial \boldsymbol{\chi}_j} \mathrm{d}\boldsymbol{\chi}_j + \frac{\partial \boldsymbol{\lambda}_{c,j}^{+}}{\partial \lambda_0} \mathrm{d}\lambda_0 + \frac{\mathrm{d}\boldsymbol{\lambda}_{c,j}^{+}}{\mathrm{d}t_j} \mathrm{d}t_j + \sum_{q=1}^{j-1} \frac{\partial \boldsymbol{\lambda}_{c,j}^{+}}{\partial t_q} \mathrm{d}t_q \end{aligned} \tag{5.62}$$

where

$$\frac{\partial \boldsymbol{\lambda}_{c,j}^{+}}{\partial \boldsymbol{y}_{j-1}^{+}} = \frac{\partial \boldsymbol{\lambda}_{c,j}^{-}}{\partial \boldsymbol{y}_{j-1}^{+}}, \quad \frac{\partial \boldsymbol{\lambda}_{c,j}^{+}}{\partial \boldsymbol{\chi}_j} = -\left(\boldsymbol{h}_{c,j}^{\top}, 0\right), \quad \frac{\mathrm{d}\boldsymbol{\lambda}_{c,j}^{+}}{\mathrm{d}t_j} = \dot{\boldsymbol{\lambda}}_{c,j}^{-}, \quad \frac{\partial \boldsymbol{\lambda}_{c,j}^{+}}{\partial \lambda_0} = \frac{\partial \boldsymbol{\lambda}_{c,j}^{-}}{\partial \lambda_0}, \quad \frac{\partial \boldsymbol{\lambda}_{c,j}^{+}}{\partial t_q} = \frac{\partial \boldsymbol{\lambda}_{c,j}^{-}}{\partial t_q} \tag{5.63}$$

From Eq. (5.33), the differential of $\boldsymbol{\lambda}_{d,j}^{+}$ is

$$\begin{aligned} \mathrm{d}\boldsymbol{\lambda}_{d,j}^{+} &= -\mathrm{d}\left(\boldsymbol{\phi}_{d,j+}^{\top}\chi_{n,j}\right) - \mathrm{d}\left(\boldsymbol{\sigma}_{d,j+}^{\top}\kappa_j\right) \\ &= \frac{\partial \boldsymbol{\lambda}_{d,j}^{+}}{\partial \boldsymbol{y}_{j-1}^{+}} \mathrm{d}\boldsymbol{y}_{j-1}^{+} + \frac{\partial \boldsymbol{\lambda}_{d,j}^{+}}{\partial \boldsymbol{\chi}_j} \mathrm{d}\boldsymbol{\chi}_j + \frac{\partial \boldsymbol{\lambda}_{d,j}^{+}}{\partial \kappa_j} \mathrm{d}\kappa_j + \frac{\mathrm{d}\boldsymbol{\lambda}_{d,j}^{+}}{\mathrm{d}t_j} \mathrm{d}t_j + \frac{\partial \boldsymbol{\lambda}_{d,j}^{+}}{\partial \lambda_0} \mathrm{d}\lambda_0 + \frac{\partial \boldsymbol{\lambda}_{d,j}^{+}}{\partial \boldsymbol{x}_{d,j}^{+}} \mathrm{d}\boldsymbol{x}_{d,j}^{+} + \sum_{q=1}^{j-1} \frac{\partial \boldsymbol{\lambda}_{d,j}^{+}}{\partial t_q} \mathrm{d}t_q \end{aligned} \tag{5.64}$$

where $\boldsymbol{\phi}_{d,j+}(t,\boldsymbol{x}_{d,j}^+) = \partial\phi_j/\partial\boldsymbol{x}_{d,j}^+$, $\boldsymbol{\sigma}_{d,j+}(t,\boldsymbol{x}_{d,j}^-,\boldsymbol{x}_{d,j}^+) = \partial\sigma_j/\partial\boldsymbol{x}_{d,j}^+$, and

$$\begin{aligned}
\frac{\partial\boldsymbol{\lambda}_{d,j}^+}{\partial\boldsymbol{y}_{j-1}^+} &= -\frac{\partial\boldsymbol{\sigma}_{d,j+}^\top\kappa_j}{\partial\boldsymbol{x}_{d,j}^-}\frac{\partial\boldsymbol{x}_{d,j}^-}{\partial\boldsymbol{y}_{j-1}^+}, \quad \frac{\partial\boldsymbol{\lambda}_{d,j}^+}{\partial\boldsymbol{\chi}_j} = -\left(\mathbf{0},\boldsymbol{\phi}_{d,j+}^\top\right)\\
\frac{\mathrm{d}\boldsymbol{\lambda}_{d,j}^+}{\mathrm{d}t_j} &= -\frac{\partial\boldsymbol{\sigma}_{d,j+}^\top\kappa_j}{\partial\boldsymbol{x}_{d,j}^-}\dot{\boldsymbol{x}}_{d,j}^- - \left(\frac{\partial\boldsymbol{\phi}_{d,j+}^\top\chi_{n,j}}{\partial t_j} + \frac{\partial\boldsymbol{\sigma}_{d,j+}^\top\kappa_j}{\partial t_j}\right)\\
\frac{\partial\boldsymbol{\lambda}_{d,j}^+}{\partial\kappa_j} &= -\boldsymbol{\sigma}_{d,j+}^\top, \quad \frac{\partial\boldsymbol{\lambda}_{d,j}^+}{\partial\lambda_0} = -\frac{\partial\boldsymbol{\sigma}_{d,j+}^\top\kappa_j}{\partial\boldsymbol{x}_{d,j}^-}\frac{\partial\boldsymbol{x}_{d,j}^-}{\partial\lambda_0}, \quad \frac{\partial\boldsymbol{\lambda}_{d,j}^+}{\partial\boldsymbol{x}_{d,j}^+} = -\left(\frac{\partial\boldsymbol{\phi}_{d,j+}^\top\chi_{n,j}}{\partial\boldsymbol{x}_{d,j}^+} + \frac{\partial\boldsymbol{\sigma}_{d,j+}^\top\kappa_j}{\partial\boldsymbol{x}_{d,j}^+}\right)
\end{aligned} \tag{5.65}$$

The differential of $\tilde{\boldsymbol{\lambda}}_j^+$ is

$$\mathrm{d}\tilde{\boldsymbol{\lambda}}_j^+ = \mathrm{d}\tilde{\boldsymbol{\lambda}}_j^- = \frac{\partial\tilde{\boldsymbol{\lambda}}_j^-}{\partial\boldsymbol{y}_{j-1}^+}\mathrm{d}\boldsymbol{y}_{j-1}^+ + \frac{\partial\tilde{\boldsymbol{\lambda}}_j^-}{\partial\lambda_0}\mathrm{d}\lambda_0 + \dot{\tilde{\boldsymbol{\lambda}}}_j^-\mathrm{d}t_j + \sum_{q=1}^{j-1}\frac{\partial\tilde{\boldsymbol{\lambda}}_j^-}{\partial t_q}\mathrm{d}t_q \tag{5.66}$$

Combining Eqs. (5.60) - (5.66) yields

$$\mathrm{d}\boldsymbol{y}_j^+ = \frac{\partial\boldsymbol{y}_j^+}{\partial\boldsymbol{y}_{j-1}^+}\mathrm{d}\boldsymbol{y}_{j-1}^+ + \frac{\partial\boldsymbol{y}_j^+}{\partial\boldsymbol{\chi}_j}\mathrm{d}\boldsymbol{\chi}_j + \frac{\partial\boldsymbol{y}_j^+}{\partial\kappa_j}\mathrm{d}\kappa_j + \frac{\mathrm{d}\boldsymbol{y}_j^+}{\mathrm{d}t_j}\mathrm{d}t_j + \frac{\partial\boldsymbol{y}_j^+}{\partial\lambda_0}\mathrm{d}\lambda_0 + \frac{\partial\boldsymbol{y}_j^+}{\partial\boldsymbol{x}_{d,j}^+}\mathrm{d}\boldsymbol{x}_{d,j}^+ + \sum_{q=1}^{j-1}\frac{\partial\boldsymbol{y}_j^+}{\partial t_q}\mathrm{d}t_q \tag{5.67}$$

where

$$\frac{\partial\boldsymbol{y}_j^+}{\partial\boldsymbol{y}_{j-1}^+} = \begin{bmatrix}\frac{\partial\boldsymbol{x}_{c,j}^-}{\partial\boldsymbol{y}_{k-1}^+}\\ \mathbf{0}\\ \frac{\partial\tilde{\boldsymbol{x}}_j^-}{\partial\boldsymbol{y}_{j-1}^+}\\ \frac{\partial\boldsymbol{\lambda}_{c,j}^-}{\partial\boldsymbol{y}_{j-1}^+}\\ \frac{\partial\boldsymbol{\lambda}_{d,j}^+}{\partial\boldsymbol{y}_{j-1}^+}\\ \frac{\partial\tilde{\boldsymbol{\lambda}}_j^-}{\partial\boldsymbol{y}_{j-1}^+}\end{bmatrix}, \quad \frac{\partial\boldsymbol{y}_j^+}{\partial\boldsymbol{\chi}_j} = \begin{bmatrix}\mathbf{0}\\ \mathbf{0}\\ \mathbf{0}\\ \frac{\mathrm{d}\boldsymbol{\lambda}_{c,j}^+}{\mathrm{d}\boldsymbol{\chi}_j}\\ \frac{\mathrm{d}\boldsymbol{\lambda}_{d,j}^+}{\mathrm{d}\boldsymbol{\chi}_j}\\ \mathbf{0}\end{bmatrix}, \quad \frac{\partial\boldsymbol{y}_j^+}{\partial\kappa_j} = \begin{bmatrix}\mathbf{0}\\ \mathbf{0}\\ \mathbf{0}\\ \mathbf{0}\\ \frac{\mathrm{d}\boldsymbol{\lambda}_{d,j}^+}{\mathrm{d}\kappa_j}\\ \mathbf{0}\end{bmatrix}, \quad \frac{\partial\boldsymbol{y}_j^+}{\partial\lambda_0} = \begin{bmatrix}\frac{\partial\boldsymbol{x}_{c,j}^-}{\partial\lambda_0}\\ \mathbf{0}\\ \frac{\partial\tilde{\boldsymbol{x}}_j^-}{\partial\lambda_0}\\ \frac{\partial\boldsymbol{\lambda}_{c,j}^-}{\partial\lambda_0}\\ \frac{\partial\boldsymbol{\lambda}_{d,j}^+}{\partial\lambda_0}\\ \frac{\partial\tilde{\boldsymbol{\lambda}}_j^-}{\partial\lambda_0}\end{bmatrix}, \quad \frac{\partial\boldsymbol{y}_j^+}{\partial\boldsymbol{x}_{d,j}^+} = \begin{bmatrix}\mathbf{0}\\ \boldsymbol{I}\\ \mathbf{0}\\ \mathbf{0}\\ \frac{\mathrm{d}\boldsymbol{\lambda}_{d,j}^+}{\mathrm{d}\boldsymbol{x}_{d,j}^+}\\ \mathbf{0}\end{bmatrix}, \quad \frac{\partial\boldsymbol{y}_j^+}{\partial t_q} = \begin{bmatrix}\frac{\partial\boldsymbol{x}_{c,j}^-}{\partial t_q}\\ \mathbf{0}\\ \frac{\partial\tilde{\boldsymbol{x}}_j^-}{\partial t_q}\\ \frac{\partial\boldsymbol{\lambda}_{c,j}^-}{\partial t_q}\\ \frac{\partial\boldsymbol{\lambda}_{d,j}^+}{\partial t_q}\\ \frac{\partial\tilde{\boldsymbol{\lambda}}_j^-}{\partial t_q}\end{bmatrix} \tag{5.68}$$

and

$$\frac{\mathrm{d}\boldsymbol{y}_j^+}{\mathrm{d}t_j} = \hat{\boldsymbol{y}}_{t,j}^+ + \check{\boldsymbol{y}}_{t,j}^+ \tag{5.69}$$

with

$$\hat{\boldsymbol{y}}_{t,j}^+ = \begin{bmatrix}\dot{\boldsymbol{x}}_{c,j}^-\\ \mathbf{0}\\ \dot{\tilde{\boldsymbol{x}}}_j^-\\ \dot{\boldsymbol{\lambda}}_{c,j}^-\\ -\frac{\partial\sigma_{d,j+}^\top\kappa_j}{\partial\boldsymbol{x}_j^-}\dot{\boldsymbol{x}}_j^-\\ \dot{\tilde{\boldsymbol{\lambda}}}_j^-\end{bmatrix} \quad \check{\boldsymbol{y}}_{t,j}^+ = \begin{bmatrix}\mathbf{0}\\ \mathbf{0}\\ \mathbf{0}\\ \mathbf{0}\\ -\left(\frac{\partial\boldsymbol{\phi}_{d,j+}^\top\chi_{n,j}}{\partial t_j} + \frac{\partial\sigma_{d,j+}^\top\kappa_j}{\partial t_j}\right)\\ \mathbf{0}\end{bmatrix} \tag{5.70}$$

The value of $\boldsymbol{\zeta}_j^+$ is

$$\boldsymbol{\zeta}_j^+ = \begin{bmatrix} \boldsymbol{I}_{3\times 3} & & & & \\ & \boldsymbol{0}_{3\times 3} & & & \\ & & 1 & & \\ & & & \boldsymbol{I}_{3\times 3} & \\ & -\dfrac{\partial \sigma_{d,j+}^\top \kappa}{\partial \boldsymbol{x}_{d,j}^-} & & & \\ & & & & 1 \end{bmatrix} \boldsymbol{\zeta}_j^- \tag{5.71}$$

The vectors

$$\boldsymbol{y}_j^+ = [\boldsymbol{x}_{c,j}^-, \boldsymbol{x}_{d,j}^+, \tilde{\boldsymbol{x}}_j^-, \boldsymbol{\lambda}_{c,j}^- - \boldsymbol{h}_{c,j}^\top \boldsymbol{\chi}_{c,j}, -\boldsymbol{\phi}_{d,j+}^\top \chi_{n,j} - \boldsymbol{\sigma}_{d,j+}^\top \kappa_j, \tilde{\boldsymbol{\lambda}}_j^-]$$

and $\boldsymbol{\zeta}_k^+$ in Eq. (5.71) are used to integrate Eq. (5.38) within $[t_j^+, t_{j+1}^-]$. The matrix $\Phi(t_j^+, t_{j-1}^+)$ is computed using Eq. (5.68).

5.2.3 Partial Derivatives of Constraints

The calculation of gradients of the constraints at t_j involves two steps. The first step is to derive the constraints w.r.t. decision variables at t_j, and the next step is to apply the chain rule to derive the derivatives of the constraints w.r.t. decision variables at t_{j-q}, $q \geqslant 1$. This section focuses on the first step.

Intermediate flyby and rendezvous transfer 1) For constraints Eqs. (5.18) and (5.19),

$$\mathrm{d}\boldsymbol{h}_j = \frac{\partial \boldsymbol{h}_j}{\partial \boldsymbol{y}_{j-1}^+}\mathrm{d}\boldsymbol{y}_{j-1}^+ + \frac{\mathrm{d}\boldsymbol{h}_j}{\mathrm{d}t_j}\mathrm{d}t_j + \frac{\partial \boldsymbol{h}_j}{\partial \lambda_0}\mathrm{d}\lambda_0 + \sum_{q=1}^{j-1} \frac{\partial \boldsymbol{h}_j}{\partial t_q}\mathrm{d}t_q \tag{5.72}$$

where

$$\frac{\partial \boldsymbol{h}_j}{\partial \boldsymbol{y}_{j-1}^+} = \frac{\partial \boldsymbol{h}_j}{\partial \boldsymbol{x}_{c,j}}\frac{\partial \boldsymbol{x}_{c,j}}{\partial \boldsymbol{y}_{j-1}^+}, \quad \frac{\mathrm{d}\boldsymbol{h}_j}{\mathrm{d}t_j} = \widehat{\boldsymbol{h}}_{t,j} + \check{\boldsymbol{h}}_{t,j}, \quad \frac{\partial \boldsymbol{h}_j}{\partial \lambda_0} = \frac{\partial \boldsymbol{h}_j}{\partial \boldsymbol{x}_{c,j}}\frac{\partial \boldsymbol{x}_{c,j}}{\partial \lambda_0} \tag{5.73}$$

and

$$\widehat{\boldsymbol{h}}_{t,j} = \frac{\partial \boldsymbol{h}_j}{\partial \boldsymbol{x}_{c,j}}\dot{\boldsymbol{x}}_{c,j}, \quad \check{\boldsymbol{h}}_{t,j} = \frac{\partial \boldsymbol{h}_j}{\partial t_j} \tag{5.74}$$

Therefore we have

$$\frac{\mathrm{d}\boldsymbol{h}_j}{\mathrm{d}\lambda_0} = \frac{\partial \boldsymbol{h}_j}{\partial \lambda_0} + \frac{\partial \boldsymbol{h}_j}{\partial \boldsymbol{y}_{j-1}^+}\frac{\partial \boldsymbol{y}_{j-1}^+}{\partial \lambda_0} = \frac{\partial \boldsymbol{h}_j}{\partial \boldsymbol{x}_{c,j}}\frac{\mathrm{d}\boldsymbol{x}_{c,j}}{\mathrm{d}\lambda_0} \tag{5.75}$$

The full differentials of other constraints w.r.t. λ_0 have the similar process as Eq. (5.75) in the following.

2) For constraint Eq. (5.20), let $\mathscr{H}_j$ be

$$\mathscr{H}_j = \boldsymbol{\chi}_j^\top \boldsymbol{h}_{t,j} + L_j^- - L_j^+ + \left(\boldsymbol{\lambda}_j^-\right)^\top \boldsymbol{f}_j^- - \left(\boldsymbol{\lambda}_j^+\right)^\top \boldsymbol{f}_j^+ \tag{5.76}$$

The differential of $\mathscr{H}_j$ is

$$\mathrm{d}\mathscr{H}_j = \frac{\partial \mathscr{H}_j}{\partial \boldsymbol{y}_{j-1}^+}\mathrm{d}\boldsymbol{y}_{j-1}^+ + \frac{\partial \mathscr{H}_j}{\partial \boldsymbol{\chi}_j}\mathrm{d}\boldsymbol{\chi}_j + \frac{\mathrm{d}\mathscr{H}_j}{\mathrm{d}t_j}\mathrm{d}t_j + \frac{\partial \mathscr{H}_j}{\partial \lambda_0}\mathrm{d}\lambda_0 + \sum_{q=1}^{j-1} \frac{\partial \mathscr{H}_j}{\partial t_q}\mathrm{d}t_q \tag{5.77}$$

where

$$
\begin{aligned}
\frac{\partial \mathscr{H}_j}{\partial \boldsymbol{y}_{j-1}^+} &= \frac{\partial L_j^-}{\partial \boldsymbol{y}_j^-}\frac{\partial \boldsymbol{y}_j^-}{\partial \boldsymbol{y}_{j-1}^+} - \frac{\partial L_j^+}{\partial \boldsymbol{y}_j^+}\frac{\partial \boldsymbol{y}_j^+}{\partial \boldsymbol{y}_{j-1}^+} + \left(\boldsymbol{f}_j^-\right)^\top \frac{\partial \boldsymbol{\lambda}_j^-}{\partial \boldsymbol{y}_{j-1}^+} + \left(\boldsymbol{\lambda}_j^-\right)^\top \frac{\partial \boldsymbol{f}_j^-}{\partial \boldsymbol{y}_j^-}\frac{\partial \boldsymbol{y}_j^-}{\partial \boldsymbol{y}_{j-1}^+} - \left(\boldsymbol{f}_j^+\right)^\top \frac{\partial \boldsymbol{\lambda}_j^+}{\partial \boldsymbol{y}_{j-1}^+} - \left(\boldsymbol{\lambda}_j^+\right)^\top \frac{\partial \boldsymbol{f}_j^+}{\partial \boldsymbol{y}_j^+}\frac{\partial \boldsymbol{y}_j^+}{\partial \boldsymbol{y}_{j-1}^+} \\
\frac{\partial \mathscr{H}_j}{\partial \boldsymbol{\chi}_j} &= \boldsymbol{h}_{t,j} - \frac{\partial L_j^+}{\partial \boldsymbol{y}_j^+}\frac{\partial \boldsymbol{y}_j^+}{\partial \boldsymbol{\chi}_j} - \left(\boldsymbol{f}_j^+\right)^\top \frac{\partial \boldsymbol{\lambda}_j^+}{\partial \boldsymbol{\chi}_j} - \left(\boldsymbol{\lambda}_j^+\right)^\top \frac{\partial \boldsymbol{f}_j^+}{\partial \boldsymbol{y}_j^+}\frac{\partial \boldsymbol{y}_j^+}{\partial \boldsymbol{\chi}} \\
\frac{\mathrm{d}\mathscr{H}_j}{\mathrm{d}\lambda_0} &= \frac{\partial L_j^-}{\partial \boldsymbol{y}_j^-}\frac{\mathrm{d}\boldsymbol{y}_j^-}{\mathrm{d}\lambda_0} + \frac{\partial L_j^-}{\partial \lambda_0} - \frac{\partial L_j^+}{\partial \boldsymbol{y}_j^+}\frac{\mathrm{d}\boldsymbol{y}_j^+}{\mathrm{d}\lambda_0} - \frac{\partial L_j^+}{\partial \lambda_0} + \left(\boldsymbol{f}_j^-\right)^\top \frac{\mathrm{d}\boldsymbol{\lambda}_j^-}{\mathrm{d}\lambda_0} + \left(\boldsymbol{\lambda}_j^-\right)^\top \frac{\partial \boldsymbol{f}_j^-}{\partial \boldsymbol{y}_j^-}\frac{\mathrm{d}\boldsymbol{y}_j^-}{\mathrm{d}\lambda_0} + \left(\boldsymbol{\lambda}_j^-\right)^\top \frac{\partial \boldsymbol{f}_j^-}{\partial \lambda_0} \\
&\quad - \left(\boldsymbol{f}_j^+\right)^\top \frac{\mathrm{d}\boldsymbol{\lambda}_j^+}{\mathrm{d}\lambda_0} - \left(\boldsymbol{\lambda}_j^+\right)^\top \frac{\partial \boldsymbol{f}_j^+}{\partial \boldsymbol{y}_j^+}\frac{\mathrm{d}\boldsymbol{y}_j^+}{\mathrm{d}\lambda_0} - \left(\boldsymbol{\lambda}_j^+\right)^\top \frac{\partial \boldsymbol{f}_j^+}{\partial \lambda_0} \\
\frac{\mathrm{d}\mathscr{H}_j}{\mathrm{d}t_j} &= \widehat{\mathscr{H}}_{t,j} + \breve{\mathscr{H}}_{t,j}
\end{aligned}
\tag{5.78}
$$

and

$$
\begin{aligned}
\widehat{\mathscr{H}}_{t,j} &= \frac{\partial L_j^-}{\partial \boldsymbol{y}_j^-}\dot{\boldsymbol{y}}_j^- - \frac{\partial L_j^+}{\partial \boldsymbol{y}_j^+}\widehat{\boldsymbol{y}}_{t,j}^+ + \left(\boldsymbol{f}_j^-\right)^\top \dot{\boldsymbol{\lambda}}_j^- + \left(\boldsymbol{\lambda}_j^-\right)^\top \frac{\partial \boldsymbol{f}_j^-}{\partial \boldsymbol{y}_j^-}\dot{\boldsymbol{y}}_j^- - \left(\boldsymbol{f}_j^+\right)^\top \frac{\partial \boldsymbol{\lambda}_j^+}{\partial \boldsymbol{y}_j^+}\widehat{\boldsymbol{y}}_{t,j}^+ - \left(\boldsymbol{\lambda}_j^+\right)^\top \frac{\partial \boldsymbol{f}_j^+}{\partial \boldsymbol{y}_j^+}\widehat{\boldsymbol{y}}_{t,j}^+ \\
\breve{\mathscr{H}}_{t,j} &= \boldsymbol{\chi}_j^\top \boldsymbol{h}_{tt,j}
\end{aligned}
\tag{5.79}
$$

where $\boldsymbol{h}_{tt,j} = \partial \boldsymbol{h}_{t,j}/\partial t_j$.

Intermediate gravity-assist transfer 1) For constraint Eq. (5.25), there satisfies

$$
\mathrm{d}\boldsymbol{h}_j = \frac{\partial \boldsymbol{h}_j}{\partial \boldsymbol{y}_{j-1}^+}\mathrm{d}\boldsymbol{y}_{j-1}^+ + \frac{\mathrm{d}\boldsymbol{h}_j}{\mathrm{d}t_j}\mathrm{d}t_j + \frac{\partial \boldsymbol{h}_j}{\partial \lambda_0}\mathrm{d}\lambda_0 + \sum_{q=1}^{j-1}\frac{\partial \boldsymbol{h}_j}{\partial t_q}\mathrm{d}t_q \tag{5.80}
$$

where

$$
\frac{\partial \boldsymbol{h}_j}{\partial \boldsymbol{y}_{j-1}^+} = \frac{\partial \boldsymbol{h}}{\partial \boldsymbol{x}_{c,j}}\frac{\partial \boldsymbol{x}_{c,j}}{\partial \boldsymbol{y}_{j-1}^+}, \quad \frac{\mathrm{d}\boldsymbol{h}_j}{\mathrm{d}t_j} = \widehat{\boldsymbol{h}}_{t,j} + \check{\boldsymbol{h}}_{t,j}, \quad \frac{\mathrm{d}\boldsymbol{h}_j}{\mathrm{d}\lambda_0} = \frac{\partial \boldsymbol{h}_j}{\partial \boldsymbol{x}_{c,j}}\frac{\mathrm{d}\boldsymbol{x}_{c,j}}{\mathrm{d}\lambda_0} \tag{5.81}
$$

and

$$
\widehat{\boldsymbol{h}}_{t,j} = \frac{\partial \boldsymbol{h}_j}{\partial \boldsymbol{x}_{c,j}}\dot{\boldsymbol{x}}_{c,j}, \quad \check{\boldsymbol{h}}_{t,j} = \frac{\partial \boldsymbol{h}_j}{\partial t_j} \tag{5.82}
$$

2) For constraint Eq. (5.26), there satisfies

$$
\mathrm{d}\phi_j = \frac{\partial \phi_j}{\partial \boldsymbol{y}_{j-1}^+}\mathrm{d}\boldsymbol{y}_{j-1}^+ + \frac{\partial \phi_j}{\partial \boldsymbol{x}_{d,j}^+}\mathrm{d}\boldsymbol{x}_{d,j}^+ + \frac{\mathrm{d}\phi_j}{\mathrm{d}t_j}\mathrm{d}t_j + \frac{\partial \phi_j}{\partial \lambda_0}\mathrm{d}\lambda_0 + \sum_{q=1}^{j-1}\frac{\partial \phi_j}{\partial t_q}\mathrm{d}t_q \tag{5.83}
$$

where

$$
\frac{\partial \phi_j}{\partial \boldsymbol{y}_{j-1}^+} = \frac{\partial \phi}{\partial \boldsymbol{x}_{d,j}^-}\frac{\partial \boldsymbol{x}_{d,j}^-}{\partial \boldsymbol{y}_{j-1}^+}, \quad \frac{\mathrm{d}\phi_j}{\mathrm{d}t_j} = \widehat{\phi}_{t,j} + \check{\phi}_{t,j}, \quad \frac{\mathrm{d}\phi_j}{\mathrm{d}\lambda_0} = \frac{\partial \phi_j}{\partial \boldsymbol{x}_{d,j}^-}\frac{\mathrm{d}\boldsymbol{x}_{d,j}^-}{\mathrm{d}\lambda_0} \tag{5.84}
$$

and

$$
\widehat{\phi}_{t,j} = \frac{\partial \phi_j}{\partial \boldsymbol{x}_{d,j}^-}\dot{\boldsymbol{x}}_{d,j}^-, \quad \check{\phi}_{t,j} = \frac{\partial \phi_j}{\partial t_j} \tag{5.85}
$$

3) For constraint Eq. (5.32), let $\boldsymbol{\psi}_j = \chi_{n,j}\phi_{d,j-}^\top - \boldsymbol{\lambda}_{d,j}^- + \kappa_j\sigma_{d,j-}^\top$, where $\phi_{d,j-}(t, \boldsymbol{x}_{d,j}^-) = \partial\phi_j/\partial\boldsymbol{x}_{d,j}^-$, $\boldsymbol{\sigma}_{d,j-}(t_j, \boldsymbol{x}_{d,j}^-, \boldsymbol{x}_{d,j}^+) = \partial\sigma_j/\partial\boldsymbol{x}_{d,j}^-$, there satisfies

$$
\mathrm{d}\boldsymbol{\psi}_j = \frac{\partial \boldsymbol{\psi}_j}{\partial \boldsymbol{y}_{j-1}^+}\mathrm{d}\boldsymbol{y}_{j-1}^+ + \frac{\partial \boldsymbol{\psi}_j}{\partial \boldsymbol{x}_{d,j}^+}\mathrm{d}\boldsymbol{x}_{d,j}^+ + \frac{\partial \boldsymbol{\psi}_j}{\partial \boldsymbol{\chi}_j}\mathrm{d}\boldsymbol{\chi}_j + \frac{\partial \boldsymbol{\psi}_j}{\partial \kappa_j}\mathrm{d}\kappa_j + \frac{\mathrm{d}\boldsymbol{\psi}_j}{\mathrm{d}t_j}\mathrm{d}t_j + \frac{\partial \boldsymbol{\psi}_j}{\partial \lambda_0}\mathrm{d}\lambda_0 + \sum_{q=1}^{j-1}\frac{\partial \boldsymbol{\psi}_j}{\partial t_q}\mathrm{d}t_q \tag{5.86}
$$

where

$$\begin{aligned}
\frac{\partial \boldsymbol{\psi}_j}{\partial \boldsymbol{y}_{j-1}^+} &= \left(\frac{\partial \boldsymbol{\phi}_{d,j-}^\top \chi_{n,j}}{\partial \boldsymbol{x}_{d,j}^-} + \frac{\partial \boldsymbol{\sigma}_{d,j-}^\top \kappa_j}{\partial \boldsymbol{x}_{d,j}^-}\right)\frac{\partial \boldsymbol{x}_{d,j}^-}{\partial \boldsymbol{y}_{j-1}^+} - \frac{\partial \boldsymbol{\lambda}_{d,j}^-}{\partial \boldsymbol{y}_{j-1}^+} \\
\frac{\partial \boldsymbol{\psi}_j}{\partial \boldsymbol{x}_{d,j}^+} &= \frac{\partial \boldsymbol{\sigma}_{d,j-}^\top \kappa_j}{\partial \boldsymbol{x}_{d,j}^+}, \quad \frac{\partial \boldsymbol{\psi}_j}{\partial \boldsymbol{\chi}_j} = [0, \boldsymbol{\phi}_{d,j-}^\top], \quad \frac{\partial \boldsymbol{\psi}_j}{\partial \kappa_j} = \boldsymbol{\sigma}_{d,j-}^\top, \quad \frac{\mathrm{d}\boldsymbol{\psi}_j}{\mathrm{d}t_j} = \widehat{\boldsymbol{\psi}}_{t,j} + \check{\boldsymbol{\psi}}_{t,j} \\
\frac{\mathrm{d}\boldsymbol{\psi}_j}{\mathrm{d}\lambda_0} &= \left(\frac{\partial \boldsymbol{\phi}_{d,j-}^\top \chi_{n,j}}{\partial \boldsymbol{x}_{d,j}^-} + \frac{\partial \boldsymbol{\sigma}_{d,j-}^\top \kappa}{\partial \boldsymbol{x}_{d,j}^-}\right)\frac{\mathrm{d}\boldsymbol{x}_{d,j}^-}{\mathrm{d}\lambda_0} - \frac{\mathrm{d}\boldsymbol{\lambda}_{d,j}^-}{\mathrm{d}\lambda_0}
\end{aligned} \tag{5.87}$$

and

$$\widehat{\boldsymbol{\psi}}_{t,j} = -\dot{\boldsymbol{\lambda}}_{d,j}^- + \left(\frac{\partial \boldsymbol{\phi}_{d,j-}^\top \chi_{n,j}}{\partial \boldsymbol{x}_{d,j}^-} + \frac{\partial \boldsymbol{\sigma}_{d,j-}^\top \kappa_j}{\partial \boldsymbol{x}_{d,j}^-}\right)\dot{\boldsymbol{x}}_{d,j}^-, \quad \check{\boldsymbol{\psi}}_{t,j} = \frac{\partial \boldsymbol{\phi}_{d,j-}^\top \chi_{n,j}}{\partial t_j} + \frac{\partial \boldsymbol{\sigma}_{d,j-}^\top \kappa_j}{\partial t_j} \tag{5.88}$$

4) For constraint Eq. (5.30), let $\mathscr{H}_j$ be

$$\mathscr{H}_j = \boldsymbol{\chi}_j^\top [\boldsymbol{h}_{t,j}, \phi_{t,j}] + \kappa_j \sigma_{t,j} + L_j^- - L_j^+ + \left(\boldsymbol{\lambda}_j^-\right)^\top \boldsymbol{f}_j^- - \left(\boldsymbol{\lambda}_j^+\right)^\top \boldsymbol{f}_j^+ \tag{5.89}$$

where $\phi_{t,j} = \partial \phi_j / \partial t_j$ and $\sigma_{t,j} = \partial \sigma_j / \partial t_j$. The differential of $\mathscr{H}_j$ is

$$\mathrm{d}\mathscr{H}_j = \frac{\partial \mathscr{H}_j}{\partial \boldsymbol{y}_{j-1}^+}\mathrm{d}\boldsymbol{y}_{j-1}^+ + \frac{\partial \mathscr{H}_j}{\partial \boldsymbol{x}_{d,j}^+}\mathrm{d}\boldsymbol{x}_{d,j}^+ + \frac{\partial \mathscr{H}_j}{\partial \boldsymbol{\chi}_j}\mathrm{d}\boldsymbol{\chi}_j + \frac{\partial \mathscr{H}_j}{\partial \kappa_j}\mathrm{d}\kappa_j + \frac{\mathrm{d}\mathscr{H}_j}{\mathrm{d}t_j}\mathrm{d}t_j + \frac{\partial \mathscr{H}_j}{\partial \lambda_0}\mathrm{d}\lambda_0 + \sum_{q=1}^{j-1}\frac{\partial \mathscr{H}_j}{\partial t_q}\mathrm{d}t_q \tag{5.90}$$

where

$$\begin{aligned}
\frac{\partial \mathscr{H}_j}{\partial \boldsymbol{y}_{j-1}^+} &= \left(\frac{\partial \boldsymbol{\chi}_j^\top [\boldsymbol{h}_{t,j}, \phi_{t,j}]}{\partial \boldsymbol{x}_j^-} + \frac{\partial \sigma_{t,j}\kappa}{\partial \boldsymbol{x}_j^-}\right)\frac{\partial \boldsymbol{x}_j^-}{\partial \boldsymbol{y}_{j-1}^+} + \frac{\partial L_j^-}{\partial \boldsymbol{y}_j^-}\frac{\partial \boldsymbol{y}_j^-}{\partial \boldsymbol{y}_{j-1}^+} - \frac{\partial L_j^+}{\partial \boldsymbol{y}_j^+}\frac{\partial \boldsymbol{y}_j^+}{\partial \boldsymbol{y}_{j-1}^+} + \left(\boldsymbol{f}_j^-\right)^\top \frac{\partial \boldsymbol{\lambda}_j^-}{\partial \boldsymbol{y}_{j-1}^+} + \left(\boldsymbol{\lambda}_j^-\right)^\top \frac{\partial \boldsymbol{f}_j^-}{\partial \boldsymbol{y}_j^-}\frac{\partial \boldsymbol{y}_j^-}{\partial \boldsymbol{y}_{j-1}^+} \\
&\quad - \left(\boldsymbol{f}_j^+\right)^\top \frac{\partial \boldsymbol{\lambda}_j^+}{\partial \boldsymbol{y}_{j-1}^+} - \left(\boldsymbol{\lambda}_j^+\right)^\top \frac{\partial \boldsymbol{f}_j^+}{\partial \boldsymbol{y}_j^+}\frac{\partial \boldsymbol{y}_j^+}{\partial \boldsymbol{y}_{j-1}^+} \\
\frac{\partial \mathscr{H}_j}{\partial \boldsymbol{x}_{d,j}^+} &= \left(\frac{\partial \phi_{t,j}\chi_{n,j}}{\partial \boldsymbol{x}_{d,j}^+} + \frac{\partial \sigma_{t,j}\kappa_j}{\partial \boldsymbol{x}_{d,j}^+}\right) - \frac{\partial L_j^+}{\partial \boldsymbol{y}_j^+}\frac{\partial \boldsymbol{y}_j^+}{\partial \boldsymbol{x}_d^+} - \left(\boldsymbol{f}_j^+\right)^\top \frac{\partial \boldsymbol{\lambda}_j^+}{\partial \boldsymbol{x}_d^+} - \left(\boldsymbol{\lambda}_j^+\right)^\top \frac{\partial \boldsymbol{f}_j^+}{\partial \boldsymbol{y}_j^+}\frac{\partial \boldsymbol{y}_j^+}{\partial \boldsymbol{x}_d^+} \\
\frac{\partial \mathscr{H}_j}{\partial \boldsymbol{\chi}_j} &= [\boldsymbol{h}_{t,j}, \phi_{t,j}] - \frac{\partial L_j^+}{\partial \boldsymbol{y}_j^+}\frac{\partial \boldsymbol{y}_j^+}{\partial \boldsymbol{\chi}_j} - \left(\boldsymbol{f}_j^+\right)^\top \frac{\partial \boldsymbol{\lambda}_j^+}{\partial \boldsymbol{\chi}_j} - \left(\boldsymbol{\lambda}_j^+\right)^\top \frac{\partial \boldsymbol{f}_j^+}{\partial \boldsymbol{y}_j^+}\frac{\partial \boldsymbol{y}_j^+}{\partial \boldsymbol{\chi}_j} \\
\frac{\partial \mathscr{H}_j}{\partial \kappa_j} &= \sigma_{t,j} - \frac{\partial L_j^+}{\partial \boldsymbol{y}_j^+}\frac{\partial \boldsymbol{y}_j^+}{\partial \kappa_j} - \left(\boldsymbol{f}_j^+\right)^\top \frac{\partial \boldsymbol{\lambda}_j^+}{\partial \kappa_j} - \left(\boldsymbol{\lambda}_j^+\right)^\top \frac{\partial \boldsymbol{f}_j^+}{\partial \boldsymbol{y}_j^+}\frac{\partial \boldsymbol{y}_j^+}{\partial \kappa_j} \\
\frac{\mathrm{d}\mathscr{H}_j}{\mathrm{d}\lambda_0} &= \left(\frac{\partial \boldsymbol{\chi}_j^\top [\boldsymbol{h}_{t,j}, \phi_{t,j}]}{\partial \boldsymbol{x}_j^-} + \frac{\partial \sigma_{t,j}\kappa_j}{\partial \boldsymbol{x}_j^-}\right)\frac{\mathrm{d}\boldsymbol{x}_j^-}{\mathrm{d}\lambda_0} + \frac{\partial L_j^-}{\partial \boldsymbol{y}_j^-}\frac{\mathrm{d}\boldsymbol{y}_j^-}{\mathrm{d}\lambda_0} + \frac{\partial L_j^-}{\partial \lambda_0} - \frac{\partial L_j^+}{\partial \boldsymbol{y}_j^+}\frac{\mathrm{d}\boldsymbol{y}_j^+}{\mathrm{d}\lambda_0} - \frac{\partial L_j^+}{\partial \lambda_0} + \left(\boldsymbol{f}_j^-\right)^\top \frac{\mathrm{d}\boldsymbol{\lambda}_j^-}{\mathrm{d}\lambda_0} + \left(\boldsymbol{\lambda}_j^-\right)^\top \frac{\partial \boldsymbol{f}_j^-}{\partial \boldsymbol{y}_j^-}\frac{\mathrm{d}\boldsymbol{y}_j^-}{\mathrm{d}\lambda_0} \\
&\quad + \left(\boldsymbol{\lambda}_j^-\right)^\top \frac{\partial \boldsymbol{f}_j^-}{\partial \lambda_0} - \left(\boldsymbol{f}_j^+\right)^\top \frac{\mathrm{d}\boldsymbol{\lambda}_j^+}{\mathrm{d}\lambda_0} - \left(\boldsymbol{\lambda}_j^+\right)^\top \frac{\partial \boldsymbol{f}_j^+}{\partial \boldsymbol{y}_j^+}\frac{\mathrm{d}\boldsymbol{y}_j^+}{\mathrm{d}\lambda_0} - \left(\boldsymbol{\lambda}_j^+\right)^\top \frac{\partial \boldsymbol{f}_j^+}{\partial \lambda_0} \\
\frac{\mathrm{d}\mathscr{H}_j}{\mathrm{d}t_j} &= \widehat{\mathscr{H}}_{t,j} + \check{\mathscr{H}}_{t,j}
\end{aligned} \tag{5.91}$$

and

$$\widehat{\mathscr{H}}_{t,j} = \left(\frac{\partial \boldsymbol{\chi}_j^\top [\boldsymbol{h}_{t,j}, \phi_{t,j}]}{\partial \boldsymbol{x}_j^-} + \frac{\partial \sigma_{t,j} \kappa_j}{\partial \boldsymbol{x}_j^-} \right) \dot{\boldsymbol{x}}_j^- + \frac{\partial L_j^-}{\partial \boldsymbol{y}_j^-} \dot{\boldsymbol{y}}_j^- - \frac{\partial L_j^+}{\partial \boldsymbol{y}_j^+} \widehat{\boldsymbol{y}}_{t,j} + \left(\boldsymbol{f}_j^-\right)^\top \dot{\boldsymbol{\lambda}}_j^- + \left(\boldsymbol{\lambda}_j^-\right)^\top \frac{\partial \boldsymbol{f}_j^-}{\partial \boldsymbol{y}_j^-} \dot{\boldsymbol{y}}_j^-$$
$$- \left(\boldsymbol{f}_j^+\right)^\top \frac{\partial \boldsymbol{\lambda}_j^+}{\partial \boldsymbol{y}_j^+} \widehat{\boldsymbol{y}}_{t,j} - \left(\boldsymbol{\lambda}_j^+\right)^\top \frac{\partial \boldsymbol{f}_j^+}{\partial \boldsymbol{y}_j^+} \widehat{\boldsymbol{y}}_{t,j}$$
$$\breve{\mathscr{H}}_{t,j} = \frac{\partial \boldsymbol{\chi}_j^\top [\boldsymbol{h}_{t,j}, \phi_{t,j}]}{\partial t_j} + \frac{\partial \sigma_{t,j} \kappa_j}{\partial t_j} - \frac{\partial L_j^+}{\partial \boldsymbol{y}_j^+} \breve{\boldsymbol{y}}_{t,j} - \left(\boldsymbol{f}_j^+\right)^\top \frac{\partial \boldsymbol{\lambda}_j^+}{\partial \boldsymbol{y}_j^+} \breve{\boldsymbol{y}}_{t,j} - \left(\boldsymbol{\lambda}_j^+\right)^\top \frac{\partial \boldsymbol{f}_j^+}{\partial \boldsymbol{y}_j^+} \breve{\boldsymbol{y}}_{t,j} \tag{5.92}$$

5) For constraint Eq. (5.28), the differential of $\eta_j = \sigma_j + \alpha_j^2$ is

$$\mathrm{d}\eta_j = \frac{\partial \eta_j}{\partial \boldsymbol{y}_{j-1}^+} \mathrm{d}\boldsymbol{y}_{j-1}^+ + \frac{\partial \eta_j}{\partial \alpha_j} \mathrm{d}\alpha_j + \frac{\partial \eta_j}{\partial \boldsymbol{x}_{d,j}^+} \mathrm{d}\boldsymbol{x}_{d,j}^+ + \frac{\mathrm{d}\eta_j}{\mathrm{d}t_j} \mathrm{d}t_j + \frac{\partial \eta_j}{\partial \lambda_0} \mathrm{d}\lambda_0 + \sum_{q=1}^{j-1} \frac{\partial \eta_j}{\partial t_q} \mathrm{d}t_q \tag{5.93}$$

where

$$\frac{\partial \eta_j}{\partial \boldsymbol{y}_{j-1}^+} = \frac{\partial \eta_j}{\partial \boldsymbol{x}_{d,j}^-} \frac{\partial \boldsymbol{x}_{d,j}^-}{\partial \boldsymbol{y}_{j-1}^+}, \quad \frac{\partial \eta_j}{\partial \alpha_j} = 2\alpha_j, \quad \frac{\mathrm{d}\eta_j}{\mathrm{d}t_j} = \widehat{\eta}_{t,j} + \breve{\eta}_{t,j}, \quad \frac{\mathrm{d}\eta_j}{\mathrm{d}\lambda_0} = \frac{\partial \eta_j}{\partial \boldsymbol{x}_{d,j}^-} \frac{\mathrm{d}\boldsymbol{x}_{d,j}^-}{\mathrm{d}\lambda_0} \tag{5.94}$$

and

$$\widehat{\eta}_{t,j} = \frac{\partial \eta_j}{\partial \boldsymbol{x}_{d,j}^-} \dot{\boldsymbol{x}}_{d,j}^-, \quad \breve{\eta}_{t,j} = \frac{\partial \eta_j}{\partial t_j} \tag{5.95}$$

6) For constraint Eq. (5.29), the differential of $\kappa_j \alpha_j$ is

$$\mathrm{d}(\kappa_j \alpha_j) = \kappa_j \mathrm{d}\alpha_j + \alpha_j \mathrm{d}\kappa_j \tag{5.96}$$

Terminal and multiplier constraints The derivatives of terminal conditions and multiplier normalization condition apply to both categories of missions. Let $\boldsymbol{C}(t_f, \boldsymbol{x}(t_f), \boldsymbol{r}_t(t_f), \boldsymbol{v}_t(t_f)) = [\boldsymbol{r}(t_f) - \boldsymbol{r}_T(t_f), \boldsymbol{v}(t_f) - \boldsymbol{v}_T(t_f), \lambda_m(t_f)]$, the differential of it is

$$\mathrm{d}\boldsymbol{C} = \frac{\partial \boldsymbol{C}}{\partial \boldsymbol{y}_w^+} \mathrm{d}\boldsymbol{y}_w^+ + \frac{\mathrm{d}\boldsymbol{C}}{\mathrm{d}t_f} \mathrm{d}t_f + \frac{\partial \boldsymbol{C}}{\partial \lambda_0} \mathrm{d}\lambda_0 + \sum_{q=1}^{w-1} \frac{\partial \boldsymbol{C}}{\partial t_q} \mathrm{d}t_q \tag{5.97}$$

where

$$\frac{\partial \boldsymbol{C}}{\partial \boldsymbol{y}_w^+} = \frac{\partial \boldsymbol{C}}{\partial \boldsymbol{y}_f} \frac{\partial \boldsymbol{y}_f}{\partial \boldsymbol{y}_w^+}, \quad \frac{\mathrm{d}\boldsymbol{C}}{\mathrm{d}t_f} = \widehat{\boldsymbol{C}}_{t,j} + \breve{\boldsymbol{C}}_{t,j}, \quad \frac{\mathrm{d}\boldsymbol{C}}{\mathrm{d}\lambda_0} = \frac{\partial \boldsymbol{C}}{\partial \boldsymbol{y}_f} \frac{\mathrm{d}\boldsymbol{y}_f}{\mathrm{d}\lambda_0} \tag{5.98}$$

and

$$\widehat{\boldsymbol{C}}_{t,j} = \frac{\partial \boldsymbol{C}}{\partial \boldsymbol{y}_f} \dot{\boldsymbol{y}}_f, \quad \breve{\boldsymbol{C}}_{t,j} = \frac{\partial \boldsymbol{C}}{\partial t_f} \tag{5.99}$$

Besides, the differential of $\boldsymbol{C}_\lambda = \sqrt{\lambda_0^2 + \boldsymbol{\lambda}_i^\top \boldsymbol{\lambda}_i + \sum_{j1=1}^{\hat{w}} (\boldsymbol{\chi}_{j1}^\top \boldsymbol{\chi}_{j1} + \kappa_{j1}^2) + \sum_{j2=\hat{w}+1}^{w} \boldsymbol{\chi}_{j2}^\top \boldsymbol{\chi}_{j2}} - 1$ in Eq. (5.35) satisfies

$$\mathrm{d}\boldsymbol{C}_\lambda = \frac{\lambda_0 \mathrm{d}\lambda_0 + \boldsymbol{\lambda}_i^\top \mathrm{d}\boldsymbol{\lambda}_i + \sum_{j1=1}^{\hat{w}} (\boldsymbol{\chi}_{j1}^\top \mathrm{d}\boldsymbol{\chi}_{j1} + \kappa_{j1} \mathrm{d}\kappa_{j1}) + \sum_{j2=\hat{w}+1}^{w} (\boldsymbol{\chi}_{j2}^\top \mathrm{d}\boldsymbol{\chi}_{j2})}{\sqrt{\lambda_0^2 + \boldsymbol{\lambda}_i^\top \boldsymbol{\lambda}_i + \sum_{j1=1}^{\hat{w}} (\boldsymbol{\chi}_{j1}^\top \boldsymbol{\chi}_{j1} + \kappa_{j1}^2) + \sum_{j2=\hat{w}+1}^{w} \boldsymbol{\chi}_{j2}^\top \boldsymbol{\chi}_{j2}}} \tag{5.100}$$

5.2.4 Chain Rules

The differentials of the constraints at t_j w.r.t. decision variables at t_{j-q}, $q \geqslant 1$ are obtained in this section. Since the interior-point constraints are explicitly dependent on time, the derivatives are splitted based on whether they are derived w.r.t. the time. Let a general constraint at t_j be $\mathscr{N}_j$. The derivatives of $\mathscr{N}_j$ w.r.t. $\boldsymbol{\chi}_{j-q}$, $\boldsymbol{x}^+_{d,j-q}$, α_{j-q} and κ_{j-q} are similar. Take the differential of $\mathscr{N}_j$ w.r.t. $\boldsymbol{\chi}_{j-q}$ as an example. When $q = 1$, there exists

$$\frac{\mathrm{d}\mathscr{N}_j}{\mathrm{d}\boldsymbol{\chi}_{j-1}} = \frac{\partial \mathscr{N}_j}{\partial \boldsymbol{y}^+_{j-1}} \frac{\partial \boldsymbol{y}^+_{j-1}}{\partial \boldsymbol{\chi}_{j-1}} \tag{5.101}$$

while the derivative of $\mathscr{N}_j$ w.r.t. $\boldsymbol{\chi}_{j-q}$, $q > 1$ is

$$\frac{\mathrm{d}\mathscr{N}_j}{\mathrm{d}\boldsymbol{\chi}_{j-q}} = \frac{\partial \mathscr{N}_j}{\partial \boldsymbol{y}^+_{j-1}} \frac{\partial \boldsymbol{y}^+_{j-1}}{\partial \boldsymbol{y}^+_{j-2}} \cdots \frac{\partial \boldsymbol{y}^+_{j-q+1}}{\partial \boldsymbol{y}^+_{j-q}} \frac{\partial \boldsymbol{y}^+_{j-q}}{\partial \boldsymbol{\chi}_{j-q}} \tag{5.102}$$

The analysis of the derivative of $\mathscr{N}_j$ w.r.t. t_{j-q} is more complex. When $q = 1$, the derivative is divided into two parts. That is

$$\frac{\mathrm{d}\mathscr{N}_j}{\mathrm{d}t_{j-1}} = \frac{\partial \mathscr{N}_j}{\partial \boldsymbol{y}^+_{j-1}} \frac{\mathrm{d}\boldsymbol{y}^+_{j-1}}{\mathrm{d}t_{j-1}} + \frac{\partial \mathscr{N}_j}{\partial t_{j-1}} \tag{5.103}$$

The first term can be obtained directly, while the analysis of the second term is depicted in the following. As shown in Fig. 5.3, when $\boldsymbol{y}^+_{j-1}$ remains unchanged, the effect of the slight increment Δt is to move the trajectory horizontally. Thus there exists

$$\frac{\partial \boldsymbol{y}(t_j^-)}{\partial t_{j-1}} = \lim_{\Delta t \to 0} \frac{\boldsymbol{y}(t_j^- - \Delta t) - \boldsymbol{y}(t_j^-)}{\Delta t} = -\dot{\boldsymbol{y}}(t_j^-) \tag{5.104}$$

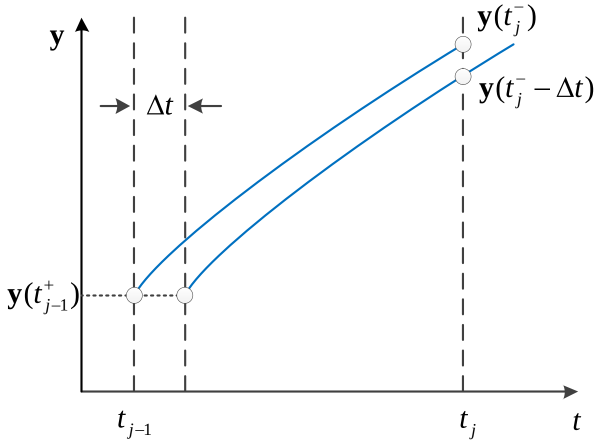

Figure 5.3: *Analysis of the derivative of* $\boldsymbol{y}(t_j^-)$ *w.r.t.* t_{j-1}.

The derivative of $\boldsymbol{y}^+_j$ w.r.t. t_{j-1} is

$$\frac{\partial \boldsymbol{y}^+_j}{\partial t_{j-1}} = \frac{\partial \boldsymbol{y}^+_j}{\partial \boldsymbol{y}^-_j} \frac{\partial \boldsymbol{y}^-_j}{\partial t_{j-1}} = -\widehat{\boldsymbol{y}}_{t,j} \tag{5.105}$$

where the term $\check{\boldsymbol{y}}_{t,j}$ is not involved since t_j is unaltered. Applying the chain rule, the derivative of $\boldsymbol{y}_j^{\pm}$ w.r.t. t_{j-q}, $q \geqslant 2$ is

$$\frac{\mathrm{d}\boldsymbol{y}_j^{\pm}}{\mathrm{d}t_{j-q}} = \frac{\partial \boldsymbol{y}_j^{\pm}}{\partial \boldsymbol{y}_{j-1}^{+}} \frac{\partial \boldsymbol{y}_{j-1}^{+}}{\partial \boldsymbol{y}_{j-2}^{+}} \cdots \frac{\partial \boldsymbol{y}_{j-q+1}^{+}}{\partial \boldsymbol{y}_{j-q}^{+}} \frac{\mathrm{d}\boldsymbol{y}_{j-q}^{+}}{\mathrm{d}t_{j-q}} + \frac{\partial \boldsymbol{y}_j^{\pm}}{\partial t_{j-q}} \tag{5.106}$$

where

$$\frac{\partial \boldsymbol{y}_j^{\pm}}{\partial t_{j-q}} = -\frac{\partial \boldsymbol{y}_j^{\pm}}{\partial \boldsymbol{y}_{j-1}^{+}} \frac{\partial \boldsymbol{y}_{j-1}^{+}}{\partial \boldsymbol{y}_{j-2}^{+}} \cdots \frac{\partial \boldsymbol{y}_{j-q+2}^{+}}{\partial \boldsymbol{y}_{j-q+1}^{+}} \widehat{\boldsymbol{y}}_{t,j-q+1} \tag{5.107}$$

Similarly, the derivative of $\mathscr{N}_j$ w.r.t. t_{j-1} is

$$\frac{\partial \mathscr{N}_j}{\partial t_{j-1}} = \frac{\partial \mathscr{N}_j}{\partial \boldsymbol{y}_j^{-}} \frac{\partial \boldsymbol{y}_j^{-}}{\partial t_{j-1}} + \frac{\partial \mathscr{N}_j}{\partial \boldsymbol{y}_j^{+}} \frac{\partial \boldsymbol{y}_j^{+}}{\partial t_{j-1}} = -\widehat{\mathscr{N}_{t,j}} \tag{5.108}$$

Thus

$$\frac{\mathrm{d}\mathscr{N}_j}{\mathrm{d}t_{j-1}} = \frac{\partial \mathscr{N}_j}{\partial \boldsymbol{y}_{j-1}^{+}} \frac{\mathrm{d}\boldsymbol{y}_{j-1}^{+}}{\mathrm{d}t_{j-1}} - \widehat{\mathscr{N}_{t,j}} \tag{5.109}$$

Applying the chain rule, the derivative of $\mathscr{N}_j$ w.r.t. t_{j-q}, $q \geqslant 2$ is

$$\frac{\mathrm{d}\mathscr{N}_j}{\mathrm{d}t_{j-q}} = \frac{\partial \mathscr{N}_j}{\partial \boldsymbol{y}_{j-1}^{+}} \frac{\partial \boldsymbol{y}_{j-1}^{+}}{\partial \boldsymbol{y}_{j-2}^{+}} \cdots \frac{\partial \boldsymbol{y}_{j-q+1}^{+}}{\partial \boldsymbol{y}_{j-q}^{+}} \frac{\mathrm{d}\boldsymbol{y}_{j-q}^{+}}{\mathrm{d}t_{j-q}} + \frac{\partial \mathscr{N}_j}{\partial t_{j-q}} \tag{5.110}$$

where

$$\frac{\partial \mathscr{N}_j}{\partial t_{j-q}} = -\frac{\partial \mathscr{N}_j}{\partial \boldsymbol{y}_{j-1}^{+}} \frac{\partial \boldsymbol{y}_{j-1}^{+}}{\partial \boldsymbol{y}_{j-2}^{+}} \cdots \frac{\partial \boldsymbol{y}_{j-q+2}^{+}}{\partial \boldsymbol{y}_{j-q+1}^{+}} \widehat{\boldsymbol{y}}_{t,j-q+1} \tag{5.111}$$

In order to recursively calculate Eqs. (5.102) and (5.110), B_{j-1} is defined first as follows

$$B_{j-1} = \frac{\partial \mathscr{N}_j}{\partial \boldsymbol{y}_{j-1}^{+}} \tag{5.112}$$

Next, B_l, $l = j-q, \cdots, j-2$ is computed as

$$B_l = B_{l+1} \frac{\partial \boldsymbol{y}_{l+1}^{+}}{\partial \boldsymbol{y}_l^{+}} \tag{5.113}$$

then

$$\frac{\mathrm{d}\mathscr{N}_j}{\mathrm{d}\boldsymbol{\chi}_{j-q}} = B_{j-q} \frac{\mathrm{d}\boldsymbol{y}_{j-q}^{+}}{\mathrm{d}\boldsymbol{\chi}_{j-q}} \tag{5.114}$$

and

$$\frac{\mathrm{d}\mathscr{N}_j}{\mathrm{d}t_{j-q}} = B_{j-q} \frac{\mathrm{d}\boldsymbol{y}_{j-q}^{+}}{\mathrm{d}t_{j-q}} - B_{j-q+1} \widehat{\boldsymbol{y}}_{t,j-q+1} \tag{5.115}$$

The integration flowchart for each segment is extracted from [47]. The process to construct the shooting function along with analytic gradients is shown in Algorithm 1, where the following abbreviations are used to label the transfer types: `MF`: asteroid flyby; `MR`: asteroid rendezvous; `MG`: gravity assist.

Algorithm 1 Shooting functions and their gradients.

Require: Guess solution, w
for $k = 0 : w$ **do**{Loop each segment}
  Integrate Eq. (5.38) using flowchart in [47] from t_k^+ to t_{k+1}^-. Return $\boldsymbol{y}_{k+1}^-$, $\Phi(t_{k+1}^-, t_k^+)$ and $\boldsymbol{\zeta}_{k+1}^-$.
  if $k \leqslant w - 1$ **then**
    $j = k + 1$.
    Compute $\boldsymbol{r}_{T,j}(t_j)$, $\dot{\boldsymbol{r}}_{T,j}(t_j)$, $\ddot{\boldsymbol{r}}_{T,j}(t_j)$, $\boldsymbol{v}_T(t_j)$, $\dot{\boldsymbol{v}}_{T,j}(t_j)$, $\ddot{\boldsymbol{v}}_{T,j}(t_j)$.
    Compute $\boldsymbol{y}_j^+$ based on Section 5.2.2.
    Compute interior-point constraints: `MF`: Eqs. (5.18) and (5.20); `MR`: Eq. (5.19) and (5.20); `MG`: Eqs. (5.25), (5.26), (5.28), (5.29), (5.30) and (5.32).
    Compute partial derivatives of $\boldsymbol{y}_j^+$, `MF` and `MR`: Eqs. (5.55); `MG`: Eqs. (5.67).
    Formulate $\boldsymbol{z}_j^+$ based on Section 5.2.2.
    for $l = j : -1 : 0$ **do**
      if $l = j$ **then**
        Compute derivatives of the constraints at t_j w.r.t. decision variables at t_j, `MF` and `MR`: Eqs. (5.72), (5.77); `MG`: Eqs. (5.80), (5.83), (5.86), (5.90), (5.93), (5.96) (not computing terms related to $\mathrm{d}t_q$.)
      else
        Compute derivatives of the constraints at t_j w.r.t. decision variables at t_l: Eqs. (5.101), (5.102), (5.109) and (5.110).
      end if
    end for
  end if
end for
Compute terminal constraints: (5.4) and (5.13).
Compute differentials in Eq. (5.98).
for $l = w : -1 : 0$ **do**
  Compute derivatives of terminal constraints w.r.t. decision variables at t_l: Eqs. (5.101), (5.102), (5.109) and (5.110).
end for
Compute $\boldsymbol{C}_\lambda$ and Eq. (5.100).

5.3 Numerical Simulations

Three simulation examples for a variety of deep-space transfers are presented. All simulations are implemented under an Intel Core i7-9750H, CPU@2.6 GHz, Windows 10 system with MATLAB R2019a. The code for the integration of Eq. (5.38) is converted to MEX file to speed up simulations. In the following, the physical constants g_0, AU, TU, VU, Sun mass parameter μ_s are reported in Table 2.1. The position and velocity of the planet and asteroid are computed from NASA HORIZON[1]and MPC[2], respectively. The method to generate the initial guess solution for the energy-optimal problem is not discussed since it is outside of the scope of this work. In the following, the energy-optimal solutions are found by trial and errors. MATLAB function `fsolve` is employed to solve the shooting problem. The initial ε step is $\Delta\varepsilon = 0.05$. When the solution for current ε succeeds, a slightly larger $\Delta\varepsilon$ step is awarded, as $\Delta\varepsilon \leftarrow 1.01 \times \Delta\varepsilon$, otherwise half of $\Delta\varepsilon$ step is used, as $\Delta\varepsilon \leftarrow 0.5 \times \Delta\varepsilon$.

5.3.1 Earth-Jupiter Transfer via Mars Gravity Assist

The example of Earth-Jupiter transfer from [44] is reproduced. The task is to find the fuel-optimal trajectory that rendezvouses with Jupiter via Mars gravity assist, with the transfer time $t_f = 2201$ days. The spacecraft parameters, Mars parameters and boundary conditions are given in Table 5.1, where the initial and terminal heliocentric position and velocity are set to coincide with those of the Earth and Jupiter, respectively. The boundary conditions

[1]See `https://ssd.jpl.nasa.gov/planets/approx_pos.html`
[2]See `https://minorplanetcenter.net/`

generated are slightly different from [44], but their impact on the fuel-optimal solution is ignorable.

The unknowns are $[\lambda_0, \boldsymbol{\lambda}_i, \boldsymbol{\chi}_1, \boldsymbol{x}_{d,1}^+, \alpha_1, \kappa_1, t_1] \in \mathbb{R}^{18}$, with $\boldsymbol{\lambda}_i \in \mathbb{R}^7$, $\boldsymbol{\chi}_1 \in \mathbb{R}^4$ and $\boldsymbol{x}_{d,1}^+ \in \mathbb{R}^3$, corresponding to the shooting function in Eq. (5.34). Both energy-optimal and fuel-optimal solutions are summarized in Table 5.2, where the fuel-optimal final mass of the spacecraft is 16027.3 kg. The fuel-optimal trajectory is shown in Fig. 5.4, involving four thrust segments and three coast segments. The corresponding fuel-optimal variations of u, S, m are shown in Fig. 5.5, where accurate bang-bang control profile coincides with [44]. The variations of costates are shown in Fig. 5.6, where the discontinuity of the costate across the gravity-assist time is illustrated. In terms of computational time, the ε continuation using the presented method takes around 2.4 mins, while the ε continuation with the finite difference method inherently imbeded in MATLAB takes around 1.4 hours. The computational efficiency of the former is apparently superior than the later. The computational time is less than [44] ($\simeq$ 3 mins), but the improvement is not apparent, maybe because of the differences in the platform (Microsoft Visual C++ 6.0 in [44]) and the integrator (RK4 in [44]).

Table 5.1: *Parameters for Earth-Jupiter rendezvous via Mars gravity assist.*

Physical constant	Value
I_{sp}, s	6000
$T_{\max}$, N	2.26
Mass Unit, kg	20000.0
Mars mass parameter, km^3/s^2	42828.3
Mars $r_{\min}$, km	3889.9
Mars radius, km	3389.9
Initial time	16-Nov-2021, 00:00:00
Flight time, days	2201.0
Initial position, AU	[0.587638, 0.795476, -3.953062×10^{-5}]
Initial velocity, VU	[-0.820718, 0.590502, -2.934460×10^{-5}]
terminal position, AU	[-5.205108, 1.491385, 0.110274]
terminal velocity, VU	[-0.126219, -0.401428, 4.494423×10^{-3}]

Table 5.2: *Energy-optimal and fuel-optimal solutions for Earth-Jupiter rendezvous via Mars gravity assist.*

Terms	Energy-optimal solution	Fuel-optimal solution
λ_0	0.615841	0.819085
$\boldsymbol{\lambda}_{ri}$	[-0.278574, -0.459643, -0.053818]	[-0.211713, -0.293488, -0.031748]
$\boldsymbol{\lambda}_{vi}$	[0.362598, -0.334005, -0.055783]	[0.279598, -0.208178, -0.085726]
$\boldsymbol{\lambda}_{mi}$	0.176741	0.177985
$\boldsymbol{\chi}_1$	[-0.007492, -0.103902, 0.062598, -0.191078]	[0.026271, -0.058226, 0.077165, -0.161649]
$\boldsymbol{x}_{d,1}^+$, VU	[0.912146, 0.285079, -0.004974]	[0.820778, 0.514477, -0.003464]
α_1	0.017361	0.020703
κ_1	0	0
GA date t_1	19-Feb-2024 14:09:23	19-Mar-2024 04:10:34
GA v_∞, km/s	3.189	3.602
GA altitude, km	500	500
Final mass, kg	15742.7	16027.3

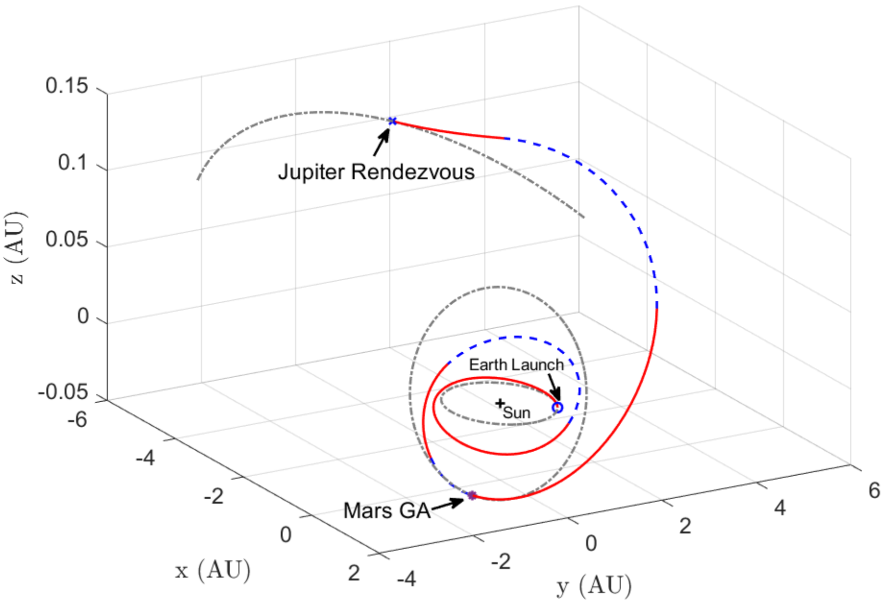

Figure 5.4: *Fuel-optimal trajectory for Earth-Mars-Jupiter transfer. Red solid line: thrust segment; blue dashed line: coast segment. Gray dashed line: orbits of the Earth, Mars and Jupiter.*

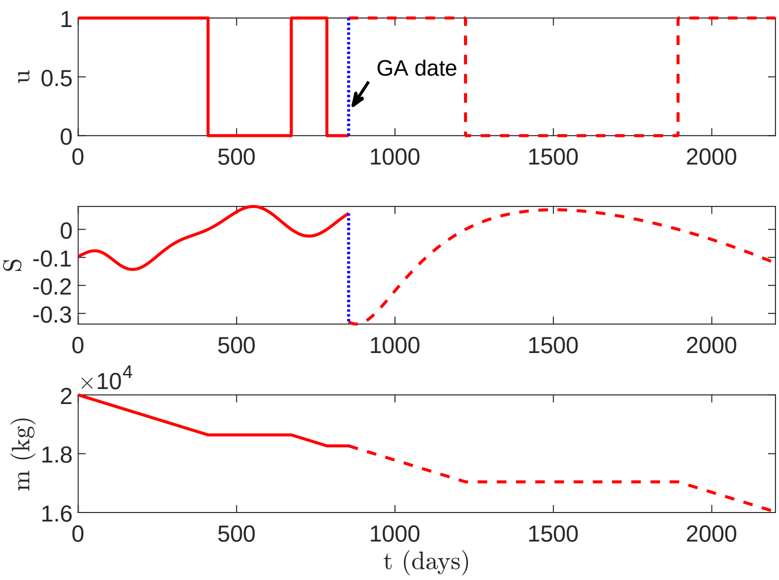

Figure 5.5: *Fuel-optimal variations of u, S, and m for Earth-Mars-Jupiter transfer.*

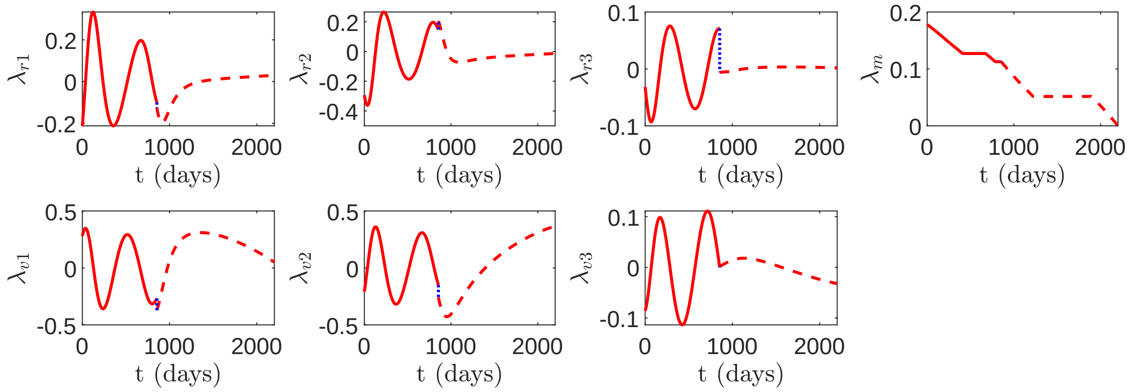

Figure 5.6: *Fuel-optimal variations of costates for Earth-Mars-Jupiter transfer.*

5.3.2 Earth-Earth Transfer via Asteroids Flyby and Rendezvous

The problem of Earth-Earth transfer via asteroid 2014 YD flyby, 2000 SG344 rendzvous and 2010 UE51 flyby is solved. Spacecraft parameters and boundary conditions are shown in Table 5.3, where the initial and terminal heliocentric position and velocity are set to coincide with those of the Earth. The unknowns to solve are $[\lambda_0, \boldsymbol{\lambda}_i, \boldsymbol{\chi}_1, \boldsymbol{\chi}_2, \boldsymbol{\chi}_3, t_1, t_2, t_3] \in \mathbb{R}^{19}$, with $\boldsymbol{\chi}_1 \in \mathbb{R}^3$, $\boldsymbol{\chi}_2 \in \mathbb{R}^6$ and $\boldsymbol{\chi}_3 \in \mathbb{R}^3$, corresponding to the shooting function in Eq. (5.22). Both energy-optimal and fuel-optimal solutions are summarized in Table 5.4, with fuel-optimal final mass of the spacecraft as 535.07 kg. The fuel-optimal trajectory is shown in Fig. 5.7, involving four thrust segments and three coast segments. The fuel-optimal variations of u, S, m are shown in Fig. 5.8. The fuel-optimal variations of costates are shown in Fig. 5.9, where $\boldsymbol{\lambda}_r$ discontinuity appears at flyby and rendezvous time, $\boldsymbol{\lambda}_v$ discontinuity exists only at rendezvous time and λ_m is continuously varied. In terms of computational time, the ε continuation using the presented method takes around 10 mins. On the other hand, the ε continuation with the finite difference method fails to converge since the inaccurate gradients prevent the continuation process.

Table 5.3: *Parameters for Earth-Earth transfer via 2014 YD flyby, 2000 SG344 rendezvous and 2010 UE51 flyby.*

Physical constant	Value
I_{sp}, s	2500
T_{max}, N	0.3
Mass unit MU, kg	1500
Initial time	01-Feb-2023, 00:00:00
terminal time	01-Mar-2026
Initial position, AU	[-0.653263, 0.737562, -3.866946×10^{-5}]
Initial velocity, VU	[-0.764969, -0.666884, 3.496388×10^{-5}]
terminal position, AU	[-0.931249, 0.338086, -2.007635×10^{-5}]
terminal velocity, VU	[-0.357572, -0.943864, 5.604891×10^{-5}]

Table 5.4: *Energy-optimal and Fuel-optimal solutions for Earth-Earth transfer via 2014 YD flyby, 2000 SG344 rendezvous and 2010 UE51 flyby.*

Terms	Energy-optimal solution	Fuel-optimal solution
λ_0	0.211647	0.271881
$\boldsymbol{\lambda}_{ri}$	[-0.202188, 0.206945, 0.028747]	[-0.202201, 0.198694, 0.026776]
$\boldsymbol{\lambda}_{vi}$	[-0.305011, -0.226613, -0.037294]	[-0.298819, -0.215361, -0.032584]
$\boldsymbol{\lambda}_{mi}$	0.282487	0.272639
$\boldsymbol{\chi}_1$	[0.049098, -0.004485, 0.048495]	[0.047540, -0.005221, 0.047607]
$\boldsymbol{\chi}_2$	[-0.129290, -0.356127, 0.002973	[-0.149403, -0.345161, -0.001346
	-0.496797, 0.210566, -0.002674]	-0.482830, 0.229925, -0.006558]
$\boldsymbol{\chi}_3$	[0.360288, 0.275325, -0.000372]	[0.365608, 0.261172, -0.002431]
Flyby date t_1	29-Oct-2023 11:07:23	27-Oct-2023 19:39:44
Rendzvous date t_2	14-Nov-2024 04:07:59	11-Nov-2024 01:36:59
Flyby date t_3	30-May-2025 19:29:21	28-May-2025 16:20:37
Final mass, kg	509.72	535.07

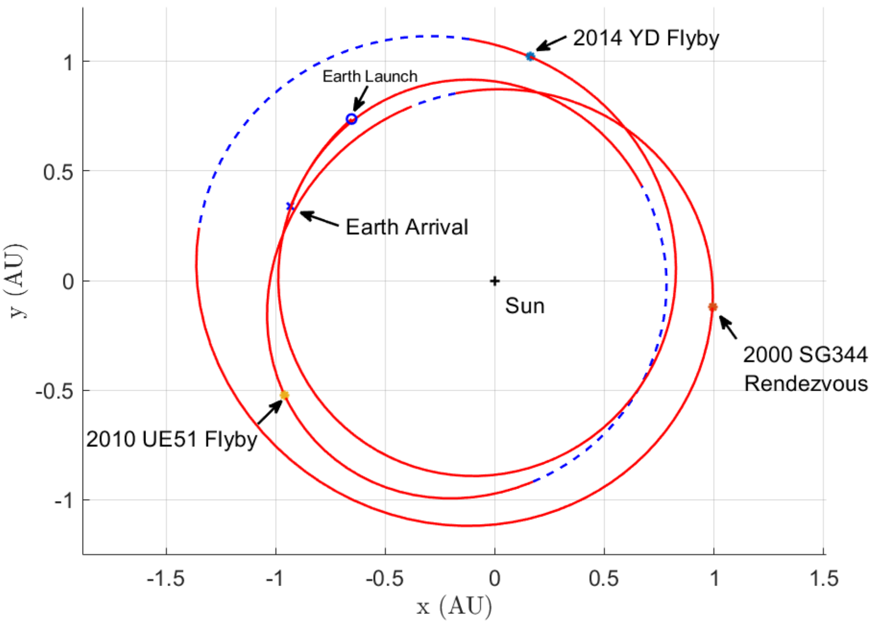

Figure 5.7: *Fuel-optimal trajectory for Earth-Earth transfer via 2014 YD flyby, 2000 SG344 rendezvous and 2010 UE51 flyby.*

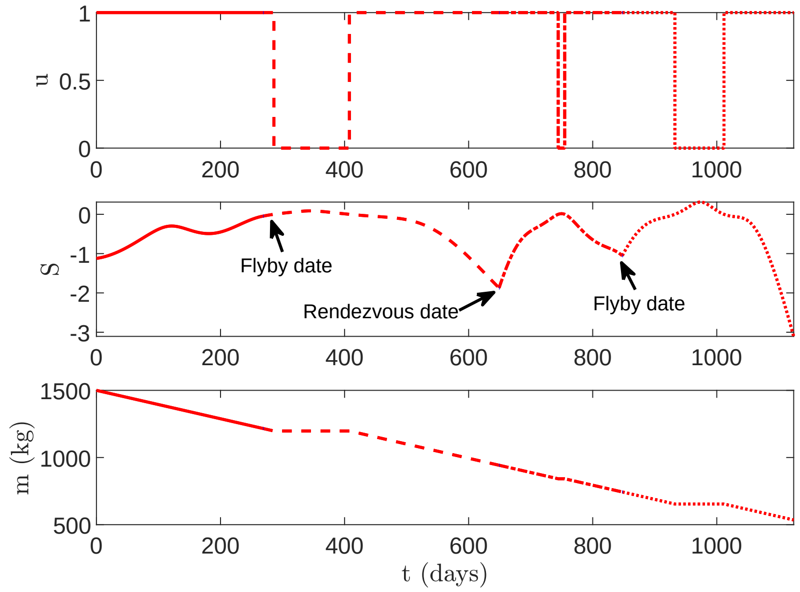

Figure 5.8: *Fuel-optimal variations of u, S and m for Earth-Earth transfer via 2014 YD flyby, 2000 SG344 rendezvous and 2010 UE51 flyby.*

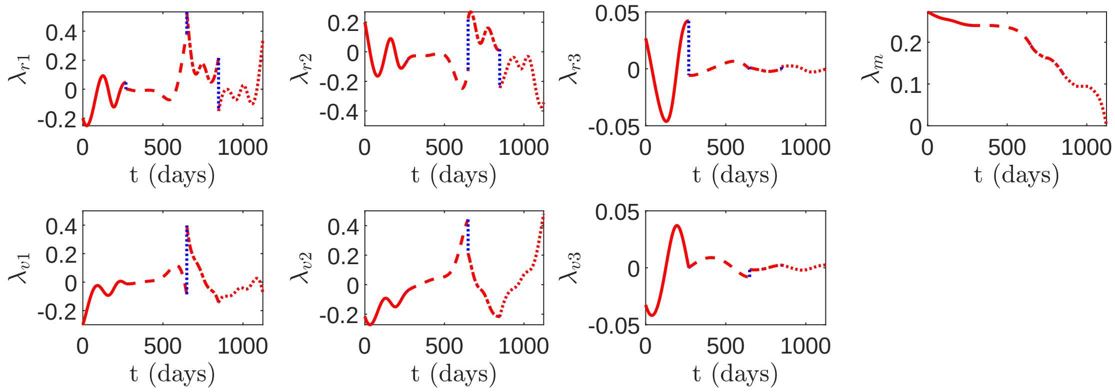

Figure 5.9: *Fuel-optimal variations of costates for Earth-Earth transfer via 2014 YD flyby, 2000 SG344 rendezvous and 2010 UE51 flyby.*

5.3.3 Earth-Mars Transfer via Venus Gravity Assist and 2014 YD Flyby

The problem of Earth-Mars rendezvous via Venus gravity assist and asteroid 2014 YD flyby, consisting of both two types of intermediate events, is solved. Spacecraft parameters, Venus parameters and boundary conditions are shown in Table 5.5, where the initial and terminal heliocentric position and velocity are set to coincide with those of the Earth and Mars, respectively. The unknowns to solve are $[\lambda_0, \boldsymbol{\lambda}_i, \boldsymbol{\chi}_1, \kappa_1, \alpha_1, \boldsymbol{x}_{d,1}^{+}, t_1, \boldsymbol{\chi}_2, t_2] \in \mathbb{R}^{22}$, with $\boldsymbol{\chi}_1 \in \mathbb{R}^4$, $\boldsymbol{x}_{d,1}^{+} \in \mathbb{R}^3$ and $\boldsymbol{\chi}_2 \in \mathbb{R}^3$, corresponding to the shooting function as Eq. (5.35). Both energy-optimal and fuel-optimal solutions are summarized in Table 5.6, with fuel-optimal final mass of the spacecraft as 153.59 kg. The fuel-optimal trajectory is shown in Fig. 5.10, consisting of three thrust segments and two coast segments. The fuel-optimal variations of u, S and m are shown in Fig. 5.11. The fuel-optimal variations of costates are shown in Fig. 5.12, where $\boldsymbol{\lambda}_r$ discontinuity exists at both gravity-assist and flyby moment, $\boldsymbol{\lambda}_v$ discontinuity exists only at gravity-assist moment and λ_m is continuously varied. In terms of computational time, the ε continuation using the presented method takes around 5.3 mins. On the other hand, the ε continuation with the finite difference method takes around 3.2 hours.

Table 5.5: *Parameters for Earth-Mars transfer via Venus gravity assist and 2014 YD flyby.*

Physical constant	Value
$I_{\rm sp}$, s	2300
$T_{\max}$, N	0.75
Initial mass, kg	1300
Venus mass parameter, km^3/s^2	324858.6
Venus $r_{\min}$, km	35000
Venus radius, km	6051.8
Initial time	13-Apr-2015, 00:00:00
terminal time	01-Aug-2016, 00:00:00
Initial position, AU	[-0.925875, -0.384412, 1.337409×10^{-5}]
Initial velocity, VU	[0.367225, -0.927443, 3.226668×10^{-5}]
terminal position, AU	[0.268192, -1.408461, -0.036094]
terminal velocity, VU	[0.829838, 0.222071, -0.015714]

Table 5.6: *Energy-optimal and fuel-optimal solutions for Earth-Mars rendezvous via Venus gravity assist and 2014 YD flyby.*

Terms	Energy-optimal solution	Fuel-optimal solution
λ_0	0.361074	0.521907
$\boldsymbol{\lambda}_{ri}$	[0.178198, 0.166881, -0.032364]	[0.164820, 0.147779, -0.022443]
$\boldsymbol{\lambda}_{vi}$	[0.233904, -0.000741, 0.009953]	[0.202269, 0.009468, 0.007458]
$\boldsymbol{\lambda}_{mi}$	0.573123	0.548787
$\boldsymbol{\chi}_1$	[0.527044, 0.137126, 0.013999, -0.055746]	[0.473332, 0.107366, 0.005633, -0.040304]
κ_1	0.011789	0.010211
α_1	0	0
$\boldsymbol{x}_{d,1}^{+}$	[-0.160377, 1.344821, 0.009991]	[-0.126897, 1.349805, 0.007997]
$\boldsymbol{\chi}_2$	[-0.303371, -0.183195, 0.008816]	[-0.275167, -0.150929, 0.007256]
GA date t_1	12-Sep-2015 10:23:07	11-Sep-2015 16:55:04
GA v_∞, km/s	5.479	5.523
GA altitude, km	28948.2	28948.2
Flyby date t_2	28-Apr-2016 06:17:04	19-Apr-2016 16:38:07
Final mass, kg	126.98	153.59

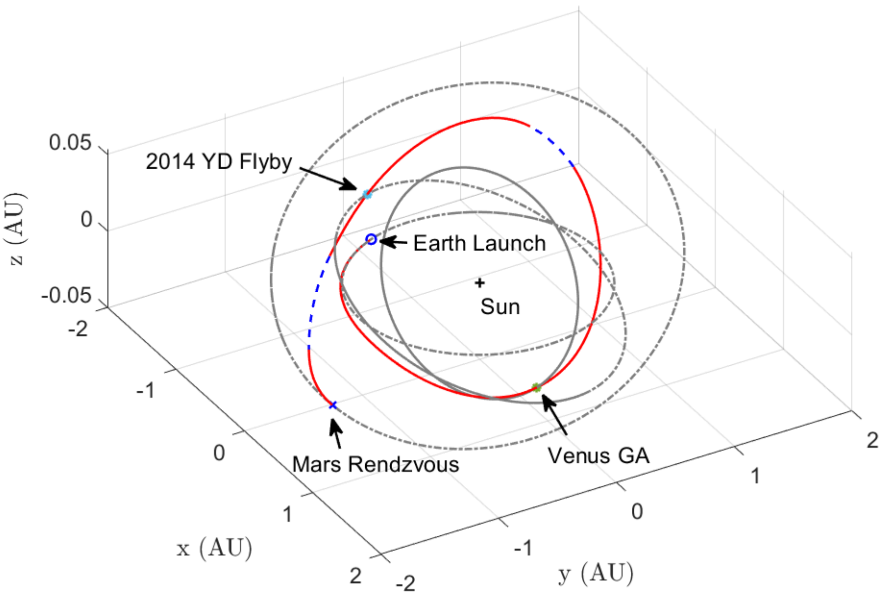

Figure 5.10: *Fuel-optimal trajectory for Earth-Mars rendezvous via Venus gravity assist and 2014 YD flyby. Red line: thrust segments; Blue dot line: coast segments; Gray dashed line: orbits of the Earth, Venus, asteroid 2014 YD and Mars.*

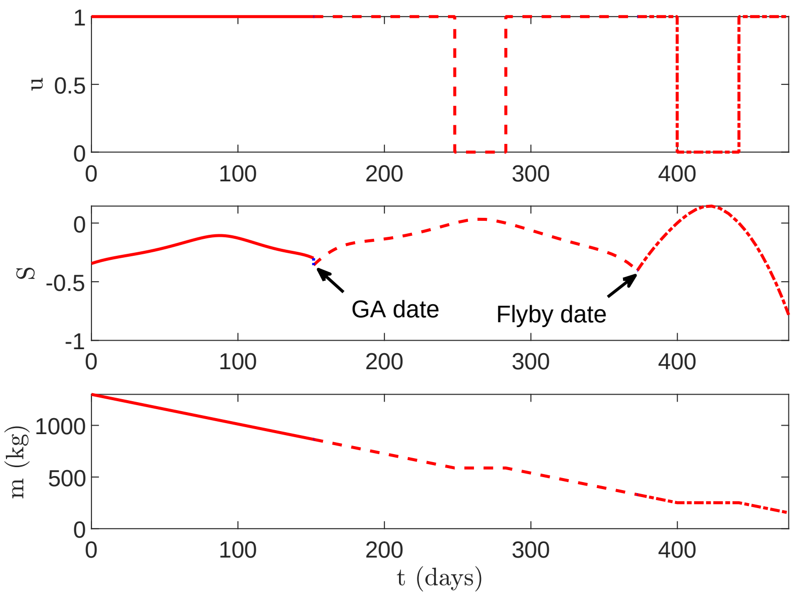

Figure 5.11: *Fuel-optimal variations of u, S and m for Earth-Mars rendezvous via Venus gravity assist and 2014 YD flyby.*

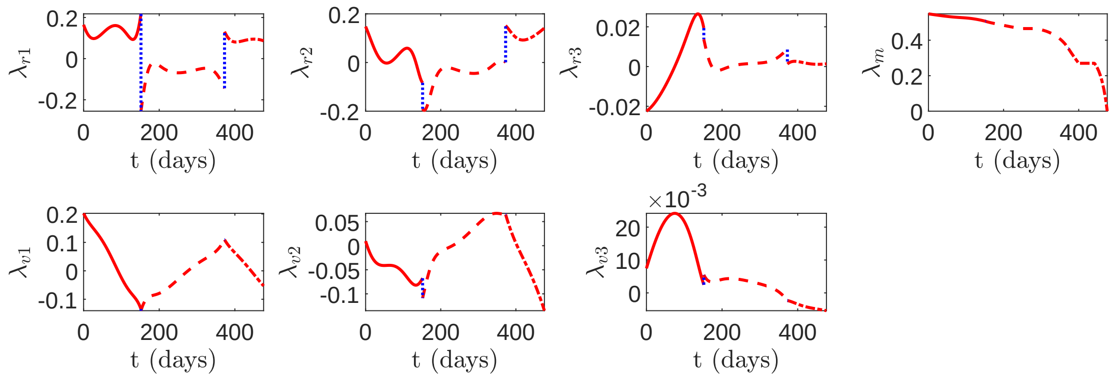

Figure 5.12: *Fuel-optimal variations of costates for Earth-Mars rendezvous via Venus gravity assist and 2014 YD flyby.*

5.4 Summary

Indirect optimization for deep-space transfers involving intermediate flyby and rendezvous and gravity-assist events are investigated. The NOCPs with explicit time-dependent multi-dimensional interior-point constraints are established. The procedure to derive and calculate the analytic gradients is depicted. The main feature of our method is the capability to offer the desired fuel-optimal bang-bang solutions and their gradients. Numerical experiments show that the presented method enables to improve effectively the solver execution speed and enhance the optimizer robustness compared to the finite difference method.

CHAPTER 6

THRUST CONTINUATION OF TIME-OPTIMAL EARTH-ORBIT TRANSFERS

The low level of the thrust usually culminates in the optimal planetocentric transfer encompassing many revolutions before reaching the desired orbit. The corresponding NOCP is difficult to solve directly since the sensitivity of the problem to the initial guess solution amplifies as the number of revolutions grows [103]. Continuation is an effective method in trajectory optimization to expand the convergence domain. A continuation scheme is always specifically designed to improve the algorithmic robustness. A natural idea is to employ thrust continuation which starts from the time-optimal solution with high thrust level and few revolutions, and gradually reduces the thrust to the desired level. This chapter studies the indirect optimization of the low-thrust, time-optimal Earth-orbit transfers toward a general orbit specified by a subset of orbital elements. The main difficulty is the failure of thrust continuation when the thrust is reduced down to a certain level. This chapter presents a simple method that allows thrust continuation by connecting local solutions with different revolutions.

6.1 Problem Statement

The time-optimal Earth-orbit transfer is studied, with the terminal orbit specified by a given subset of orbital elements (orbit transfer problem), instead of terminal fixed points (it is not a rendezvous problem). The equations of motion of the spacecraft subject to the gravitational attraction of the Earth under Cartesian coordinate are employed based on the following facts:

1. Classical orbital elements are not used to represent the state due to the singularity of their dynamics at zero inclination and zero eccentricity [104].

2. The analytical reduced transversality conditions introduced in [85] allow tackling different kinds of soft terminal orbital conditions without solving the corresponding multipliers.
3. Even though MEE shows a good numerical robustness in planetocentric transfers, the terminal multipliers are required to solve when the final orbit is specified by a subset of orbital elements (except fixed final orbit specified by a, e, i, Ω and w), unless the corresponding reduced conditions are derived analytically.

The equations are the same as Eq. (2.1), where both $T_{\max}$ and I_{sp} are assumed constant. The performance index of the time-optimal problem and the Hamiltonian function are given by Eqs. (2.21) and (2.22). By virtue of the PMP [26], the optimal thrust direction $\boldsymbol{\alpha}^*$ is in Eq. (2.11), while the optimal thrust throttle factor u^* is

$$u^* = \begin{cases} 1 & S < 0 \\ 0 & S > 0 \end{cases} \tag{6.1}$$

where the switching function S is Eq. (2.24).

Once $\boldsymbol{\alpha}^*$ and u^* are determined, the motion of the spacecraft is determined by integrating the following equations

$$\dot{\boldsymbol{y}} = \boldsymbol{F}(\boldsymbol{y}) \Rightarrow \begin{cases} \dot{\boldsymbol{r}} = \boldsymbol{v} \\ \dot{\boldsymbol{v}} = -\dfrac{\mu}{r^3}\boldsymbol{r} - u\dfrac{T_{\max}}{m}\dfrac{\boldsymbol{\lambda}_v}{\lambda_v} \\ \dot{m} = -u\dfrac{T_{\max}}{c} \\ \dot{\boldsymbol{\lambda}}_r = -\dfrac{3\mu\boldsymbol{\lambda}_v^\top \boldsymbol{r}}{r^5}\boldsymbol{r} + \dfrac{\mu}{r^3}\boldsymbol{\lambda}_v \\ \dot{\boldsymbol{\lambda}}_v = -\boldsymbol{\lambda}_r \\ \dot{\lambda}_m = -u\lambda_v\dfrac{T_{\max}}{m^2} \end{cases} \tag{6.2}$$

where $\boldsymbol{y} = [\boldsymbol{x}, \boldsymbol{\lambda}]$ is a 14-dimensional canonical variable.

Since the terminal mass is free and the augmented terminal cost does not explicitly depend on the mass, there exists

$$\lambda_m(t_f) = 0 \tag{6.3}$$

Since $\dot{\lambda}_m \geqslant 0$ and $\lambda_m(t_f) = 0$, thus $\lambda_m(t) \geqslant 0$, which implies $S < 0$ and therefore $u^* = 1$ for the whole trajectory. The initial condition is

$$\boldsymbol{x}(t_i) = \boldsymbol{x}_i \tag{6.4}$$

where t_i is the initial time.

When a subset of orbital elements, e.g., a, e and i, are specified, by applying the transformation between Cartesian coordinates and orbital elements, the terminal conditions are labeled as

$$\boldsymbol{\phi}(\boldsymbol{r}_f, \boldsymbol{v}_f) = \boldsymbol{0} \in \mathbb{R}^k, \quad k \leqslant 6 \tag{6.5}$$

The reduced transversality conditions [85] allows to solve the problem by shooting the terminal conditions (including Eq. (6.3))

$$\boldsymbol{\Phi}(\boldsymbol{y}_f) = \boldsymbol{0} \in \mathbb{R}^7 \tag{6.6}$$

without solving explicitly terminal Lagrange multipliers. Additionally, the transversality condition at terminal time t_f is

$$H(\boldsymbol{y}_f) = 0 \tag{6.7}$$

Remark 6.1. *Let $\boldsymbol{\varphi}(t, t_i, [\boldsymbol{\lambda}_i, \boldsymbol{x}_i], T_{\max})$ be the solution of Eq.* (6.2) *integrated from t_i to a general time t with the given $T_{\max}$, the time-optimal problem is to find the optimal $\boldsymbol{\xi}^* = [\boldsymbol{\lambda}_i^*, t_f^*] \in \mathbb{R}^8$ such that*

$$\boldsymbol{\varphi}(t_f^*, t_i, [\boldsymbol{\lambda}_i^*, \boldsymbol{x}_i], T_{\max}) \text{ satisfies } \begin{cases} \boldsymbol{\Phi}(\boldsymbol{y}_f) = \boldsymbol{0} \\ H(\boldsymbol{y}_f) = 0 \end{cases} \tag{6.8}$$

Proper guessed initial costates and transfer time are required to determine the time-optimal solution. However, the major difficulty is the sensitivity of the solution to the a priori unknown initial costate, which further amplifies when the trajectory is made of many revolutions [103].

6.2 Methodology

6.2.1 Thrust Continuation

The idea of thrust continuation is to solve the easier time-optimal problem with high thrust level and few revolutions first. Then the solution with low thrust level is approached by gradually reducing the $T_{\max}$ value. Suppose the time-optimal solution $\boldsymbol{\lambda}_i^*$ and t_f^* with the given $T_{\max}$ value is found, for the small thrust variation $T_{\max} + \mathrm{d}T_{\max}$, there satisfies

$$\begin{cases} \boldsymbol{\Phi}(\boldsymbol{y}_f(\boldsymbol{\lambda}_i^* + \mathrm{d}\boldsymbol{\lambda}_i, T_{\max} + \mathrm{d}T_{\max}, t_f^* + \mathrm{d}t_f)) = \boldsymbol{0} \\ H(\boldsymbol{y}_f(\boldsymbol{\lambda}_i^* + \mathrm{d}\boldsymbol{\lambda}_i, T_{\max} + \mathrm{d}T_{\max}, t_f^* + \mathrm{d}t_f), T_{\max} + \mathrm{d}T_{\max}) = 0 \end{cases} \tag{6.9}$$

Take the full differential of above equations yields

$$\begin{cases} \mathrm{d}\boldsymbol{\Phi} = \dfrac{\partial \boldsymbol{\Phi}}{\partial \boldsymbol{y}_f}\dfrac{\partial \boldsymbol{y}_f}{\partial \boldsymbol{\lambda}_i^*}\mathrm{d}\boldsymbol{\lambda}_i^* + \dfrac{\partial \boldsymbol{\Phi}}{\partial \boldsymbol{y}_f}\dot{\boldsymbol{y}}_f \mathrm{d}t_f^* + \dfrac{\partial \boldsymbol{\Phi}}{\partial \boldsymbol{y}_f}\dfrac{\partial \boldsymbol{y}_f}{\partial T_{\max}}\mathrm{d}T_{\max} = \boldsymbol{0} \\ \mathrm{d}H = \dfrac{\partial H}{\partial \boldsymbol{y}_f}\dfrac{\partial \boldsymbol{y}_f}{\partial \boldsymbol{\lambda}_i^*}\mathrm{d}\boldsymbol{\lambda}_i^* + \dfrac{\partial H}{\partial \boldsymbol{y}_f}\dot{\boldsymbol{y}}_f \mathrm{d}t_f^* + \left(\dfrac{\partial H}{\partial \boldsymbol{y}_f}\dfrac{\partial \boldsymbol{y}_f}{\partial T_{\max}} + \dfrac{\partial H}{\partial T_{\max}}\right)\mathrm{d}T_{\max} = 0 \end{cases} \tag{6.10}$$

Then we have

$$\begin{bmatrix} \dfrac{\mathrm{d}\boldsymbol{\lambda}_i^*}{\partial T_{\max}} \\ \dfrac{\mathrm{d}t_f^*}{\partial T_{\max}} \end{bmatrix} = -A^{-1}\boldsymbol{b} \tag{6.11}$$

where

$$A = \begin{bmatrix} \dfrac{\partial \boldsymbol{\Phi}}{\partial \boldsymbol{y}_f}\dfrac{\partial \boldsymbol{y}_f}{\partial \boldsymbol{\lambda}_i^*} & \dfrac{\partial \boldsymbol{\Phi}}{\partial \boldsymbol{y}_f}\dot{\boldsymbol{y}}_f \\ \dfrac{\partial H}{\partial \boldsymbol{y}_f}\dfrac{\partial \boldsymbol{y}_f}{\partial \boldsymbol{\lambda}_i^*} & \dfrac{\partial H}{\partial \boldsymbol{y}_f}\dot{\boldsymbol{y}}_f \end{bmatrix}, \quad \boldsymbol{b} = \begin{bmatrix} \dfrac{\partial \boldsymbol{\Phi}}{\partial \boldsymbol{y}_f}\dfrac{\partial \boldsymbol{y}_f}{\partial T_{\max}} \\ \dfrac{\partial H}{\partial \boldsymbol{y}_f}\dfrac{\partial \boldsymbol{y}_f}{\partial T_{\max}} + \dfrac{\partial H}{\partial T_{\max}} \end{bmatrix} \tag{6.12}$$

In the vector $\boldsymbol{b}$,

$$\frac{\partial H}{\partial T_{\max}} = u\,\frac{S}{c} \tag{6.13}$$

and $\partial \boldsymbol{y}_f/\partial T_{\max}$ is computed by integrating the following dynamical equations

$$\frac{\mathrm{d}}{\mathrm{d}t}\frac{\partial \boldsymbol{y}}{\partial T_{\max}} = \frac{\partial \boldsymbol{F}}{\partial \boldsymbol{y}}\frac{\partial \boldsymbol{y}}{\partial T_{\max}} + \frac{\partial \boldsymbol{F}}{\partial T_{\max}} \tag{6.14}$$

with the initial condition $\partial \boldsymbol{y}/\partial T_{\max}(t_i) = \mathbf{0}_{14\times 1}$ and $\partial \boldsymbol{F}/\partial T_{\max} = [\mathbf{0}_{1\times 3}, -u\frac{\boldsymbol{\lambda}_v^\top}{m\lambda_v}, -\frac{u}{c}, \mathbf{0}_{1\times 6}, -u\frac{\lambda_v}{m^2}]^\top$.

Generally, the thrust continuation process can proceed if Eq. (6.11) can be solved, i.e., A is regular. However, it is observed that Eq. (6.11) goes off to infinity at certain $T_{\max}$ value. As shown in Fig 6.1, it is possible that 1) the costate remains finite, and the corresponding termination point is called limit point [65]; 2) the costate goes to infinity as well. For both cases, thrust continuation fails to proceed by gradually reducing $T_{\max}$, since there are no solutions corresponding to the reduced $T_{\max}$ in the neighborhood of current solution point. Simultaneously, the shooting method is a local method which searches the solution nearby the guessed solution.

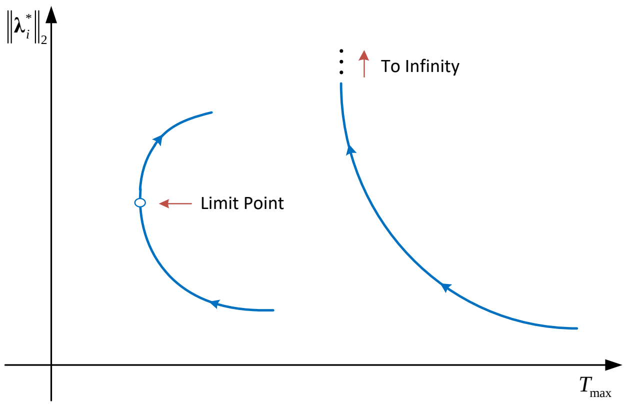

Figure 6.1: *Failures of thrust continuation.*

6.2.2 Manifold Connection

Fixed-point terminal conditions This work is inspired by the thrust continuation for the time-optimal low-thrust problem with fixed-point terminal conditions designed in [105], which is reported here first. The method is based on the fact that the time-optimal problem has multiple local solutions with different spirals. In Fig. 6.2, suppose that the solution manifold α is currently traced, until the continuation becomes difficult to proceed at the solution $\boldsymbol{\xi}^*_{\alpha,f}$. The idea in [105] is to switch to and trace another manifold β. The manifold connection is achieved by searching the solution $\boldsymbol{\xi}^*_{\beta,0}$ which is another local solution with the same $T_{\max}$ as $\boldsymbol{\xi}^*_{\alpha,f}$, but involving more revolutions than $\boldsymbol{\xi}^*_{\alpha,f}$. The more revolutions allow the trajectory with smaller thrust to reach the terminal conditions. The thrust continuation enables to proceed by tracing another manifold β starting from the solution $\boldsymbol{\xi}^*_{\beta,0}$. The manifold connection developed is the process to search local solutions with different revolutions for the fixed $T_{\max}$.

Figure 6.3 shows the process to find the solution $\boldsymbol{\xi}^*_{\beta,0}$ involving one more revolution than the solution $\boldsymbol{\xi}^*_{\alpha,f}$. The auxiliary orbit that frees the true anomaly of the terminal point is identified first. Starting from solution $\boldsymbol{\xi}^*_{\alpha,f}$, a succession of auxiliary problems, with the terminal points moving forward on the auxiliary orbit by gradually increasing the true anomaly, are solved. The solution $\boldsymbol{\xi}^*_{\beta,0}$ is found once the true anomaly increases by 2π. It can be summarized that the thrust continuation for fixed-point terminal conditions is effective since it satisfies the following three criteria:

1. the switch from the solutions $\boldsymbol{\xi}^*_{\alpha,f}$ to the solution of the auxiliary problem is smooth;
2. the criterion when the solution $\boldsymbol{\xi}^*_{\beta,0}$ is reached is clear;
3. the switch from the solutions of the auxiliary problem to the solution $\boldsymbol{\xi}^*_{\beta,0}$ is smooth.

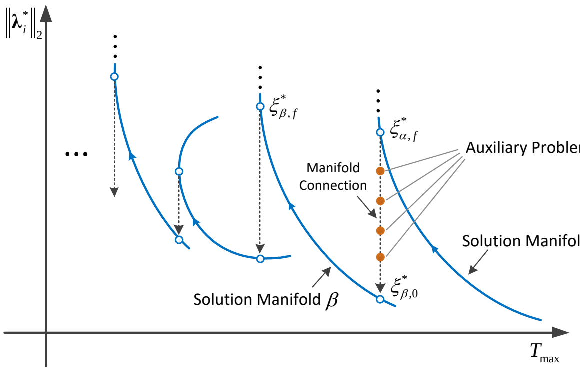

Figure 6.2: *Manifold connection.*

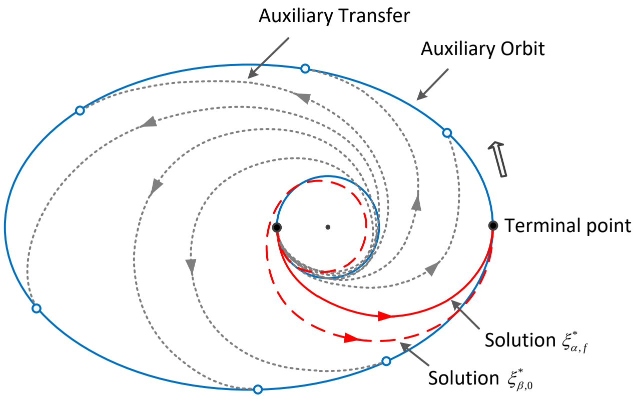

Figure 6.3: *Solution connection for fixed-point terminal conditions.*

Soft terminal conditions When soft terminal conditions are taken into consideration, the key is to establish the auxiliary problem that satisfies criteria mentioned above. Suppose that the terminal orbit are specified by orbital elements a, e and i, as shown in Fig. 6.4, we still hope to connect solutions with different revolutions through solving a series of auxiliary problems by gradually increasing ζ. The solution corresponding to the increased ζ indicates that it involves more revolutions. The auxiliary orbit may be not unique anymore. One may define the auxiliary problem that targets the terminal orbit specified by a, e, i and increased true anomaly θ, where $\zeta := \theta$. Unfortunately, numerical practice reveals that the transform from the solution $\boldsymbol{\xi}^*_{\alpha,f}$ to the solution of this auxiliary problem is not smooth, due to the differences in reduced transversality conditions [85] for the orbits specified by a, e, i and by a, e, i, θ. The auxiliary problem will be established by using the augmented dynamics elaborated below.

6.2.3 Augmented Dynamics

The variable ζ which represents the angle that trajectory has swept through is used, with the following dynamics

$$\dot{\zeta} = \frac{h}{r^2} \tag{6.15}$$

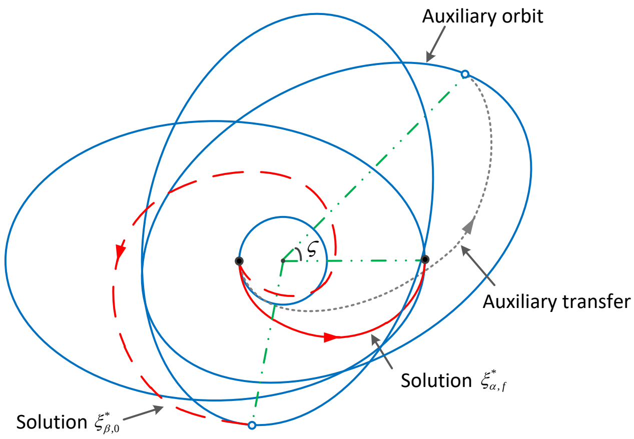

Figure 6.4: *Solution connection for soft terminal conditions.*

where $\dot{\zeta} > 0$ regardless of the direction of the thrust, h is the magnitude of the instantaneous momentum $\boldsymbol{h} = \boldsymbol{r} \times \boldsymbol{v}$. The ture anomaly θ is not employed to define ζ because θ is singular when the eccentricity $e = 0$. Also, the value of true anomaly is affected by the value of Ω and w which are varied during the transfer. Additionally, the dynamics of ζ is simpler since the control variables are not involved. The number of revolutions of the trajectory is defined as

$$N_{\text{rev}} = \frac{\zeta_f - \zeta_i}{2\pi} \tag{6.16}$$

where ζ_i and ζ_f are the values of ζ at initial and terminal time.

The equations of augmented dynamics are

$$\frac{\mathrm{d}\hat{\boldsymbol{x}}}{\mathrm{d}t} = \boldsymbol{f}(\hat{\boldsymbol{x}}, u, \boldsymbol{\alpha}) \Rightarrow \begin{cases} \dot{\boldsymbol{r}} = \boldsymbol{v} \\ \dot{\boldsymbol{v}} = -\dfrac{\mu}{r^3}\boldsymbol{r} + u\dfrac{T_{\max}}{m}\boldsymbol{\alpha} \\ \dot{m} = -u\dfrac{T_{\max}}{I_{\text{sp}}\, g_0} \\ \dot{\zeta} = \dfrac{h}{r^2} \end{cases} \tag{6.17}$$

with the initial value $\hat{\boldsymbol{x}}_i = [\boldsymbol{x}_i, 0]$.

The corresponding augmented Hamiltonian function is

$$\hat{H} = 1 + \boldsymbol{\lambda}_r^\top \boldsymbol{v} + \boldsymbol{\lambda}_v^\top \left(-\frac{\mu}{r^3}\boldsymbol{r} + u\frac{T_{\max}}{m}\boldsymbol{\alpha} \right) - \lambda_m u \frac{T_{\max}}{I_{\text{sp}} g_0} + \lambda_\zeta \frac{h}{r^2} \tag{6.18}$$

The $\boldsymbol{\alpha}^*$ and u^* are the same as Eqs. (2.11) and (6.1). The motion of the spacecraft is determined by integrating the following augmented state-costate dynamics

$$\frac{\mathrm{d}\hat{\boldsymbol{y}}}{\mathrm{d}t} = \hat{\boldsymbol{F}}(\hat{\boldsymbol{y}}) \Rightarrow \begin{cases} \dot{\boldsymbol{r}} = \boldsymbol{v} \\ \dot{\boldsymbol{v}} = -\dfrac{\mu}{r^3}\boldsymbol{r} - u\dfrac{T_{\max}}{m}\dfrac{\boldsymbol{\lambda}_v}{\lambda_v} \\ \dot{m} = -u\dfrac{T_{\max}}{I_{\text{sp}}\, g_0} \\ \dot{\zeta} = \dfrac{h}{r^2} \\ \dot{\boldsymbol{\lambda}}_r = -\dfrac{3\mu\boldsymbol{\lambda}_v^\top\boldsymbol{r}}{r^5}\boldsymbol{r} + \dfrac{\mu}{r^3}\boldsymbol{\lambda}_v + \lambda_\zeta\left(\dfrac{\partial h/r^2}{\partial \boldsymbol{r}}\right)^\top \\ \dot{\boldsymbol{\lambda}}_v = -\boldsymbol{\lambda}_r + \lambda_\zeta\left(\dfrac{\partial h/r^2}{\partial \boldsymbol{v}}\right)^\top \\ \dot{\lambda}_m = -u\lambda_v\dfrac{T_{\max}}{m^2} \\ \dot{\lambda}_\zeta = 0 \end{cases} \tag{6.19}$$

where $\hat{\boldsymbol{y}} = [\hat{\boldsymbol{x}}, \hat{\boldsymbol{\lambda}}]$ and

$$\left(\frac{\partial h/r^2}{\partial \boldsymbol{r}}\right)^\top = -2\frac{h}{r^3}\frac{\boldsymbol{r}}{r} + \frac{\boldsymbol{h}\times\boldsymbol{v}}{r^2}, \quad \left(\frac{\partial h/r^2}{\partial \boldsymbol{v}}\right)^\top = \frac{\boldsymbol{r}\times\boldsymbol{h}}{r^2} \tag{6.20}$$

In Eq. (6.19), $\dot{\lambda}_\zeta = 0$ implies that λ_ζ is constant during the flight. Moreover, the solution of the augmented problem is equivalent to the solution of the original problem if

$$\lambda_\zeta(t_f) = 0 \tag{6.21}$$

Let $\hat{\boldsymbol{\varphi}}(t, t_i, [\hat{\boldsymbol{\lambda}}_i, \hat{\boldsymbol{x}}_i])$ be the solution integrating Eq. (6.19) from t_i to a general time t, the following two problems are defined:

Definition 6.1 (Problem $\mathtt{P}_0$)**.** *Find the optimal* $\hat{\boldsymbol{\lambda}}_i^*$ *and* t_f^* *such that*

$$\hat{\boldsymbol{\varphi}}(t_f^*, t_i, [\hat{\boldsymbol{\lambda}}_i^*, \hat{\boldsymbol{x}}_i]) \text{ satisfies } \begin{cases} \boldsymbol{\Phi}(\hat{\boldsymbol{y}}_f) = \boldsymbol{0} \\ \hat{H}(\hat{\boldsymbol{y}}_f) = 0 \\ \lambda_\zeta(t_f) = 0 \end{cases} \tag{6.22}$$

Definition 6.2 (Problem $\mathtt{P}_1$)**.** *Find the optimal* $\hat{\boldsymbol{\lambda}}_i^*$ *and* t_f^* *such that*

$$\hat{\boldsymbol{\varphi}}(t_f^*, t_i, [\hat{\boldsymbol{\lambda}}_i^*, \hat{\boldsymbol{x}}_i]) \text{ satisfies } \begin{cases} \boldsymbol{\Phi}(\hat{\boldsymbol{y}}_f) = \boldsymbol{0} \\ \hat{H}(\hat{\boldsymbol{y}}_f) = 0 \\ \zeta(t_f) = \hat{\zeta} \end{cases} \tag{6.23}$$

where $\hat{\zeta}$ *is a prescribed value.*

Here, Problem $\mathtt{P}_0$ is equivalent to the original problem as stated in Remark 6.1, while Problem $\mathtt{P}_1$ is the auxiliary problem. The solution to Problem $\mathtt{P}_0$ is equivalent to the solution to Problem $\mathtt{P}_1$ if $\hat{\zeta}$ is set to the ζ_f calculated from the solution to $\mathtt{P}_0$. The solution to Problem

$\mathtt{P}_1$ is equivalent to the solution to Problem $\mathtt{P}_0$ if $\lambda_\zeta(t_f) = 0$ is additionally satisfied. Thus, the solution switching between $\mathtt{P}_0$ and $\mathtt{P}_1$ is smooth. Besides, Problem $\mathtt{P}_0$ offers a simple criteria to switch back from $\mathtt{P}_1$ to $\mathtt{P}_0$, i.e., $\lambda_\zeta(t_f) = 0$. Thus, the definition of the auxiliary problem elegantly satisfies the three criteria.

The indirect method featuring analytic gradients is employed to solve the time-optimal problem. The gradients are computed through the state transition matrix (STM) and the chain rule, with the STM subject to

$$\dot{\Phi}(t_i, t) = D_y \hat{\boldsymbol{F}} \Phi(t_i, t) \quad \Phi(t_i, t_i) = \boldsymbol{I}_{16\times 16} \tag{6.24}$$

where $D_{\boldsymbol{y}} \hat{\boldsymbol{F}}$ is the jacobian matrix of $\hat{\boldsymbol{F}}(\hat{\boldsymbol{y}})$ w.r.t. $\hat{\boldsymbol{y}}$. Let $\boldsymbol{z} = [\hat{\boldsymbol{y}}, \mathrm{vec}(\Phi)]$ be a vector containing $\hat{\boldsymbol{y}}$ and columns of Φ. There exists

$$\dot{\boldsymbol{z}} = \boldsymbol{G}(\boldsymbol{z}) \Rightarrow \begin{pmatrix} \dot{\hat{\boldsymbol{y}}} \\ \mathrm{vec}(\dot{\Phi}) \end{pmatrix} = \begin{pmatrix} \hat{\boldsymbol{F}}(\hat{\boldsymbol{y}}) \\ \mathrm{vec}(D_{\boldsymbol{y}} \hat{\boldsymbol{F}} \Phi) \end{pmatrix} \tag{6.25}$$

Moreover, Eq. (6.14) is integrated along with Eq. (6.25), using variable–step seventh/eighth Runge–Kutta integration scheme.

It is observed that the frequency to execute the manifold connection increases rapidly as the $T_{\max}$ value decreases. More executions of the manifold connection indicate more computational load. In order to reduce the frequency of solution manifold connection, minimum $\zeta_{\min}$ has to be satisfied before checking whether a new solutions is found. In the simulation part, $\zeta_{\min}$ is set according to numerical experiences as

$$\zeta_{\min} = 2\pi \times \left(\mathrm{Ceil}\left(\frac{\zeta_{\alpha,f}}{2\pi} \right) + \mathrm{Ceil}(4 \times (|\log \frac{T_{\max}}{m_0}| - 2)) \right) \tag{6.26}$$

where $\zeta_{\alpha,f}$ is the terminal ζ_f for the solution $\boldsymbol{\xi}^*_{\alpha,f}$ and 'Ceil' is the round up operator.

6.3 Numerical Simulations

In the following, orbital elements of the terminal orbit is specified by a, e and i, while freeing Ω, ω and θ. The corresponding terminal conditions are [85]

$$\boldsymbol{\Phi}(\hat{\boldsymbol{y}}_f) = \begin{cases} \boldsymbol{h}_f^\top \boldsymbol{h}_f - h^2 \\ \frac{1}{2} \boldsymbol{v}_f^\top \boldsymbol{v}_f - \frac{1}{r_f} + \frac{\mu}{2a} \\ \boldsymbol{I}_z^\top \boldsymbol{h}_f - h_f \cos i \\ (\boldsymbol{\lambda}_{rf} \times \boldsymbol{r}_f + \boldsymbol{\lambda}_{vf} \times \boldsymbol{v}_f)^\top \boldsymbol{h}_f \\ (\boldsymbol{\lambda}_{rf} \times \boldsymbol{r}_f + \boldsymbol{\lambda}_{vf} \times \boldsymbol{v}_f)^\top \boldsymbol{I}_z \\ \boldsymbol{\lambda}_{rf}^\top \boldsymbol{v}_f - \frac{\mu}{r_f^3} \boldsymbol{\lambda}_{vf}^\top \boldsymbol{r}_f \\ \lambda_m(t_f) \end{cases} \tag{6.27}$$

where $\boldsymbol{I}_z = [0, 0, 1]^\top$. The physical constants and spacecraft parameters are listed in Table 6.1, where the initial spacecraft mass is equivalent to the mass unit. Orbit transfers from GTO to GEO and from GTO to Elliptic Inclined Geosynchronous Orbits (EIGSO) are simulated to verify the algorithmic effectiveness. The corresponding orbital elements are given in

Table 6.2. It can be seen that the departure orbit GTO is highly eccentric with $e = 0.7$. The semi-major axis of EIGSO is the same as GEO, but eccentricity and inclination are non-zero.

Table 6.1: *Physical constants and spacecraft parameters.*

Physical constant	Value
Mass parameter, μ	398600.4418 km^3/s^2
Gravitational field, g_0	9.80665 m/s^2
Length unit, LU	6378.137 km
Time unit, TU	806.8111 s
Velocity unit, VU	7.9054 km/s
Mass unit, MU	1500 kg
Specific Impulse, I_{sp}	1994.75 s

Table 6.2: *Orbital elements for departure orbit GTO and terminal orbits GEO and EIGSO.*

Orbit	a (km)	e	i (deg)	Ω (deg)	w (deg)	θ (deg)
GTO	26571.43	0.75	7.004	360	0	180
GEO	42165	0	0	free	free	free
EIGSO	42165	0.3	50	free	free	free

6.3.1 GTO to GEO

The simulation of GTO to GEO transfer extracted from [106] is reported. The thrust continuation starts from the time-optimal transfer with $T_{\max} = 60$ N. The corresponding optimal trajectory requires the transfer time $t_f^* = 14.80$ h and involves only 1.05 revolutions; see case A in Table 6.3. The optimal initial costate is

$$\boldsymbol{\lambda}_i^* = [-2.206184, -1.192697, -0.401076, -47.309921, 48.309300, -21.856674, 29.145137]^\top$$

The procedure of thrust continuation by using manifold connections are illustrated in Fig. 6.5, including the variations of the norm of optimal initial costate and the optimal transfer time with respect to the variation of $T_{\max}$. From Fig. 6.5a, it can be seen that the frequency to execute the manifold connection increases as $T_{\max}$ approaches to 0. The manifold connection is triggered mainly in cases when the costate goes off to infinity. Figure 6.5b shows that t_f^* grows exponentially as $T_{\max}$ is reduced. The zoom-in curve of Fig. 6.5a implies that the t_f^* variation is not smooth. The overview of sample solutions for different thrust levels are provided in Table 6.3, including the optimal transfer time, final mass and orbital revolutions. It can be seen that the number of revolutions increases drastically when $T_{\max}$ is reduced. The time-optimal trajectories, corresponding variations of u, S, m, and a, e, i for sample solutions A-D in Fig. 6.5a are shown in Fig. 6.6. It can be seen that as number of revolution increases, the evolution of a, e and i becomes more flat.

Time-optimal solutions obtained in Fig. 6.5a only represent one single local solution for one specific $T_{\max}$. Better solutions maybe be reached through searching local solutions with different revolutions by using the proposed manifold connection method. Figure 6.7 shows the multiple local solutions for $T_{\max} = 12$ N (case B) and $T_{\max} = 3$ N (case C) by applying forward and backward manifold connections. It is interesting to see that the optimal transfer time t_f^* of local solutions does not monotonously vary with respect to N_{rev}. In Fig. 6.7a, the solution B1 is consistent with the time-optimal solution obtained in [106], with the transfer time 70.249 days. A slightly better solution B2 with $N_{\text{rev}} = 3.57$ and $t_f^* = 70.19$ h is found. The solution B2 is the local solution with fewest revolutions and shortest transfer time that can be obtained by the presented method for this example. Time-optimal trajectories for solutions B1 and B2 are illustrated in Figs. 6.8a and 6.8b, respectively. As shown in Fig. 6.7b, the same process is executed for $T_{\max} = 3$. The solution C1 is consistent with the solution obtained in [106], with the transfer time 285.77 h. On the other hand, only 281.97 h is required for the solution C. Thus, the local solution C performs better than C1. Moreover, the local solution C2 with fewest revolution is found, with the transfer time 283.33 h, which is longer then the solution C. It indicates that the solution with minimum revolution may not be the same to the one with minimum transfer time, but their transfer time is close. The time-optimal trajectories for solutions C1 and C2 are shown in Figs. 6.8c and 6.8d, respectively. Additionally, it can be seen from Figs. 6.7 that the norm of costate increases as the revolution decreases, and the minimum-revolution solution has the largest norm of costate. Thus the solution $\boldsymbol{\xi}^*_{\alpha,f}$ in Fig. 6.2 is at least close to the best solution for the corresponding $T_{\max}$.

Table 6.3: *Summary of solution points A-H.*

Case	$T_{\max}$ (N)	Transfer time (hours)	Final mass (kg)	N_{rev}
A	60	14.80	1336.58	1.05
B	12	75.12	1334.09	5.15
B1	12	70.25	1344.86	4.15
B2	12	70.19	1344.98	3.57
C	3	281.97	1344.32	15.16
C1	3	285.77	1342.23	15.84
C2	3	283.33	1343.58	14.66
D	0.5	1698.56	1343.71	89.64
E	60	23.56	1239.80	1.39
F	12	114.58	1246.96	4.05
G	3	455.91	1248.29	18.75
H	0.5	2801.81	1242.19	110.21

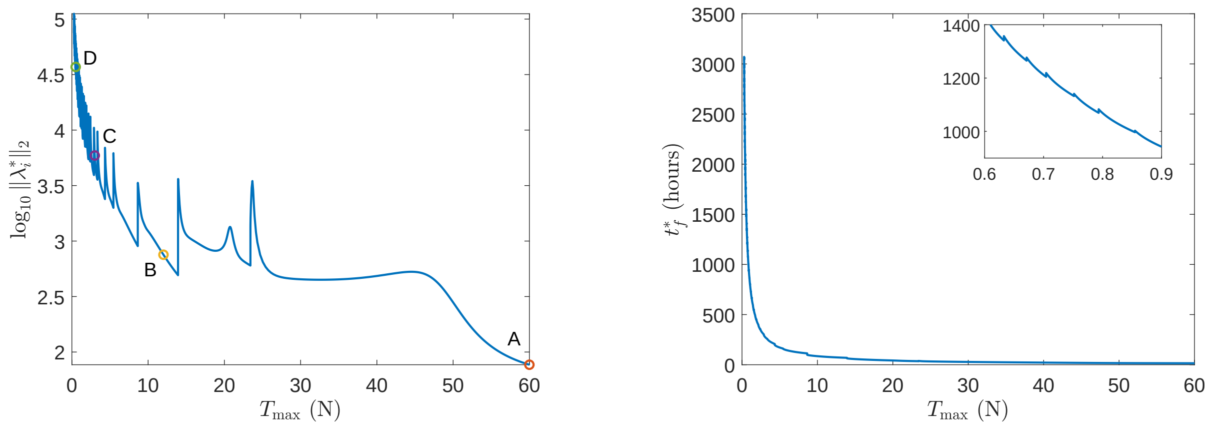

(a) *Variations of* $\boldsymbol{\lambda}_i^*$.

(b) *Variations of* t_f^*.

Figure 6.5: *Variations of optimal initial costate* $\boldsymbol{\lambda}_i^*$ *and optimal transfer time* t_f^* *w.r.t.* $T_{\max}$.

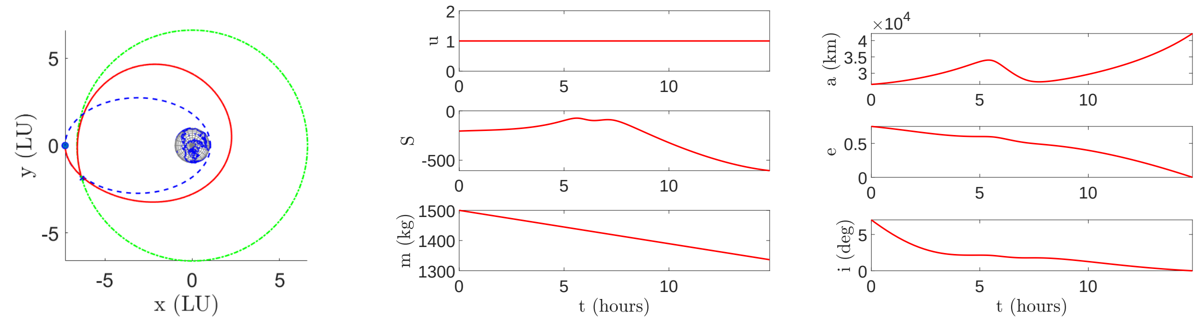

(a) *Time-optimal solution with* $T_{\max} = 60N$ *(Point A in Fig. 6.5a).*

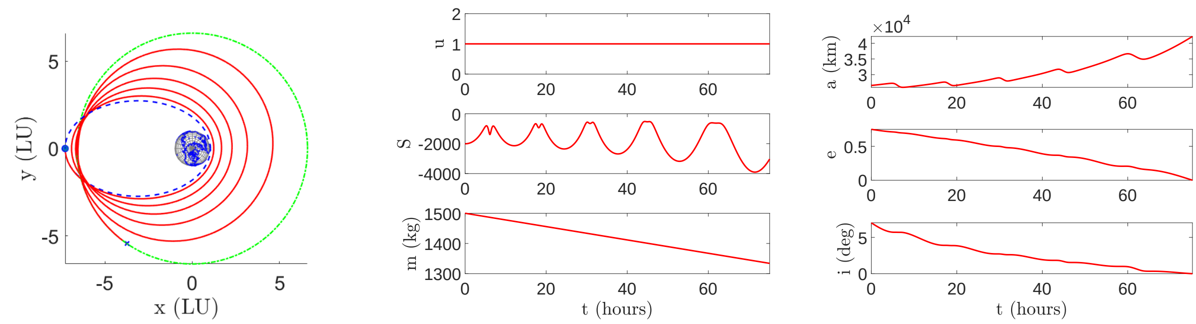

(b) *Time-optimal solution with* $T_{\max} = 12N$ *(Point B in Fig. 6.5a).*

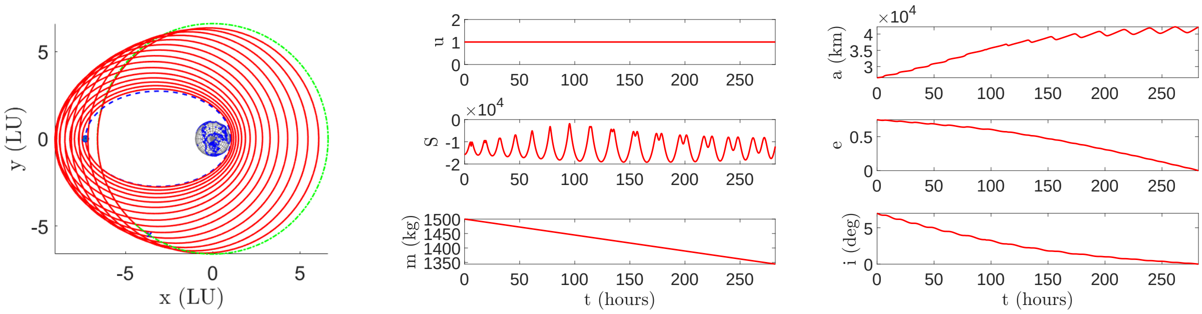

(c) *Time-optimal solution with* $T_{\max} = 3N$ *(Point C in Fig. 6.5a).*

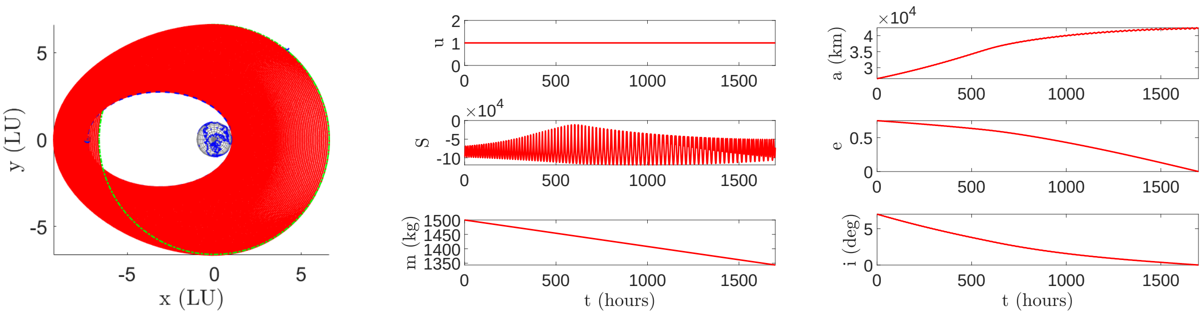

(d) *Time-optimal solution with* $T_{\max} = 0.5N$ *(Point D in Fig. 6.5a).*

Figure 6.6: *Sample solutions A-D in Fig. 6.5a. Blue dashed line: GTO; green line: GEO.*

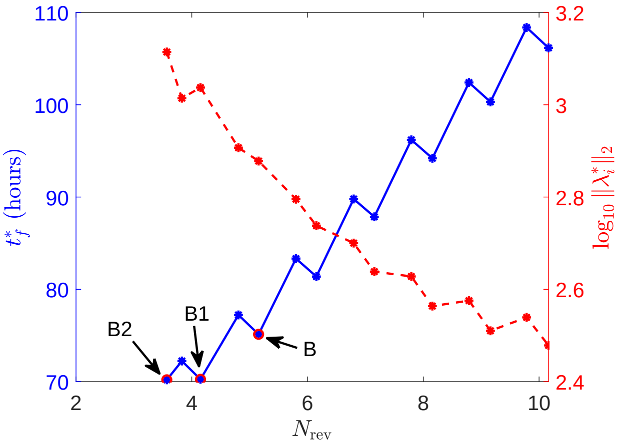

(a) $T_{\max} = 12$ *N.*

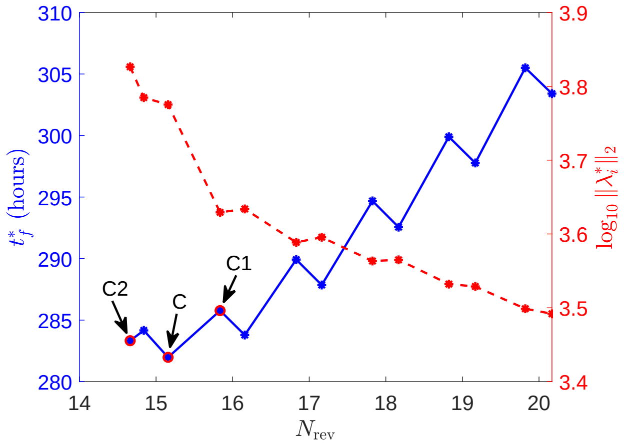

(b) $T_{\max} = 3$ *N.*

Figure 6.7: *Multiple local solutions (labeled as dots) for* $T_{\max} = 12$ *N and* $T_{\max} = 3$ *N.*

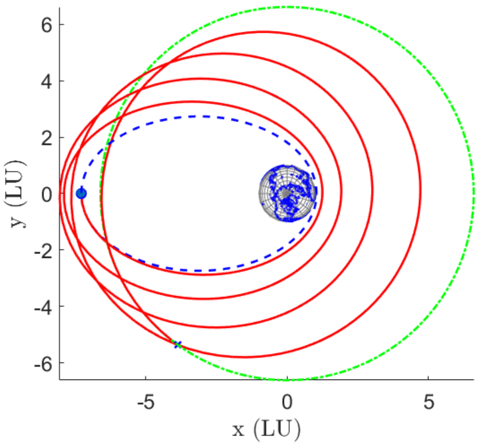

(a) *Time-optimal trajectory of solution B1*

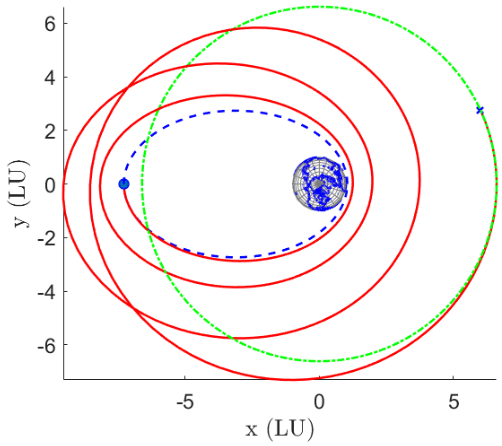

(b) *Time-optimal trajectory of solution B2*

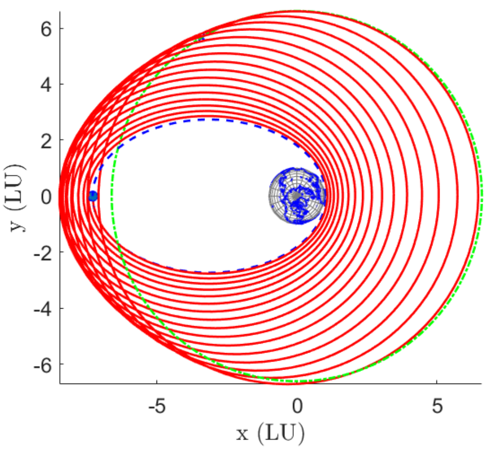

(c) *Time-optimal trajectory of solution C1*

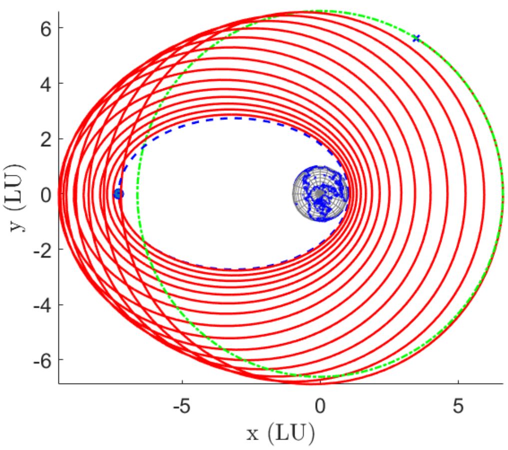

(d) *Time-optimal trajectory of solution C2*

Figure 6.8: *Time-optimal trajectories for solution B1, B2, C1 and C2 in Fig. 6.7. Blue dashed line: GTO; green line: GEO.*

6.3.2 GTO to EIGSO

The orbit transfer from GTO to EIGSO is simulated. Since e and i are non-zero values, the terminal orbit is not a fixed orbit. The thrust continuation starts from the time-optimal transfer with $T_{\max} = 60$ N. The corresponding optimal trajectory requires the transfer time $t_f^* = 23.56$ h and involves only 1.39 revolutions; see case E in Table 6.3. The optimal initial costate is

$$\boldsymbol{\lambda}_i^* = [0.650360, -0.103051, -0.669053, -4.087638, -16.199545, 200.110687, 83.272316]^\top$$

Variations of the norm of optimal initial costate and the optimal transfer time with respect to $T_{\max}$ are shown in Fig. 6.9, indicating that the proposed method is also effective for this case. Similar to Fig. 6.5, the t_f^* profile is non-smoothly and exponentially varied. The sample solutions E-H in Fig. 6.9a are extracted and shown in Fig. 6.10. From the variations of semi-major axis, it can be seen that the spacecraft increases the orbital energy higher than that of EIGSO first, and then it decreases the orbital energy to match EIGSO. On the other hand, from Fig. 6.6, the spacecraft gradually increases the orbital energy in the GTO-GEO transfer. The optimal transfer time, final mass and revolutions are reported in Table 6.3. It shows that longer transfer time and more orbital revolutions are required than those in the GTO-GEO transfer for the same $T_{\max}$. Moreover, compared to the GTO-GEO transfer, the transfer time is increased more rapidly as $T_{\max}$ is reduced.

Figure 6.11 illustrates the near constancy of $t_f \times T_{\max}$ for both studied cases. The slope for GTO-EIGSO transfers is steeper than GTO-GEO transfers, indicating that it is more expansive to transfer to EIGSO than GEO. This empirical result has been observed for GTO to GEO, intercept and rendezvous transfers in [106–108]. This work indicates that this conclusion exists for more general orbit transfers, with the slope dependent on the terminal conditions.

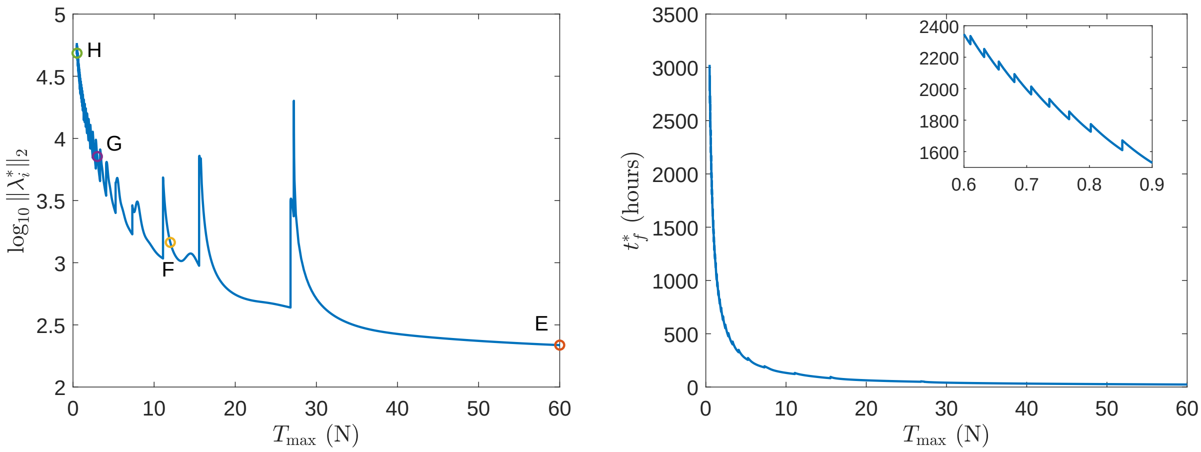

(a) *Variations of* $\boldsymbol{\lambda}_i^*$.

(b) *Variations of* t_f^*.

Figure 6.9: *Variation of optimal initial costate* $\boldsymbol{\lambda}_i^*$ *and optimal transfer time* t_f^* *w.r.t.* $T_{\max}$.

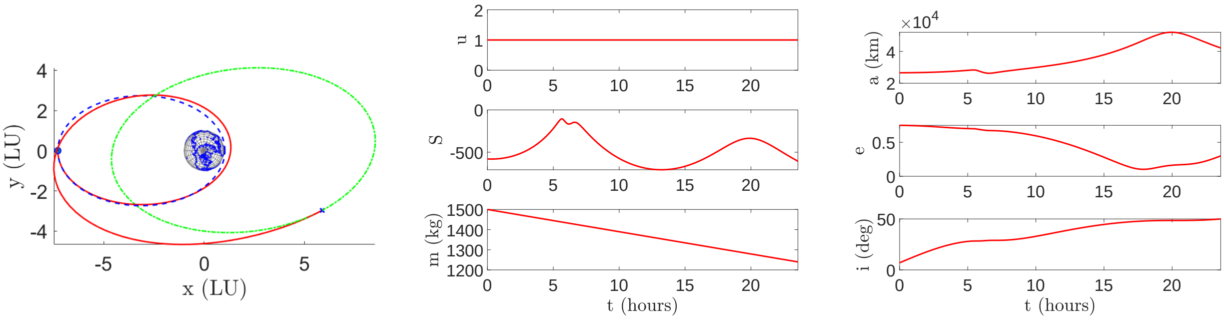

(a) *Time-optimal solution with $T_{\max} = 60N$ (Point A in Fig. 6.9a).*

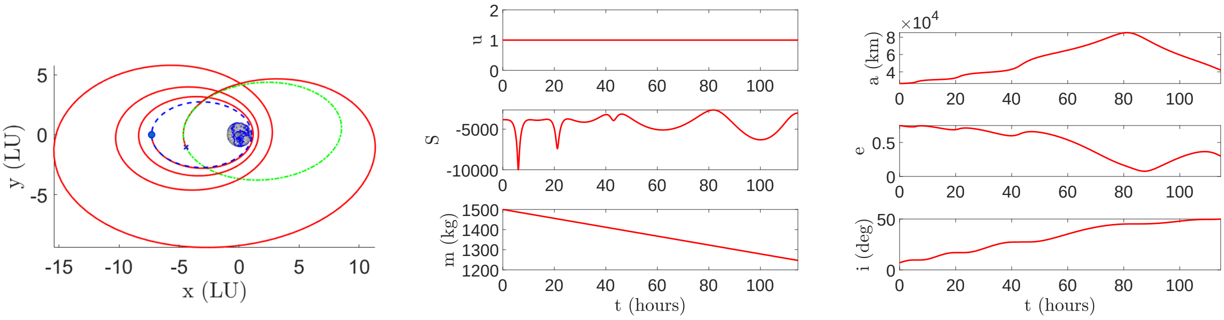

(b) *Time-optimal solution with $T_{\max} = 12N$ (Point B in Fig. 6.9a).*

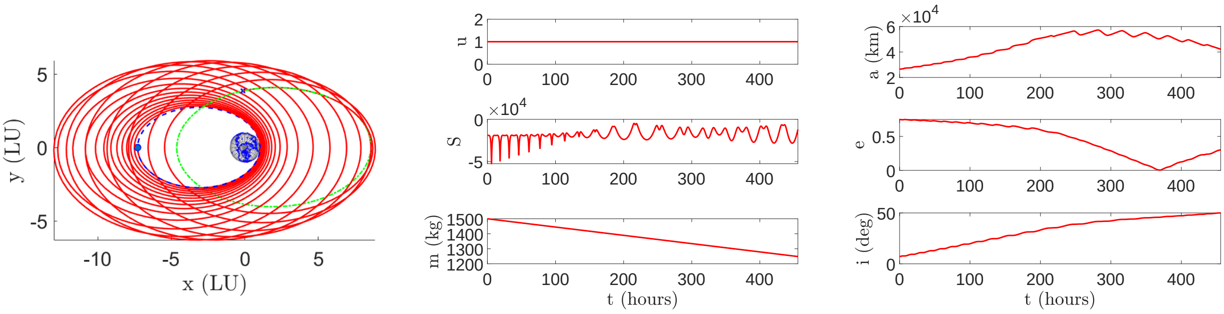

(c) *Time-optimal solution with $T_{\max} = 3N$ (Point C in Fig. 6.9a).*

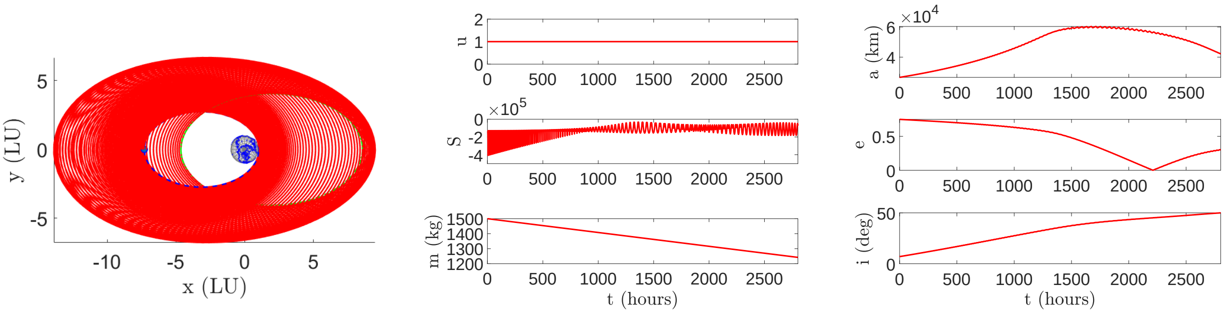

(d) *Time-optimal solution with $T_{\max} = 0.5N$ (Point D in Fig. 6.9a).*

Figure 6.10: *Sample solutions E-H in Fig. 6.9a. Blue dashed line: GTO; green line: EIGSO.*

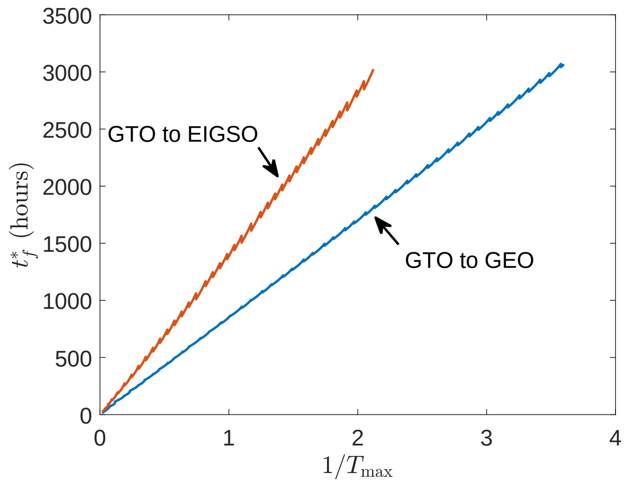

Figure 6.11: *Near constancy of the product $t_f \times T_{\max}$ for both cases.*

6.4 Summary

In this chapter, indirect optimization of low-thrust time-optimal Earth-orbit transfers with terminal conditions specified by a subset of orbital elements is studied. Since the shooting method alone is not effective to find the multi-revolution solutions, the combination of thrust continuation and the shooting method is developed. The failure of thrust continuation is analyzed and tackled by developing an enhanced thrust continuation method that is able to connect local solutions with different revolutions. GTO to GEO and GTO to EIGSO transfers are simulated to verify the effectiveness of the presented method. Better solutions, compared to the solutions reported in literature, are found for the GTO to GEO transfer. Also, it is found that the minimum-revolution solution may not coincide with the minimum-time solution. Moreover, numerical evidences indicate the near constancy of $t_f \times T_{\max}$ exists for more general orbital transfers.

CHAPTER 7

A HOMOTOPY METHOD USING THEORY OF FUNCTIONAL CONNECTIONS

NUMERICAL homotopy continuation is widely used in optimization methods to expand their convergence domain. By traversing a series of auxiliary problems, the homotopy method solves the objective problem by tracking the homotopy path, which is comprised of solutions of former [66]. Developing the method to tackle failures in the continuation process is essential to enhance the algorithmic robustness. Chapter 6 designed an effective method to remedy the failure of the thrust continuation, tailored to low-thrust orbital transfers. Inspired by the conceptual similarity between homotopy and TFC, this chapter presents a TFC-based homotopy method for general optimization problems, which paves the way to resolve continuation failures by leveraging the freedom in the selection of the homotopy line.

7.1 Fundamentals of Homotopy Methods

7.1.1 Homotopy Function

Consider the zero-finding problem

$$\boldsymbol{F}(\boldsymbol{x}) = \boldsymbol{0} \tag{7.1}$$

where $\boldsymbol{x} \in \mathbb{R}^n$ and $\boldsymbol{F} : \mathbb{R}^n \to \mathbb{R}^n$ is a $\mathcal{C}^2$ function. Newton's method is widely used to solve problem (7.1). However, it fails if the initial guess solution lies beyond its convergence domain, or singular points are encountered during iterations. These issues are likely in high-sensitive, nonlinear systems.

Homotopy is an effective strategy to solve difficult zero-finding problems, which lacks a priori knowledge on good initial guesses [66]. To solve Eq. (7.1), one may define a homotopy or deformation function $\boldsymbol{\Gamma}(\kappa, \boldsymbol{x}) : \mathbb{R} \times \mathbb{R}^n \to \mathbb{R}^n$ such that

$$\boldsymbol{\Gamma}(0, \boldsymbol{x}) = \boldsymbol{G}(\boldsymbol{x}), \qquad \boldsymbol{\Gamma}(1, \boldsymbol{x}) = \boldsymbol{F}(\boldsymbol{x}) \tag{7.2}$$

where $\kappa \in [0, 1]$ is the homotopy parameter and $\boldsymbol{G}(\boldsymbol{x}) : \mathbb{R}^n \to \mathbb{R}^n$ is a user-defined, auxiliary function. $\boldsymbol{G}(\boldsymbol{x})$ is usually defined to be similar to $\boldsymbol{F}(\boldsymbol{x})$, and the solution $\boldsymbol{x}_0$ to $\boldsymbol{G}(\boldsymbol{x}) = \mathbf{0}$ is easier to determine. The convex homotopy function is the commonly used form for $\boldsymbol{\Gamma}$:

$$\boldsymbol{\Gamma}(\kappa, \boldsymbol{x}) := \kappa\, \boldsymbol{F}(\boldsymbol{x}) + (1 - \kappa)\, \boldsymbol{G}(\boldsymbol{x})$$

Three types of homotopy are commonly used [109], depending on $\boldsymbol{G}$:

1. Newton homotopy, $\boldsymbol{G}(\boldsymbol{x}) := \boldsymbol{F}(\boldsymbol{x}) - \boldsymbol{F}(\boldsymbol{x}_0)$
2. Fixed-point homotopy, $\boldsymbol{G}(\boldsymbol{x}) := \boldsymbol{x} - \boldsymbol{x}_0$
3. Affine homotopy, $\boldsymbol{G}(\boldsymbol{x}) := A\,(\boldsymbol{x} - \boldsymbol{x}_0)$

where A is a $n \times n$ matrix.

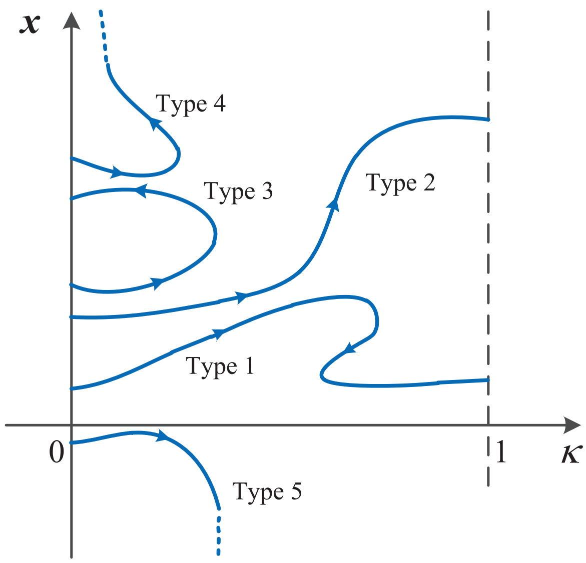

Figure 7.1: *Different types of homotopy paths* $[\boldsymbol{x}(\theta), \kappa(\theta)] = \boldsymbol{\Gamma}^{-1}(\mathbf{0})$ *starting from* $\kappa = 0$.

Under regularity assumptions [66, 110], defining the homotopy function inherently generates a unique curve $\boldsymbol{c}(\theta) := [\kappa(\theta), \boldsymbol{x}(\theta)] = \boldsymbol{\Gamma}^{-1}(\mathbf{0}) : J \to \mathbb{R}^{n+1}$ for some open interval $J \subset \mathbb{R}$ starting from $\boldsymbol{x}_0$, which contains points satisfying the consistency condition $\boldsymbol{\Gamma}(\kappa, \boldsymbol{x}) = \mathbf{0}$. θ is the continuation parameter that varies monotonously. The tracked solution curve in $\mathbb{R}^{n+1}$ is called homotopy path or zero curve. With reference to Fig. 7.1, the homotopy paths can be mainly classified in five Types [111]:

1) The homotopy path ends in $\{1\} \times \mathbb{R}^n$, with non-monotonic κ;
2) The homotopy path ends in $\{1\} \times \mathbb{R}^n$, with monotonic κ;
3) The homotopy path returns to a solution of $\boldsymbol{\Gamma}(0, \boldsymbol{x})$ in $\{0\} \times \mathbb{R}^n$;
4) The homotopy path is unbounded, with non-monotonic $\kappa \in [0, 1)$;
5) The homotopy path is unbounded, with monotonic $\kappa \in [0, 1)$.

Homotopy methods attempt to track the homotopy path starting from $(0, \boldsymbol{x}_0)$ to $(1, \boldsymbol{x}^*)$. When this happens, one zero of Eq. (7.1) is found. The sufficient conditions for the existence of the homotopy path are given by probability-one homotopy theory [111, 112], based on differential geometry concepts.

Definition 7.1 (Transversality). *Let $U \subset \mathbb{R}^n$ and $V \subset \mathbb{R}^p$ be open sets, and let $\boldsymbol{\rho}$: $[0,1) \times U \times V \to \mathbb{R}^n$ be a $\mathcal{C}^2$ map. $\boldsymbol{\rho}$ is said to be transversal to zero if the Jacobian $D\boldsymbol{\rho} \in \mathbb{R}^{n\times(1+n+p)}$ has full rank on $\boldsymbol{\rho}^{-1}(\mathbf{0})$.*

Theorem 7.1 (Sard's theorem). *Let $\boldsymbol{\rho}$: $[0,1) \times U \times V \to \mathbb{R}^n$ be a $\mathcal{C}^2$ map. If $\boldsymbol{\rho}$ is transversal to zero, then for almost all $\boldsymbol{a} \in U$, the map*

$$\boldsymbol{\rho}_a(\kappa, \boldsymbol{x}) := \boldsymbol{\rho}(\kappa, \boldsymbol{x}, \boldsymbol{a})$$

is also transversal to zero.

The parametrized Sard's theorem indicates that for almost all $\boldsymbol{a} \in U$, the zero set of $\boldsymbol{\rho}_a$ consists of smooth, nonintersecting curves [111]. In the following, we take $U \equiv \mathbb{R}^n$ and $V \equiv \mathbb{R}^p$.

Theorem 7.2 (Homotopy path). *Let $\boldsymbol{\rho}$: $[0,1) \times \mathbb{R}^n \times \mathbb{R}^p \to \mathbb{R}^n$ be a $\mathcal{C}^2$ map, and let $\boldsymbol{\rho}_a(\kappa, \boldsymbol{x}) = \boldsymbol{\rho}(\kappa, \boldsymbol{x}, \boldsymbol{a})$. Suppose that:*

i) for each fixed $\boldsymbol{a} \in \mathbb{R}^p$, $\boldsymbol{\rho}$ is transversal to zero;

ii) $\boldsymbol{\rho}_a(0, \boldsymbol{x}) = \mathbf{0}$ has a unique nonsingular solution $\boldsymbol{x}_0$;

iii) $\boldsymbol{\rho}_a(1, \boldsymbol{x}) = \boldsymbol{F}(\boldsymbol{x})$;

iv) $\boldsymbol{\rho}_a^{-1}(\mathbf{0})$ is bounded;

then, the solution curve reaches a point $(1, \boldsymbol{x}^*)$ such that $\boldsymbol{F}(\boldsymbol{x}^*) = \mathbf{0}$. Furthermore, if $D\boldsymbol{F}(\boldsymbol{x}^*)$ is invertible, then the homotopy path has finite arc length.

Transversality is hard to verify for arbitrary $\boldsymbol{a} \in \mathbb{R}^p$, and a proper $\boldsymbol{a}$ is required to construct the homotopy function. For example, fixed-point homotopy methods require selecting a proper $\boldsymbol{x}_0$. However, in current homotopy methods [66], $\boldsymbol{a}$ is manually selected and it cannot vary during iterations. Thus, the success of the entire procedure relies heavily on the initial point chosen, and thus once again on the empirical knowledge of the problem.

Remark 7.1. *The homotopy satisfying the hypotheses of Theorem 7.2 is called a globally convergent probability-one homotopy [111]. Designing probability-one homotopy algorithms for general applications is still an open problem. Theorem 7.2 is a guideline for robust homotopy algorithm design.*

Remark 7.2. *The $\mathcal{C}^2$ class is required for $\boldsymbol{\rho}$, and this condition cannot be relaxed [111]. $\mathcal{C}^2$ is used to ease the following arguments.*

Remark 7.3. *Predicting the homotopy path in the later iterations is generally difficult, unless the conditions of Theorem 7.2 are satisfied or the problem is simple enough (see the example in [70]). The behavior in the small neighborhood of current solution point is known if the conditions of Implicit Function Theorem are satisfied.*

7.1.2 Path Tracking Methods

Once the homotopy function is defined, the focus is on tracking its implicitly defined path. Two predictor-corrector methods are reviewed: Discrete Continuation Method (DCM) and Pseudo-arclength Method (PAM).

7.1.2.1 Discrete Continuation Method

DCM tries to solve $\mathbf{\Gamma}(\kappa, \boldsymbol{x}) = \mathbf{0}$ with monotonous variation of κ [43], i.e., $\theta := \kappa$. The solution curve $\boldsymbol{c}(\theta)$ is reduced as $\boldsymbol{c}(\theta) := \boldsymbol{x}(\kappa)$ As shown in Fig. 7.2, starting from initial solution at $\kappa = 0$, DCM solves the next solution on homotopy path using the former solution as initial guess. This process continues until the $\kappa = 1$ line is reached. DCM is simple and easy to implement, but it fails when the homotopy path exhibits limit points (Type 1, 3, 4) or goes off to infinity (Type 5). Limit points are points where the Jacobian $\mathbf{\Gamma}_{\boldsymbol{x}}(\kappa, \boldsymbol{x})$ is singular, thus DCM cannot continue by monotonously varying κ [65]. In Fig. 7.2, the simple zero-order DCM method is shown. In principles, one can construct a higher-order predictor using polynomial extrapolation [66]. This could result in a more efficient algorithm, yet higher-order DCM will still fail at limit points. Another type of singular points are bifurcation points where homotopy path branches emanate [65]. For the problems considered in this work, it is assumed that DCM failure is caused by limit points or infinite paths.

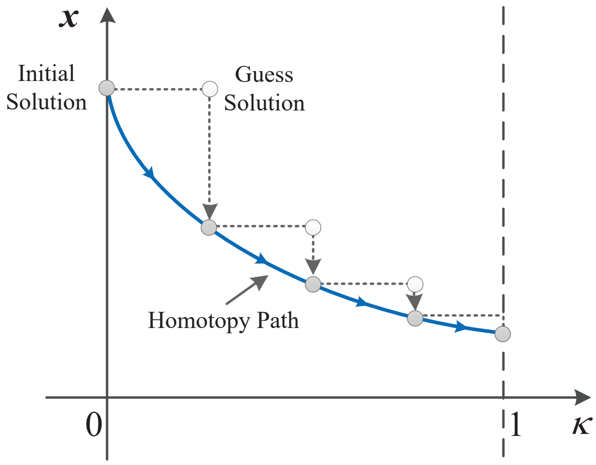

Figure 7.2: *Graphical interpretation of DCM.*

7.1.2.2 Pseudo-Arclength Method

PAM is an alternative to pass limit points that uses the arclength s as the continuation variable θ. Suppose that a solution point $(\kappa_i, \boldsymbol{x}_i)$ satisfies the consistency condition and its unit tangent direction $(\hat{\kappa}_i, \hat{\boldsymbol{x}}_i)$ is known, where the hat is the derivative w.r.t. s. In order to find the next solution point $(\kappa_{i+1}, \boldsymbol{x}_{i+1})$, the following augmented system is to be solved for $(\kappa, \boldsymbol{x})$

$$\begin{cases} \mathbf{\Gamma}(\kappa, \boldsymbol{x}) = \mathbf{0} \\ (\boldsymbol{x} - \boldsymbol{x}_i)^\top \hat{\boldsymbol{x}}_i + (\kappa - \kappa_i)\,\hat{\kappa}_i - \mathrm{d}s = 0 \end{cases} \tag{7.3}$$

The augmented Jacobian of system (7.3) evaluated at $(\kappa_i, \boldsymbol{x}_i)$, that is,

$$\boldsymbol{J}_a(\kappa_i, \boldsymbol{x}_i) = \begin{bmatrix} \mathbf{\Gamma}_x(\kappa_i, \boldsymbol{x}_i) & \mathbf{\Gamma}_\kappa(\kappa_i, \boldsymbol{x}_i) \\ \hat{\boldsymbol{x}}_i^\top & \hat{\kappa}_i \end{bmatrix}$$

is generally regular [66].

The ability of PAM to pass a limit point is graphically shown in Fig. 7.3. When a limit point is approached, PAM attempts to track the homotopy path by predicting the solution along the tangent direction, and refining the solution until system (7.3) is solved. Geometrically,

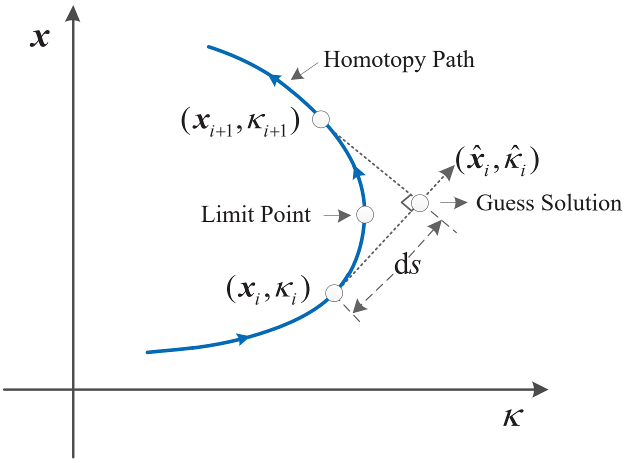

Figure 7.3: *Graphical interpretation of PAM near a limit point.*

the solution curve continues on the opposite κ direction (in Fig. 7.3, κ decreases across the limit point). PAM can elegantly satisfy condition *i)* in Theorem 7.2, but it still fails when dealing with homotopy path Types 3–5. Compared to DCM, PAM has broader convergence domain, but its implementation is more involved [113].

7.2 Theory of Functional Connection Homotopy Method

7.2.1 Theory of Functional Connections

The Theory of Functional Connections (TFC) is the extension of the Theory of Connections (TOC) [72]. The latter investigates the arbitrary connections between points by constructing a constrained function expressed in terms of an auxiliary function [72]. It has the property that no matter what the auxiliary function is, the constrained function always satisfies a prescribed set of constraints.

Suppose we define the scalar function

$$y(\eta) := g(\eta) + \frac{\eta - \eta_0}{\eta_f - \eta_0}(y_f - g_f) + \frac{\eta_f - \eta}{\eta_f - \eta_0}(y_0 - g_0) \tag{7.4}$$

where $y(\eta)$ and $g(\eta)$ are the *constrained function* and *auxiliary function*, respectively, whereas $\eta \in [\eta_0, \eta_f]$ is the independent variable. It is easy to verify that Eq. (7.4) inherently satisfies $y(\eta_0) = y_0$ and $y(\eta_f) = y_f$ regardless of the specific choice of $g(\eta)$ (note that $g_0 = g(\eta_0)$ and $g_f = g(\eta_f)$). Therefore, the line $y(\eta)$ will always connect the points $P_0 = (\eta_0, y_0)$ and $P_f = (\eta_f, y_f)$. Equation (7.4) is the generalization of interpolation formulae: it is not the interpolating expression for a class of functions but for all functions [72].

In the multi-dimensional case, the two-point condition is

$$\boldsymbol{y}(\eta_0) = \boldsymbol{y}_0, \qquad \boldsymbol{y}(\eta_f) = \boldsymbol{y}_f \tag{7.5}$$

where $\boldsymbol{y} \in \mathbb{R}^n$. The general expression of the constrained function $\boldsymbol{y}(\eta)$ is

$$\boldsymbol{y}(\eta) = \boldsymbol{g}(\eta) + P_1(\eta)\boldsymbol{c}_1 + P_2(\eta)\boldsymbol{c}_2 \tag{7.6}$$

where $P_{1,2} : \mathbb{R} \to \mathbb{R}^{n\times n}$ are matrices whose elements are scalar-valued functions of η, while $\boldsymbol{c}_{1,2} \in \mathbb{R}^n$ are constant vectors of weights [72]. Substituting Eq. (7.5) into Eq. (7.6) and solving for $\boldsymbol{c}_{1,2}$ yields

$$\begin{bmatrix} \boldsymbol{c}_1 \\ \boldsymbol{c}_2 \end{bmatrix} = \begin{bmatrix} P_1(\eta_0) & P_2(\eta_0) \\ P_1(\eta_f) & P_2(\eta_f) \end{bmatrix}^{-1} \begin{bmatrix} \boldsymbol{y}_0 - \boldsymbol{g}_0 \\ \boldsymbol{y}_f - \boldsymbol{g}_f \end{bmatrix} = \begin{bmatrix} Q_{11} & Q_{12} \\ Q_{21} & Q_{22} \end{bmatrix} \begin{bmatrix} \boldsymbol{y}_0 - \boldsymbol{g}_0 \\ \boldsymbol{y}_f - \boldsymbol{g}_f \end{bmatrix} \tag{7.7}$$

where again $\boldsymbol{g}_0 = \boldsymbol{g}(\eta_0)$ and $\boldsymbol{g}_f = \boldsymbol{g}(\eta_f)$. Moreover

$$\begin{aligned} Q_{11} &= \left[P_1(\eta_0) - P_2(\eta_0)P_2^{-1}(\eta_f)P_1(\eta_f)\right]^{-1} \\ Q_{21} &= -P_2^{-1}(\eta_f)P_1(\eta_f)\; Q_{11} \\ Q_{12} &= -P_1^{-1}(\eta_0)P_2(\eta_0)\; Q_{22} \\ Q_{22} &= \left[P_2(\eta_f) - P_1(\eta_f)P_1^{-1}(\eta_0)P_2(\eta_0)\right]^{-1} \end{aligned} \tag{7.8}$$

The selection of $P_{1,2}(\eta)$ in Eq. (7.6) must ensure the existence of Q_{ij} in Eq. (7.8). Substituting Eq. (7.7) into Eq. (7.6) gives the general form of constrained function

$$\boldsymbol{y}(\eta) = \boldsymbol{g}(\eta) + \sum_{i=1}^{2} P_i(\eta)Q_{i1}(\boldsymbol{y}_0 - \boldsymbol{g}_0) + \sum_{i=1}^{2} P_i(\eta)Q_{i2}(\boldsymbol{y}_f - \boldsymbol{g}_f) \tag{7.9}$$

The constrained function $\boldsymbol{y}(\eta)$ in Eq. (7.9) defines arbitrary connection paths between $\boldsymbol{y}_0$ and $\boldsymbol{y}_f$ produced by the infinitely possible choices of $\boldsymbol{g}(\eta)$. The constrained function for arbitrary boundary conditions can also be established [72]. The TFC extends the idea above to construct the constrained function on a functional domain [114].

7.2.2 TFC-Based Homotopy Function

From a geometrical point of view, the homotopy function defines the solution curve connecting the two zero-finding problems defined at the boundaries of κ, which satisfy Eq. (7.2). Analogously, the constrained function in the TFC connects points at the boundaries of η. Interpreting the constrained function as describing an homotopy path is therefore natural.

In Eq. (7.9), replacing the constrained function $\boldsymbol{y}(\eta)$ by the homotopy function $\boldsymbol{\Gamma}(\eta, \boldsymbol{x})$, and $\boldsymbol{y}_0$, $\boldsymbol{y}_f$ by $\boldsymbol{G}(\boldsymbol{x})$, $\boldsymbol{F}(\boldsymbol{x})$, respectively, we have

$$\boldsymbol{\Gamma}(\eta, \boldsymbol{x}) = \boldsymbol{g}(\eta) + \sum_{i=1}^{2} P_i(\eta)Q_{i1}(\boldsymbol{G}(\boldsymbol{x}) - \boldsymbol{g}_0) + \sum_{i=1}^{2} P_i(\eta)Q_{i2}(\boldsymbol{F}(\boldsymbol{x}) - \boldsymbol{g}_f) \tag{7.10}$$

The auxiliary function $\boldsymbol{g}(\eta)$ can be expressed as a linear combination of basis functions with corresponding weights, that is

$$\boldsymbol{g}(\eta) = \Omega \boldsymbol{h}(\eta) \tag{7.11}$$

where $\boldsymbol{h}(\eta) : \mathbb{R} \to \mathbb{R}^m$ is the vector of basis functions, whereas $\Omega \in \mathbb{R}^{n\times m}$ is the matrix of weights. Note that $\boldsymbol{g}_0 = \Omega \boldsymbol{h}_0$ and $\boldsymbol{g}_f = \Omega \boldsymbol{h}_f$, where $\boldsymbol{h}_0 = \boldsymbol{h}(\eta_0)$ and $\boldsymbol{h}_f = \boldsymbol{h}(\eta_f)$. A linear map between $\kappa \in [0, 1]$ and $\eta \in [\eta_0, \eta_f]$ is also used:

$$\eta(\kappa) = (1 - \kappa)\,\eta_0 + \kappa\,\eta_f \tag{7.12}$$

Substituting Eq. (7.11) and Eq. (7.12) into Eq. (7.10) yields

$$\boldsymbol{\Gamma}(\kappa, \boldsymbol{x}, \Omega) = \Omega \boldsymbol{h}(\kappa) + \sum_{i=1}^{2} P_i(\kappa)Q_{i1}\left(\boldsymbol{G}(\boldsymbol{x}) - \Omega \boldsymbol{h}_0\right) + \sum_{i=1}^{2} P_i(\kappa)Q_{i2}\left(\boldsymbol{F}(\boldsymbol{x}) - \Omega \boldsymbol{h}_f\right) \tag{7.13}$$

Notice that $\boldsymbol{\Gamma}$ in Eq. (7.13), beside the natural dependence on κ and $\boldsymbol{x}$, is also a function of the free parameter Ω, which can be varied to steer the solution curve from $\boldsymbol{G}^{-1}(\mathbf{0})$ to $\boldsymbol{F}^{-1}(\mathbf{0})$.

It is convenient to isolate in Eq. (7.13) the part depending on κ and $\boldsymbol{x}$ only

$$\boldsymbol{\Gamma}(\kappa, \boldsymbol{x}, \Omega) = \Omega \left(\boldsymbol{h}(\kappa) - \sum_{i=1}^{2} P_i(\kappa) Q_{i1} \boldsymbol{h}_0 - \sum_{i=1}^{2} P_i(\kappa) Q_{i2} \boldsymbol{h}_f \right) + \boldsymbol{\Gamma}_0(\kappa, \boldsymbol{x}) \tag{7.14}$$

where

$$\boldsymbol{\Gamma}_0(\kappa, \boldsymbol{x}) := \sum_{i=1}^{2} P_i(\kappa) Q_{i1} \boldsymbol{G}(\boldsymbol{x}) + \sum_{i=1}^{2} P_i(\kappa) Q_{i2} \boldsymbol{F}(\boldsymbol{x})$$

By taking the partial derivative of Eq. (7.14) w.r.t. $\boldsymbol{x}$, we find that

$$\frac{\partial \boldsymbol{\Gamma}(\kappa, \boldsymbol{x}, \Omega)}{\partial \boldsymbol{x}} = \frac{\partial \boldsymbol{\Gamma}_0(\kappa, \boldsymbol{x})}{\partial \boldsymbol{x}}$$

indicating that when a limit point is encountered, both Jacobian matrices are singular, regardless of the selection of Ω. In order to regularize $\partial \boldsymbol{\Gamma}/\partial \boldsymbol{x}$ by varying Ω, we let the basis functions $\boldsymbol{h}$ to depend on the present solution $\boldsymbol{x}$ as well; that is, $\boldsymbol{h} = \boldsymbol{h}(\kappa, \boldsymbol{x})$. Thus, Eq. (7.14) becomes

$$\boldsymbol{\Gamma}(\kappa, \boldsymbol{x}, \Omega) = \Omega \boldsymbol{\Gamma}_\Omega(\kappa, \boldsymbol{x}) + \boldsymbol{\Gamma}_0(\kappa, \boldsymbol{x}) \tag{7.15}$$

where

$$\boldsymbol{\Gamma}_\Omega(\kappa, \boldsymbol{x}) := \boldsymbol{h}(\kappa, \boldsymbol{x}) - \sum_{i=1}^{2} P_i(\kappa) Q_{i1} \boldsymbol{h}_0(\boldsymbol{x}) - \sum_{i=1}^{2} P_i(\kappa) Q_{i2} \boldsymbol{h}_f(\boldsymbol{x})$$

Inspired by Eq. (7.15), the formal definition of TFC-based homotopy is given.

Definition 7.2 (TFC-based homotopy function)**.** *Let $\hat{\boldsymbol{\rho}}(\kappa, \boldsymbol{x}, \boldsymbol{\varepsilon}, \boldsymbol{a}) : [0,1) \times \mathbb{R}^n \times \mathbb{R}^q \times \mathbb{R}^p \to \mathbb{R}^n$ be a $\mathcal{C}^2$ map, and let $\hat{\boldsymbol{\rho}}_a(\kappa, \boldsymbol{x}, \boldsymbol{\varepsilon}) = \hat{\boldsymbol{\rho}}(\kappa, \boldsymbol{x}, \boldsymbol{\varepsilon}, \boldsymbol{a})$ for fixed $\boldsymbol{a}$. $\hat{\boldsymbol{\rho}}_a(\kappa, \boldsymbol{x}, \boldsymbol{\varepsilon})$ is called TFC-based homotopy function if*

i) it automatically satisfies the boundary conditions

$$\hat{\boldsymbol{\rho}}_a(0, \boldsymbol{x}, \boldsymbol{\varepsilon}) = \boldsymbol{G}(\boldsymbol{x}) \qquad \text{and} \qquad \hat{\boldsymbol{\rho}}_a(1, \boldsymbol{x}, \boldsymbol{\varepsilon}) = \boldsymbol{F}(\boldsymbol{x})$$

for arbitrary $\boldsymbol{\varepsilon}$;

ii) $\forall \kappa \in (0,1)$ and $\forall \boldsymbol{x} \in \mathbb{R}^n$, $\exists$ $\boldsymbol{\varepsilon}$ such that $\partial \hat{\boldsymbol{\rho}}_a(\kappa, \boldsymbol{x}, \boldsymbol{\varepsilon})/\partial \boldsymbol{x}$ is regular.

In traditional homotopy methods (e.g., Newton homotopy), the term $\boldsymbol{a}$ in the homotopy function $\boldsymbol{\rho}_a(\kappa, \boldsymbol{x})$ in Theorem 7.1 is set at the beginning of the continuation procedure (e.g., by providing the solution $\boldsymbol{x}_0$ to the initial problem $\boldsymbol{G}(\boldsymbol{x}) = \mathbf{0}$) and so is the homotopy path. The TFC-based homotopy function $\hat{\boldsymbol{\rho}}_a(\kappa, \boldsymbol{x}, \boldsymbol{\varepsilon})$ is the generalization of $\boldsymbol{\rho}_a(\kappa, \boldsymbol{x})$. Here, although $\boldsymbol{a}$ is fixed, $\boldsymbol{\varepsilon}$ brings in flexibility in the homotopy path while not affecting the boundary conditions Eq. (7.2). The TFC-based homotopy function implicitly defines infinite homotopy paths because of the infinite possible selections of $\boldsymbol{\varepsilon}$. Moreover, condition ii) in Definition 7.2 enables regularizing the path by varying $\boldsymbol{\varepsilon}$. Therefore, it is a tool to recover improperly defined paths, by detecting them and switching to different, yet feasible, homotopy paths.

Equation (7.15) provides a general form of TFC-based homotopy function. Here, $\boldsymbol{\Gamma}_0(\kappa, \boldsymbol{x})$ is equivalent to $\boldsymbol{\rho}_a(\kappa, \boldsymbol{x})$ and Ω can be seen as $\boldsymbol{\varepsilon}$ (see Remark 7.4). Let $\tau = e^{\eta_0 - \eta_f}$, the following three examples are given based on different choice of $P_{1,2}(\eta)$

1. For $P_1 = I$ and $P_2 = \eta I$

$$\boldsymbol{\Gamma}(\kappa, \boldsymbol{x}, \Omega) = \Omega\left(\boldsymbol{h}(\kappa, \boldsymbol{x}) + (\kappa - 1)\boldsymbol{h}_0(\boldsymbol{x}) - \kappa \boldsymbol{h}_f(\boldsymbol{x})\right) + \boldsymbol{\Gamma}_0(\kappa, \boldsymbol{x}) \tag{7.16}$$

2. For $P_1 = I$ and $P_2 = e^{\eta} I$

$$\boldsymbol{\Gamma}(\kappa, \boldsymbol{x}, \Omega) = \Omega\left(\boldsymbol{h}(\kappa, \boldsymbol{x}) - \frac{1 - \tau^{(1-\kappa)}}{1 - \tau}\boldsymbol{h}_0(\boldsymbol{x}) - \frac{-\tau + \tau^{(1-\kappa)}}{1 - \tau}\boldsymbol{h}_f(\boldsymbol{x})\right) + \boldsymbol{\Gamma}_0(\kappa, \boldsymbol{x}) \tag{7.17}$$

3. For $P_1 = I$ and $P_2 = e^{-\eta} I$

$$\boldsymbol{\Gamma}(\kappa, \boldsymbol{x}, \Omega) = \Omega\left(\boldsymbol{h}(\kappa, \boldsymbol{x}) - \frac{\tau - \tau^{\kappa}}{\tau - 1}\boldsymbol{h}_0(\boldsymbol{x}) - \frac{-1 + \tau^{\kappa}}{\tau - 1}\boldsymbol{h}_f(\boldsymbol{x})\right) + \boldsymbol{\Gamma}_0(\kappa, \boldsymbol{x}) \tag{7.18}$$

Remark 7.4. *Let $\Omega_{\text{col}} = \text{vec}(\Omega) \in \mathbb{R}^{\text{mn}\times 1}$, where 'vec' is an operator that converts matrices into column vectors. Then, $\Omega\boldsymbol{\Gamma}_{\Omega}(\kappa, \boldsymbol{x}) = \tilde{\boldsymbol{\Gamma}}_{\Omega}(\kappa, \boldsymbol{x})\Omega_{\text{col}}$, where*

$$\tilde{\boldsymbol{\Gamma}}_{\Omega}(\kappa, \boldsymbol{x}) := \begin{bmatrix} \tilde{\boldsymbol{h}}^{\top}(\kappa, \boldsymbol{x}) & & & \\ & \tilde{\boldsymbol{h}}^{\top}(\kappa, \boldsymbol{x}) & & \\ & & \ddots & \\ & & & \tilde{\boldsymbol{h}}^{\top}(\kappa, \boldsymbol{x}) \end{bmatrix} \in \mathbb{R}^{n \times mn}$$

and

$$\tilde{\boldsymbol{h}}(\kappa, \boldsymbol{x}) := \left(\boldsymbol{h}(\kappa, \boldsymbol{x}) - \sum_{i=1}^{2} P_i(\kappa) Q_{i1} \boldsymbol{h}_0(\boldsymbol{x}) - \sum_{i=1}^{2} P_i(\kappa) Q_{i2} \boldsymbol{h}_f(\boldsymbol{x})\right)$$

Thus, Ω can be seen as a column vector $\boldsymbol{\varepsilon} \in \mathbb{R}^q$ where $q = mn$.

7.2.3 Regularization

This section shows the sufficient conditions for point ii) in Definition 7.2.

Lemma 7.1. *Suppose that a matrix $A \in \mathbb{R}^{n\times n}$ is the product of two matrices $B \in \mathbb{R}^{n\times m}$ and $C \in \mathbb{R}^{m\times n}$; $A = BC$. If $m < n$, then A is singular.*

Proof. Consider the linear equation

$$C\boldsymbol{x} = \boldsymbol{0}$$

if $m < n$, the number of equations is less than that of unknowns, thus there exists nonzero solution $\tilde{\boldsymbol{x}}$ such that

$$C\tilde{\boldsymbol{x}} = \boldsymbol{0}$$

then

$$BC\tilde{\boldsymbol{x}} = A\tilde{\boldsymbol{x}} = \boldsymbol{0}$$

indicating that the matrix A is singular. □

Lemma 7.2. *If $A \in \mathbb{R}^{m\times n}$ is full row rank and $m \leqslant n$, then $B = AA^{\top} \in \mathbb{R}^{m\times m}$ is regular.*

Proof. Consider the linear equation

$$B\boldsymbol{x} = AA^\top \boldsymbol{x} = \mathbf{0}$$

which equals to

$$\boldsymbol{x}^\top AA^\top \boldsymbol{x} = \left(A^\top \boldsymbol{x}\right)^\top A^\top \boldsymbol{x} = \mathbf{0} \;\rightarrow\; A^\top \boldsymbol{x} = \mathbf{0}$$

Since $m \leqslant n$ and A is full row rank, thus $\boldsymbol{x} = \mathbf{0}$. Therefore, B is regular. □

Theorem 7.3 (Sufficient Conditions)**.** *Let $\boldsymbol{\Gamma}(\kappa, \boldsymbol{x}, \Omega) = \Omega\boldsymbol{\Gamma}_\Omega(\kappa, \boldsymbol{x}) + \boldsymbol{\Gamma}_0(\kappa, \boldsymbol{x})$ be a candidate TFC-based homotopy function. If $m = n$ and $\partial\boldsymbol{\Gamma}_\Omega(\kappa, \boldsymbol{x})/\partial\boldsymbol{x} \in \mathbb{R}^{m\times n}$ is regular, then $\exists\ \Omega \in \mathbb{R}^{n\times m}$ such that $\partial\boldsymbol{\Gamma}(\kappa, \boldsymbol{x}, \Omega)/\partial\boldsymbol{x}$ is regular.*

Proof. Taking the derivative of Eq. (7.15) w.r.t. $\boldsymbol{x}$ yields

$$\frac{\partial\boldsymbol{\Gamma}(\kappa, \boldsymbol{x}, \Omega)}{\partial\boldsymbol{x}} = \Omega\frac{\partial\boldsymbol{\Gamma}_\Omega(\kappa, \boldsymbol{x})}{\partial\boldsymbol{x}} + \frac{\partial\boldsymbol{\Gamma}_0(\kappa, \boldsymbol{x})}{\partial\boldsymbol{x}}$$

Applying singular value decomposition to $\partial\boldsymbol{\Gamma}_0(\kappa, \boldsymbol{x})/\partial\boldsymbol{x}$, there exists

$$\frac{\partial\boldsymbol{\Gamma}_0(\kappa, \boldsymbol{x})}{\partial\boldsymbol{x}} = U^\top \begin{bmatrix} \Sigma_1 & \\ & \Sigma_2 \end{bmatrix} V$$

where Σ_1 are nonzero singular values, and Σ_2 are zero singular values if $\partial\boldsymbol{\Gamma}_0(\kappa, \boldsymbol{x})/\partial\boldsymbol{x}$ is singular. U and V are corresponding singular vectors. We can construct a regular matrix $S \in \mathbb{R}^{n\times n}$ as

$$S = U^\top \begin{bmatrix} \Lambda_1 & \\ & \Lambda_2 \end{bmatrix} V$$

where Λ_1 and Λ_2 are non-zero singular values. There always exists Λ_1 and Λ_2 such that the matrix

$$\frac{\partial\boldsymbol{\Gamma}(\kappa, \boldsymbol{x}, \Omega)}{\partial\boldsymbol{x}} = S + \frac{\partial\boldsymbol{\Gamma}_0(\kappa, \boldsymbol{x})}{\partial\boldsymbol{x}} = U^\top \begin{bmatrix} \Lambda_1 + \Sigma_1 & \\ & \Lambda_2 + \Sigma_2 \end{bmatrix} V \in \mathbb{R}^{n\times n}$$

is regular. Let $S := \Omega\ \partial\boldsymbol{\Gamma}_\Omega(\kappa, \boldsymbol{x})/\partial\boldsymbol{x}$. From Lemma 7.1, this requires $m \geqslant n$. Since $\partial\boldsymbol{\Gamma}_\Omega(\kappa, \boldsymbol{x})/\partial\boldsymbol{x}$ is full rank and $m = n$, from Lemma 7.2, $\exists\ \Omega$ such that

$$\Omega = S\left(\frac{\partial\boldsymbol{\Gamma}_\Omega(\kappa, \boldsymbol{x})}{\partial\boldsymbol{x}}\right)^\top \left[\left(\frac{\partial\boldsymbol{\Gamma}_\Omega(\kappa, \boldsymbol{x})}{\partial\boldsymbol{x}}\right)\left(\frac{\partial\boldsymbol{\Gamma}_\Omega(\kappa, \boldsymbol{x})}{\partial\boldsymbol{x}}\right)^\top\right]^{-1}$$

□

According to Theorem 7.3, the following criteria are provided. Firstly, $m = n$. Secondly, monotonous functions such as exponential functions are preferred to construct each element of $\boldsymbol{h}(\kappa, \boldsymbol{x})$. Thirdly, the selection of $\boldsymbol{h}(\kappa, \boldsymbol{x})$ should consider the concrete form of TFC homotopy function. In Eqs. (7.16)–(7.18), $\boldsymbol{h}(\kappa, \boldsymbol{x})$ should be nonlinear in κ to ensure the explicit dependence of $\boldsymbol{\Gamma}_\Omega(\kappa, \boldsymbol{x})$ on κ. In Section 4, the TFC homotopy function in Eq. (7.16) is used. The state-dependent basis function $\boldsymbol{h}(\kappa, \boldsymbol{x})$ is constructed as

$$\boldsymbol{h}(\kappa, \boldsymbol{x}) = \begin{bmatrix} \mathrm{e}^{x_1}\kappa^2 \\ \mathrm{e}^{x_2}\kappa^2 \\ \vdots \\ \mathrm{e}^{x_n}\kappa^2 \end{bmatrix}$$

and then $\mathbf{\Gamma}_\Omega$ becomes

$$\mathbf{\Gamma}_\Omega(\kappa, \boldsymbol{x}) = \begin{bmatrix} e^{x_1}(\kappa^2 - \kappa) \\ e^{x_2}(\kappa^2 - \kappa) \\ \vdots \\ e^{x_n}(\kappa^2 - \kappa) \end{bmatrix}$$

Thus, since the derivative of $e^{x_i}, i = 1, 2, \cdots, n$, is not zero, the Jacobian of $\mathbf{\Gamma}_\Omega$ w.r.t. $\boldsymbol{x}$ is regular, $\forall \kappa \in (0, 1)$.

7.2.4 A Two-Layer TFC-based DCM Algorithm

Following the definition of the TFC-based homotopy function in Eq. (7.15), a two-layer DCM algorithm is proposed.

7.2.4.1 Singular Point Management

Fig. 7.4 illustrates the method, with a focus on limit point management. Starting from $\boldsymbol{x}_0$ at $\kappa = 0$, the DCM is used first to track the initial homotopy path, defined by $\mathbf{\Gamma}_0(\kappa, \boldsymbol{x})$. Since the DCM terminates at limit points, limit points can be detected if the step-size is small enough, and the solution point satisfies $\|\boldsymbol{x}\|_\infty \leqslant T_h$ where T_h is the threshold defined in Section 7.2.4.2. When a limit point $\boldsymbol{x}_{L,0}$ is encountered at $\kappa_{L,0}$, another feasible homotopy path defined by $\mathbf{\Gamma}(\kappa, \boldsymbol{x}, \Omega_1)$ is found by searching for a proper Ω_1. Then, the new starting point $\boldsymbol{x}_{0,1}$ at $\kappa_{L,0}$ triggers a new homotopy path, again tracked by DCM. At $\boldsymbol{x}_{L,1}$, the new homotopy path defined by $\mathbf{\Gamma}(\boldsymbol{\kappa}, \boldsymbol{x}, \Omega_2)$ is found and tracked. This process is repeated until the line $\kappa = 1$ is reached.

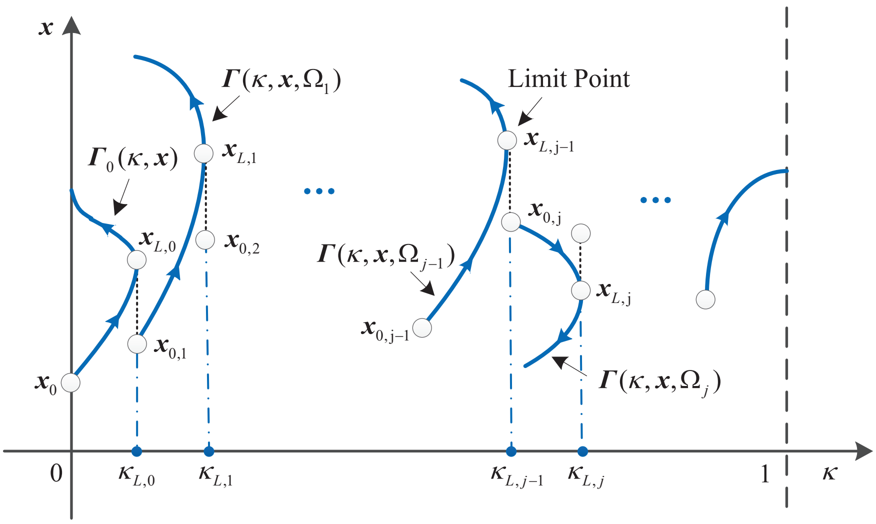

Figure 7.4: *Graphical layout of the singular point management.*

In general, suppose that the DCM encounters a limit point $\boldsymbol{x}_{L,j-1}$ at $\kappa_{L,j-1}$ while tracking the homotopy path defined by $\mathbf{\Gamma}(\kappa, \boldsymbol{x}, \Omega_{j-1})$. The goal is to switch to a new solution curve by finding a new homotopy path defined by $\mathbf{\Gamma}(\kappa, \boldsymbol{x}, \Omega_j)$ starting from $\boldsymbol{x}_{0,j}$ at $\kappa_{L,j-1}$. The unknown variables for the j-th homotopy path are Ω_j and $\boldsymbol{x}_{0,j}$; that is, a total of $(m+1) \times n$ unknowns against the n-dimensional consistency condition. The problem is clearly underdetermined, and therefore Ω_j and $\boldsymbol{x}_{0,j}$ are found by solving an optimization problem.

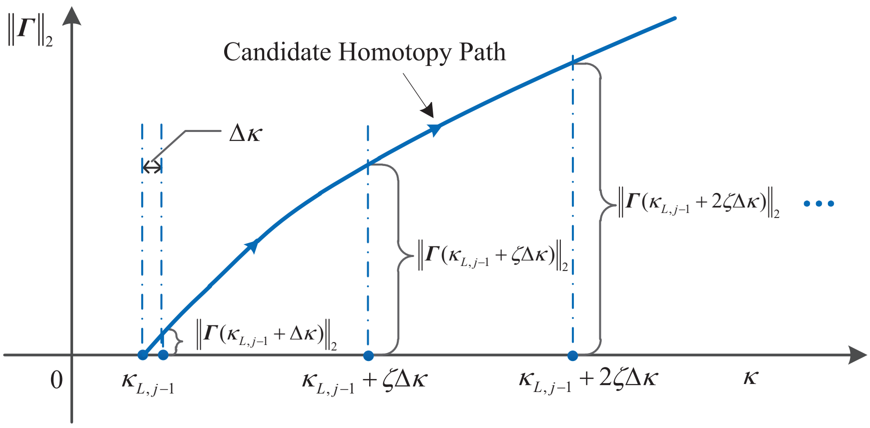

Figure 7.5: *Error trend along a candidate homotopy path.*

The main feature sought in a candidate homotopy path are feasibility and an easy progression of the DCM. Ideally, one may want to switch to a new feasible horizontal path, which would easily lead to the solution of the objective problem ($\kappa = 1$). In this respect, the projected $\|\boldsymbol{\Gamma}\|_2$ error trend along a candidate homotopy path is considered. In Fig. 7.5, the projected error is discerned into a near-side error, $\boldsymbol{\Gamma}(\kappa_{L,j-1} + \Delta\kappa, \boldsymbol{x}, \Omega_j)$, and a far-side error $\boldsymbol{\Gamma}(\min(\kappa_{L,j-1} + i\zeta\Delta\kappa, 1), \boldsymbol{x}, \Omega_j)$. The former is minimized to ease restart of the DCM, while the latter is weighted to select a mild path. The problem is therefore to

$$\min_{\Omega_j, \boldsymbol{x}_{0,j}} J \quad \text{s.t.} \quad \boldsymbol{c}_{\text{eq}} = \boldsymbol{0} \tag{7.19}$$

where

$$J := \|\boldsymbol{\Gamma}\left(\min(\kappa_{L,j-1} + \Delta\kappa, 1), \boldsymbol{x}_{0,j}, \Omega_j\right)\|_2 + \sum_{i=1}^{N} \gamma^i \|\boldsymbol{\Gamma}\left(\min(\kappa_{L,j-1} + i\zeta\Delta\kappa, 1), \boldsymbol{x}_{0,j}, \Omega_j\right)\|_2 \tag{7.20}$$

and

$$\boldsymbol{c}_{\text{eq}} := \begin{cases} \mathbf{1}_{n\times 1}, & \text{if } \left|\det\left(\partial\boldsymbol{\Gamma}\left(\kappa_{L,j-1}, \boldsymbol{x}_{0,j}, \Omega_j\right)/\partial\boldsymbol{x}\right)\right| \leqslant \delta \\ \boldsymbol{\Gamma}\left(\kappa_{L,j-1}, \boldsymbol{x}_{0,j}, \Omega_j\right), & \text{otherwise} \end{cases} \tag{7.21}$$

In Eq. (7.20), $\gamma \in [0, 1)$ is a discount factor, ζ is the predicted horizon, and N is the number of predicted points. An artificial violation of the equality constraint in Eq. (7.21) is introduced to avoid near-singular paths. Moreover, Ω_{j-1} and $\boldsymbol{x}_{L,j-1}$ are taken as initial guess for the optimization problem in Eq. (7.19).

7.2.4.2 Indefinite Growth Management

Beside tackling limit points, paths of Type 5 in Fig. 7.1 are also considered. As shown in Fig. 7.6, indefinite growth is managed through thresholding. An a-priori threshold T_h on $\|\boldsymbol{x}\|_\infty$ is set. Once the homotopy path crosses the threshold line, the second layer is triggered to switch to an alternative, feasible homotopy path.

In Fig. 7.6, when the initial homotopy path exceeds T_h, the solution point $\boldsymbol{x}_{\text{I},0}$ at $\kappa_{\text{I},0}$ is detected. This is used as initial guess to solve the optimization problem in Eq. (7.19), and a new homotopy path (using Ω_1 and starting from $\boldsymbol{x}_{0,1}$) is tracked. If this new homotopy path exceeds T_h (Failed Case 1) or the solver fails to converge (Failed Case 2), the solution point near but below $T_h/2$ is considered, until a new feasible path is found. In Fig. 7.6, the new homotopy path defined by $\boldsymbol{\Gamma}(\kappa, \boldsymbol{x}, \Omega_3)$ starting from $\boldsymbol{x}_{0,3}$ at $\kappa_{\text{I},2}$ is found by using $T_h/4$.

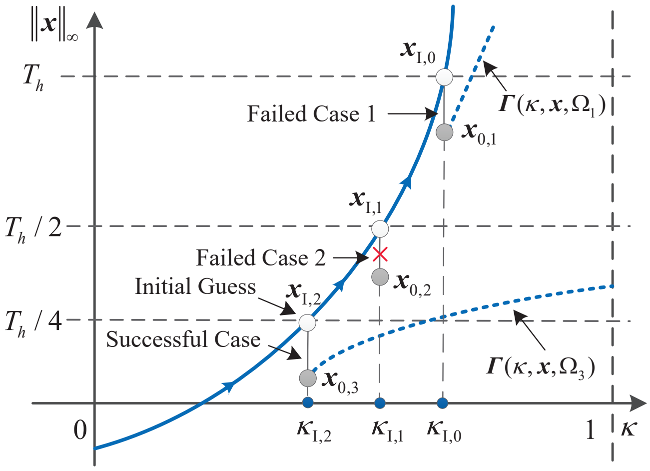

Figure 7.6: *Graphical layout of the indefinite growth management.*

The algorithmic rationale of the two-layer, TFC-based homotopy method is summarized in Algorithm 2, where $\Delta\kappa_{\min}$ is the step-size threshold to detect the limit point, and N_s is the total times of path switching.

7.3 Numerical Simulations

In this section, three numerical experiments are performed using the TFC-based DCM method. To ease assessment of the developed algorithm, the outcome of each problem is compared to the solution obtained using PAM. The zero-finding and optimization problems are solved using Matlab's `fzero` and `fmincon` implementing interior-point method, respectively. In both algorithms, the function residual (`TolFun`) and solution tolerance (`TolX`) are both set to 10^{-12}. All test cases have been performed using Matlab R2019a with Intel Core i7-9750H CPU @2.60 GHz, Windows 10 operating system. The parameters of the optimization problem in Eqs. (7.20)–(7.21) are $\gamma = 0.5$, $\zeta = 15$, $N = 3$, $\delta = 1 \times 10^{-4}$ and $\Delta\kappa_{\min} = 1 \times 10^{-8}$.

7.3.1 Algebraic Zero-Finding Problem

The zero of the following two-dimensional function is sought [115]

$$\boldsymbol{F}(x_1, x_2) = \begin{bmatrix} a(x_1 + x_2) \\ a(x_1 + x_2) + (x_1 - x_2)\left((x_1 - b)^2 + x_2^2 - c\right) \end{bmatrix} \tag{7.22}$$

where $a = 4, b = 2, c = 1$. The state-dependent basis function $\boldsymbol{h}(\kappa, \boldsymbol{x})$ is

$$\boldsymbol{h}(\kappa, \boldsymbol{x}) = \begin{bmatrix} \mathrm{e}^{x_1}\kappa^2 \\ \mathrm{e}^{x_2}\kappa^2 \end{bmatrix}$$

and $\Delta\kappa = 0.001$.

In [115, 116], it is stated that if the initial condition is located inside the circle $(x_1-2)^2+x_2^2 = 1$, the Newton homotopy function implementing PAM will fail to find the solution. This property is independently confirmed by our numerical experiment. In Fig. 7.7, Newton homotopy function is used. Both PAM and TFC-based DCM for various initial conditions $\boldsymbol{x}_0$ (the solution to $\boldsymbol{G}(\boldsymbol{x}) = \boldsymbol{0}$) are executed. For cases $\boldsymbol{x}_0 = [1.5, 0.5]^\top$ and $\boldsymbol{x}_0 = [1.5, -0.5]^\top$

Algorithm 2 Two-layer TFC-based DCM Algorithm

Require: $\Delta\kappa$, $\Delta\kappa_{\min}$, $\boldsymbol{h}(\kappa, \boldsymbol{x})$, $\boldsymbol{G}(\boldsymbol{x})$, and T_h.
Ensure: Solution to $\boldsymbol{F}(\boldsymbol{x}) = \boldsymbol{0}$.

Set $\kappa = 0$, $\kappa_{\text{old}} = 0$, $j = 0$, $\Delta\kappa_{\text{iter}} = \Delta\kappa$, and $\Omega_0 = 0_{n\times n}$, $N_s = 0$.
Solve the auxiliary problem $\boldsymbol{G}(\boldsymbol{x}) = \boldsymbol{0}$.
while $\kappa < 1$ **do**
  $\kappa \leftarrow \kappa + \Delta\kappa_{\text{iter}}$.
  Solve the zero-finding problem $\boldsymbol{\Gamma}(\kappa, \boldsymbol{x}, \Omega_j) = \boldsymbol{0}$.
  if Converged but the solution satisfies $\|\boldsymbol{x}\|_\infty > T_h$ **then**
    Solve the optimization problem Eq. (7.19).
    Switch to the new homotopy path $\boldsymbol{\Gamma}(\kappa, \boldsymbol{x}, \Omega_{j+1})$, $j \leftarrow j + 1$.
    $\Delta\kappa_{\text{iter}} \leftarrow \min(1 - \kappa, \Delta\kappa)$, $\kappa_{\text{old}} \leftarrow \kappa$, $N_s \leftarrow N_s + 1$.
  else
    if Converged **then**
      $\Delta\kappa_{\text{iter}} \leftarrow \min(1 - \kappa, \Delta\kappa)$. $\kappa_{\text{old}} \leftarrow \kappa$.
    else
      if $\Delta\kappa_{\text{iter}} \leqslant \Delta\kappa_{\min}$ and the solution satisfies $\|\boldsymbol{x}\|_\infty \leqslant T_h$ **then**
        Solve the optimization problem Eq. (7.19).
        Switch to the new homotopy path $\boldsymbol{\Gamma}(\kappa, \boldsymbol{x}, \Omega_{j+1})$, $j \leftarrow j + 1$.
        $\Delta\kappa_{\text{iter}} \leftarrow \min(1 - \kappa, \Delta\kappa)$, $\kappa_{\text{old}} \leftarrow \kappa$, $N_s \leftarrow N_s + 1$.
      else
        $\Delta\kappa_{\text{iter}} \leftarrow \Delta\kappa_{\text{iter}}/2$. $\kappa \leftarrow \kappa_{\text{old}}$.
      end if
    end if
  end if
end while

inside the disc, PAM effectively passes a singular point but the paths return back to $\kappa = 0$, while the presented method reaches the solution by switching the path $N_s = 1$ and $N_s = 4$ times, respectively. For the case $\boldsymbol{x}_0 = [3, -0.5]^\top$, PAM passes two singular points before reaching the solution, while the presented method switches to another feasible homotopy path that eventually converges to the solution of the objective problem.

When the TFC-based DCM method is used for the case $\boldsymbol{x}_0 = [1.5, 0.5]^\top$, the limit point $\boldsymbol{x}_{L,0} = [1.3406, -0.6978]^\top$ is detected at $\kappa_{L,0} = 0.6786$. Here, the second-layer of the algorithm is triggered, and a new homotopy path is followed, starting from $\boldsymbol{x}_{0,1} = [-0.2269, -0.2570]^\top$ with

$$\Omega_1 = \begin{bmatrix} -15.4518 & -10.7949 \\ -6.7812 & -18.0602 \end{bmatrix}$$

The new homotopy path leads smoothly to $\kappa = 1$ where $\boldsymbol{x}^* = [0, 0]^\top$.

When fixed-point homotopy method is employed, numerical experiments show that it performs worse than Newton homotopy. In Fig. 7.8, fixed-point homotopy function is used. Both PAM and TFC-based DCM for the same $\boldsymbol{x}_0$ in Fig. 7.7 are simulated. For all cases, PAM fails and the x_2 paths go to infinity, while the paths generated by the presented method successfully reach the solution after few path switching. Thus, there is evidence that the presented method is robust to different user-defined homotopy functions for the current problem.

From Eq. (7.20), it is noticed that the step-size $\Delta\kappa$ affects the selection of the new path. In Fig. 7.9, the paths generated by the TFC-based DCM method with user-defined fixed-point homotopy function and $\boldsymbol{x}_0 = [2.5, 0.5]^\top$ for various $\Delta\kappa$ are illustrated. It can be seen that when $\Delta\kappa = 0.03$ is used, one more path switching arises compared to other values of $\Delta\kappa$.

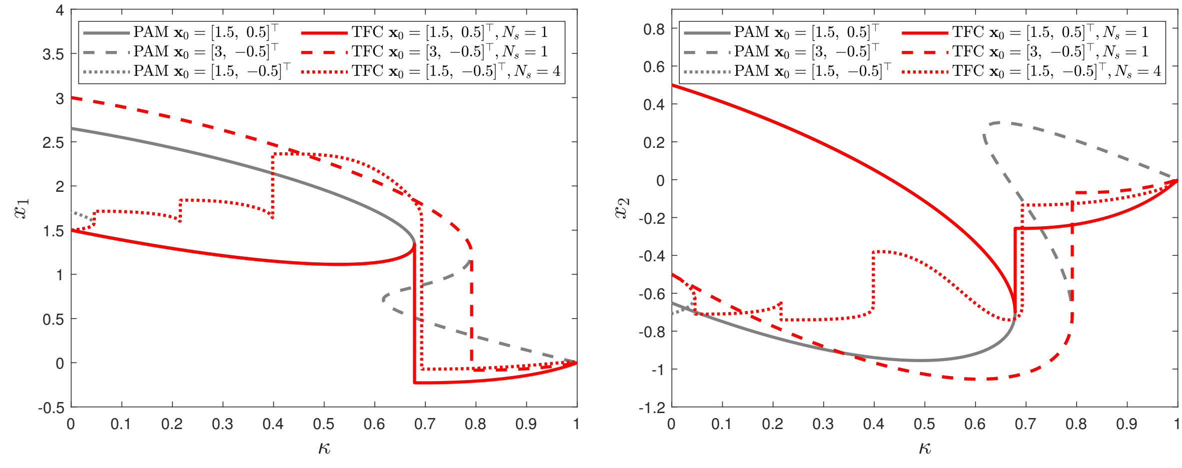

Figure 7.7: *Homotopy paths generated by the Newton homotopy method using PAM and the TFC-based DCM while attempting to find the zero of the function in Eq.* (7.22).

Thus, smaller values of $\Delta\kappa$ are preferred that favour smooth paths. As a general rule, $\Delta\kappa$ has to be smaller when the problem complexity increases.

Moreover, the effect of number of predicted points N in Eq. (7.20) on the new path selection is studied in Fig. 7.10. It can be seen that the new paths for $N = 8$ and $N = 20$ are very close, implying that the effect of N decreases as N increases if $\mathbf{\Gamma}(\kappa, \boldsymbol{x}, \Omega)$ is not abruptly changed when κ varies. Small N are preferred since larger N involve increased computational costs.

7.3.2 Nonlinear Optimal Control Problem

Solving a nonlinear optimal control problem means find the zero of a shooting function, which solves the associated two-point boundary value problem [26]. Consider the dynamical system

$$\begin{aligned} \dot{x}_1 &= x_1 + x_2 + u_1 \\ \dot{x}_2 &= \tan x_1^2 + u_2 \end{aligned} \tag{7.23}$$

along with the performance index

$$J = \frac{1}{2}\int_0^{t_f} \left(u_1^2 + u_2^2\right) \mathrm{d}t$$

where the terminal time is $t_f = 1$, and the boundary conditions are set to $\boldsymbol{x}_0 = [-1, -1]^\top$ and $\boldsymbol{x}_f = [0, 0]^\top$. An homotopy from linear to nonlinear dynamics is constructed by embedding κ into Eq. (7.23), i.e.,

$$\begin{aligned} \dot{x}_1 &= x_1 + x_2 + u_1 \\ \dot{x}_2 &= \kappa \tan x_1^2 + u_2 \end{aligned}$$

Based on the optimal control theory [26], the Euler–Lagrange equations are

$$\begin{aligned} \dot{x}_1 &= x_1 + x_2 - \lambda_1 \\ \dot{x}_2 &= \kappa \tan x_1^2 - \lambda_2 \\ \dot{\lambda}_1 &= -\lambda_1 - 2\kappa x_1 \lambda_2 / \cos^2 x_1^2 \\ \dot{\lambda}_2 &= -\lambda_1 \end{aligned} \tag{7.24}$$

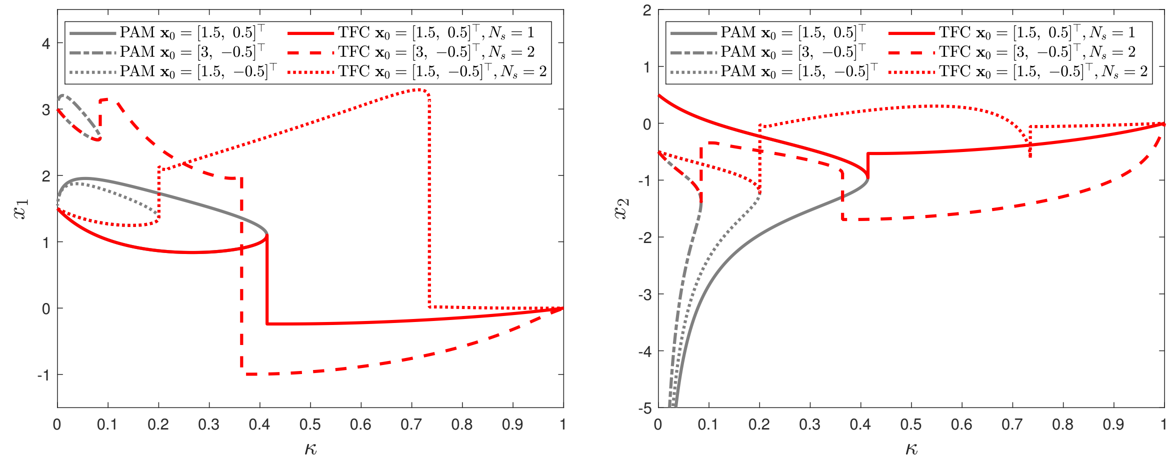

(a) **(b)**

Figure 7.8: *Homotopy paths generated by the fixed-point homotopy method using PAM and the TFC-based DCM while attempting to find the zero of the function in Eq.* (7.22)*.*

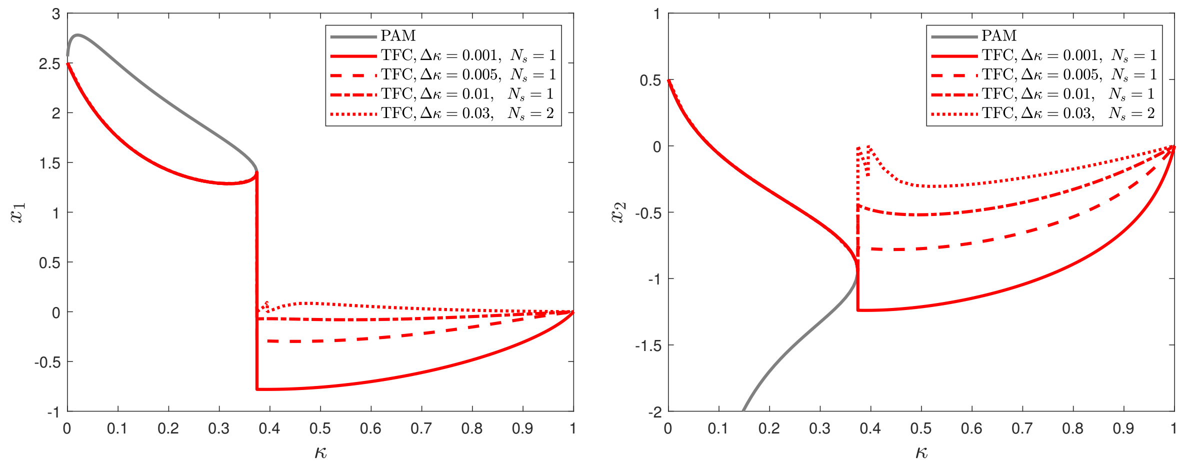

(a) **(b)**

Figure 7.9: *Homotopy paths generated by the TFC-based DCM method with user-defined fixed-point homotopy function and* $\boldsymbol{x}_0 = [2.5, 0.5]^\top$ *for different* $\Delta\kappa$*.*

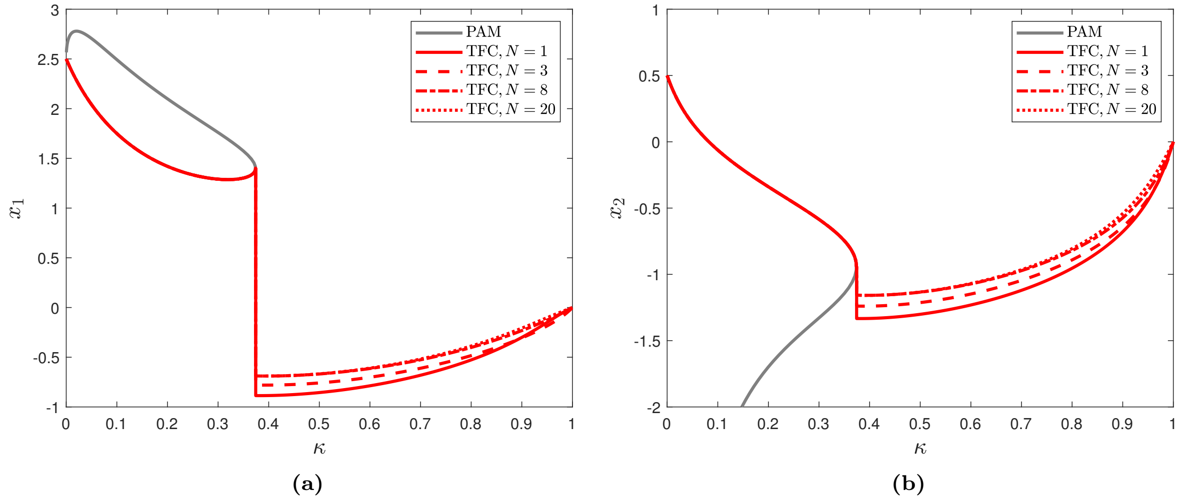

Figure 7.10: *Homotopy paths generated by the TFC-based DCM method with user-defined fixed-point homotopy function and* $\boldsymbol{x}_0 = [2.5, 0.5]^\top$ *for different* N.

For a given κ, the flow $\boldsymbol{x}(t, \boldsymbol{x}_0, \boldsymbol{\lambda}_0)$ can be obtained by integrating Eq. (7.24) with initial conditions $\boldsymbol{x}_0$ and $\boldsymbol{\lambda}_0$, where $\boldsymbol{\lambda}_0 = [\lambda_1(t_0), \lambda_2(t_0)]^\top$ is the initial costate vector. The zero-finding problem is to find $\boldsymbol{\lambda}_0$ such that $\boldsymbol{F}(\boldsymbol{\lambda}_0) = \boldsymbol{0}$, where

$$\boldsymbol{F}(\boldsymbol{\lambda}_0) = \boldsymbol{x}(t_f, \boldsymbol{x}_0, \boldsymbol{\lambda}_0) - \boldsymbol{x}_f$$

When $\kappa = 0$, the system is linear, and the corresponding initial costate is $\boldsymbol{\lambda}_0 = [-2.9411, -2.0820]^\top$. In this example, the state-dependent function $\boldsymbol{h}(\kappa, \boldsymbol{\lambda})$ is selected as

$$\boldsymbol{h}(\kappa, \boldsymbol{\lambda}) = \begin{bmatrix} \mathrm{e}^{\lambda_1}\kappa^2 \\ \mathrm{e}^{\lambda_2}\kappa^2 \end{bmatrix}$$

and $\Delta\kappa = 0.001$.

The simulation results are shown in Fig. 7.11, where the comparison of the homotopy paths for PAM (grey dashed line) and TFC-based DCM (red solid line) is shown in Fig. 7.11a, whereas the optimal trajectory is shown in Fig. 7.11b. Notice that in Fig. 7.11a the solution curve tracked by PAM successfully passes a limit point but returns back to $\kappa \simeq 0$. PAM fails to reach the solution to the objective problem at $\kappa = 1$.

When the TFC-based DCM method is used, the limit point $\boldsymbol{\lambda}_{L,0} = [-1.2251, -1.5879]^\top$ is detected at $\kappa_{L,0} = 0.5376$. The second layer switches to a new homotopy path starting from $\boldsymbol{\lambda}_{0,1} = [-0.9834, -0.6184]^\top$ with

$$\Omega_1 = \begin{bmatrix} -5.7765 & -4.1086 \\ -7.6160 & 5.7975 \end{bmatrix}$$

The new homotopy path leads smoothly to the solution of the objective problem, where $\boldsymbol{\lambda}^*(t_0) = [0.4728, -0.0739]^\top$.

7.3.3 Elastic Rod Problem

While in Sections 7.3.1 and 7.3.2 the issue was overcoming a singular point (Type 1, 3, and 4 in Fig. 7.1), in this example the path goes off to infinity without encountering any limit

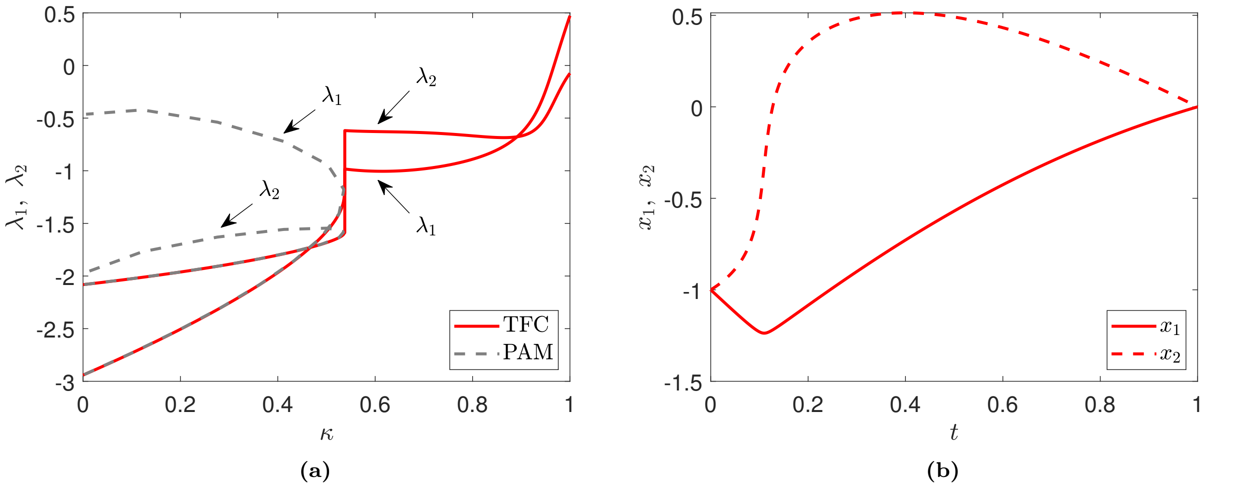

Figure 7.11: *Simulation results for the nonlinear optimal control problem. (a): Comparison of homotopy paths tracked by PAM and TFC-based DCM method; (b): Optimal trajectories $x_1(t)$ and $x_2(t)$.*

point (Type 5 in Fig. 7.1). The cantilever beam problem, which is to find the position (a, b) of the tip of the rod given the force $Q \neq 0$ and $P = 0$, has a closed-form solution in terms of elliptic integrals. The inverse problem, where the tip's position (a, b) and orientation c are specified, while the forces (Q, P) and torque (M) are to be determined, has no similar closed-form solution. It is a nonlinear problem that is difficult to solve [117]. The inverse problem is solved in this section. The dynamic equations

$$\begin{aligned}\dot{x} &= \cos\theta \\ \dot{y} &= \sin\theta \\ \dot{\theta} &= Qx - Py + M\end{aligned}$$

are supported by the boundary conditions

$$x(0) = y(0) = \theta(0) = 0, \quad x(1) = a, \quad y(1) = b, \quad \theta(1) = c$$

The unknown variables are denoted as $\boldsymbol{v} = [Q, P, M]^\top$, and the corresponding flow is denoted as $x(t, \boldsymbol{v}), y(t, \boldsymbol{v}), \theta(t, \boldsymbol{v})$. The problem is to find $\boldsymbol{v}^*$ such that

$$\boldsymbol{F}(\boldsymbol{v}^*) = \begin{bmatrix} x(t_f, \boldsymbol{v}^*) - a \\ y(t_f, \boldsymbol{v}^*) - b \\ \theta(t_f, \boldsymbol{v}^*) - c \end{bmatrix} = \boldsymbol{0} \tag{7.25}$$

A fixed-point homotopy function is defined as

$$\boldsymbol{\Gamma}_0(\kappa, \boldsymbol{v}) = (1 - \kappa)\boldsymbol{F}(\boldsymbol{v}) + \kappa\boldsymbol{G}(\boldsymbol{v}) \quad \text{with} \quad \boldsymbol{G}(\boldsymbol{v}) = (\boldsymbol{v} - \boldsymbol{v}_0)$$

where $\boldsymbol{v}_0$ is the initial guess solution. The parameters are set to $a = 0$, $b = 2\pi$, $c = \pi$, and $\boldsymbol{v}_0 = [0, 0, 1.85]^\top$. In this case, the solution to the objective problem in Eq. (7.25) is known to be $\boldsymbol{v}^* = [0, 0, \pi]^\top$ [118]. The Jacobian matrix of Eq. (7.25) w.r.t $\boldsymbol{v}$ has been computed using finite differences, and the limit threshold T_h is set to 100. The selected state-dependent basis function $\boldsymbol{h}(\kappa, \boldsymbol{v})$ is

$$\boldsymbol{h}(\kappa, \boldsymbol{v}) = \begin{bmatrix} \mathrm{e}^{Q}\kappa^2 \\ \mathrm{e}^{P}\kappa^2 \\ \mathrm{e}^{M}\kappa^2 \end{bmatrix}$$

and $\Delta\kappa = 0.001$.

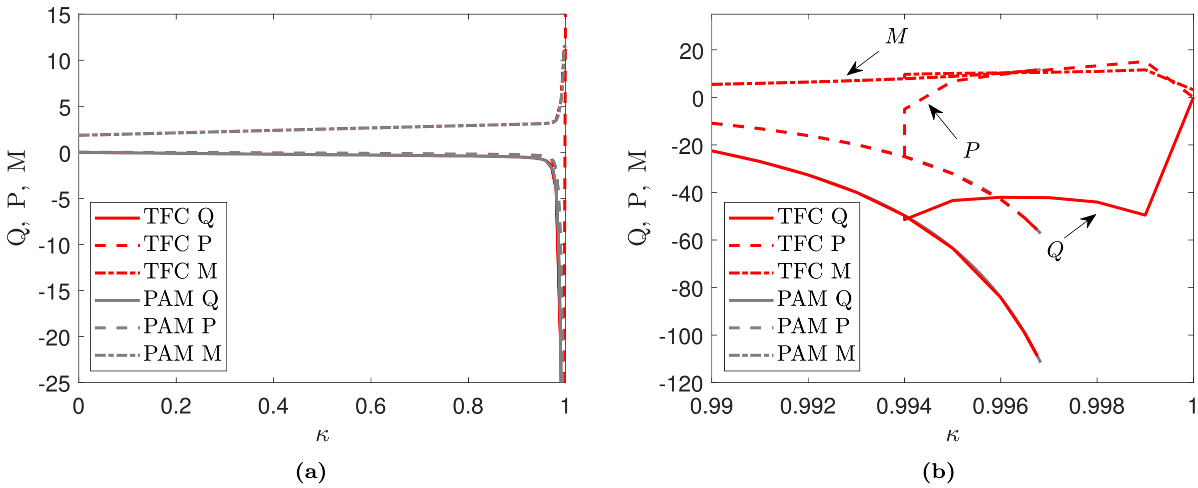

Figure 7.12: *Simulation results for elastic red problem. (a): Comparison of homotopy paths tracked by PAM (grey dashed lines) and TFC-based DCM (red solid lines); (b): Zoom-in comparison of homotopy paths when $\kappa \to 1$.*

The simulation results are shown in Fig. 7.12, where the homotopy paths generated by PAM (grey lines) and TFC-based DCM (red lines) are shown (Fig. 7.12b shows an enlarged view of Fig. 7.12a when $\kappa \to 1$). PAM is not able to reach $\boldsymbol{v}^*$ because the homotopy path grows indefinitely when $\kappa \to 1$.

Using TFC-based DCM, the failure of the initial homotopy path is detected when $\|\boldsymbol{v}\|_\infty$ exceeds T_h. The point $\boldsymbol{v}_{\mathrm{I},0} = [-99.2011, -50.7766, 11.0163]^\top$ at $\kappa_{\mathrm{I},0} = 0.9965$ is used as initial guess for problem (7.19). A new start point $\boldsymbol{v}_{0,1} = [-99.1925, -50.7788, 11.0155]^\top$ is found, with

$$\Omega_1 = \begin{bmatrix} 0 & 0 & -2.56 \times 10^{-5} \\ 0 & 0 & -1.60 \times 10^{-5} \\ 0 & 0 & 3.21 \times 10^{-4} \end{bmatrix}$$

which is very close to the initial path. Since this homotopy path excesses T_h again, a second switch is attempted using $T_h/2$. The initial guess $\boldsymbol{v}_{\mathrm{I},1} = [-49.6995, -24.9227, 7.8530]^\top$ at $\kappa_{\mathrm{I},1} = 0.9940$ is detected, and problem (7.19) is solved gain. The new homotopy path with starting point $\boldsymbol{v}_{0,2} = [-51.4515, -4.9992, 9.6862]^\top$ and

$$\Omega_2 = \begin{bmatrix} 0 & 9.03 \times 10^{-6} & -2.60 \times 10^{-3} \\ 0 & -1.60 \times 10^{-6} & 1.73 \times 10^{-3} \\ 0 & 1.27 \times 10^{-5} & 7.44 \times 10^{-4} \end{bmatrix}$$

is found. From this point on, the TFC-based DCM successfully reaches $\boldsymbol{v}^*$.

7.4 Summary

Homotopy is a deformation used in zero-finding problems. The idea is to connect an initial easy-to-solve problem to the final, objective problem through the solution of a number of intermediate, auxiliary problems that define the homotopy path. Traditional techniques based on pure DCM or PAM fail to reach the objective problem, e.g., when the homotopy path exhibits singular points or indefinite growth. The fate of these methods is already determined when the homotopy function is formulated and the initial condition is given.

The TFC-based homotopy function presented in this paper implicitly defines infinite homotopy paths. This property can be leveraged whenever either a singularity is found or the path tends to go off to infinity. In these cases, the algorithm is able to switch to a new homotopy path, which attempts to reach the objective problem. A two-layer TFC-based DCM algorithm has been developed to support our intuition. The effectiveness of this algorithm has been proved by solving sample problems where the traditional continuation methods fail.

CHAPTER 8

CONCLUSIONS

8.1 Answers to Research Questions

Answer to the first research question

> For low-thrust trajectory optimization problems with interior-point constraints, how to derive, calculate and assess analytic gradients in the indirect method ?

This thesis successfully derived analytic gradients by using calculus of variations, calculated them through establishing the computational framework, and assessed their performance with comparison to the finite difference method, for low-thrust trajectory optimization with interior-point constraints in Chapters 2, 4, and 5.

For low-thrust optimization with scalar interior-point constraints, analytical formulas of multipliers for both time-optimal and energy-to-fuel-optimal problems are obtained and leveraged such that the MPBVP is solved as a TPBVP by using the developed methods. The STM for two categories of costate and dynamics discontinuities, produced by interior-point constraints and bang-bang control, respectively, are derived. The flowchart in [47] is further augmented to involve interior-point event branches. Overall, the computational framework is established by combining analytic derivatives, continuation and switching detection into an augmented integration flowchart, which enables to achieve the desired discontinuous bang-bang solutions and their accurate gradients. The developed indirect methods have been applied to solve power-limited asteroid rendezvous (Chapter 2) and fuel-optimal many-revolution Earth-orbit transfers with eclipses (Chapter 4). Moreover, the developed method in Chapter 2 has been used to solve thousands of time-optimal and fuel-optimal trajectories to favor asteroid screening in the M-ARGO mission (Chapter 3).

For low-thrust optimization with multi-dimensional interior-point constraints, the multi-dimensional multipliers have to be sought along with other unknowns. In this case, both state and costate may be discontinuous across interior-point time instants. Analytic gradients are derived for the deep-space transfer with intermediate flyby, rendezvous and gravity-assist events in Chapter 5. The analysis is carried out for each segment first, then extends to the whole domain by using the chain rule. Special attention is paid to the derivatives of state, costate and constraints with respect to interior-point time instants, since the constraints considered are time-dependent. The recursive formulae of derivatives of each constraint with respect to unknowns at previous interior-point time instants are established. The fuel-optimal bang-bang solutions for deep-space transfers with intermediate flyby, rendezvous and gravity-assist events have been achieved.

A number of simulations have been executed in Chapters 2, 4 and 5 to assess the performance of analytic gradients. For low-thrust trajectory optimization with interior-point constraints, numerical evidences show that analytic gradients improve both computational efficiency and convergence robustness of the indirect method effectively against the finite difference method.

Answer to the second research question

> How to design homotopy continuation methods to widen the convergence domain, reduce computational load and recover failures in low-thrust trajectory optimization ?

This thesis designed tailored homotopy continuation methods for various low-thrust trajectory optimization problems. In Chapter 2, the combination of energy-to-fuel-optimal continuation and hyperbolic tangent smoothing is employed to expand the convergence domain. In Chapter 3, continuation strategies are designed to compute hundreds of asteroid pockchops, in order to reduce the computational load. In Chapter 4, an effective continuation process is proposed to determine many-revolution, fuel-optimal transfers by gradually increasing the number of the shadow pass through.

Additionally, the homotopy methods are designed to recover failures in homotopy continuation. In Chapter 6, the failure of thrust continuation for orbital transfers is resolved by connecting solutions with different revolutions. In Chapter 7, a potential TFC-based homotopy continuation method, which remedies the failure of the homotopy process for general problems through flexible path switching, is presented.

8.2 Limitations and Future Work

The limitations and future work are stated in the following.

Power-limited asteroid rendezvous trajectory design Future work will focus on the following aspects: 1) The analysis of this work does not consider singular arcs. Handling singular arcs will improve the solver robustness; 2) The assessment of the presented method for solving low-thrust fuel-optimal problems with free terminal time is of interest; 3) The extension of the presented method for the low-thrust optimization using the engine with dual-I_{sp} engine [119] and multiple operation modes [80] benefits to expanding the scope of applications of our method.

Target screening of M-ARGO mission The outcome of this work is valid for M-ARGO mission under current assumptions of departure dates and thruster model. As for the latter, it is worth observing that $P_{\min}$ is never reached by optimal solutions. Should this be the case in future iterations, the rankings would be affected. The same applies to $P_{\max}$ as well as to the other thruster coefficients.

More realistic dynamics model will be used in the next mission phase. The computation of asteroid pockchops using 3-body dynamics model (Sun-Earth-Spacecraft) is ongoing. Comparisons of 2000 SG344 and 2010 UE51 pockchops using 2-body and 3-body dynamics are shown in Fig. 8.1. Initial results indicate that 2-body pockchops enable capturing main structural characteristics of 3-body pockchops. Also, the difference on the fuel consumption is minimal. However, these preliminary conclusions have to be verified after more results coming out. Additionally, the methods to fast estimate fuel-optimal trajectories are worthy to explore [120].

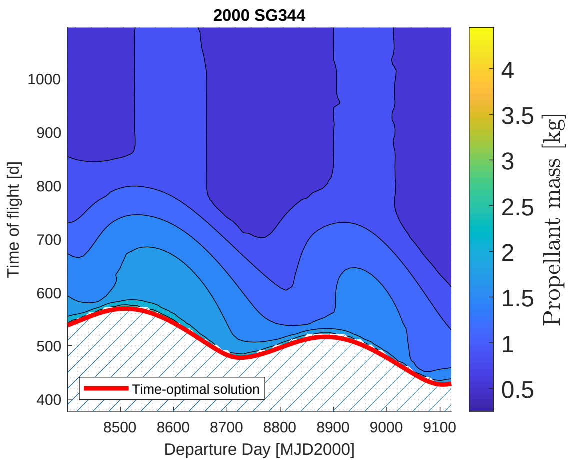

(a) *2-body 2000 SG344 pork chop*

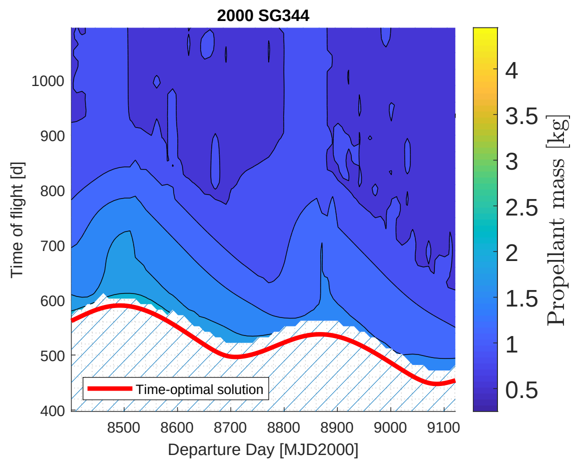

(b) *3-body 2000 SG344 pork chop*

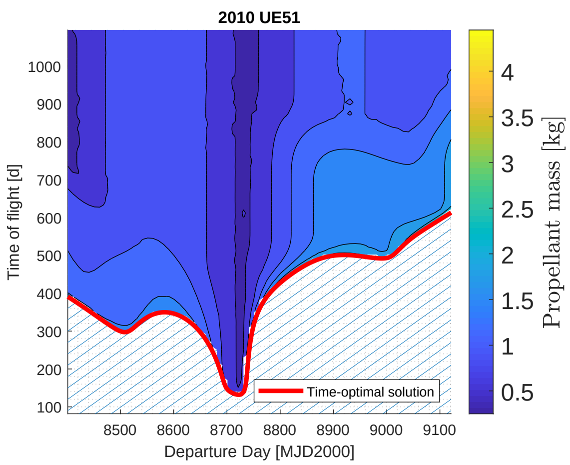

(c) *2-body 2010 UE51 pork chop*

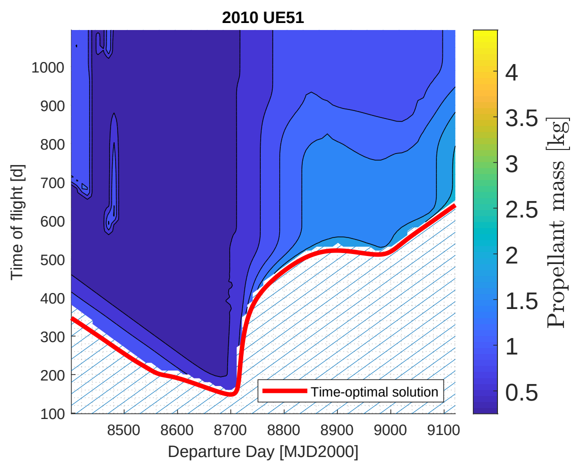

(d) *3-body 2010 UE51 pork chop*

Figure 8.1: *Pork chop plots for asteroids 2000 SG344 and 2010 UE51 under 2-body and 3-body dynamics.*

Earth-orbit transfers with eclipses Evidences from numerical simulations show that the proposed method allows effectively determining many-revolution, fuel-optimal transfers with

Earth-shadow eclipses. Our computational framework is also effective for time-optimal transfers, see [49]. However, the issue arises when trying to solve many-revolution time-optimal transfers. In this case, the transfer time is one of the unknowns to solve. When the continuation fails, it is difficult to find out the reason behind the failure, i.e., it is not clear if the failure is caused by the ill-conditioned STM or by the fact that the guessed transfer time is not long enough. Future work will try to solve this issue from two aspects. One is to redesign a better continuation procedure. The other is to develop a mathematical method to regularize the possibility of the ill-conditioned STM.

Space missions with multi-dimensional interior-point constraints The method by trial and errors is used to search a good initial guess solution. The number of tries is dozens of times until one solution is found. The probability of convergence is low. Thus, the automatic method to generate a good initial guess is necessary to improve the algorithmic effectiveness, especially for the interplanetary transfers with intermediate gravity-assist events where many unknowns are involved. In this aspect, particle swarm algorithm has been developed in [44] to generate the initial guess. Future work will try to develop global optimization methods and the combination with direct methods to search a good initial guess with higher solution efficiency.

Thrust continuation for Earth-orbit transfers The developed method is tailored to the planetocentric transfers. However, the method is unable to directly solve the trajectory optimization problems in the three-body system, such as the Earth-Moon system. Moreover, the computational effort is high, which may require several days. Future work will investigate the possibility to extend the idea of this work to the three-body system, and the method to further reduce the computational burden.

TFC-based homotopy continuation method The effectiveness of the presented TFC-based homotopy method is demonstrated through simple examples. Future work will investigate the following aspects to enhance the robustness of TFC-based homotopy method: 1) Methods with high computational efficiency such as convex programming, least-square methods or Lyapunov methods, etc., are worth to explore; 2) The presented method is a local continuation method, yet it is a valuable direction towards designing probability-one homotopy methods for general applications; 3) The extension of this method to aerospace applications is of interest.

Appendices

APPENDIX $\mathcal{A}$

APPENDIX A

A.1 Rankings of Time-Optimal Transfers

Time-optimal transfers are ranked here below. #: position in the ranking; Name: asteroid name; $\tau_{\min}$: minimum transfer time; $m_p(\tau_{\min})$: fuel consumption corresponding to the minimum-time solution; Dep. Date: departure date; H: absolute magnitude; D: estimated diameter; N_{obs}: number of observations; N_{opp}: number of oppositions.

#	Name	$\tau_{\min}$ [d]	$m_p(\tau_{\min})$ [kg]	Dep. Date	H [-]	D [m]	N_{obs}	N_{opp}
1	2010 UE51	131.82	0.693	04 Mar 2023	28.3	7.5	175	1
2	2015 KK57	295.28	1.359	03 Oct 2023	27.5	10.9	43	1
3	2011 MD	302.11	1.597	07 Jan 2023	28	8.6	1487	1
4	2009 BD	312.82	1.441	01 Jan 2023	28.1	8.2	178	3
5	2016 TB57	340.70	1.611	05 Dec 2024	26.1	20.7	137	1
6	2014 JR24	345.15	1.966	01 Jan 2023	29.3	4.7	54	1
7	2019 DJ1	349.56	1.770	31 Dec 2024	26.7	15.7	82	2
8	2016 CF137	352.89	1.656	05 Dec 2024	25.6	26.0	50	1
9	2014 BA3	355.69	2.032	17 Nov 2023	28.2	7.9	69	1
10	2012 BB14	361.40	1.793	04 Apr 2023	25	34.3	35	2
11	2014 LJ	367.31	1.699	21 May 2024	28.5	6.8	25	1
12	2017 YW3	370.33	1.968	31 Dec 2024	26.5	17.2	53	1
13	2008 CM74	373.96	2.028	24 Apr 2024	28.1	8.2	17	1
14	2012 EP10	378.58	2.066	16 Dec 2024	29.1	5.2	31	1
15	2008 ST	384.77	2.098	19 Jun 2023	27.1	13.0	49	1
16	2014 YD	395.10	1.932	31 Dec 2024	24.3	47.4	104	1
17	2017 RL2	402.66	1.860	22 Jul 2023	26.1	20.7	44	1
18	2001 QJ142	410.17	2.005	15 May 2023	23.7	62.4	91	2
19	2011 BQ50	419.76	2.488	01 Jan 2023	28	8.6	25	1
20	2010 JR34	421.98	2.464	31 Dec 2024	27.7	9.9	36	1

21	2012 UV136	423.38	2.088	06 Feb 2023	25.5	27.3	125	7
22	2000 SG344	427.48	2.109	10 Jun 2024	24.7	39.4	31	2
23	2015 VO142	427.82	2.339	15 Nov 2024	28.9	5.7	112	1
24	2008 JL24	432.43	2.390	01 Jan 2023	29.6	4.1	81	1
25	2015 VU64	435.24	2.507	01 Jan 2023	30.6	2.6	30	1
26	2018 GE	441.42	2.430	31 Dec 2024	27.5	10.9	54	1
27	2016 EU84	446.65	2.576	31 Dec 2024	29	5.4	94	1
28	2015 XD169	446.86	2.330	18 Jul 2023	26.9	14.3	46	1
29	2016 WQ3	452.13	2.077	31 Dec 2024	28.8	6.0	37	1
30	2019 ED	459.03	2.723	31 Dec 2024	26.9	14.3	67	1
31	2017 KJ32	459.49	2.670	12 Mar 2023	28.9	5.7	37	1
32	2017 HK1	459.85	2.646	13 Apr 2023	25.1	32.8	78	1
33	2019 AP8	461.14	1.989	31 Dec 2024	24.3	47.4	68	2
34	2019 GF1	472.58	2.810	22 Aug 2024	27.4	11.4	27	1
35	2008 DL4	479.15	2.790	31 Dec 2024	26.9	14.3	29	1
36	2017 DV35	479.49	2.755	24 Oct 2024	27.2	12.5	43	1
37	2011 WU2	479.65	2.152	19 Jun 2023	24.9	35.9	14	1
38	2014 YN	485.35	2.799	19 Nov 2023	25.7	24.9	80	1
39	2009 HC	487.47	2.757	15 Jun 2024	24.7	39.4	145	1
40	2018 TS4	493.54	2.671	20 Jul 2023	27.6	10.4	28	1
41	1999 AO10	497.74	2.773	31 Dec 2024	23.9	56.9	73	1
42	2016 TB18	502.17	2.822	18 Jun 2023	24.8	37.6	96	1
43	2015 BM510	503.39	2.676	03 Aug 2024	25.1	32.8	58	1
44	2013 TG6	504.07	2.882	17 Oct 2024	26.6	16.4	63	1
45	2012 SX49	510.97	2.885	31 Dec 2024	26.2	19.7	35	1
46	2018 PK21	511.00	3.025	12 Oct 2023	25.9	22.7	72	1
47	2016 BQ	511.59	2.598	30 Apr 2023	26.8	15.0	40	1
48	2016 FU12	514.43	2.631	24 Oct 2023	26.9	14.3	19	1
49	2016 HF19	515.16	2.960	11 Nov 2024	26.5	17.2	90	1
50	2018 PN22	516.02	2.932	01 Jan 2023	27.5	10.9	17	1
51	2018 DC4	516.59	3.016	18 May 2023	27.3	11.9	19	1
52	2011 ED12	520.33	2.824	31 Dec 2024	26.8	15.0	82	1
53	2016 CH30	521.75	2.872	01 Jan 2023	28	8.6	34	1
54	2011 CL50	526.32	3.016	03 Jun 2023	27.6	10.4	28	1
55	2012 VC26	531.30	2.897	09 Jul 2024	28.7	6.2	28	1
56	2012 TF79	531.37	2.998	04 Jun 2024	27.4	11.4	59	1
57	2008 HU4	532.62	2.979	31 Dec 2024	28.3	7.5	77	2
58	2015 XZ378	536.69	2.486	14 Apr 2024	27.2	12.5	35	1
59	2016 DF	542.00	2.623	15 Jun 2024	27	13.7	45	1
60	2010 HA	545.07	2.865	20 Sep 2023	23.9	56.9	62	2
61	2018 VN5	549.44	2.892	31 Dec 2024	25.4	28.5	94	1
62	2007 BB	550.99	2.986	01 Jan 2023	27.8	9.5	20	1
63	2019 GE1	552.81	2.896	26 Jun 2023	27	13.7	17	1
64	2000 SZ162	568.64	3.119	15 Aug 2023	27.3	11.9	30	1
65	2014 FW32	569.12	3.311	31 Dec 2024	27	13.7	23	1
66	2014 HW	569.71	2.852	03 Mar 2023	28.4	7.2	28	1
67	2018 NX	572.39	3.200	26 Apr 2024	27.7	9.9	28	1
68	2001 GP2	574.12	2.613	14 Jul 2023	26.9	14.3	28	1
69	2018 KP1	576.44	2.782	01 Jan 2023	25.1	32.8	50	2
70	2011 CE22	581.04	2.837	19 Jun 2023	25.4	28.5	18	1
71	2007 RO17	582.26	3.148	13 Jan 2023	25.8	23.7	18	1
72	2010 TE55	583.87	3.557	06 Oct 2024	28	8.6	139	1
73	2006 RH120	589.52	3.376	12 Mar 2023	29.5	4.3	133	2
74	2019 GV5	590.94	3.116	15 Mar 2023	29.3	4.7	31	1
75	2013 GH66	591.70	3.417	31 Dec 2024	28	8.6	46	1
76	2014 EK24	592.30	2.950	24 Oct 2024	23.3	75.1	583	2

77	2012 WH	593.13	3.319	27 May 2024	25.5	27.3	43	1
78	2004 VJ1	594.69	3.010	07 Jan 2023	24.1	51.9	98	2
79	2017 QB35	595.29	3.314	31 Dec 2024	29.3	4.7	33	1
80	2014 YP44	597.54	3.665	17 Sep 2024	26.1	20.7	13	1
81	2013 BS45	604.69	3.710	30 Aug 2023	25.9	22.7	92	2
82	2010 WU8	605.66	3.103	14 Jul 2024	24.2	49.6	24	1
83	2018 PM28	605.99	2.742	01 Jan 2023	25.7	24.9	46	2
84	2018 LQ2	606.60	3.363	31 Dec 2024	24.9	35.9	468	1
85	2016 GK135	607.52	3.679	17 Jul 2023	28.1	8.2	21	1
86	2018 SD2	611.04	3.161	16 Oct 2024	28.6	6.5	14	1
87	2019 LB1	614.23	3.471	01 Jan 2023	27	13.7	61	1
88	2017 TP4	615.43	3.403	18 Sep 2024	26.3	18.9	41	1
89	2008 UA202	616.60	3.687	31 Dec 2024	29.4	4.5	16	1
90	2018 FM3	617.95	2.961	22 Oct 2023	27.2	12.5	47	1
91	2014 QN266	618.60	3.707	14 Mar 2023	26.3	18.9	81	1
92	2011 AA37	619.08	3.373	01 Jan 2023	22.8	94.5	130	2
93	2018 VT7	619.15	3.784	04 Dec 2023	27.9	9.0	23	1
94	2013 RZ53	619.45	2.775	24 Apr 2023	31.1	2.1	31	1
95	2017 QW1	619.56	3.741	17 Aug 2023	26.2	19.7	36	1
96	2016 CO248	620.02	3.592	10 Dec 2023	27.5	10.9	30	1
97	2016 SX1	620.71	3.584	08 Dec 2024	28.6	6.5	37	1
98	2015 YK	623.23	2.960	16 Dec 2023	25.9	22.7	96	1
99	2014 HN2	625.70	3.810	02 Jan 2023	26.5	17.2	64	1
100	2015 JD3	629.20	3.583	01 Jan 2023	25.5	27.3	37	1
101	2017 UA45	632.36	3.526	14 Nov 2023	26.1	20.7	39	1
102	2019 AU	634.09	3.168	12 Nov 2024	26.7	15.7	48	1
103	2015 PS228	639.44	3.830	24 Mar 2023	28.8	6.0	38	1
104	2019 HM	640.18	3.761	25 Feb 2023	25.9	22.7	32	1
105	2017 YS1	644.07	3.913	01 Jan 2023	28.9	5.7	31	1
106	2018 GR4	644.78	3.150	31 Dec 2024	27.1	13.0	64	1
107	2016 RN20	645.02	3.463	31 Dec 2024	28.2	7.9	19	1
108	2012 PB20	646.80	3.431	31 Dec 2024	24.9	35.9	45	1
109	2010 FY9	647.95	3.522	31 Dec 2024	26.7	15.7	22	1
110	2012 AQ	653.45	2.821	01 Jan 2023	30.7	2.5	24	1
111	2017 YD1	654.94	3.665	16 Jan 2024	30	3.4	29	1
112	2019 FS2	657.28	3.952	01 Jan 2023	27.3	11.9	46	1
113	1999 CG9	662.48	3.058	11 Jan 2023	25.2	31.3	42	1
114	2018 RO5	662.50	3.592	16 Jun 2024	25.6	26.0	96	1
115	2017 BZ6	662.73	3.469	13 Sep 2024	26.1	20.7	71	1
116	2012 HK31	666.02	2.988	01 Nov 2023	25.4	28.5	63	1
117	2010 XF3	666.52	3.990	16 Feb 2024	24.4	45.2	94	1
118	2014 UN114	666.60	3.520	01 Jan 2023	24.5	43.2	177	1
119	2016 FZ13	668.88	3.346	19 Feb 2023	28.3	7.5	20	1
120	2015 XC352	670.87	3.177	26 Jan 2023	25.7	24.9	75	2
121	2015 DU	671.74	2.859	15 Sep 2023	26.6	16.4	96	1
122	2016 HF2	675.09	3.860	23 Jul 2023	26.1	20.7	77	1
123	2018 ER1	680.94	3.541	31 Dec 2024	25.6	26.0	61	1
124	2016 LC9	685.49	3.803	05 Jul 2024	27	13.7	30	1
125	2019 JN2	689.59	3.396	07 Apr 2023	25.7	24.9	47	1
126	2006 JY26	690.41	3.111	31 Dec 2024	28.4	7.2	76	1
127	2005 QP11	698.41	3.345	31 Dec 2024	26.4	18.0	53	1
128	2012 FM35	698.42	3.108	25 Jul 2024	27.3	11.9	77	1
129	2019 GM1	699.46	3.804	31 Dec 2024	27.5	10.9	14	1
130	2008 KT	699.94	3.140	22 Jul 2023	28.2	7.9	30	1
131	2007 UN12	704.27	3.080	31 Dec 2024	28.7	6.2	120	1
132	2017 RL16	707.17	3.241	29 Jul 2024	25	34.3	51	1

133	2018 SF3	708.99	3.605	08 Aug 2023	25.2	31.3	31	1
134	2019 AC3	712.91	3.230	31 Oct 2024	27.3	11.9	43	1
135	2013 UT4	714.24	3.335	27 Jun 2024	26.2	19.7	24	1
136	2018 UE1	723.22	3.416	01 Jan 2023	26.7	15.7	55	1
137	2017 DR109	724.49	3.414	31 Dec 2024	27.6	10.4	28	1
138	2017 UQ6	726.82	3.532	25 Sep 2024	27.2	12.5	25	1
139	2017 KU34	729.10	3.418	02 Sep 2023	23.6	65.4	78	3
140	2014 AE29	729.65	3.824	15 Jan 2023	27.4	11.4	26	1
141	2011 MQ3	736.52	3.326	31 Dec 2024	24.8	37.6	71	1
142	2013 VM13	739.72	3.572	09 Mar 2023	23.9	56.9	46	2
143	2008 EA9	744.24	3.118	04 Apr 2023	27.7	9.9	56	1
144	2014 MZ17	745.60	3.549	05 Jan 2023	24.1	51.9	47	2
145	2018 FM2	746.00	3.497	08 Apr 2023	26.6	16.4	18	1
146	2017 FP101	747.34	3.972	01 Jan 2023	24.7	39.4	48	1
147	2008 GM2	747.74	3.254	20 Jul 2024	28.3	7.5	54	1
148	2016 YR	748.47	3.279	31 Dec 2024	27.2	12.5	52	1
149	2017 JB2	749.62	3.418	24 Jan 2023	29.2	5.0	33	1
150	2007 WU3	750.25	3.382	23 Dec 2024	23.8	59.6	35	3
151	2016 EE28	752.08	3.391	25 Feb 2023	26.8	15.0	22	1
152	1991 VG	755.50	3.193	18 Nov 2024	28.3	7.5	66	3
153	2009 CV	763.83	3.240	02 Jul 2023	24.3	47.4	174	4
154	2013 WR45	776.78	3.620	01 Jan 2023	25.7	24.9	22	1
155	2019 KM2	788.09	3.420	27 Jul 2023	25.5	27.3	14	1
156	2018 FH1	794.30	3.866	20 Dec 2024	26.6	16.4	43	1
157	2019 DH1	796.84	3.423	14 Mar 2023	26.2	19.7	53	1
158	2018 LE1	799.03	3.489	13 Apr 2024	27.5	10.9	55	1
159	2018 PR7	804.18	3.534	27 Apr 2023	28.5	6.8	55	1
160	2014 JX54	810.60	3.425	16 Jun 2023	24.4	45.2	17	1
161	2011 OJ45	811.69	3.551	17 Oct 2023	26	21.6	21	1
162	YORP	818.52	3.687	30 Sep 2023	22.7	99.0	533	5
163	2009 BK2	830.55	3.780	15 Aug 2024	25.3	29.9	27	1
164	2001 GO2	842.00	3.780	13 Jul 2023	24.3	47.4	23	1
165	2018 WV1	843.23	3.636	22 Jul 2024	30.3	3.0	87	1
166	2004 QA22	844.14	3.845	25 Sep 2024	27.9	9.0	44	1
167	2016 TY55	852.18	3.724	26 Jan 2023	26.9	14.3	44	1
168	2014 WU200	855.27	3.558	08 Sep 2023	29.1	5.2	46	1
169	2015 TC25	858.58	3.716	01 Jan 2023	29.3	4.7	44	2
170	2007 VU6	864.20	3.890	07 May 2023	26.5	17.2	38	1
171	2019 LE1	875.50	3.831	01 Jan 2023	26.4	18.0	28	1
172	2018 XX3	878.36	3.778	09 Jan 2023	29.7	3.9	23	1

Table A.1: *Ranking of time-optimal transfers.*

A.2 Ranking of Fuel-Optimal Transfers

Fuel-optimal transfers are ranked here below. $m_{p,\min}$: minimum fuel consumption; TOF: time of flight corresponding to the minimum-fuel solution.

#	Name	$m_{p,\min}$ [kg]	TOF [d]	Dep. Date	H [-]	D [m]	N_{obs}	N_{opp}
1	2010 UE51	0.452	1095	07 Nov 2023	28.3	7.5	175	1
2	2009 BD	0.638	1095	05 Feb 2024	28.1	8.2	178	3
3	2000 SG344	0.717	972.93	01 Jan 2023	24.7	39.4	31	2
4	2001 GP2	0.740	967.70	09 Aug 2023	26.9	14.3	28	1
5	2015 KK57	0.848	720.62	01 Jan 2023	27.5	10.9	43	1
6	2016 TB57	0.873	920.64	05 Feb 2024	26.1	20.7	137	1

7	2008 JL24	0.917	1089.18	27 Nov 2023	29.6	4.1	81	1
8	2014 YD	0.969	1089.88	21 Apr 2023	24.3	47.4	104	1
9	2012 TF79	0.985	1072.06	14 Jun 2024	27.4	11.4	59	1
10	2008 HU4	1.033	1095	05 May 2024	28.3	7.5	77	2
11	2011 MD	1.035	1071.06	11 Dec 2024	28	8.6	1487	1
12	2016 TB18	1.052	1093.60	30 Jul 2023	24.8	37.6	96	1
13	2012 EP10	1.056	1059.41	21 Dec 2024	29.1	5.2	31	1
14	2016 WQ3	1.100	1038.50	21 May 2023	28.8	6.0	37	1
15	2015 VO142	1.122	1000.31	01 Apr 2023	28.9	5.7	112	1
16	2014 QN266	1.173	1079.37	09 Aug 2023	26.3	18.9	81	1
17	2018 TS4	1.192	1070.21	02 Mar 2023	27.6	10.4	28	1
18	2019 GF1	1.208	1095	15 May 2024	27.4	11.4	27	1
19	2006 RH120	1.221	1095	28 Oct 2023	29.5	4.3	133	2
20	2015 XZ378	1.240	1095	01 Jan 2023	27.2	12.5	35	1
21	2017 TP4	1.242	1095	11 Jan 2023	26.3	18.9	41	1
22	2008 UA202	1.261	1095	14 Jul 2024	29.4	4.5	16	1
23	2015 PS228	1.277	1080.73	06 Mar 2024	28.8	6.0	38	1
24	2006 JY26	1.307	1095	19 Aug 2023	28.4	7.2	76	1
25	2007 UN12	1.316	1095	16 Jan 2024	28.7	6.2	120	1
26	2017 RL2	1.323	1084.56	11 Apr 2023	26.1	20.7	44	1
27	2018 FM2	1.335	1072.13	26 Jan 2024	26.6	16.4	18	1
28	2018 GR4	1.339	933.23	07 Dec 2023	27.1	13.0	64	1
29	2016 CF137	1.352	912.60	08 Sep 2023	25.6	26.0	50	1
30	2018 PM28	1.358	1048.49	01 Jan 2023	25.7	24.9	46	2
31	2014 JR24	1.369	1095	21 May 2023	29.3	4.7	54	1
32	2013 RZ53	1.374	1095	21 Nov 2024	31.1	2.1	31	1
33	2008 EA9	1.375	1095	20 Jul 2023	27.7	9.9	56	1
34	2014 LJ	1.396	795.84	17 Nov 2023	28.5	6.8	25	1
35	2018 PK21	1.401	968.35	10 Jul 2023	25.9	22.7	72	1
36	2017 UQ6	1.401	1095	21 Dec 2024	27.2	12.5	25	1
37	2019 AP8	1.404	1095	10 Jul 2023	24.3	47.4	68	2
38	2015 BM510	1.415	1037.66	21 Apr 2023	25.1	32.8	58	1
39	2017 YW3	1.417	845.92	15 Feb 2024	26.5	17.2	53	1
40	2018 LQ2	1.442	1095	01 Jan 2023	24.9	35.9	468	1
41	2008 ST	1.451	903.82	01 May 2023	27.1	13.0	49	1
42	2011 BQ50	1.474	1017.07	11 Dec 2024	28	8.6	25	1
43	2018 KP1	1.478	1095	01 Jan 2023	25.1	32.8	50	2
44	2008 KT	1.487	1095	30 Jul 2023	28.2	7.9	30	1
45	2018 GE	1.505	939.72	15 May 2024	27.5	10.9	54	1
46	2010 JR34	1.521	1061.92	21 Apr 2023	27.7	9.9	36	1
47	2013 BS45	1.524	1068.37	21 Dec 2024	25.9	22.7	92	2
48	2012 FM35	1.561	1073.42	02 Mar 2023	27.3	11.9	77	1
49	2008 CM74	1.618	1023.81	31 May 2023	28.1	8.2	17	1
50	2018 VN5	1.638	1095	03 Aug 2024	25.4	28.5	94	1
51	2012 BB14	1.645	1051.41	01 Jan 2023	25	34.3	35	2
52	1991 VG	1.645	1055.50	20 Jun 2023	28.3	7.5	66	3
53	2000 SZ162	1.645	982.97	10 Jul 2023	27.3	11.9	30	1
54	2019 DJ1	1.671	834.90	01 Jan 2023	26.7	15.7	82	2
55	2014 BA3	1.683	1095	10 Jul 2023	28.2	7.9	69	1
56	2012 UV136	1.686	1080.14	30 Jul 2023	25.5	27.3	125	7
57	2016 FU12	1.706	1041.21	01 Apr 2023	26.9	14.3	19	1
58	2001 QJ142	1.721	1078.27	05 Apr 2024	23.7	62.4	91	2
59	2015 JD3	1.772	1095	20 Jun 2023	25.5	27.3	37	1
60	2011 ED12	1.783	1095	24 Jun 2024	26.8	15.0	82	1
61	2004 VJ1	1.789	1090.48	01 Jan 2023	24.1	51.9	98	2
62	2015 VU64	1.792	902.88	10 Jul 2023	30.6	2.6	30	1

63	2010 TE55	1.827	1026.83	10 Jul 2023	28	8.6	139	1
64	2011 AA37	1.834	1058.16	21 Dec 2024	22.8	94.5	130	2
65	2015 DU	1.855	1095	28 Sep 2023	26.6	16.4	96	1
66	2011 WU2	1.865	1034.97	26 Mar 2024	24.9	35.9	14	1
67	2014 YN	1.867	933.26	21 Apr 2023	25.7	24.9	80	1
68	2013 GH66	1.873	1051.13	20 Feb 2023	28	8.6	46	1
69	1999 AO10	1.884	1072.70	31 May 2023	23.9	56.9	73	1
70	2012 HK31	1.884	1095	21 May 2023	25.4	28.5	63	1
71	2016 HF19	1.901	1095	07 Nov 2023	26.5	17.2	90	1
72	2007 VU6	1.911	1093.00	12 Mar 2023	26.5	17.2	38	1
73	2019 ED	1.916	1095	01 Jan 2023	26.9	14.3	67	1
74	2014 WU200	1.921	1095	27 Nov 2023	29.1	5.2	46	1
75	2012 AQ	1.929	1088.45	01 Dec 2024	30.7	2.5	24	1
76	2017 DV35	1.931	977.24	01 Jan 2023	27.2	12.5	43	1
77	2018 DC4	1.935	977.05	11 Dec 2024	27.3	11.9	19	1
78	2017 YD1	1.937	1095	21 Dec 2024	30	3.4	29	1
79	2016 DF	1.964	1016.21	27 Nov 2023	27	13.7	45	1
80	2018 VT7	1.965	1095	25 Feb 2024	27.9	9.0	23	1
81	2009 CV	1.985	1095	11 Jan 2023	24.3	47.4	174	4
82	2016 BQ	1.989	1095	01 Dec 2024	26.8	15.0	40	1
83	2011 CL50	1.993	972.21	20 Jul 2023	27.6	10.4	28	1
84	2008 DL4	1.998	875.56	01 Jan 2023	26.9	14.3	29	1
85	2018 WV1	2.012	1083.23	12 Mar 2023	30.3	3.0	87	1
86	2015 XD169	2.022	1095	31 Jan 2023	26.9	14.3	46	1
87	2014 EK24	2.029	1095	06 Jan 2024	23.3	75.1	583	2
88	2016 YR	2.046	1095	30 Jul 2023	27.2	12.5	52	1
89	2018 SD2	2.050	1095	21 May 2023	28.6	6.5	14	1
90	2013 VM13	2.056	1077.70	21 Dec 2024	23.9	56.9	46	2
91	2018 FM3	2.057	1093.49	22 Oct 2024	27.2	12.5	47	1
92	2016 CH30	2.067	1062.13	10 Jul 2023	28	8.6	34	1
93	2010 HA	2.071	1095	03 Aug 2024	23.9	56.9	62	2
94	2019 DH1	2.075	1095	01 Jan 2023	26.2	19.7	53	1
95	2018 PN22	2.099	1095	21 Nov 2024	27.5	10.9	17	1
96	2009 HC	2.101	1089.68	21 Dec 2024	24.7	39.4	145	1
97	2017 HK1	2.112	1095	28 Sep 2023	25.1	32.8	78	1
98	2004 QA22	2.127	1095	20 Feb 2023	27.9	9.0	44	1
99	2011 OJ45	2.129	1095	02 Oct 2024	26	21.6	21	1
100	2017 KJ32	2.146	971.47	21 Jan 2023	28.9	5.7	37	1
101	2012 SX49	2.147	1095	31 May 2023	26.2	19.7	35	1
102	2016 GK135	2.150	1095	10 Jun 2023	28.1	8.2	21	1
103	2019 GV5	2.169	1067.54	01 Jan 2023	29.3	4.7	31	1
104	2016 EU84	2.169	926.65	16 Jan 2024	29	5.4	94	1
105	2014 FW32	2.182	1095	21 Nov 2024	27	13.7	23	1
106	2012 VC26	2.185	1095	19 Aug 2023	28.7	6.2	28	1
107	2014 YP44	2.189	1095	02 Oct 2024	26.1	20.7	13	1
108	1999 CG9	2.198	1095	01 Dec 2024	25.2	31.3	42	1
109	2011 CE22	2.201	1095	11 Apr 2023	25.4	28.5	18	1
110	2019 AU	2.210	1095	20 Jun 2023	26.7	15.7	48	1
111	2014 HN2	2.269	1016.28	31 May 2023	26.5	17.2	64	1
112	2007 WU3	2.277	1095	10 Jun 2023	23.8	59.6	35	3
113	2016 SX1	2.279	1095	11 Jan 2023	28.6	6.5	37	1
114	2015 YK	2.295	948.47	10 Jul 2023	25.9	22.7	96	1
115	2017 RL16	2.318	1095	08 Sep 2023	25	34.3	51	1
116	2013 TG6	2.321	1007.76	13 Aug 2024	26.6	16.4	63	1
117	2019 KM2	2.331	1095	01 Jan 2023	25.5	27.3	14	1
118	2019 AC3	2.341	1095	02 Mar 2023	27.3	11.9	43	1

119	2016 RN20	2.352	1095	02 Mar 2023	28.2	7.9	19	1
120	2007 BB	2.395	1065.55	01 Apr 2023	27.8	9.5	20	1
121	2017 JB2	2.410	1095	25 Apr 2024	29.2	5.0	33	1
122	2010 WU8	2.412	1044.28	14 Jun 2024	24.2	49.6	24	1
123	2018 UE1	2.420	1095	02 Oct 2024	26.7	15.7	55	1
124	2018 LE1	2.423	1095	13 Aug 2024	27.5	10.9	55	1
125	2007 RO17	2.457	1050.54	12 Mar 2023	25.8	23.7	18	1
126	2016 FZ13	2.461	1095	17 Nov 2023	28.3	7.5	20	1
127	2014 HW	2.468	1023.04	30 Jun 2023	28.4	7.2	28	1
128	2015 TC25	2.488	1095	21 Dec 2024	29.3	4.7	44	2
129	2014 MZ17	2.510	1095	01 Jan 2023	24.1	51.9	47	2
130	2008 GM2	2.522	1095	16 Jan 2024	28.3	7.5	54	1
131	2017 BZ6	2.536	1095	14 Jul 2024	26.1	20.7	71	1
132	2012 WH	2.555	1078.02	04 Jun 2024	25.5	27.3	43	1
133	2017 QW1	2.560	1020.03	11 Jan 2023	26.2	19.7	36	1
134	2018 PR7	2.561	1095	30 Jun 2023	28.5	6.8	55	1
135	2017 QB35	2.579	1000.15	21 Dec 2024	29.3	4.7	33	1
136	2019 GE1	2.592	1095	03 Aug 2024	27	13.7	17	1
137	2014 UN114	2.598	922.45	01 Jan 2023	24.5	43.2	177	1
138	2005 QP11	2.603	1095	21 Jan 2023	26.4	18.0	53	1
139	2018 FH1	2.613	1095	04 Jul 2024	26.6	16.4	43	1
140	2012 PB20	2.626	1095	01 Jan 2023	24.9	35.9	45	1
141	2018 NX	2.634	1032.48	10 Jun 2023	27.7	9.9	28	1
142	2015 XC352	2.647	1092.40	05 Apr 2024	25.7	24.9	75	2
143	2016 TY55	2.702	1095	21 Dec 2024	26.9	14.3	44	1
144	2017 YS1	2.722	1095	11 May 2023	28.9	5.7	31	1
145	2019 LB1	2.726	1095	01 Nov 2024	27	13.7	61	1
146	2011 MQ3	2.765	1095	01 May 2023	24.8	37.6	71	1
147	YORP	2.776	1095	01 Apr 2023	22.7	99.0	533	5
148	2010 FY9	2.791	994.37	01 Jan 2023	26.7	15.7	22	1

Table A.2: *Ranking of fuel-optimal transfers.*

A.3 Fuel-Optimal Porkchops Plots

Fuel-optimal porkchop plots for the 172 targets in A.1. The plots style has been simplified to favour readability, and common axes and color range have been adopted to ease comparison. The following conventions are used:

- x-axis: departure date; Range: Jan 1st, 2023–Dec 31st, 2024 (8401–9131 MJD2000);
- y-axis: time of flight; Range: 290–1095 days;
- Color code: fuel consumption; Range: 0.25–4.45 kg, same color code as in Fig. 3.11;
- Isolines step: 0.3 kg.

In all plots, the tick red line is the locus of time-optimal solutions, while the black dashed line (if present) indicates the available propellant mass isoline (2.8 kg).

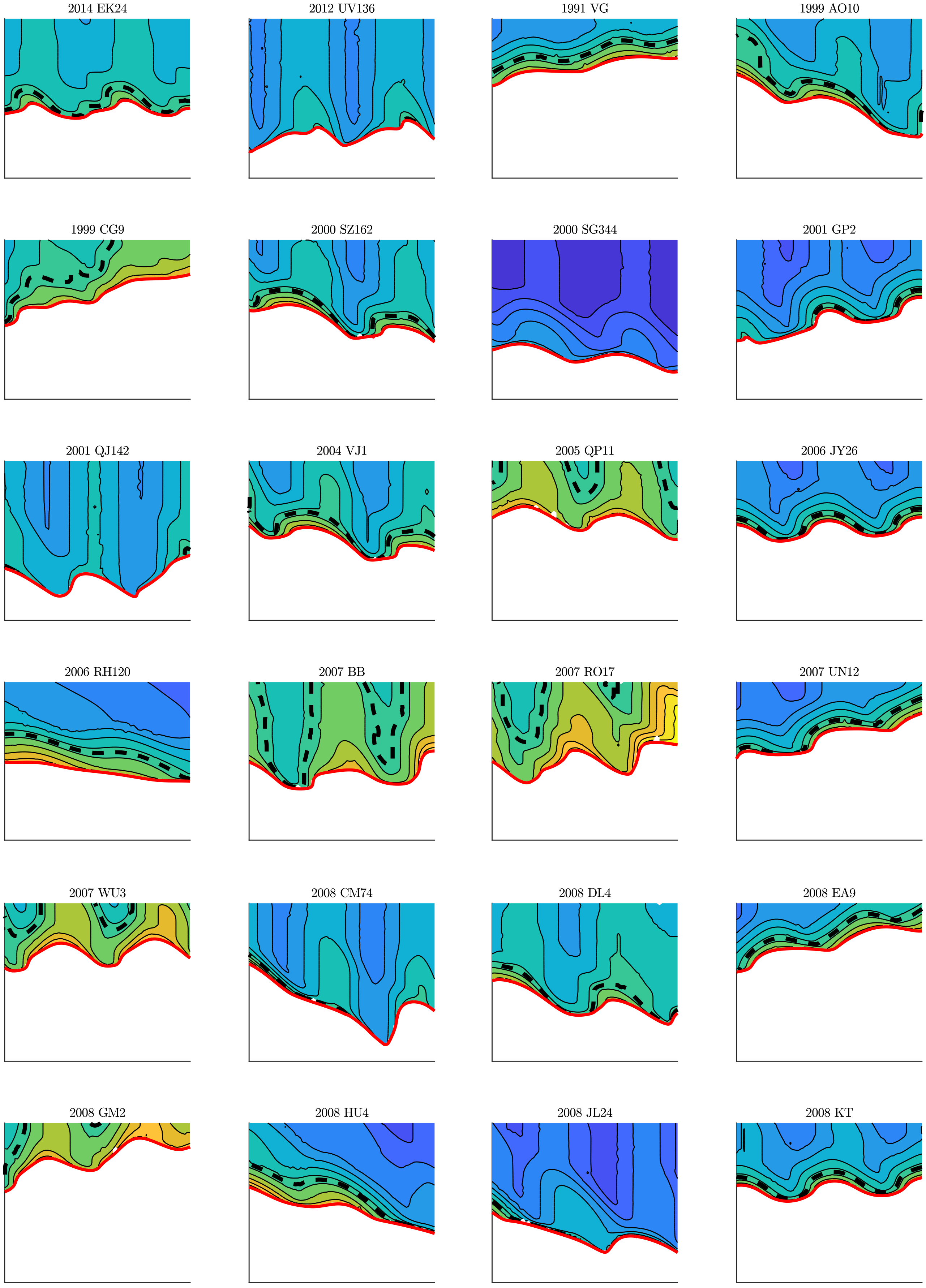
2014 EK24
2012 UV136
1991 VG
1999 AO10
1999 CG9
2000 SZ162
2000 SG344
2001 GP2
2001 QJ142
2004 VJ1
2005 QP11
2006 JY26
2006 RH120
2007 BB
2007 RO17
2007 UN12
2007 WU3
2008 CM74
2008 DL4
2008 EA9
2008 GM2
2008 HU4
2008 JL24
2008 KT

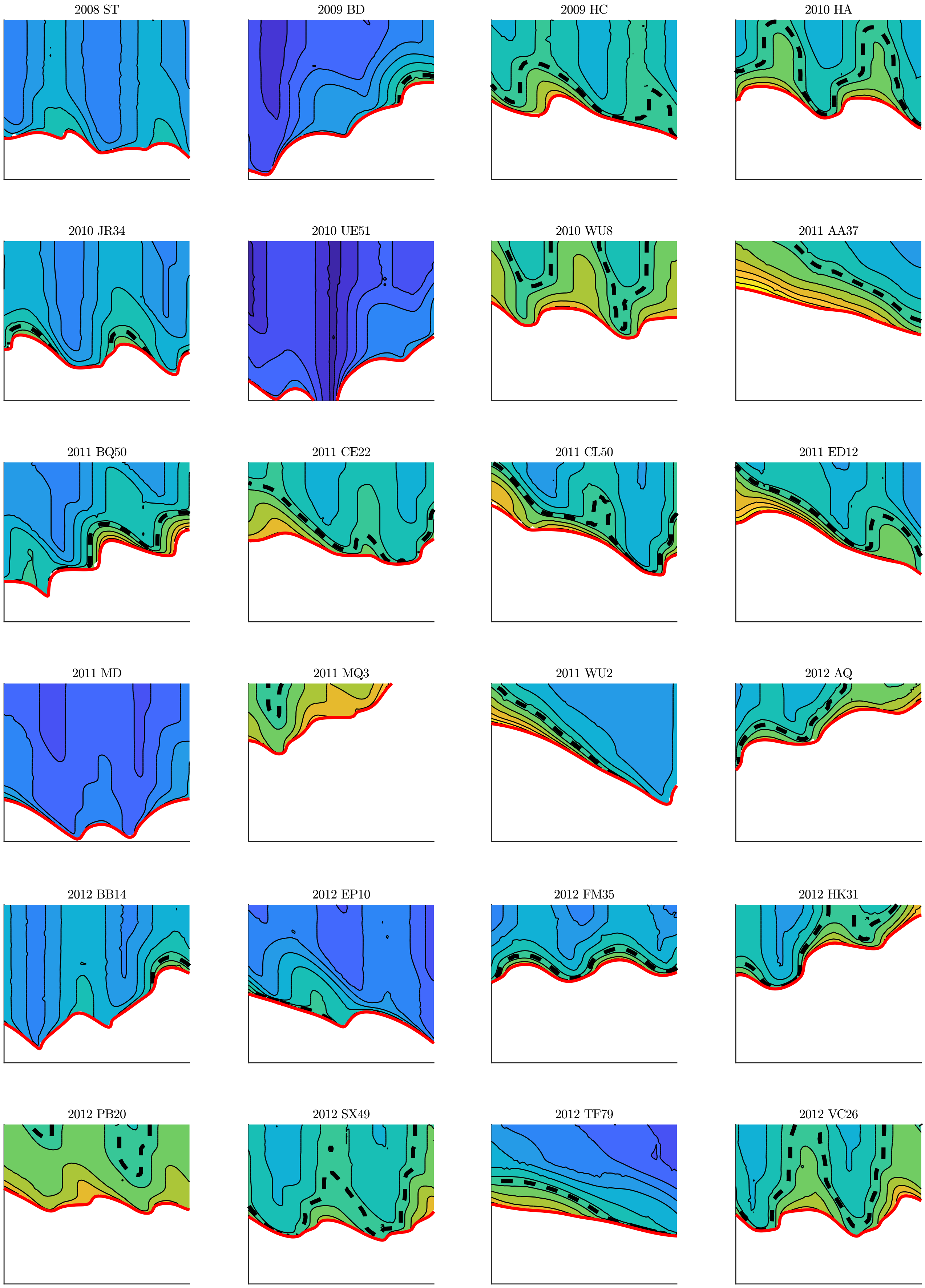
2008 ST
2009 BD
2009 HC
2010 HA
2010 JR34
2010 UE51
2010 WU8
2011 AA37
2011 BQ50
2011 CE22
2011 CL50
2011 ED12
2011 MD
2011 MQ3
2011 WU2
2012 AQ
2012 BB14
2012 EP10
2012 FM35
2012 HK31
2012 PB20
2012 SX49
2012 TF79
2012 VC26

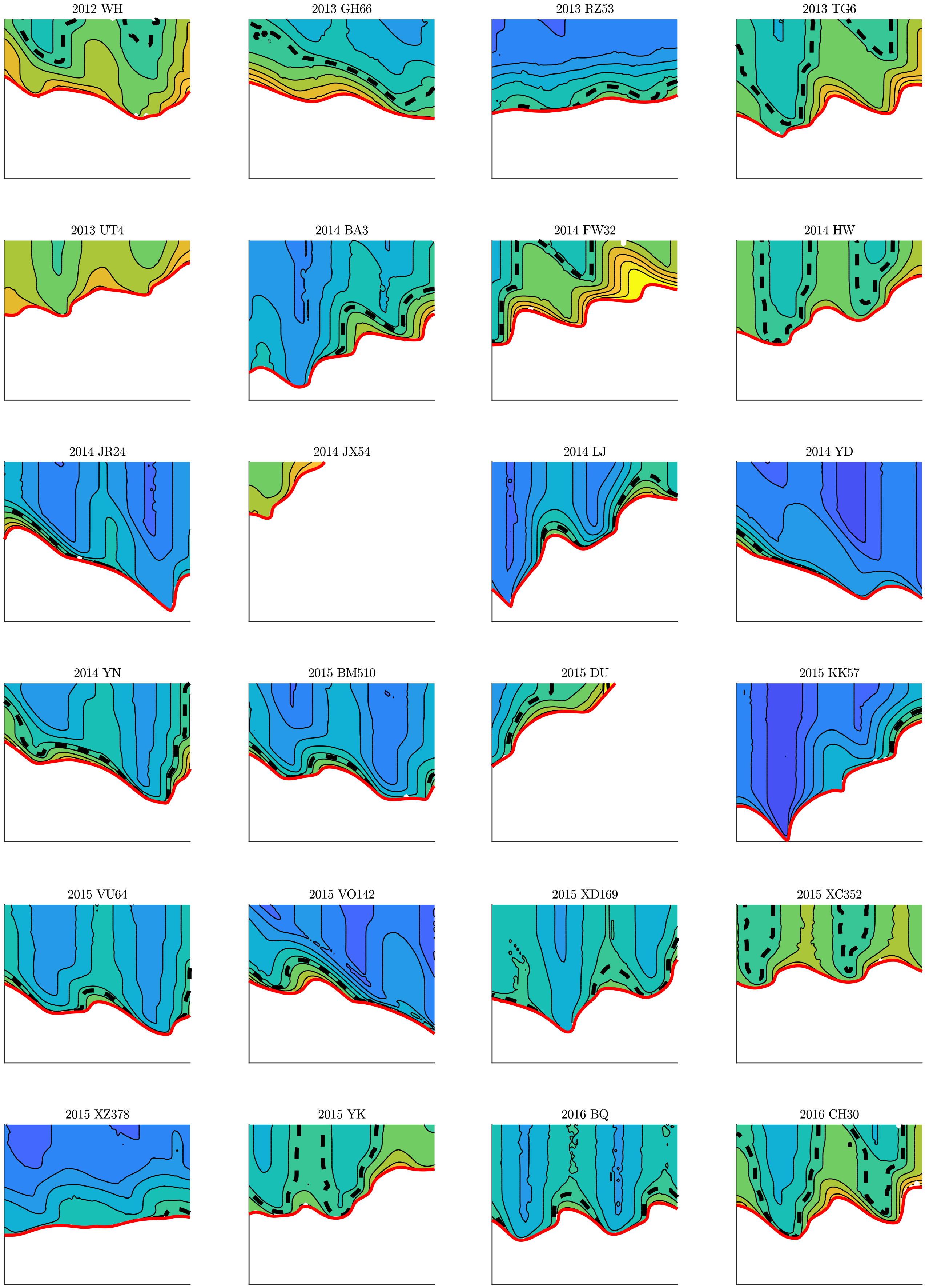
2012 WH
2013 GH66
2013 RZ53
2013 TG6
2013 UT4
2014 BA3
2014 FW32
2014 HW
2014 JR24
2014 JX54
2014 LJ
2014 YD
2014 YN
2015 BM510
2015 DU
2015 KK57
2015 VU64
2015 VO142
2015 XD169
2015 XC352
2015 XZ378
2015 YK
2016 BQ
2016 CH30

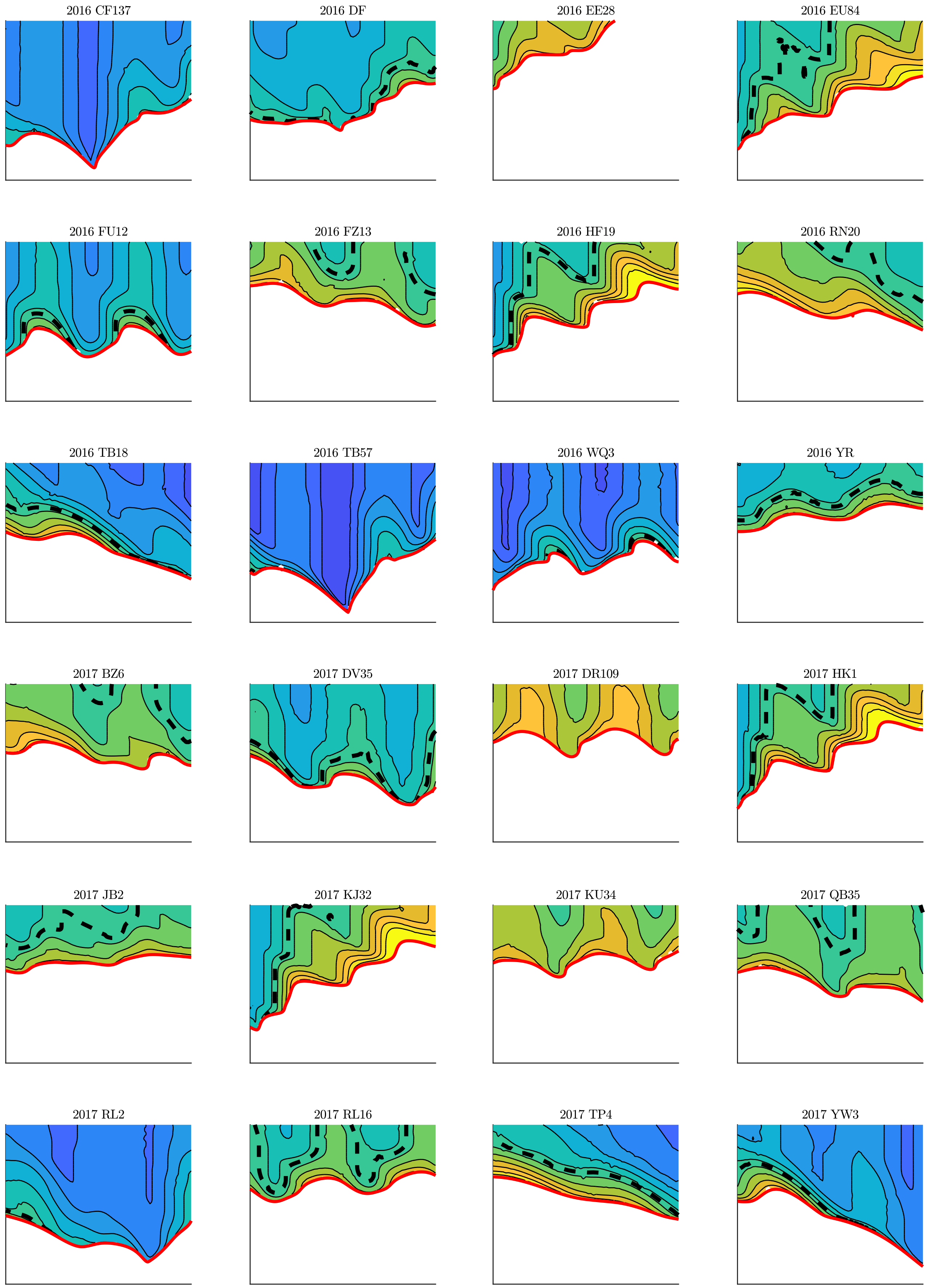
2016 CF137
2016 DF
2016 EE28
2016 EU84
2016 FU12
2016 FZ13
2016 HF19
2016 RN20
2016 TB18
2016 TB57
2016 WQ3
2016 YR
2017 BZ6
2017 DV35
2017 DR109
2017 HK1
2017 JB2
2017 KJ32
2017 KU34
2017 QB35
2017 RL2
2017 RL16
2017 TP4
2017 YW3

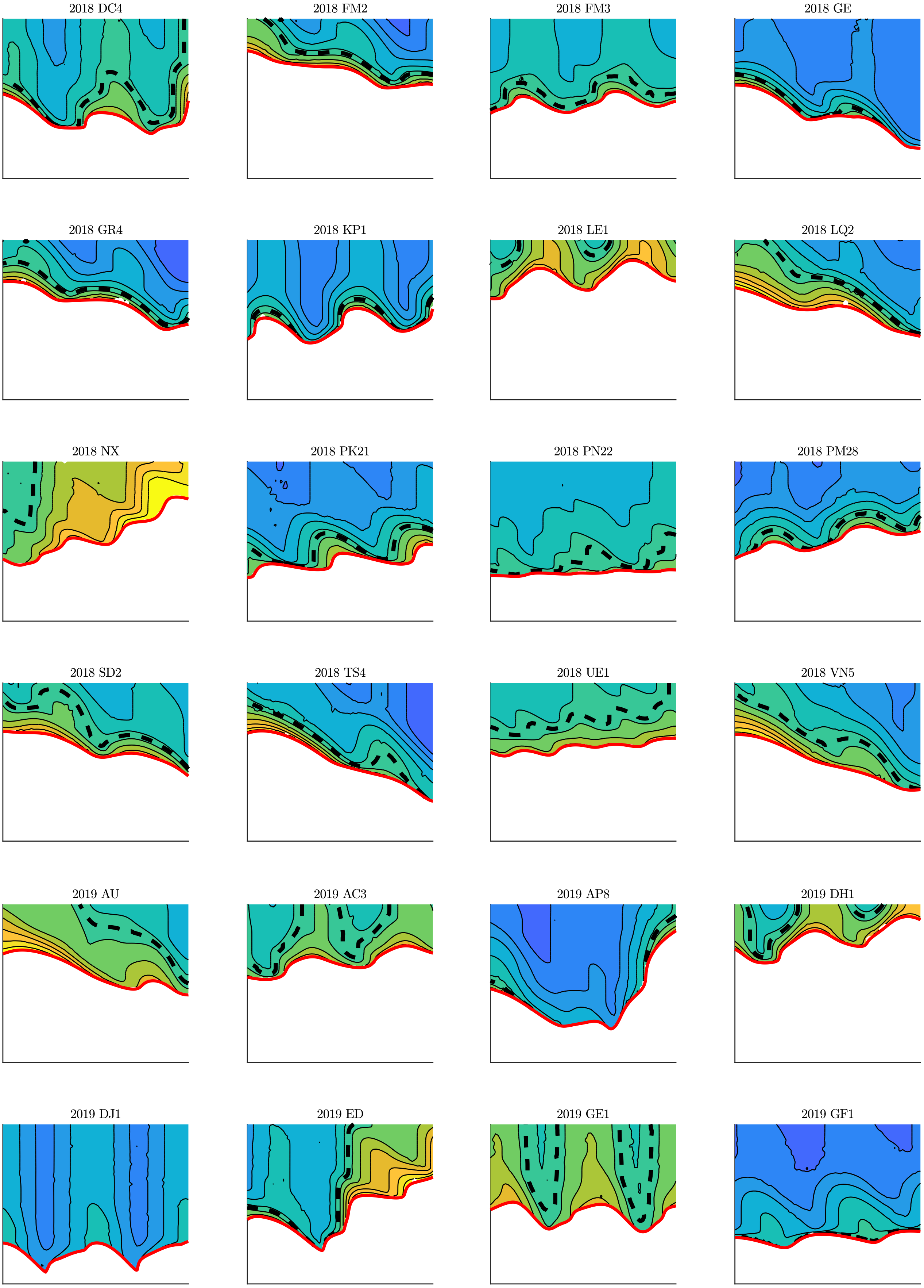
2018 DC4
2018 FM2
2018 FM3
2018 GE
2018 GR4
2018 KP1
2018 LE1
2018 LQ2
2018 NX
2018 PK21
2018 PN22
2018 PM28
2018 SD2
2018 TS4
2018 UE1
2018 VN5
2019 AU
2019 AC3
2019 AP8
2019 DH1
2019 DJ1
2019 ED
2019 GE1
2019 GF1

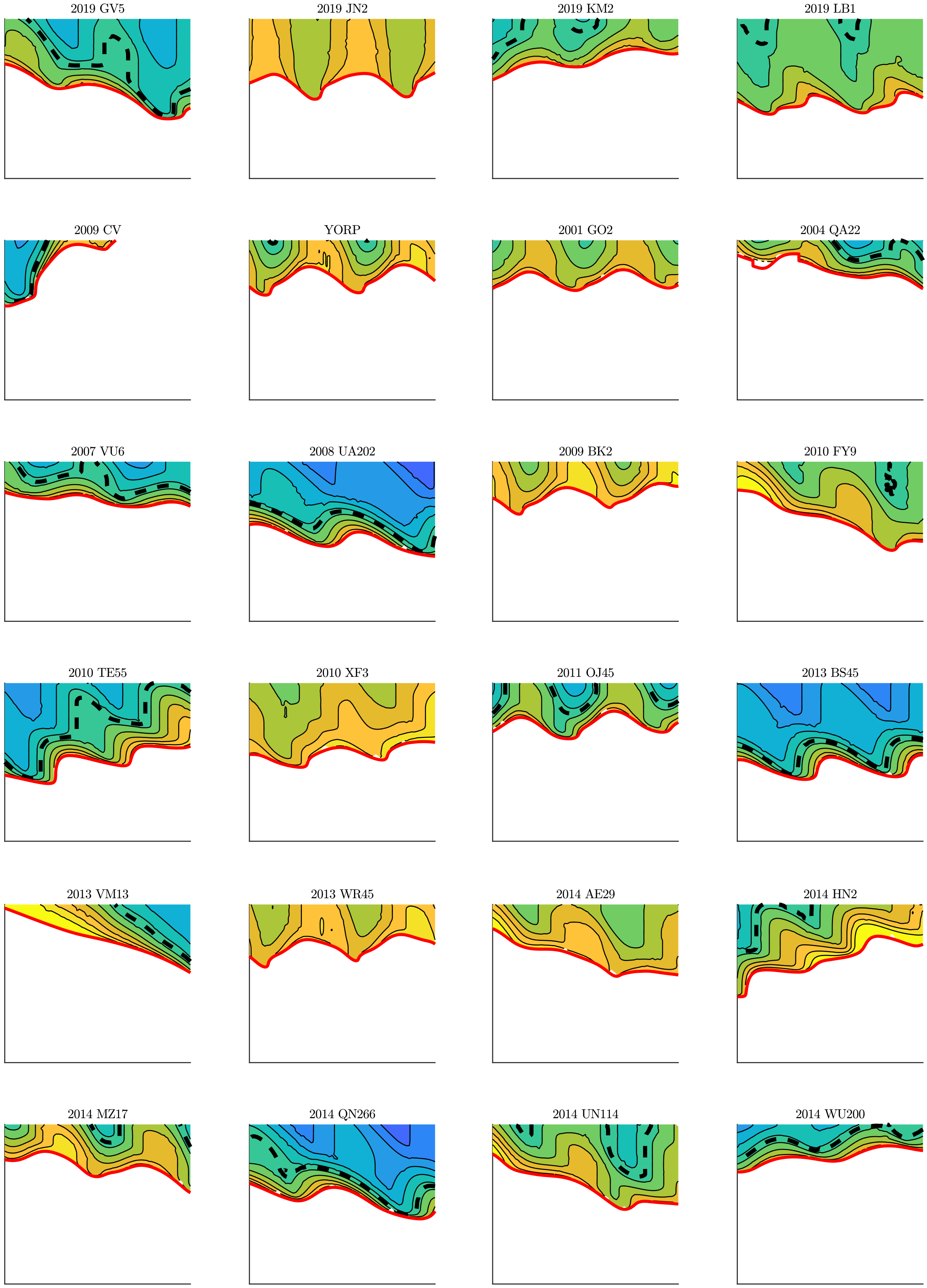
2019 GV5
2019 JN2
2019 KM2
2019 LB1
2009 CV
YORP
2001 GO2
2004 QA22
2007 VU6
2008 UA202
2009 BK2
2010 FY9
2010 TE55
2010 XF3
2011 OJ45
2013 BS45
2013 VM13
2013 WR45
2014 AE29
2014 HN2
2014 MZ17
2014 QN266
2014 UN114
2014 WU200

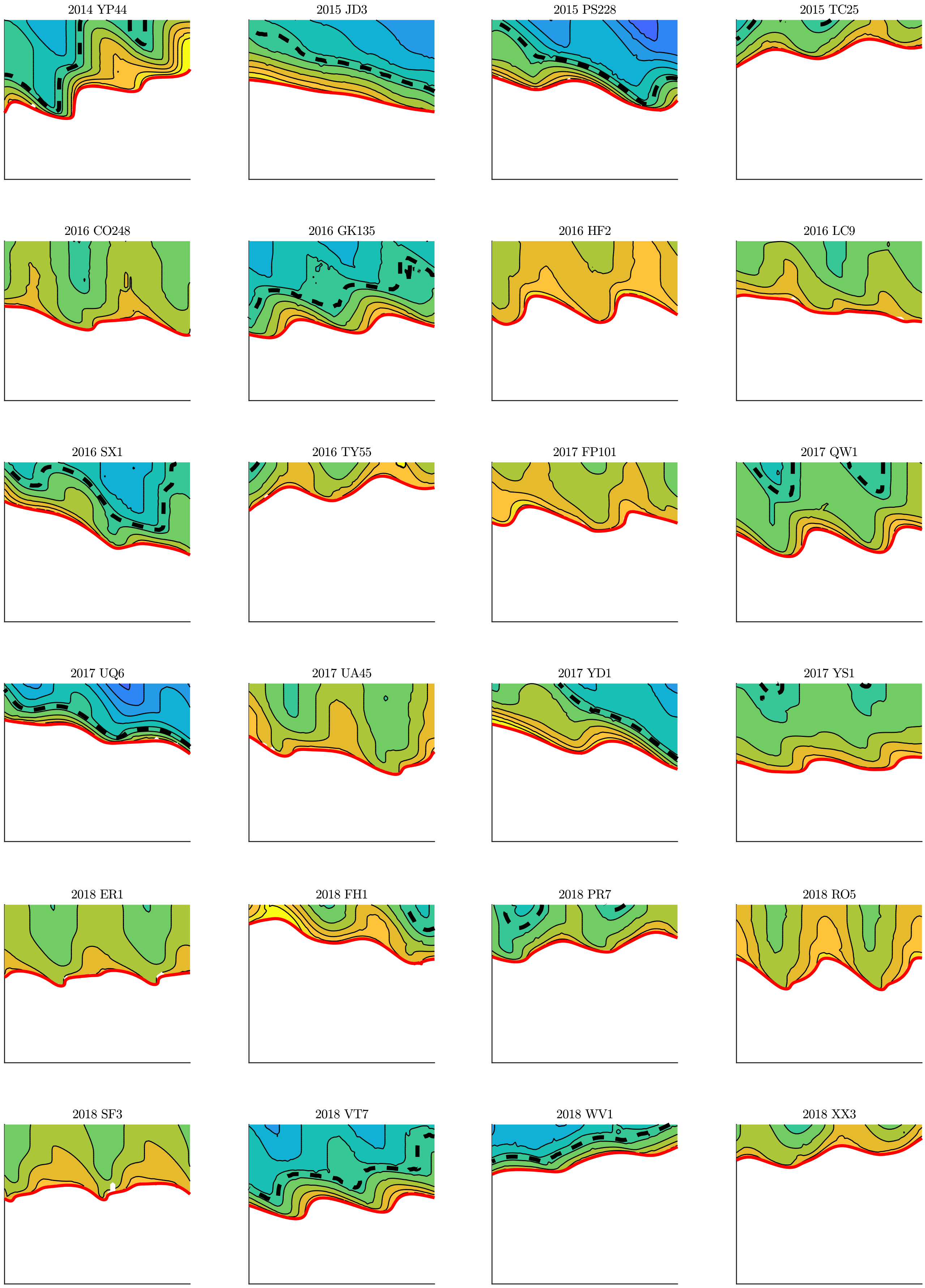
2014 YP44
2015 JD3
2015 PS228
2015 TC25
2016 CO248
2016 GK135
2016 HF2
2016 LC9
2016 SX1
2016 TY55
2017 FP101
2017 QW1
2017 UQ6
2017 UA45
2017 YD1
2017 YS1
2018 ER1
2018 FH1
2018 PR7
2018 RO5
2018 SF3
2018 VT7
2018 WV1
2018 XX3

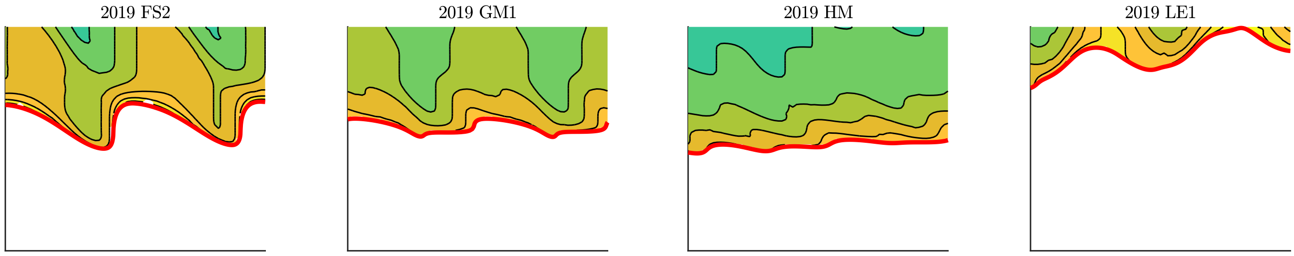
2019 FS2
2019 GM1
2019 HM
2019 LE1

BIBLIOGRAPHY

[1] Howard Curtis. *Orbital Mechanics for Engineering Students*. 3rd ed. Elsevier Butterworth-Heinemann, 2014. DOI: 10.1016/C2011-0-69685-1 (cit. on p. 1).

[2] Karthik Mani. "Combined Chemical–Electric Propulsion Design and Hybrid Trajectories for Stand-Alone Deep-Space CubeSats". PhD thesis. Politecnico di Milano, 2020 (cit. on p. 1).

[3] Stéphane Mazouffre. "Electric Propulsion for Satellites and Spacecraft: Established Technologies and Novel Approaches". In: *Plasma Sources Science and Technology* 25.3 (2016), p. 033002. DOI: 10.1088/0963-0252/25/3/033002 (cit. on pp. 1, 2).

[4] Laurent Garrigues and Philippe Coche. "Electric Propulsion: Comparisons between Different Concepts". In: *Plasma Physics and Controlled Fusion* 53.12 (2011), p. 124011. DOI: 10.1088/0741-3335/53/12/124011 (cit. on pp. 1, 2).

[5] David Morante, Manuel Sanjurjo Rivo, and Manuel Soler. "A Survey on Low-Thrust Trajectory Optimization Approaches". In: *Aerospace* 8.3 (2021), p. 88. DOI: 10.3390/aerospace8030088 (cit. on pp. 2–5).

[6] Marc Rayman and Steven Williams. "Design of the First Interplanetary Solar Electric Propulsion Mission". In: *Journal of Spacecraft and Rockets* 39.4 (2002), pp. 589–595. DOI: 10.2514/2.3848 (cit. on p. 2).

[7] Jun'ichiro Kawaguchi, Akira Fujiwara, and Tono Uesugi. "The Ion Engines Cruise Operation and the Earth Swingby of 'Hayabusa' (MUSES-C)". In: *55th International Astronautical Congress*. Vancouver, Canada, 2004, pp. 1–5 (cit. on p. 2).

[8] Joakim Kugelberg, Per Bodin, Staffan Persson, and Peter Rathsman. "Accommodating Electric Propulsion on SMART-1". In: *Acta Astronautica* 55.2 (2004), pp. 121–130. DOI: 10.1016/j.actaastro.2004.04.003 (cit. on p. 2).

[9] John Dankanich. "Low-Thrust Mission Design and Application". In: *46th AIAA/ASME/SAE/ASEE Joint Propulsion Conference & Exhibit*. Nashville, Tennessee, 2010, pp. 1–19. DOI: 10.2514/6.2010-6857 (cit. on p. 2).

[10] Bruce Conway. "A Survey of Methods Available for the Numerical Optimization of Continuous Dynamic Systems". In: *Journal of Optimization Theory and Applications* 152.2 (2012), pp. 271–306. DOI: 10.1007/s10957-011-9918-z (cit. on pp. 2–5).

[11] Anil Rao. "A Survey of Numerical Methods for Optimal Control". In: *Advances in the Astronautical Sciences* 135.1 (2009), pp. 497–528 (cit. on pp. 3, 4).

[12] John Betts. "Survey of Numerical Methods for Trajectory Optimization". In: *Journal of guidance, control, and dynamics* 21.2 (1998), pp. 193–207. DOI: 10.2514/2.4231 (cit. on pp. 3, 4).

[13] Abolfazl Shirazi, Josu Ceberio, and Jose Lozano. "Spacecraft Trajectory Optimization: A Review of Models, Objectives, Approaches and Solutions". In: *Progress in Aerospace Sciences* 102 (2018), pp. 76–98. DOI: 10.1016/j.paerosci.2018.07.007 (cit. on p. 3).

[14] Francesco Topputo and Chen Zhang. "Survey of Direct Transcription for Low-Thrust Space Trajectory Optimization with Applications". In: *Abstract and Applied Analysis* 2014 (2014). DOI: 10.1155/2014/851720 (cit. on p. 3).

[15] Dario Izzo, Marcus Märtens, and Binfeng Pan. "A Survey on Artificial Intelligence Trends in Spacecraft Guidance Dynamics and Control". In: *Astrodynamics* 3.4 (2019), pp. 287–299. DOI: 10.1007/s42064-018-0053-6 (cit. on pp. 3, 5).

[16] Benoit Chachuat. *Nonlinear and Dynamic Optimization: From Theory to Practice*. Tech. rep. Switzerland: Automatic Control Laboratory, EPFL, 2007 (cit. on p. 3).

[17] Anil Rao, David Benson, Christopher Darby, Michael Patterson, Camila Francolin, Ilyssa Sanders, and Geoffrey Huntington. "Algorithm 902: GPOPS, A MATLAB Software for Solving Multiple-Phase Optimal Control Problems Using the Gauss Pseudospectral Method". In: *ACM Transactions on Mathematical Software* 37 (2010), pp. 1–39. DOI: 10.1145/1731022.1731032 (cit. on pp. 3, 30).

[18] Victor Becerra. "Solving Complex Optimal Control Problems at no Cost with PSOPT". In: *2010 IEEE International Symposium on Computer-Aided Control System Design*. IEEE. 2010, pp. 1391–1396. DOI: 10.1109/CACSD.2010.5612676 (cit. on p. 3).

[19] Chen Zhang, Francesco Topputo, Franco Bernelli-Zazzera, Yu-Shan Zhao, et al. "An Exploration of Numerical Methods for Low-Thrust Trajectory Optimization in N-Body Models". In: *Proceedings of the 64th International Astronautical Congress, Beijing, China*. 2013, pp. 23–27 (cit. on p. 3).

[20] Daniel Grebow and Thomas Pavlak. "MColl: Monte Collocation Trajectory Design Tool". In: *AAS/AIAA Astrodynamics Specialist Conference*. Stevenson, Washington: Jet Propulsion Laboratory, National Aeronautics and Space, 2017 (cit. on p. 3).

[21] Jonathan Herman, Aline Zimmer, Johannes Reijneveld, Kathryn Dunlop, Yu Takahashi, Simon Tardivel, and Daniel Scheeres. "Human Exploration of Near Earth Asteroids: Mission Analysis for Chemical and Electric Propulsion". In: *Acta Astronautica* 104.1 (2014), pp. 313–323. DOI: 10.1016/j.actaastro.2014.07.034 (cit. on p. 3).

[22] Albert Herman and Bruce Conway. "Direct Optimization Using Collocation Based on High-Order Gauss-Lobatto Quadrature Rules". In: *Journal of Guidance, Control, and Dynamics* 19.3 (1996), pp. 592–599. DOI: 10.2514/3.21662 (cit. on p. 3).

[23] Tieding Guo, Junfeng Li, Hexi Baoyin, and Fanghua Jiang. "Pseudospectral Methods for Trajectory Optimization with Interior Point Constraints: Verification and Applications". In: *IEEE Transactions on Aerospace and Electronic Systems* 49.3 (2013), pp. 2005–2017. DOI: 10.1109/TAES.2013.6558034 (cit. on pp. 4, 5, 19).

[24] Herbert Keller. *Numerical Methods for Two-Point Boundary-Value Problems*. Courier Dover Publications, 2018 (cit. on p. 4).

[25] Richard Bellman. *Dynamic Programming*. New Jersey: Princeton University Press, 1957 (cit. on p. 4).

[26] Arthur Bryson and Yu-Chi Ho. *Applied Optimal Control: Optimization, Estimation and Control*. Taylor and Francis Group, 1975. DOI: 10.1109/TSMC.1979.4310229 (cit. on pp. 4, 15, 17, 58, 72, 74, 98, 126).

[27] Nagavenkat Adurthi, Puneet Singla, and Manoranjan Majji. "Sparse Approximation-Based Collocation Scheme for Nonlinear Optimal Feedback Control Design". In: *Journal of Guidance, Control, and Dynamics* 40.2 (2017), pp. 248–264. DOI: 10.2514/1.G001755 (cit. on p. 4).

[28] Srinivas Vadali and Rajnish Sharma. "Optimal Finite-Time Feedback Controllers for Nonlinear Systems with Terminal Constraints". In: *Journal of Guidance, Control, and Dynamics* 29.4 (2006), pp. 921–928. DOI: 10.2514/1.16790 (cit. on p. 4).

[29] Jonathan Aziz. "Low-Thrust Many-Revolution Trajectory Optimization". PhD thesis. University of Colorado at Boulder, 2018 (cit. on pp. 4, 5).

[30] Chandeok Park, Vincent Guibout, and Daniel Scheeres. "Solving Optimal Continuous Thrust Rendezvous Problems with Generating Functions". In: *Journal of Guidance, Control, and Dynamics* 29.2 (2006), pp. 321–331. DOI: 10.2514/1.14580 (cit. on p. 4).

[31] Lars Grüne. "An Adaptive Grid Scheme for the Discrete Hamilton-Jacobi-Bellman Equation". In: *Numerische Mathematik* 75.3 (1997), pp. 319–337. DOI: 10.1007/s002110050241 (cit. on p. 4).

[32] Murad Abu-Khalaf and Frank Lewis. "Nearly Optimal Control Laws for Nonlinear Systems with Saturating Actuators Using a Neural Network HJB Approach". In: *Automatica* 41.5 (2005), pp. 779–791. DOI: 10.1016/j.automatica.2004.11.034 (cit. on p. 4).

[33] Camilla Colombo, Massimiliano Vasile, and Gianmarco Radice. "Optimal Low-Thrust Trajectories to Asteroids through an Algorithm based on Differential Dynamic Programming". In: *Celestial mechanics and dynamical astronomy* 105.1 (2009), pp. 75–112. DOI: 10.1007/s10569-009-9224-3 (cit. on p. 5).

[34] Gregory Lantoine and Ryan Russell. "A Hybrid Differential Dynamic Programming Algorithm for Constrained Optimal Control Problems. Part 2: Application". In: *Journal of Optimization Theory and Applications* 154.2 (2012), pp. 418–442. DOI: 10.1007/s10957-012-0038-1 (cit. on p. 5).

[35] David Goldberg. *Genetic Algorithms in Search, Optimization, and Machine Learning*. New York: Addison-Wesley Publishing Company, Inc., 1989 (cit. on p. 5).

[36] Massimiliano Vasile, Edmondo Minisci, and Marco Locatelli. "An Inflationary Differential Evolution Algorithm for Space Trajectory Optimization". In: *IEEE Transactions on Evolutionary Computation* 15.2 (2011), pp. 267–281. DOI: 10.1109/TEVC.2010.2087026 (cit. on p. 5).

[37] Mauro Pontani and Bruce Conway. "Particle Swarm Optimization Applied to Space Trajectories". In: *Journal of Guidance, Control, and Dynamics* 33.5 (2010), pp. 1429–1441. DOI: 10.2514/1.48475 (cit. on p. 5).

[38] Jugo Igarashi and David Spencer. "Optimal Continuous Thrust Orbit Transfer Using Evolutionary Algorithms". In: *Journal of guidance, control, and dynamics* 28.3 (2005), pp. 547–549. DOI: 10.2514/1.11135 (cit. on p. 5).

[39] Jacob Englander and Bruce Conway. "Automated Solution of the Low-Thrust Interplanetary Trajectory Problem". In: *Journal of Guidance, Control, and Dynamics* 40.1 (2017), pp. 15–27. DOI: 10.2514/1.G002124 (cit. on p. 5).

[40] Matteo Ceriotti and Massimiliano Vasile. "MGA Trajectory Planning with an ACO-Inspired Algorithm". In: *Acta Astronautica* 67.9-10 (2010), pp. 1202–1217. DOI: 10.1016/j.actaastro.2010.07.001 (cit. on p. 5).

[41] Régis Bertrand and Richard Epenoy. "New Smoothing Techniques for Solving Bang–Bang Optimal Control Problems–Numerical Results and Statistical Interpretation". In: *Optimal Control Applications and Methods* 23.4 (2002), pp. 171–197. DOI: 10.1002/oca.709 (cit. on pp. 5, 7, 15, 72).

[42] Ehsan Taheri and John Junkins. "Generic Smoothing for Optimal Bang-Off-Bang Spacecraft Maneuvers". In: *Journal of Guidance, Control, and Dynamics* 41.11 (2018), pp. 2470–2475. DOI: 10.2514/1.G003604 (cit. on pp. 5, 8, 19, 20).

[43] Thomas Haberkorn, Pierre Martinon, and Joseph Gergaud. "Low-Thrust Minimum-Fuel Orbital Transfer: a Homotopic Approach". In: *Journal of Guidance, Control, and Dynamics* 27.6 (2004), pp. 1046–1060. DOI: 10.2514/1.4022 (cit. on pp. 5, 7, 116).

[44] Fanghua Jiang, Hexi Baoyin, and Junfeng Li. "Practical Techniques for Low-Thrust Trajectory Optimization with Homotopic Approach". In: *Journal of Guidance, Control, and Dynamics* 35.1 (2012), pp. 245–258. DOI: 10.2514/1.52476 (cit. on pp. 5, 7, 72, 74, 88, 89, 136).

[45] Ryan Russell. "Primer Vector Theory Applied to Global Low-Thrust Trade Studies". In: *Journal of Guidance, Control, and Dynamics* 30.2 (2007), pp. 460–472. DOI: 10.2514/1.22984 (cit. on pp. 5, 6, 19, 20, 38, 59).

[46] Fanghua Jiang, Gao Tang, and Junfeng Li. "Improving Low-Thrust Trajectory Optimization by Adjoint Estimation with Shape-Based Path". In: *Journal of Guidance, Control, and Dynamics* 40.12 (2017), pp. 3282–3289. DOI: 10.2514/1.G002803 (cit. on p. 5).

[47] Chen Zhang, Francesco Topputo, Franco Bernelli-Zazzera, and Yushan Zhao. "Low-Thrust Minimum-Fuel Optimization in the Circular Restricted Three-Body Problem". In: *Journal of Guidance, Control, and Dynamics* 38.8 (2015), pp. 1501–1510. DOI: 10.2514/1.G001080 (cit. on pp. 5, 6, 8, 9, 16, 23–25, 42, 57, 60, 62–64, 87, 88, 133).

[48] Pierre Martinon and Joseph Gergaud. "Using Switching Detection and Variational Equations for the Shooting Method". In: *Optimal Control Applications and Methods* 28.2 (2007), pp. 95–116. DOI: 10.1002/oca.794 (cit. on p. 5).

[49] Yang Wang and Francesco Topputo. "Indirect Optimization for Low-Thrust Transfers with Earth-Shadow Eclipses". In: *31st AAS/AIAA Space Flight Mechanics Meeting*. AAS 21-368. Virtual, 2021 (cit. on pp. 5, 136).

[50] Max Cerf. "Fast Solution of Minimum-Time Low-Thrust Transfer with Eclipses". In: *Proceedings of the Institution of Mechanical Engineers, Part G: Journal of Aerospace Engineering* 233.7 (2019), pp. 2699–2714. DOI: 10.1177/0954410018785971 (cit. on pp. 5, 53, 55, 58).

[51] Mauro Pontani. "Optimal Space Trajectories with Multiple Coast Arcs Using Modified Equinoctial Elements". In: *Journal of Optimization Theory and Applications* (2021), pp. 1–30. DOI: 10.1007/s10957-021-01867-2 (cit. on pp. 5, 53).

[52] Etienne Pellegrini and Ryan Russell. "On the Computation and Accuracy of Trajectory State Transition Matrices". In: *Journal of Guidance, Control, and Dynamics* 39.11 (2016), pp. 2485–2499. DOI: 10.2514/1.G001920 (cit. on pp. 6, 13).

[53] Gregory Lantoine, Ryan Russell, and Thierry Dargent. "Using Multicomplex Variables for Automatic Computation of High-Order Derivatives". In: *ACM Transactions on Mathematical Software* 38.3 (2012), pp. 1–21. DOI: 10.1145/2168773.2168774 (cit. on p. 6).

[54] Donald Ellison, Bruce Conway, Jacob Englander, and Martin Ozimek. "Analytic Gradient Computation for Bounded-Impulse Trajectory Models Using Two-Sided Shooting". In: *Journal of Guidance, Control, and Dynamics* 41.7 (2018), pp. 1449–1462. DOI: 10.2514/1.G003077 (cit. on p. 6).

[55] Andreas Griewank, David Juedes, and Jean Utke. "Algorithm 755: ADOL-C: a Package for the Automatic Differentiation of Algorithms Written in C/C++". In: *ACM Transactions on Mathematical Software* 22.2 (1996), pp. 131–167. DOI: 10.1145/229473.229474 (cit. on p. 6).

[56] Pierluigi Di Lizia, Roberto Armellin, Alessandro Morselli, and Franco Bernelli-Zazzera. "High Order Optimal Feedback Control of Space Trajectories with Bounded Control". In: *Acta Astronautica* 94.1 (2014), pp. 383–394. DOI: 10.1016/j.actaastro.2013.02.011 (cit. on p. 6).

[57] Joaquim Martins, Peter Sturdza, and Juan Alonso. "The Complex-Step Derivative Approximation". In: *ACM Transactions on Mathematical Software (TOMS)* 29.3 (2003), pp. 245–262. DOI: 10.1145/838250.838251 (cit. on p. 6).

[58] William Squire and George Trapp. "Using Complex Variables to Estimate Derivatives of Real Functions". In: *SIAM review* 40.1 (1998), pp. 110–112. DOI: 10.1137/S003614459631241X (cit. on p. 6).

[59] Cesar Ocampo and Jean-Philippe Munoz. "Variational Equations for a Generalized Spacecraft Trajectory Model". In: *Journal of Guidance, Control, and Dynamics* 33.5 (2010), pp. 1615–1622. DOI: 10.2514/1.46953 (cit. on p. 6).

[60] Hong-Xin Shen, Lorenzo Casalino, and Ya-Zhong Luo. "Global Search Capabilities of Indirect Methods for Impulsive Transfers". In: *The Journal of the Astronautical Sciences* 62.3 (2015), pp. 212–232. DOI: 10.1007/s40295-015-0073-x (cit. on p. 6).

[61] Lorenzo Casalino, Guido Colasurdo, and Dario Pastrone. "Indirect Approach for Minimum-Fuel Aeroassisted Transfers". In: *Astrodynamics Conference*. San Diego, 1996, pp. 192–200. DOI: 10.2514/6.1996-3592 (cit. on p. 6).

[62] Guido Colasurdo and Dario Pastrone. "Indirect Optimization Method for Impulsive Transfers". In: *Astrodynamics Conference*. Scottsdale, 1994, pp. 441–448. DOI: 10.2514/6.1994-3762 (cit. on p. 6).

[63] Donald Ellison, Bruce Conway, Jacob Englander, and Martin Ozimek. "Application and Analysis of Bounded-Impulse Trajectory Models with Analytic Gradients". In: *Journal of Guidance, Control, and Dynamics* 41.8 (2018), pp. 1700–1714. DOI: 10.2514/1.G003078 (cit. on p. 6).

[64] Kenta Oshima, Francesco Topputo, and Tomohiro Yanao. "Low-energy Transfers to the Moon with Long Transfer Time". In: *Celestial Mechanics and Dynamical Astronomy* 131.1 (2019), p. 4. DOI: 10.1007/s10569-019-9883-7 (cit. on p. 6).

[65] Binfeng Pan, Ping Lu, Xun Pan, and Yangyang Ma. "Double-Homotopy Method for Solving Optimal Control Problems". In: *Journal of Guidance, Control, and Dynamics* 39.8 (2016), pp. 1706 –1720. DOI: 10.2514/1.G001553 (cit. on pp. 7, 100, 116).

[66] Eugene Allgower and Kurt Georg. *Introduction to Numerical Continuation Methods*. Society for Industrial and Applied Mathematics, 2003. DOI: 10.1137/1.9780898719154 (cit. on pp. 7, 113–116).

[67] Robert Kalaba and Leigh Tesfatsion. "Solving Nonlinear Equations by Adaptive Homotopy Continuation". In: *Applied Mathematics and Computation* 41.2 (1991), pp. 99–115. DOI: 10.1016/0096-3003(91)90064-T (cit. on p. 7).

[68] Denise Wolf and Seth Sanders. "Multiparameter Homotopy Methods for Finding DC Operating Points of Nonlinear Circuits". In: *IEEE Transactions on Circuits and Systems I: Fundamental Theory and Applications* 43.10 (1996), pp. 824–838. DOI: 10.1109/81.538989 (cit. on p. 7).

[69] Thomas Wayburn and J Seader. "Homotopy Continuation Methods for Computer-Aided Process Design". In: *Computers and Chemical Engineering* 11.1 (1987), pp. 7–25. DOI: 10.1016/0098-1354(87)80002-9 (cit. on p. 7).

[70] Jorge Nocedal and Stephen Wright. *Numerical Optimization*. 2nd ed. p. 296–302. New York: Springer, 2006. DOI: 10.1007/978-0-387-40065-5 (cit. on pp. 7, 115).

[71] Roger Walker, Detlef Koschny, Cristina Bramanti, Ian Carnelli, et al. "Miniaturised Asteroid Remote Geophysical Observer (M-ARGO): A Stand-Alone Deep Space CubeSat System for Low-Cost Science

and Exploration Missions". In: *6th Interplanetary CubeSat Workshop, Cambridge, UK* 30 (2017), pp. 1–20 (cit. on p. 7).

[72] Daniele Mortari. "The Theory of Connections: Connecting Points". In: *Mathematics* 5.4 (2017), p. 57. DOI: 10.3390/math5040057 (cit. on pp. 7, 117, 118).

[73] Steven Williams and Victoria Coverstone-Carroll. "Benefits of Solar Electric Propulsion for the Next Generation of Planetary Exploration Missions". In: *The Journal of the Astronautical Sciences* 45.2 (1997), pp. 143–159. DOI: 10.1007/BF03546373 (cit. on p. 13).

[74] David Oh. "Evaluation of Solar Electric Propulsion Technologies for Discovery-Class Missions". In: *Journal of Spacecraft and Rockets* 44.2 (2007), pp. 399–411. DOI: 10.2514/1.21613 (cit. on p. 13).

[75] Ryan Woolley and Zubin Olikara. "Optimized Low-Thrust Missions from GTO to Mars". In: *2019 IEEE Aerospace Conference*. IEEE. 2019, pp. 1–10. DOI: 10.1109/AERO.2019.8741558 (cit. on p. 13).

[76] Alessandro Quarta and Giovanni Mengali. "Minimum-Time Space Missions with Solar Electric Propulsion". In: *Aerospace Science and Technology* 15.5 (2011), pp. 381–392. DOI: 10.1016/j.ast.2010.09.003 (cit. on p. 13).

[77] Giovanni Mengali and Alessandro Quarta. "Fuel-Optimal, Power-Limited Rendezvous with Variable Thruster Efficiency". In: *Journal of Guidance, Control, and Dynamics* 28.6 (2005), pp. 1194–1199. DOI: 10.2514/1.12480 (cit. on p. 13).

[78] Taibo Li, Zhaokui Wang, and Yulin Zhang. "Double-Homotopy Technique for Fuel Optimization of Power-Limited Interplanetary Trajectories". In: *Astrophysics and Space Science* 364.9 (2019), p. 144. DOI: 10.1007/s10509-019-3637-6 (cit. on p. 13).

[79] Vishala Arya, Ehsan Taheri, and John Junkins. "Low-Thrust Gravity-Assist Trajectory Design Using Optimal Multimode Propulsion Models". In: *Journal of Guidance, Control, and Dynamics* (2021), pp. 1–15. DOI: 10.2514/1.G005750 (cit. on p. 13).

[80] Ehsan Taheri, John Junkins, Ilya Kolmanovsky, and Anouck Girard. "A Novel Approach for Optimal Trajectory Design with Multiple Operation Modes of Propulsion System, Part 1". In: *Acta Astronautica* 172 (2020). DOI: 10.1016/j.actaastro.2020.02.042 (cit. on pp. 13, 134).

[81] Zhemin Chi, Haiyang Li, Fanghua Jiang, and Junfeng Li. "Power-Limited Low-Thrust Trajectory Optimization with Operation Point Detection". In: *Astrophysics and Space Science* 363.6 (2018), p. 122. DOI: 10.1007/s10509-018-3344-8 (cit. on pp. 13, 17).

[82] Francesco Topputo, Yang Wang, Giordano Carmine, Vittorio Franzese, Hannah Goldberg, Franco Perez-Lissi, and Roger Walker. "Envelop of Reachable Asteroids by M-ARGO CubeSat". In: *Advances in Space Research* (2021). DOI: 10.1016/j.asr.2021.02.031 (cit. on pp. 24, 27, 29).

[83] Jon Giorgini and Donald Yeomans. "On-Line System Provides Accurate Ephemeris and Related Data". In: *NASA TECH BRIEFS, NPO-20416* 48 (1999) (cit. on p. 26).

[84] Ehsan Taheri and Ossama Abdelkhalik. "Initial Three-Dimensional Low-Thrust Trajectory Design". In: *Advances in Space Research* 57.3 (2016), pp. 889–903. DOI: 10.1016/j.asr.2015.11.034 (cit. on p. 26).

[85] Binfeng Pan, Zheng Chen, Ping Lu, and Bo Gao. "Reduced Transversality Conditions in Optimal Space Trajectories". In: *Journal of Guidance, Control, and Dynamics* 36.5 (2013), pp. 1289–1300. DOI: 10.2514/1.60181 (cit. on pp. 30, 98, 101, 104).

[86] Armen Poghosyan and Alessandro Golkar. "CubeSat Evolution: Analyzing CubeSat Capabilities for Conducting Science Missions". In: *Progress in Aerospace Sciences* 88 (2017). DOI: 10.1016/j.paerosci.2016.11.002, pp. 59–83 (cit. on p. 33).

[87] Roger Walker, David Binns, Cristina Bramanti, et al. "Deep-space CubeSats: Thinking inside the Box". In: *Astronomy and Geophysics* 59.5 (2018). DOI: 10.1093/astrogeo/aty232, pp. 5–24 (cit. on pp. 33, 34).

[88] Alessio Mereta and Dario Izzo. "Target Selection for a Small Low-Thrust Mission to Near-Earth Asteroids". In: *Astrodynamics* 2.3 (2018), pp. 249–263. DOI: 10.1007/s42064-018-0024-y (cit. on pp. 35, 36).

[89] Edward Bowell, Bruce Hapke, Deborah Domingue, Kari Lumme, Jouni Peltoniemi, and Alan Harris. "Application of Photometric Models to Asteroids." In: *Asteroids II* (1989), pp. 524–556 (cit. on p. 37).

[90] Alan Harris. "On the Revision of Radiometric Albedos and Diameters of Asteroids". In: *Icarus* 126.2 (1997), pp. 450–454. DOI: 10.1006/icar.1996.5664 (cit. on p. 37).

[91] Brian Warner, Alan Harris, and Petr Pravec. "The Asteroid Lightcurve Database". In: *Icarus* 202.1 (2009), pp. 134–146. DOI: 10.1016/j.icarus.2009.02.003 (cit. on p. 37).

[92] David Vallado. *Fundamentals of Astrodynamics and Applications*. 4th ed. Hawthorne, California: Microcosm Press and Springer, 2013 (cit. on p. 40).

[93] Josselin Desmars, David Bancelin, Daniel Hestroffer, and William Thuillot. "Statistical Analysis on the Uncertainty of Asteroid Ephemerides". In: *SF2A 2011: Annual meeting of the French Society of Astronomy and Astrophysics*. 2011, pp. 639–642 (cit. on p. 51).

[94] Ch Ferrier and Richard Epenoy. "Optimal Control for Engines with Electro-Ionic Propulsion under Constraint of Eclipse". In: *Acta Astronautica* 48.4 (2001), pp. 181–192. DOI: `10.1016/S0094-5765(00)00158-2` (cit. on pp. 53, 55).

[95] Robyn Woollands and Ehsan Taheri. "Optimal Low-Thrust Gravity Perturbed Orbit Transfers with Shadow Constraints". In: *The 2019 AAS/AIAA Astrodynamics Specialist Conference, Portland, Maine*. 2019 (cit. on pp. 53, 55, 57, 63, 69).

[96] Sophie Geffroy and Richard Epenoy. "Optimal Low-Thrust Transfers with Constraints—Generalization of Averaging Techniques". In: *Acta Astronautica* 41.3 (1997), pp. 133–149. DOI: `10.1016/S0094-5765(97)00208-7` (cit. on p. 53).

[97] John Junkins and Ehsan Taheri. "Exploration of Alternative State Vector Choices for Low-Thrust Trajectory Optimization". In: *Journal of Guidance, Control, and Dynamics* 42.1 (2019), pp. 47–64. DOI: `10.2514/1.G003686` (cit. on p. 53).

[98] John Betts. "Optimal Low–Thrust Orbit Transfers with Eclipsing". In: *Optimal Control Applications and Methods* 36.2 (2015), pp. 218–240. DOI: `10.1002/oca.2111` (cit. on p. 55).

[99] Kathryn Graham and Anil Rao. "Minimum-Time Trajectory Optimization of Low-Thrust Earth-Orbit Transfers with Eclipsing". In: *Journal of Spacecraft and Rockets* 53.2 (2016), pp. 289–303. DOI: `10.2514/1.A33416` (cit. on p. 55).

[100] Bengt Fornberg. "Generation of Finite Difference Formulas on Arbitrarily Spaced Grids". In: *Mathematics of computation* 51.184 (1988), pp. 699–706. DOI: `10.1090/S0025-5718-1988-0935077-0` (cit. on p. 67).

[101] T Troy McConaghy, Theresa Debban, Anastassios Petropoulos, and James Longuski. "Design and Optimization of Low-Thrust Trajectories with Gravity Assists". In: *Journal of spacecraft and rockets* 40.3 (2003), pp. 380–387. DOI: `10.2514/2.3973` (cit. on p. 71).

[102] David Hull. *Optimal Control Theory for Applications*. Springer Science and Business Media, 2013 (cit. on p. 75).

[103] Jonathan Aziz, Jeffrey Parker, Daniel Scheeres, and Jacob Englander. "Low-Thrust Many-Revolution Trajectory Optimization via Differential Dynamic Programming and a Sundman Transformation". In: *The Journal of the Astronautical Sciences* 65.2 (2018), pp. 205–228 (cit. on pp. 97, 99).

[104] Richard Battin. *An Introduction to the Mathematics and Methods of Astrodynamics*. AIAA, 1999. DOI: `10.2514/4.861543` (cit. on p. 97).

[105] Luca Ferella. "Indirect Optimization of Long-Duration, Multi-Spiral Low-Thrust Transfers with Homotopy". MA thesis. Politecnico di Milano, 2016 (cit. on p. 100).

[106] Jean-Baptiste Caillau, Joseph Gergaud, and Joseph Noailles. "3D Geosynchronous Transfer of a Satellite: Continuation on the Thrust". In: *Journal of optimization theory and applications* 118.3 (2003), pp. 541–565. DOI: `10.1023/B:JOTA.0000004870.74778.ae` (cit. on pp. 105, 106, 109).

[107] Xincheng Yue, Ying Yang, and Zhiyong Geng. "Continuous Low-Thrust Time-Optimal Orbital Maneuver". In: *Proceedings of the 48h IEEE Conference on Decision and Control (CDC) held jointly with 2009 28th Chinese Control Conference*. IEEE. 2009, pp. 1457–1462. DOI: `10.1109/CDC.2009.5399622` (cit. on p. 109).

[108] Ehsan Taheri. "Optimization of Many-Revolution Minimum-Time Low-Thrust Trajectories Using Sundman Transformation". In: *AIAA Scitech 2021 Forum*. 2021, p. 1343. DOI: `10.2514/6.2021-1343` (cit. on p. 109).

[109] Saeed Rahimian, Farhang Jalali, J. Seader, and Ralph White. "A New Homotopy for Seeking All Real Roots of a Nonlinear Equation". In: *Computers and Chemical Engineering* 35.3 (2011), pp. 403–411. DOI: `10.1016/j.compchemeng.2010.04.007` (cit. on p. 114).

[110] Amit Bhaya and Fernando Pazos. "Homotopy Methods for Zero Finding from a Learning/Control Liapunov Function Viewpoint". In: *2013 International Conference on Control, Decision and Information Technologies, CoDIT 2013* (2013), pp. 881–886. DOI: `10.1109/CoDIT.2013.6689659` (cit. on p. 114).

[111] Layne Watson. "Probability-One Homotopies in Computational Science". In: *Journal of Computational and Applied Mathematics* 140.1-2 (2002), pp. 785–807. DOI: `10.1016/S0377-0427(01)00473-3` (cit. on pp. 114, 115).

[112] Shui Chow, John Mallet-Paret, and James Yorke. "Finding Zeroes of Maps: Homotopy Methods that are Constructive with Probability One". In: *Mathematics of Computation* 32.143 (1978), pp. 887–899. DOI: 10.1090/S0025-5718-1978-0492046-9 (cit. on p. 115).

[113] Kiyotaka Yamamura. "Simple Algorithms for Tracing Solution Curves". In: *IEEE Transactions on Circuits and Systems I: Fundamental Theory and Applications* 40.8 (1993), pp. 537–541. DOI: 10.1109/81.242328 (cit. on p. 117).

[114] Daniele Mortari. "The Theory of Connections: Connecting Functions". In: *arXiv preprint arXiv:1812.10626* (2018) (cit. on p. 118).

[115] F. H. Branin. "Widely convergent method for finding multiple solutions of simultaneous nonlinear equations". In: *IBM Journal of Research and Development* 16.5 (1972), pp. 504–522. DOI: 10.1147/rd.165.0504 (cit. on p. 124).

[116] Pedro Zufiria and Ramesh Guttalu. "On the Role of Singularities in Branin's Method from Dynamic and Continuation Perspectives". In: *Applied Mathematics and Computation* 130.2-3 (2002), pp. 593–618. DOI: 10.1016/S0096-3003(01)00120-5 (cit. on p. 124).

[117] Layne Watson. "Globally Convergent Homotopy Methods: a Tutorial". In: *Applied Mathematics and Computation* 31 (1989), pp. 369–396. DOI: 10.1016/0096-3003(89)90129-X (cit. on p. 129).

[118] Layne Watson and Chang Wang. "A Homotopy Method Applied to Elastica Problems". In: *International Journal of Solids and Structures* 17.1 (1981), pp. 29–37. DOI: 10.1016/0020-7683(81)90044-5 (cit. on p. 129).

[119] Lorenzo Casalino and Guido Colasurdo. "Optimization of Variable-Specific-Impulse Interplanetary Trajectories". In: *Journal of Guidance, Control, and Dynamics* 27.4 (2004), pp. 678–684. DOI: 10.2514/1.11159 (cit. on p. 134).

[120] Luigi Mascolo, Alessia De Iuliis, and Lorenzo Casalino. "Fast and Accurate Estimation of Fuel-Optimal Trajectories to Near-Earth Asteroids". In: *Acta Astronautica* 188 (2021), pp. 49–56. DOI: 10.1016/j.actaastro.2021.07.013 (cit. on p. 135).

Colophon

This document was typeset using the typographical look-and-feel `PhD_Dis` developed by Diogene Alessandro Dei Tos. The style is inspired by J. Stevens and L. Fossati *phdthesis Style*.

`PhD_Dis` is available for both LaTeX and LyX:

`https://gitlab.com/diogene/PhD_Dis.git`